An integrated geological-geophysical approach to subsurface interface reconstruction of muon tomography measurements in high alpine regions

Inaugural dissertation
of the Faculty of Science,
University of Bern

presented by

Alessandro Diego Lechmann

from Sumvitg GR

Supervisors of the doctoral thesis:

Prof. Dr. Fritz Schlunegger

Institute of Geological Sciences, University of Bern

Prof. Dr. Paola Scampoli

Albert Einstein Center for Fundamental Physics,
Laboratory for High Energy Physics, University of Bern

Department of Physics “Ettore Pancini”, University of Naples Federico II

Accepted by the Faculty of Science.

Bern, 09.07.2021

The Dean
Prof. Dr. Zoltan Balogh

Abstract

Muon tomography is an imaging technique that emerged in the last decades. The principal concept is similar to X-ray tomography, where one determines the spatial distribution of material densities by means of penetrating photons. It differs from this well-known technology only by the type of particle. Muons are continuously produced in the Earth's atmosphere when primary cosmic rays (mostly protons) interact with the atmosphere's molecules. Depending on their energies these muons can penetrate materials up to several hundreds of metres (or even kilometres). Consequently, they have been used for the imaging of larger objects, including large geological objects such as volcanoes, caves and fault systems. This research project aimed at applying this technology to an alpine glacier in Central Switzerland to determine its bedrock geometry, and if possible, to gain information on the bedrock erosion mechanism. To this end, two major experimental studies have been conducted with the aim to reconstruct bedrock geometries of two different glaciers. Given this framework, I present in this thesis my contribution to the project in which I worked for 5 years.

Most of the technological know-how of muon tomography still lies within physics institutes who were the key drivers in the development of this method. As the geophysical/geological community is nowadays an important user of this technology, it is important that also non-physicists familiarise themselves with the theory and concepts behind muon tomography. This can be seen as an effective method to bring more geoscientists to utilize this new technology for their own research. The first part of this thesis is designed to tackle this problem with a review article on the principles of muon tomography and a guide to best practice. A second important aspect is the reconstruction of the bedrock topography given muon flux measurements at various locations. Many to-date reconstruction algorithms include supplementary geological information such as density and/or compositional measurements only on the side. A probabilistic framework was successfully set up that allows for such additional data to be included into the inversion. This may be used to better constrain the bedrock geometry. Moreover, this flexible framework allows also for the inclusion of modelling errors in the physical models which may result in a more reliable estimate of the mean and standard deviation of the bedrock position. The third article is concerned with the determination of the effect of rock composition on the muon flux measurements. Researchers in the community use a made-up rock, called "standard-rock" in their calculations. Hitherto, it was unclear in which geological settings this is a valid assumption and in which the induced error becomes too large. Simulations that use this fantasy rock are performed and compared to simulations that use a more realistic rock model. It was found that for felsic rocks the standard-rock approximation is valid over all thickness ranges, while for mafic rocks and limestones this can lead to a serious bias if the rock is thicker than 300m.

Acknowledgements

First, I want to thank my supervisors Fritz Schlunegger and Paola Scampoli for their patience, guidance and relentless support throughout and especially during difficult phases of my PhD. You also provided me with the opportunities to glance into interesting geological and physical research fields that were not directly tied to our project. For the support you gave me in pursuing a teaching career and making it possible to unite my desire with the requirements of a PhD, I would like to express my deep gratitude. Furthermore, I would like to thank Edi Kissling for reviewing my thesis as an external supervisor. Your lectures as a professor during my undergraduate studies at ETH Zurich were a main reason for sparking my interest in Geophysics.

In the following, I thank the other members of our project group, "Eiger-mu", that were part of the laboratory of high energy physics (LHEP) at the University of Bern. Antonio Ereditato for his oversight on the project as a whole, always having in mind how we can reach out to a larger audience with our research. I would like to thank Akitaka Ariga, Tomoko Ariga, and Ryuichi Nishiyama not only for the management of the project but also for countless interesting discussions on physics, hobbies and cultural peculiarities and differences between Switzerland and Japan. I feel very grateful to you for allowing me to realise a lifelong dream of visiting Japan. You gave me an unfiltered access to Japanese culture by participating in the Judo class, bathing in an Ofuro ("does it work like in anime?"), showing cosmic rays to Japanese primary school kids, and many more. To you and your families back home in Japan, thank you very much for this unforgettable experience, どうもありがとうございました。 I thank Mykhailo Vladymyrov for his help with my coding problems. The discussions with you about code design principles and programming problems were always very enlightening. I thank Ciro Pistillo as essential part of the emulsion group for his many inputs for our project. The questions you asked during the project meetings forced us to view our procedures from another angle. Finally, I want to thank Samuel Käser. Your help with the detector installation and the data analysis of the side project was greatly appreciated. Also, the numerous discussions with you about various statistical methods were helpful for the subsequent development of my code.

Next, I would like to thank all the institutions without which this project and followingly this thesis would not have been feasible. First and foremost, I thank the Swiss National Science Foundation, SNSF that funded this project with number 159299. Further I am grateful to the staff of the Jungfraubahnen railway company. Specifically, I thank Stefan Michel who oversaw our field work in the railway tunnel, had to deal with our logistical problems, and made sure that we could always work safely. Further, I thank the staff from research station on the Jungfraujoch which is part of the foundation High Alpine Research Stations Jungfraujoch & Gornergrat (HFSJG) that provided us with accommodations during our field work in the tunnel. I name here especially the custodians Maria Otz, Urs Otz, Joan Fischer, and Martin Fischer, who welcomed us always heartily, showed us the interesting experiments that they were

maintaining, and helped us greatly whenever we had to perform some measurements around the research station.

Moreover, I would like to express my gratitude towards all the geologists who supported me even though I worked at the Geology institute only half of my PhD-time. My thanks go to Marco Herwegh who, as head of teaching at the institute. You gave me the opportunity to create a tutorial for first year students and thus discover my passion for teaching. I want to thank also all the other faculty staff for the intriguing field courses that I was able to accompany and your support of my tutorial. I am grateful to the staff of the secretariat from the geology institute for all the times you helped me with the organisational difficulties of the tutorial and my occasional civil service. Finally, thanks to all the PhD students from our office 204 for the funny and interesting discussions, the nice working atmosphere, and the occasional after work beer that I could be part of. You filled the PhD life with acutal “life”.

In this final paragraph I express my gratitude to my family and close friends. First, I would like to thank David Mair and his wife Sabrina Dötzl. Thank you for all the wonderful and fun moments during this PhD, be it as your field photographer, as your guest in Vienna, in a pub discussing weird theories, etc. Put simply, thank you for being such good friends. It was a great pleasure to work with you on this project. Then, I thank Regula Vlasek, Hansjörg Vlasek, Gabriel Vlasek, Julia Kostadinova, and especially Andrina Vlasek for supporting me emotionally, logistically, and with alpine know-how during a large part of my undergraduate and PhD studies. You also introduced me to the world of the High Alps and showed me a different perspective on hiking that resonates with my soul. For all these reasons (and many more) I am profoundly grateful to you. Further, I would like to thank my family, namely Eva Lechmann, Diego Lechmann, Nadia Lechmann, Rosmarie Baumann, and Andreas Spielhofer. You unconditionally supported me for all my life, even when I took a questionable turn or a detour. You helped me during difficult times and were always there for me when I needed it the most. Your encouragement to follow my beliefs on what to do in my life enabled me to become the person I am now. Finally, thanks to Lina Zbinden for the continuous patience and emotional support. You allowed me to retreat from the hectic of everyday life and recharge my batteries. Thank you for being there for me.

Table of Contents

List of figures

List of tables

Chapter 1
Introduction

1.1 The project

This dissertation is part of the SNF (Swiss National Science Foundation) project 159299 with the title: "Development and scientific application of nuclear emulsion particle detectors to geological problems in 3D". This work also presents my contribution within this captivating interdisciplinary research field between earth sciences and particle physics. The main objectives of the two disciplines were twofold. The particle physicists on the one hand planned to test their detector technology in a new field in the geoscience domain. The geologists on the other hand had the rather practical question of whether it is feasible to measure the bedrock geometry underneath an active glacier. The problem here was the scarcity of knowledge on subglacial erosion processes. It is always possible to examine the glacial remnants within moraines or a cirque (e.g. Hooke, 1991; Sanders et al., 2010), that means circularly shaped valleys in the top region of mountain ridges. This however only marks the end state of glacial erosion, with a time integrated erosion signal. Thus, it would be highly intriguing if erosion processes underneath an active glacier could be examined at the very moment they act. As those processes are closely linked to the glacial bedrock geometry (e.g. Brocklehurst & Whipple, 2002, 2004; Herman et al., 2011), one may gain substantial information on these erosion mechanisms by resolving the bedrock shape underneath an active glacier.

For such an undertaking, geophysical survey methods are usually the tool of choice, as they allow to gain insight on the bedrock geometry in all three dimensions. This contrasts to information from boreholes, which yield point information only. The latter does not necessarily pose a restriction as boreholes can yield important information if they are incorporated into a larger model (see Dürst Stucki & Schlunegger, 2013). At this point the question naturally emerges as to why we use a completely new technology to assess subglacial bedrock shapes, when the arsenal of geophysical methods offers other well explored and thus standard tools. This may be answered by the fact that even those well-established methods may pose major logistic and technical challenges upon employing in a high alpine, icy terrain. Gravimetry as all potential field methods suffers inherently from non-unique solutions, which makes it a great support, but not a standalone tool. Nevertheless, it is a frequently used method in alpine settings (e.g. Annecchione et al., 2001; Studinger et al., 2004). Seismological methods rely greatly on a cohesive material, which is required such as that the seismic signals are not lost or do not get scattered upon penetrating the material of interest. In particular, cracks on a glacier or generally void cavities and glacial meltwater may lead to a loss of signal. Lastly, the geometry of the subglacial bedrock must be sufficiently flat to allow for enough reflections., and thus a steep bedrock geometry may be prohibitive. Consequentially it is more frequently used in the context of overdeepened valleys (e.g. Barnaba et al., 2010). The third method, Ground penetrating radar (GPR), which usually is the primary choice for

cryospheric applications (e.g. Grab et al., 2018), does also have some shortcomings when the material of interest in situated in or close to a water table. These difficulties of the aforementioned geophysical methods leave an interesting opening for new technologies, such as muon tomography.

Our interdisciplinary team consisted of a group of particle physicists from the laboratory of high energy physics (LHEP) who contributed to the project with their know-how on the detector technology. Thus, the project could profit from the already present detector and analysis infrastructure at the physics department at the University of Bern. This infrastructure has been put in place as part of their contribution to the OPERA experiment (Acquafredda et al., 2009). On the other hand, the geologists from the University of Bern shared their knowledge on the characterisation of erosion processes in glacial and fluvial environments and the geological architecture of the target area.

1.2 The study region

1.2.1 Geographical situation

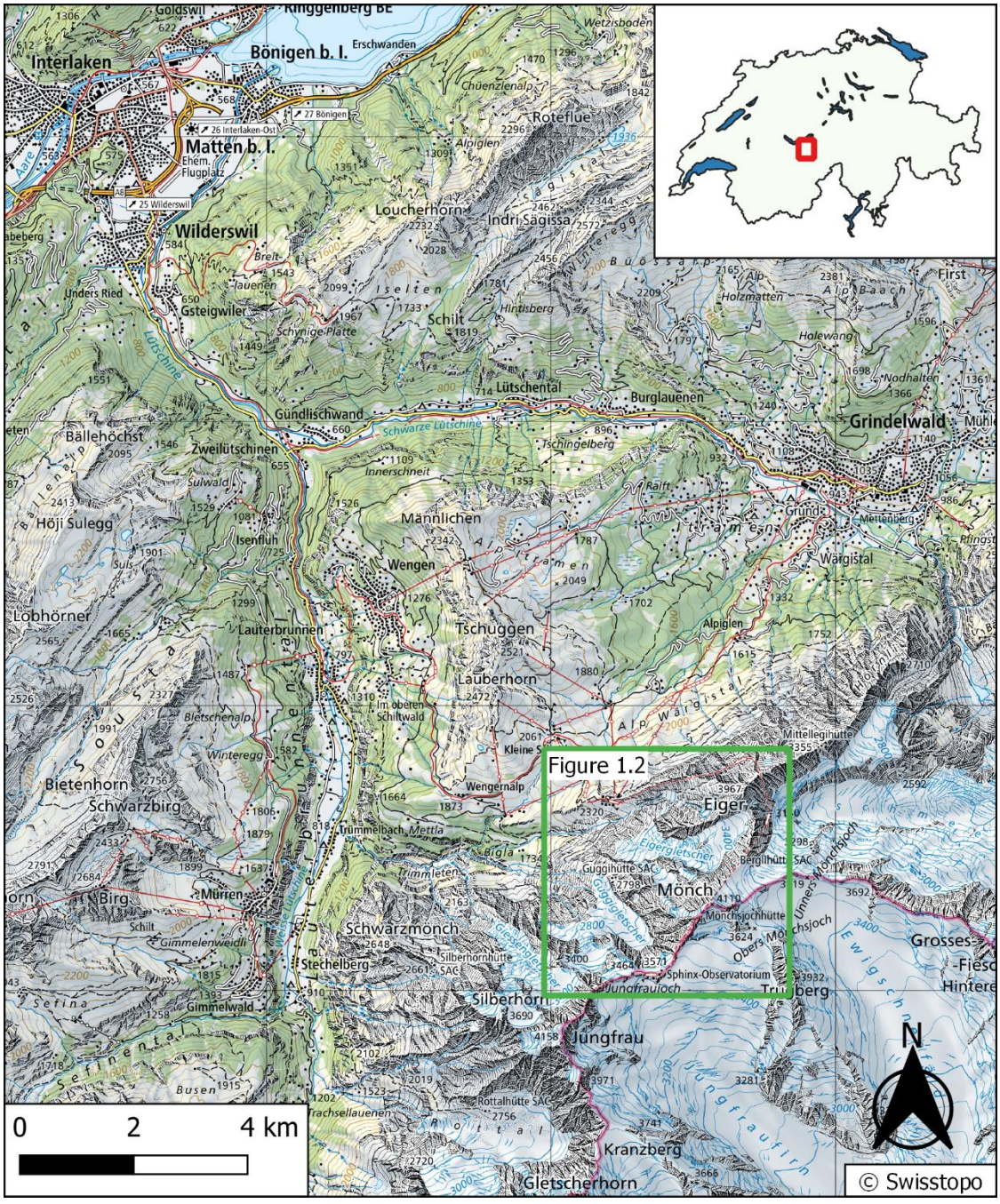

Figure 1.1: Map of the larger Jungfrau region. The city of Interlaken is located in the north, and the villages Lauterbrunnen and Grindelwald are visible in the West and Northeast respectively. The extent of the study region is shown as a green square (see Fig. 1.2 for details).

The study region is located around three prominent summits of the Central Swiss Alps: Eiger, Mönch and Jungfrau. More precisely our project investigated two different glaciers, which are highlighted in Figure 1.1. Here, I provide a rough geographical introduction to this region.

The study region can be reached by public transport from Interlaken, a well-known city in the Bernese Oberland, that is located between two lakes (Lake Thun and Lake Brienz). Farther south along the river

Lütschine, the valley splits at Zweilütschine. One valley leads towards Grindelwald in the east, whereas the other valley heads south to Lauterbrunnen. The southernmost point of the watershed between these two resulting valleys is called the Kleine Scheidegg, which can be reached from either Grindelwald or Lauterbrunnen by train. It is also the starting point of the ascent by train to the Jungfraujoch. The train tunnel, which enters the mountain to the west of Mt. Eiger ascends in a half-circle beneath Mt. Eiger and later Mt. Mönch until it leads to the Jungfraujoch, SW of Mt. Mönch. This station, although of primarily touristic interest, also contains a research station that is part of the trust High Alpine Research Station Jungfrajoch & Gornergrat (HFSJG; German: Hochalpine Forschungsstationen Jungfraujoch & Gornergrat), where even nowadays particle physics and meteorological experiments (HFSJG, 2021) are performed.

The Jungfraujoch station is located on a steep ridge that strikes from SW to NE. Interestingly this ridge is the continental watershed, that splits the catchment area of the Aare river, to the north of our study region, from the catchment area of the Rhone river to the south of our study region. While the Aare joins the Rhein river and flows towards the north through Germany, France and the Netherlands before it discharges into the North Sea, the Rhone flows into the Lake Geneva before it continues its flows across southern France, where it flows into the Mediterranean Sea. The mountains Eiger and Mönch surround one of our target glaciers, the Eiger Glacier, which flows towards the Kleine Scheidegg in the NW. The second target glacier is the very margin of the Jungfraufirn towards the south of the Jungfraujoch. This latter glacier, which is referred to as the Aletsch Glacier, is part of one of the largest remaining alpine glaciers in the Swiss Alps.

1.2.2 Geological situation

The geological structure of this region is rather intricate and still an issue of ongoing research. A detailed description of the structural architecture of the region goes beyond the scope of this thesis and I therefore gladly refer the reader to the work of Mair et al. (2018), where the geological architecture is presented at a high level of detail. However, for the sake of completeness I shortly describe the important aspects, that may affect the muon tomographic experiment.

The local geological architecture is dominated by the Aar-Massif, which is the part of the basement of the European continental plate, and which experience a phase of rapid block uplift c. 20 Ma ago (Herwegh et al., 2017). Due to this uplift in conjunction, which occurred in the course of the Alpine orogeny (i.e. the NW-SE subduction of the European plate beneath the Adriatic plate) the overlying sedimentary cover units were stacked upon each other and deformed during thrusting and folding. A geological overview is presented in Figure 2 of Mair et al. (2018). From this map I may use two crucial pieces of information. First, in the upper region of the Jungfrau Railway tunnel, where we installed one detector (see Ch. 1.3 for more detail), the rock consists mostly of gneisses from the Aar-Massif. Second, in the part of the tunnel directly south of Mt. Eiger as well as below the Eiger-glacier, the rock consists

predominantly of limestones of the Meszoic sedimentary cover. This information can be incorporated in the inversion algorithm, which is shown in more detail in Ch. 3.

1.3 Measurement campaigns

In the study region that was introduced in Fig. 1.1, we conducted two experiments. Both locations are indicated in Fig. 1.2 on a close-up map of the study region. The first experiment was a feasibility study near the top of the Jungfrau railway facing south. This project was designed to evaluate the processing chain from detector installation, over data acquisition to inversion into a sensible result. So, we could locate the nooks and crannies in the hardware, software and workflow and improve them for an application to the larger main experiment. This feasibility study was then also dubbed "Side Project", whereas the principal experiment was named "Main Project".

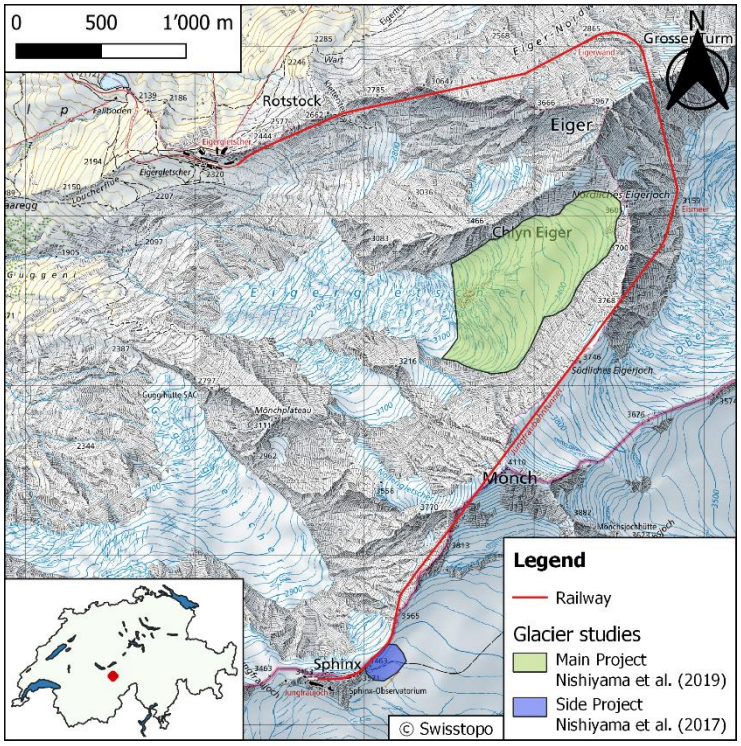

Figure 1.2: Close-up map of the study region around the mountains Eiger and Mönch. The blue patch indicates the mapped glacier bedrock region in a small feasibility study (called "Side Project") whereas the green patch shows the extent of main observational target (called "Main Project"). The red line corresponds to the railway train tunnel where the detectors for both projects were installed.

The goal of both experimental campaigns was nevertheless the same: We were interested in reconstructing the ice-bedrock interface geometry in order to gain insight into the mechanisms of subglacial erosion. In addition to that, the results of the Side Project were also interesting for the Jungfraubahnen railway company as the study region is a touristic hotspot, where tourists have access to the glacier. In light of global warming and the subsequent shrinking of the glaciers, the railway company was interested in knowing the geometry of the bedrock-ice contact for long-term safety reasons. The results of the main project on the other hand were primarily of academic interest.

More details on these two measurement campaigns, their situation and data analysis can be found in Ch. 6 & 7, where I have included the respective scientific articles.

1.4 Project goals

In order to carry this project into execution several smaller "building blocks" had to be addressed. In the following paragraphs I summarise the various goals and the consequential tasks that were defined for the subdisciplines of geology, physics, and geophysics, respectively.

From the geological side, one of the major tasks was to provide an updated 3D geological model of the study region to ensure that the experimental measurements can be constrained with independent data. Due to the scarce nature of up-to-date data in this region Mair et al. (2018) have compiled a new geological map including recent field data and condensed it into an updated and tectonically as well as stratigraphically coherent 3D model of the geological architecture. The laboratory measurements of the physical properties of the lithological units were not essential to that paper. They are presented in Chapter 3 where it is shown how these measurements may constrain the results of the muon tomography experiment. Mair et al. (2019, 2020) further investigated the erosion processes in the Eiger region by means of concentrations of cosmogenic radionuclides and frost cracking modelling. These latter two studies are mostly independent from the (geo)physical problems of the muon tomography experiment but serve to offer the geological frame of this project.

From the physics point of view several goals had to be achieved in addition to the data acquisition. The first being the construction of a facility that allows to produce our own emulsion films. This was required because our project needed a steady supply of emulsion films, which were the main component of our detectors (please refer to Ch. 2 and Ariga et al. (2018) for a justification and a description of how these detectors work). Second, the existing analysis infrastructure had to be extended by a facility that allowed to photographically develop the emulsion films. Third, as muon tomography necessitates the analysis of a big emulsion film area for the purpose of collecting statistically sufficient data, the microscope laboratory had to be upgraded for faster scanning speeds and higher data throughput. These hardware upgrades also include the development and/or upgrade of the related software.

Physicists conduct the raw measurement, whereas geologists deliver frame conditions and the embedment of the final result into a specific picture. The space in-between these two disciplines is then taken by geophysicists and this was my personal operating range within this project. Several objectives were initially defined for this project role, the main part being the development of a suitable inversion algorithm. Inversion in the geophysical sense connotes the retrieval of physical parameters and their respective uncertainties from measurements. Likewise, a major goal was to establish a common vocabulary between both disciplines. Interestingly, despite both being natural sciences, physicists and geologists have two quite different mind-sets embedded in their communities. As an illustrative example I name the handling of measurement "errors". While in particle physics uncertainties are mostly given in 5σ (i.e. 5 times the standard deviation), in geology 1σ is often good enough. On top of this, there is

an enormous difference in scale involved in research. Particle physicists work with objects that encompass several nanometres and even down to femtometres in size, whereas geologists handle length scales of metres up to kilometres. The discrepancy in timescales is even more astounding, as particle interactions occur in nanoseconds, while geological processes may take hundreds to thousands of years (in the case of glacial processes) or even millions of years (for tectonic processes).

1.5 Outline

The main findings of this doctoral thesis are condensed in 3 scientific articles that either have already been published or are currently in the publication pipeline. These papers are reformatted here into three self-contained chapters (2, 3 and 4). For the sake of offering a common thread throughout this thesis, the articles (and thus chapters) are not ordered by publication date. Instead I compiled the chapters according to their accessibility for a reader who is not familiar with muon tomography.

Chapter 2 is conceptualized as a review article on muon tomographic experiments in geoscientific research. This paper is addressed to a broader geoscientific community and thus describes the origins and the physical principles behind muon tomography. This article is designed to be a practical "handbook" for earth scientists and does not focus too much on the details of physical formulae. It covers the most basic physical models (i.e. cosmic ray muon flux, energy loss of muons in matter) as well as important concepts (like multiple scattering, or the influence of rock composition) and explains the related roles in the entire processing chain but refers the readers to other literature when necessary. Subsequently, the readers are introduced in the same manner to the various detector types and exemplary geoscientific experiments as inspiration. The study concludes with a guide to best practice, raising important points that a prospective user should consider, if he/she decides to use muon tomography in their own research.

After having established the broad topic of muon tomography and its most important building blocks in Ch. 2, Ch. 3 focuses on the development of an inversion algorithm, as a natural continuation of the equations presented in Ch. 2. Therefore, this particular study is written as a theory paper alongside a python toolbox that allows researchers to apply the methodology designed in this paper. The main idea behind this work is to introduce the broader muon tomography community to the tools that are available if a Bayesian framework is established. We show how additional, geological (field-/lab-) information can be integrated into a muon tomographic experiment and how the resulting equations can be approached. For this study we explicitly use a Monte Carlo method to solve the inverse problem.

Chapters 2 and 3 already give the reader information on the internal workings of muon tomography that we consider sufficient to devise an own experiment. Chapter 4 on the other hand covers a much more specific problem, which is centred on exploring the influence of rock composition on muon tomography measurements. This is an effect that mainly appears when one attempts to measure through a rock pile that is thicker than 300m, such that only a part of the muon tomography studies will have to consider such a correction. This effect can be traced back to the use of a "standard rock" in the community. The

correction is then necessary if the target rock deviates compositionally from that “standard rock”. Although the sensitivity of a muon tomographic experiment to rock composition is small for thin rock, the consideration of a rock-dependency muon attenuation opens up an avenue to draw further inferences on it. This study explores the magnitude of the rock composition effect for various rock types and various thicknesses.

The summary and a retrospect over the project including possible avenues for future developments of muon tomography are presented in the conclusive, fifth chapter.

For completeness, the main (muon tomographic) results of this project (Nishiyama et al., 2017, 2019) are presented as separate chapters in the appendix of this thesis.

1.6 References

Acquafredda, R. et al.: *The OPERA experiment in the CERN to Gran Sasso neutrino beam*, Journal of Instrumentation, 4, P04018, https://doi.org/10.1088/1748-0221/4/04/P04018, 2009.

Annecchione, M. A., Chouteau, M., and Keating, P.: *Gravity interpretation of bedrock topography: The case of the Oak Ridges Moraine, southern Ontario, Canada*, Journal of Applied Geophysics, 47, 63–81. https://doi.org/10.1016/S0926-9851(01)00047-7, 2001.

Ariga, A., Ariga, T., Ereditato, A., Käser, S., Lechmann, A., Mair, D., Nishiyama, R., Pistillo, C., Scampoli, P., Schlunegger, F., and Vladymyrov, M.: *A Nuclear Emulsion Detector for the Muon Radiography of a Glacier Structure*, Instruments, 2, 7, https://doi.org/10.3390/instruments2020007, 2018.

Barnaba, C., Marello, L., Vuan, A., Palmieri, F., Romanelli, M., Priolo, E., and Braitenberg, C.: *The buried shape of an alpine valley from gravity surveys, seismic and ambient noise analysis*. Geophysical Journal International, 180, 715–733. https://doi.org/10.1111/j.1365-246X.2009.04428.x, 2010.

Brocklehurst, S. H., and Whipple, K. X.: *Glacial erosion and relief production in the Eastern Sierra Nevada, California*. Geomorphology, 42, 1–24. https://doi.org/10.1016/S0169-555X(01)00069-1, 2002.

Brocklehurst, S. H., and Whipple, K. X.: *Hypsometry of glaciated landscapes*. Earth Surface Processes and Landforms, 29, 907–926. https://doi.org/10.1002/esp.1083, 2004.

Dürst Stucki, M., and Schlunegger, F.: *Identification of erosional mechanisms during past glaciations based on a bedrock surface model of the central European Alps*. Earth and Planetary Science Letters, 384, 57–70. https://doi.org/10.1016/j.epsl.2013.10.009, 2013.

Grab, M., Bauder, A., Ammann, F., Langhammer, L., Hellmann, S., Church, G. J., Schmid, L., Rabenstein, L., and Maurer, H. R.: *Ice volume estimates of Swiss glaciers using helicopter-borne GPR — an example from the Glacier de la Plaine Morte*, 2018 17th International Conference on Ground Penetrating Radar (GPR), 1–4. https://doi.org/10.1109/ICGPR.2018.8441613, 2018.

Herman, F., Beaud, F., Champagnac, J.-D., Lemieux, J.-M., and Sternai, P.: *Glacial hydrology and erosion patterns: A mechanism for carving glacial valleys*. Earth and Planetary Science Letters, 310, 498–508. https://doi.org/10.1016/j.epsl.2011.08.022, 2011.

Herwegh, M., Berger, A., Baumberger, R., Wehrens, P., and Kissling, E.: *Large-Scale Crustal-Block-Extrusion During Late Alpine Collision*. Scientific Reports, 7, 413, https://doi.org/10.1038/s41598-017-00440-0, 2017.

HFSJG: *Research topics at Jungfraujoch*, https://www.hfsjg.ch/en/jungfraujoch/research-topics/ (last access: 21.02.2021).

Hooke, R. L.*: Positive feedbacks associated with erosion of glacial cirques and overdeepenings*. GSA Bulletin, 103, 1104–1108. https://doi.org/10.1130/0016-7606(1991)103<1104:PFAWEO>2.3.CO;2, 1991.

Mair, D., Lechmann, A., Delunel, R., Yeşilyurt, S., Tikhomirov, D., Vockenhuber, C., Christl, M., Akçar, N., and Schlunegger, F.: *The role of frost cracking in local denudation of steep Alpine rockwalls over millennia (Eiger, Switzerland)*, Earth Surface Dynamics, 8, 637–659, https://doi.org/10.5194/esurf-8-637-2020, 2020.

Mair, D., Lechmann, A., Herwegh, M., Nibourel, L., and Schlunegger, F.: *Linking Alpine deformation in the Aar Massif basement and its cover units – the case of the Jungfrau–Eiger mountains (Central Alps, Switzerland)*, Solid Earth, 9, 1099–1122, https://doi.org/10.5194/se-9-1099-2018, 2018.

Mair, D., Lechmann, A., Yesilyurt, S., Tikhomirov, D., Delunel, R., Vockenhuber, C., Akçar, N., and Schlunegger, F.: *Fast long-term denudation rate of steep alpine headwalls inferred from*

cosmogenic 36 Cl depth profiles, Scientific Reports, 9, 11023, https://doi.org/10.1038/s41598-019-46969-0, 2019.

Nishiyama, R., Ariga, A., Ariga, T., Käser, S., Lechmann, A., Mair, D., Scampoli, P., Vladymyrov, M., Ereditato, A., and Schlunegger, F.: *First measurement of ice-bedrock interface of alpine glaciers by cosmic muon radiography*. Geophysical Research Letters, 44, 6244–6251, https://doi.org/10.1002/2017GL073599, 2017.

Nishiyama, R., Ariga, A., Ariga, T., Lechmann, A., Mair, D., Pistillo, C., Scampoli, P., Valla, P. G., Vladymyrov, M., Ereditato, A., and Schlunegger, F.: *Bedrock sculpting under an active alpine glacier revealed from cosmic-ray muon radiography*. Scientific Reports, 9, 6970, https://doi.org/10.1038/s41598-019-43527-6, 2019.

Sanders, J. W., Cuffey, K. M., MacGregor, K. R., Kavanaugh, J. L., and Dow, C. F.: *Dynamics of an alpine cirque glacier*. American Journal of Science, 310, 753–773. https://doi.org/10.2475/08.2010.03, 2010.

Studinger, M., Bell, R. E., and Tikku, A. A.: *Estimating the depth and shape of subglacial Lake Vostok's water cavity from aerogravity data*. Geophysical Research Letters, 31, L12401, https://doi.org/10.1029/2004GL019801, 2004.

Chapter 2

Muon tomography in geoscientific research – a guide to best practice

Alessandro Lechmann[1], David Mair[1], Akitaka Ariga[2], Tomoko Ariga[3], Antonio Ereditato[2], Ryuichi Nishiyama[2], Ciro Pistillo[2], Paola Scampoli[2,4], Mykhailo Vladymyrov[2], and Fritz Schlunegger[1]

[1]Institute of Geological Sciences, University of Bern, Bern, CH-3012, Switzerland
[2]Albert Einstein Center for Fundamental Physics, Laboratory for High Energy Physics, University of Bern, Bern, CH-3012, Switzerland
[3]Faculty of Arts and Science, Kyushu University, Fukuoka, J-812-8582, Japan
[4]Dipartimento di Fisica "E.Pancini", Università di Napoli Federico II, Napoli, I-80126, Italy

Prepared for publication in: Solid Earth, EGU Open Access Journal

2.1 Abstract

The use of muon tomography in geoscience projects has been increasing constantly over the past few years. This led to a variety of applications that often use custom tailored solutions for data acquisition and processing. The respective know-how is splintered and mainly available in semi-published state in various physics departments that developed these methods. This complicates the design of new studies and the decision whether muon tomography is a suitable tool and feasible for a specific geoscientific issue. In this study we review the current state of muon tomography in geosciences with the goal of equipping interested geoscientists with the basic knowledge on the physical basics that constitute muon tomography. After an explanation into the topics of how muons are produced, how they traverse matter and how they are recorded, a showcase is made of recent applications. These studies show the variety of applicability of muon tomography experiments, such that interested readers may implement this technology for their own research. Finally, we provide a guide to best practice to help interested geoscientists decide if and how muon tomography could be implemented in their own research. We believe that through better mutual understanding, new interdisciplinary collaborations are initiated that advance the whole field of muon tomography.

2.2 Introduction

2.2.1 General introduction

Many industrial and scientific problems dealing with geological matters require some form of geophysical exploration, or remote sensing in the broader sense. Often detailed knowledge of the local geology, i.e. lithological structures in the surroundings, is needed as an integral part of most surveys. The field of geophysics offers a rather large variety of well-established methods to meet this need. Depending on the exact nature of information that has to be gathered and the deployment constraints in the field, one is usually free to choose between seismological (sensitive to density), gravimetric (also

sensitive to density), and electromagnetic (like ground penetrating radar or electrical resistivity tomography; both sensitive to electrical resistivity) methods (e.g. Kearey et al., 2002).

A large amount of scientific work in geophysics is dedicated to the refinement of existing techniques, e.g. by deploying advanced mathematical and computational models supported by powerful computers (e.g. Reichstein et al., 2019) improving workflows for data analysis, optimising the experimental setups (e.g. Maurer et al., 2010), etc., such that these methods may be applied to new fields or even to extensive data sets that could not be handled before. It is thus rare to see a new technology emerge next to the continuously improving, established geophysical methods. Nevertheless, since the start of the millennium naturally occurring cosmic rays – they are already exploited in the geochronology community for dating purposes – have increasingly been utilised to gain insights on geological matters (see Ch. 2.4 for an overview). As only the muonic part of the cosmic ray spectrum is used, this novel research field has been given the name of "muon tomography" (see Ch. 2.3.1 for nomenclature, as also other notions are commonly used). Tanaka and Oláh (2019) show how the number of studies employing this new technology has been continuously growing.

Nowadays the technology has advanced beyond a pure proof-of-concept state, such that it may be applied as a central part of geological/geophysical research. Even though a few companies have begun to develop muon detectors at an industrial level (e.g. Harel and Yaish, 2019), the vast majority of detector design and construction is still very much concentrated at the universities. This entails that the detector know-how is splintered across the physics departments where particle detectors have been developed over the past years (e.g. Ariga et al. 2019).

This is the starting point of the present work as we see much potential for the further development of muon tomography with a large field of applications in geoscience research. We consider that a broader understanding of this technique would enable earth scientists, to shape the direction of future muon tomography research. Once geoscientists are able to clearly state their needs, while knowing the capabilities and limitations of this technique, particle physicists may be encouraged to develop their detectors accordingly. This paper addresses primarily geoscientists who have few to none experience with muon tomography. The scope of this review article is to equip them with the necessary information to approach a physics group for potential collaborations. We aim at providing a broad overview of how this technology works and setting the important geophysical equations in context, thereby considering different settings and questions, and we develop a guide that serves to facilitate decisions along with guidelines of how to proceed.

Accordingly, we first introduce in Ch. 2.2.2 the particle physical context from which this technology historically emerged. Chapter 2.3 explains central technical elements of muon tomography. This starts with a thorough description of the various muon flux models that can be utilised. The chapter continues with an explanation of the energy loss equation and possible ways to solve it. It is followed by an overview on the various detector types, their advantages, and drawbacks. The chapter then concludes

with a brief description of various methods to tackle the whole data analysis aspect, to provide the user with a few starting points for their own research. Chapter 2.4 provides the reader with a showcase of muon tomographic studies that were employed in a geoscientific setting. This is supposed to give the prospective users an overview of the range of possible applications of this technology. Chapter 2.5 outlines the most important steps that a geoscientist interested in using muon tomography for their project needs to consider.

2.2.2 A short history of muon tomography

The story of how muon tomography has evolved has to be taken as far back as to the first measurements of cosmic rays on the Eiffel tower (Wulf, 1910), underwater (Pacini, 1912) and during balloon flights (Hess, 1912) at the onset of the 20th century. These important experiments marked the beginning of numerous discoveries that were to come and eventually established the field of particle physics, which has turned out as a new branch of physics. Aided by the parallel advances in quantum mechanics, many new subatomic particles were found, most notably the proton (Bohr, 1913; Rutherford, 1919), the neutron (Chadwick, 1932), the positron (Anderson, 1932) and the muon (Neddermeyer and Anderson, 1937). Naturally occurring particles from the aforementioned cosmic ray flux were the most important sources to experimentally study particles, their interactions and decays. This has been the state of research even long before the gargantuan particles accelerators have been built.

The circumstance that electrically charged particles lose energy and/or change momentum when they penetrate any kind of material was already known at this time, as the experiments by Rutherford (1911) show. This model of energy loss is still used today as backbone for particle tomographic applications and has been refined since the early 20th century through meticulous experiments. The reader is referred to Tanabashi et al. (2018) for an overview of all the intricacies that are involved in the energy loss calculations as well as to Groom et al. (2001) for the case of muons.

These early discoveries have sparked the interest of numerous researchers to utilise cosmic rays to gain insight into a body placed between the source of cosmic rays and a particle detector. This was first done by George (1955) for the calculation of the overburden of a tunnel, which can be viewed as the first application of a tomographic setup where cosmic rays were used as the primary signal source. 15 years later Alvarez et al. (1970) set another milestone for this technology as they examined the famous pyramids at Giza, Egypt for presumed hidden chambers. However, as the detector technology as well as the physical theories of energy loss were not that advanced at this stage, and thus the quality of the results was not good enough for any further examination, following-up studies have not been undertaken for about 20 years.

The next steps of developments of the detector technology took a significant step forward with the establishment of numerous underground laboratories and the subsequent onset of large-scale experiments in particle physics. Bettini (2014b) presents an overview of different underground laboratories around the world. Among these are the Gran Sasso National Laboratory in Abruzzo in

Central Italy and the Kamioka Underground Observatory in Gifu prefecture in Central Japan that hosted the milestone neutrino oscillation experiment OPERA (Acquafredda et al., 2009) and the nucleon decay experiment KamiokaNDE (e.g. Kajita et al., 2012), respectively. The progress in detector technology was possible because physicists had to filter out noise induced by the naturally occurring cosmic rays that were interfering with their measurements. Underground laboratories provide a natural "shielding" against a large part of the cosmic ray particles that perpetually hit the Earth from above. The soil/rock overburden thus functions like a lead coat during an X-ray examination at the medical doctor, as this shield hinders particles to penetrate regions where they are undesired either for medical or technical reasons. Even though a significant part of the cosmic ray spectrum can be filtered out by performing an experiment in an underground laboratory, there exists still a component that may penetrate matter up to several kilometres and thus can be identified, measured, and analysed. These are the so-called muons. Without relying on too much particle physics theory (see reference below), these muons may be considered a "heavy version" of the electron, featuring a roughly 207-times higher mass. For more information on the physics of muons and how they were discovered, the reader is referred to the textbook by Bettini (2014a, p. 64-66). The mass difference between muons and electrons is the main reason why a muon of equal velocity penetrates more matter than its electron counterpart, which incidentally also occurs in the cosmic ray particle flux. This is one of the peculiar cases, where geoscientists (especially those working in cosmogenic nuclide dating, e.g. Gosse and Phillips, 2001) and particle physicists are confronted with the very same problem, when they are trying to quantify the muonic component in their measurements.

Particle detectors have continuously improved due to the ever-growing precision requirements of new experiments. In parallel, the theory of how charged particles lose energy while travelling through matter has been largely improved by dedicated absorption experiments (see Groom et al. 2001, and references therein). The advances in these two areas were the prerequisites for the resurgence of tomographic applications of cosmic rays (or more precisely cosmogenic muons). First attempts were made during the 90ies to characterise the internal structure of volcanoes in Japan (Nagamine, 1995; Nagamine et al., 1995). But only after the turn of the millennium the number of performed muon tomographic experiments started to increase. It was again the same Japanese research group from the Earthquake Research Institute in Tokyo (e.g. Tanaka et al., 2001, 2003, 2005) that pushed this new technology to a point where it can be considered as another valid method in the geophysical arsenal.

Several studies reviewed some technical aspects or the applications to specific sub-fields in recent years. Lesparre et al. (2010) provides a succinct overview of the technical basis of muon flux measurements, including a thorough review of time-dependent effects that might have a significant effect on result quality. They also discuss extensively different existing muon flux models. Although the subject is rather technical, the reader is referred to Groom et al. (2001) for a showcase of the central equations that govern the energy loss of muons traversing matter. Please note that the latter article does not focus on muon tomography in particular but presents the physical equations which are valid for all muons. We would

also like to point out a study by Kaiser (2019) that takes a rather unconventional standpoint. He explores the technology from an economic point of view and shows different evolving directions in the future. Marteau et al. (2012) is an earlier review that focuses mainly on volcanological applications and Procureur (2018) strongly focuses on scattering tomographic applications. Athanassas (2020) focuses in his on the muon tomography applications in the context of hazard assessment (mostly in volcanic environments).

A very detailed review on muon tomography as a whole is given by Bonechi et al. (2020). Readers will find this review to be quite complementary to this work. While we focus on compiling the most important equations, they provide a resourceful overview on detectors, applications, and common problems.

2.3 Principles of muon tomography

This section aims at introducing the corner posts of this technology. After a start where we explain of how this technology is called, we progress to an explanation of the basic equations, namely the energy loss equation and the mathematical description of the cosmic ray flux. We complement this section with an overview of the main inversion techniques. In a subsequent section, the reader is introduced to the most important types of detectors.

In this chapter, we proceed by following the path of a muon from its origin high in the stratosphere, to the matter it traverses and finally to the detector where it will be recorded. We find this the simplest way to describe the cascade of processes that are involved in the passage of muons from their origins to the site where they are registered.

2.3.1 Terminology

As already mentioned in the introduction, there exist different terms that describe this technology, that vary from one research group to another. Here, we summarise the most common notions. We begin with a rather rare term, “muon radiography”. Radiography is usually an imaging technology where absorbing qualities of an object are rendered visible by exposing them to a form of radiation. A typical example of this method is the X-ray image at a medical doctor’s or dentist’s office, where photons in the wavelength band of ca. 10 nm to 10 pm are used. This procedure is, however, not limited to only photons, as the detectors are usually sensitive to electrons which are produced by interactions of incident photons with the detector’s material and not the photons directly. Consequently, any charged particle could be utilised to produce such a radiography.

A second, widely used term is “muon tomography”. Incidentally, this is also the notion that we use throughout this work. This selection bases on our own background in geophysics, where the term “tomography” is more widely spread (i.e. seismic tomography, electric resistivity tomography) than “radiography”.

A third notion, which recently has gained some interest in the community, is “muography”. This circumvents any historically grown connotations as this fictional word composition just means “draw/write with muons”.

Until the community agrees to use a “standard” description, one may take a pragmatic approach to this issue and use the 3 terms above interchangeably. However, as the practitioner in muon tomography inevitably has to research literature at some point, it is useful to be aware of all different notions that describe this technology.

2.3.2 The cosmic ray flux

This chapter aims at providing the reader with an overview on the different available muon flux models. This is done by introducing first the mechanisms that produce the muons in the first place. Afterwards, we present the reader with four selected muon flux models and show how they are parametrised. This includes a specification of how these models account for various parameters, such as height, incidence direction, etc. We close this section with a crude analysis of the uncertainty that are attached to these muon flux models and recommendations for novice users.

2.3.2.1 Muon generation from primary cosmic rays

The starting point in our description of muon tomography is the site where the muons originate, i.e. the upper part of the atmosphere. In fact, muons are considered to be only “secondary” cosmic rays, as they are only produced by interactions of so called “primary” cosmic rays with the atoms in our atmosphere. These primary cosmic rays have different origins. Whereas the largest part of the particles originates within our own galaxy and the sun, there is also a small fraction (although consisting of much higher velocity particles) that are of an intergalactic nature. A thorough description of the incident primary particle spectra can be found in the chapter “Cosmic Rays” in Tanabashi et al. (2018, p. 424ff.).

Figure 2.1 (Fig 29.1 from Tanabashi et al., 2010, p. 424) shows the incident fluxes of different types of primary cosmic ray particles. Strikingly, the most abundant particles to hit the atmosphere are hydrogen nuclei, i.e. protons. However, towards higher energies this difference seems to shrink, as can be verified by the ratio of hydrogen to helium nuclei in the inset of Fig. 2.1. Other heavier nuclei do also hit the upper atmosphere; however, their contributions are negligible compared to hydrogen (and helium).

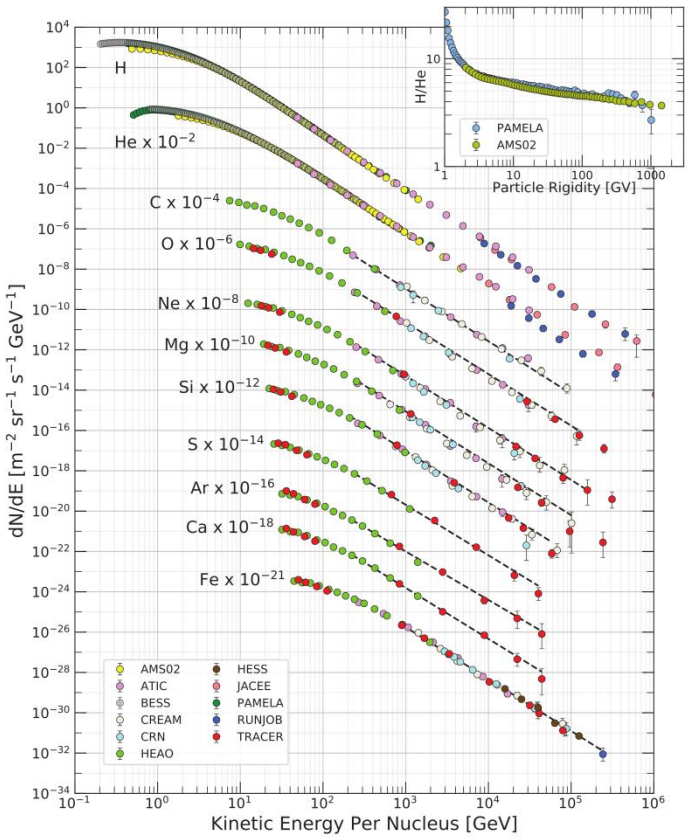

Figure 2.1: Differential energy spectrum of primary cosmic ray particles, from Tanabashi et al. (2018, p. 424). Coloured markers denote different experiments. Please refer to Tanabashi et al. (2018, p. 424ff.) and references therein for further information.

When these primary particles hit an atom in the upper atmosphere, new particles may be created (similar to collision experiments in particle accelerators). There are a large number of different interactions that might occur during these collisions. For a comprehensive overview, the reader is referred to Gosse and Phillips (2001, p. 1485ff.). Although this is a standard paper in the cosmogenic nuclide geochemistry community, we can make use of the same physical principles when we describe the cosmic ray flux (primary and secondary). As only a small portion of the overall interactions generate muons, we recreated a simplified version of Fig. 1 of Gosse and Phillips (2001, p. 1486) below (see Fig. 2.2).

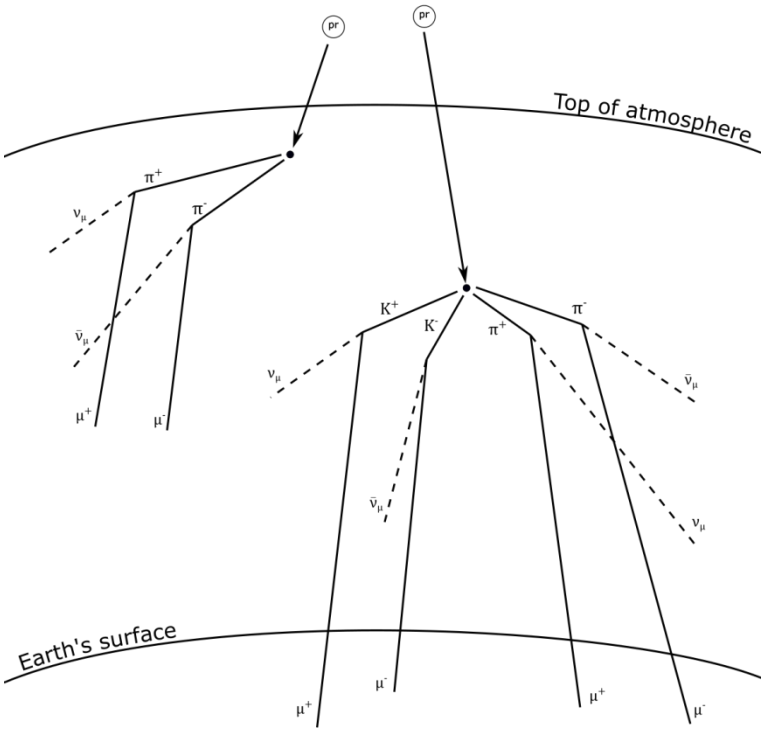

Figure 2.2: Interactions of primary cosmic ray particles (pr) with the atoms in the upper atmosphere (•). Simplified version of Fig. 1 of Gosse and Phillips (2001, p. 1486).

The incident primary cosmic ray particle (denoted with "pr" in Fig. 2.2) interacts with atoms and molecules in the upper atmosphere (the black circles, •, in Fig. 2.2) and produces so-called "mesons" (e.g. Gaisser et al., 2016). These are elementary particles that consist of only two quarks compared to the three quarks in protons and neutrons (which are part of another group, the "baryons"). The important mesons for muon tomography are the pions (π^-, π^+) and the kaons (K^-, K^+). Readers interested in additional information on these particles are referred to a standard particle physics textbook (e.g. Bettini, 2014a). Pions as shown in Fig. 2.2 decay in 99.99 % of the cases (Tanabashi et al., 2018, p. 1069f.) in the following form:

$$\pi^+ \rightarrow \mu^+ + \nu_\mu \tag{2.1a}$$

$$\pi^- \rightarrow \mu^- + \bar{\nu}_\mu \tag{2.1b}$$

The products of such decays are a muon (μ^-, μ^+) and a neutrino, ν_μ (or antineutrino, $\bar{\nu}_\mu$). Neutrinos are weakly interacting particles, which are often formed during decays of particles and as a by-product of various radioactive decays. Neutrinos are currently a very intensively studied branch of particle physics where considerable progress is being made. The award of the Nobel Prize in Physics to Takaaki Kajita and Arthur B. McDonald for their contributions to research in neutrino oscillations illustrates the importance to this development. Incidentally, this part of physics is another example of a fruitful collaboration between physicists and geoscientists, as in recent years they began to examine Earth's heat generation by radioactive elements (potassium, uranium and thorium). The emitted neutrinos during the

radioactive decay of the aforementioned elements allow inferences on their abundances (see for example Šrámek et al., 2013 or McDonough et al., 2020).

The second kind of mesons, the kaons, have experienced a more complicated cascade of decays. In general, we are safe to consider that about two thirds, i.e. ~67 % of the kaons directly decay to muons,

$$K^+ \rightarrow (\pi^0 +)\, \mu^+ + \nu_\mu \tag{2.22a}$$

$$K^- \rightarrow (\pi^0 +)\, \mu^- + \bar{\nu}_\mu \tag{2.2b}$$

where one of the two channels produces also a neutral pion (i.e. without electric charge; this is however only a by-product and has no influence on any subsequent muons). Another ~28 % decay first into pions, which in turn decay according to the channels described above. As there are too many channels for presenting them in a simple list, we resort to a schematic notation:

$$K^\pm \rightarrow \pi^\pm \rightarrow \mu^\pm \tag{2.3}$$

The rest of the kaons decay into particles that are of no particular interest to muon tomographers (but mostly electrons). For a detailed list of the kaon decay channels please refer to Tanabashi et al. (2018, p. 1188f.).

Once we know how the incoming muons are created, it is possible to construct cosmic ray flux models that describe the muon particle flux at a given location, which is defined by height above sea level, latitude and longitude, and a given incidence angle, i.e. any oblique angle with respect to the zenith (straight above).

Different researchers came up with various ways of how to describe this cosmic ray muon flux mathematically. In this work we present four commonly encountered muon flux models. We additionally show, how a reasonable model error for the muon flux, which in turn may be used in any further computation.

Generally, the best way to model the incident muon flux on an experimental site is to perform a Monte Carlo simulation with a dedicated framework, for example CORSIKA (Heck et al., 1998). Unfortunately, this is a rather tedious work, as the trajectory of every single particle has to be simulated. For the Monte Carlo simulation to be statistically meaningful many particles have to be calculated, which takes a significant amount of time. This circumstance becomes worse if the Monte Carlo flux simulation has to be included in a Monte Carlo inversion (as will be explained in Ch. 2.3.5.3). This might even be prohibitive as the computational power is not good enough to produce results in a useful amount of time. We therefore prefer an analytical form of the muon flux model to boost the calculation performance, while still conserving the correctness of the model.

2.3.2.2 Tang model (modified Gaisser model)

The basic analytical muon flux model that one learns when working with muons originating from cosmic rays can be found in Eq. 29.4 of Tanabashi et al., (2018, p. 426), which reads

$$\frac{d\Phi_{\mathrm{G}}}{dE}(E,\theta) = 0.14E^{-2.7}\left\{\frac{1}{1+\frac{1.1E\cos(\theta)}{115\ GeV}} + \frac{0.054}{1+\frac{1.1E\cos(\theta)}{850\ GeV}}\right\}, \tag{2.4}$$

This may be interpreted as a term that describes the production of muons from decaying pions and kaons, where both values are multiplied by an overall scaling factor. Here E denotes the muon's energy and θ is the incidence angle relative to the zenith. The exact derivation of Eq. (2.4) can be found in Gaisser et al. (2016), which is acknowledged by the subscript G in Φ_G. This simplified model already reproduces the muon flux quite well (see Fig. 29.5 in Tanabashi et al., 2018). However, because the agreement between model and measurements worsens especially in the low energy region, several modifications as well as other model parametrisations have been proposed. In this context, Tang et al. (2006) introduced a slight modification of the "Gaisser equation", Eq. (2.5), to account for this issue:

$$\frac{d\Phi_{\mathrm{T}}}{dE}(E,\theta) = \mathrm{A} * 0.14E^{-2.7}\left\{\frac{1}{1+\frac{1.1\tilde{E}\cos(\theta^*)}{115\ GeV}} + \frac{0.054}{1+\frac{1.1\tilde{E}\cos(\theta^*)}{850\ GeV}} + r_c\right\}. \tag{2.5}$$

Here the necessary additional parameters are given by

$$r_c = 10^{-4}\,, \tag{2.6}$$

$$\Delta = 2.06 * 10^{-3} * \left(\frac{950}{\cos(\theta^*)} - 90\right), \tag{2.7}$$

$$\tilde{E} = E + \Delta\,, \tag{2.8}$$

$$A = 1.1 * \left(\frac{90\sqrt{\cos(\theta)+0.001}}{1030}\right)^{\frac{4.5}{E\cos(\theta^*)}}, \tag{2.9}$$

where

$$\cos(\theta^*) = \sqrt{\frac{x^2+p_1^2+p_2x^{p_3}+p_4x^{p_5}}{1+p_1^2+p_2+p_4}} \tag{2.10}$$

and the muon energy E is substituted by

$$E \rightarrow \frac{3E+\frac{7}{\cos(\theta^*)}}{10}\,, \tag{2.11}$$

if it fulfils the inequality $E \leq 1/\cos(\theta^*)\ GeV$. The parameters in Eq. (2.10) are $x = \cos(\theta)$, $p_1 = 0.102573$, $p_2 = -0.068287$, $p_3 = 0.958633$, $p_4 = 0.0407253$ and $p_5 = 0.817285$.

2.3.2.3 Reyna-Bugaev model

A second muon flux model is given by Bugaev et al. (1998) who proposed an empirical fitting formula to the muon flux measurements at sea level for vertical (i.e. zenith angle $\theta = 0°$) incident muons. The related equation is given by

$$\frac{d\Phi_B}{dE}(E) = C * p^{-\left(\gamma_0+\gamma_1 \log_{10}(p)+\gamma_2 \log_{10}^2(p)+\gamma_3 \log_{10}^3(p)\right)} , \tag{2.12}$$

where $p \equiv p(E)$ is the momentum of the muon in $GeV\ c^{-1}$. This is related to the muon energy by the relativistic energy-momentum relation

$$p^2c^2 = E^2 - m_\mu^2 c^4 . \tag{2.13}$$

In Eq. (2.13), m_μ denotes the rest mass of the muon, which equals $0.10566\ GeV\ c^{-2}$. The gamma parameters in Eq. (2.12) include different values for different ranges of momentum and can be looked up in Table II of Bugaev et al. (1998). Attentive readers have realised that Eq. (2.12) does not have any zenith angle dependence. This shortcoming of the model has been accounted for by Reyna (2006) by modifying Eq. (2.12) by

$$\frac{d\Phi_{RB}}{dE}(E,\theta) = \tilde{C} * \tilde{p}^{-\left(\tilde{\gamma}_0+\tilde{\gamma}_1 \log(\tilde{p})+\tilde{\gamma}_2 \log^2(\tilde{p})+\tilde{\gamma}_3 \log^3(\tilde{p})\right)} * \cos^3(\theta) , \tag{2.14}$$

where

$$\tilde{p} = p * \cos(\theta) , \tag{2.15}$$

with p taken from Eq. (2.13). The tilde parameters in Eq. (2.14) have been re-evaluated by Reyna (2006) to $\tilde{C} = 0.00253$, $\tilde{\gamma}_0 = 0.2455$, $\tilde{\gamma}_1 = 1.288$, $\tilde{\gamma}_2 = -0.2555$ and $\tilde{\gamma}_3 = 0.0209$ respectively. The subscript RB stands for Reyna-Bugaev.

2.3.2.4 Reyna-Hebbeker model

A third model was presented by Hebbeker & Timmermans (2002). It is empirical in nature, very similar to the Bugaev model described above, and it follows a power law relationship as well,

$$\frac{d\Phi_H}{dE}(E) = \mathrm{C} * 10^{\mathrm{H(y)}} . \tag{2.16}$$

Here, $y = \log_{10}(p)$, with again p from Eq. (2.13) and

$$H(y) = H_1\left(\frac{y^3}{2} - \frac{5y^2}{2} + 3y\right) + H_2\left(-\frac{2y^3}{3} + 3y^2 - \frac{10y}{3} + 1\right)$$
$$+H_3\left(\frac{y^3}{6} - \frac{y^2}{2} + \frac{y}{3}\right) + S_2\left(\frac{y^3}{3} - 2y^2 + \frac{11y}{3} - 2\right) . \tag{2.17}$$

The parameters in Eq. (2.17) have been fitted to $C = 0.86$, $H_1 = 0.133$, $H_2 = -2.521$, $H_3 = -5.78$ and $S_2 = -2.11$. Following Lesparre et al. (2010), we may again equip this pure zenith muon flux with an angle dependency as this has been done with Eq. (2.14). The resulting RH, i.e. Reyna-Hebbeker, flux is written as

$$\frac{d\Phi_{RH}}{dE}(E,\theta) = C * 10^{H(\tilde{y})} * \cos^3(\theta), \tag{2.18}$$

with

$$\tilde{y} = \log_{10}(p * \cos(\theta)) \, . \tag{2.19}$$

2.3.2.5 Sato model

The last model that we present here is the one described by Sato (2016), which we address from here onwards as $d\Phi_S/dE$. This model is based on a Monte Carlo Simulation in the particle transport framework PHITS (Sato et al., 2013). Two variants are available for users who are interested in adapting this model into their calculations. These variants are either what is referred to as EXPACS, which lets the user calculate the (among other particles) muon flux by an Excel spreadsheet, or a more involved one, referred to as PARMA, where the user alters the input files of the model itself. In both cases the user is returned a list of energy vs. muon flux. Table 2.A1 in Appendix A (Ch. 2.7) shows our calculated muon flux at Bern, Switzerland (Lat: 46.94 °N, Lon: 7.44 °E) at sea level (see Ch. 2.3.2.7 on information on how to incorporate height information) for the three different zenith angles $\theta = 0°, 45°, 60°$. This is theoretically not possible, as the city of Bern is situated around 550 m above sea level. However, for the sake of comparability to the other fluxes, we calculated the flux for sea level.

2.3.2.6 Application to muon tomography

Usually in muon tomography one does not use the differential muon fluxes directly, because this would require a measurement device that is capable of resolving the energy of the incident particle precisely. As a consequence, most present-day muon tomography experiments rely on the measurement of the integrated muon flux (e.g. Lesparre et al., 2010). Therefore, one only measures the presence of a muon and does not consider its energy. This becomes clear if one envisions the working principles of the various detectors in the corresponding Ch. 2.3.4. This limitation to an integrated flux may be expressed by an integral formulation for the differential fluxes presented above. Because one generally measures only muons above a certain energy threshold, the integrated flux can be written as

$$\Phi(E_{cut}) = \int_{E_{cut}}^{\infty} \frac{d\Phi}{dE} dE \, , \tag{2.20}$$

where the integrand is any flux model one considers using. In order to assess the uncertainty on the flux model, we employed a straightforward scheme. For the same location (i.e. Bern, Switzerland) we calculated the differential and integrated variants of the four muon fluxes introduced above. To portray their differences in a clearer way we also calculated their ratio to the mean flux, which is given by a simple arithmetic mean,

$$\left\langle \frac{d\Phi}{dE} \right\rangle = \frac{1}{4} * \left(\frac{d\Phi_{\mathrm{T}}}{dE} + \frac{d\Phi_{\mathrm{RB}}}{dE} + \frac{d\Phi_{\mathrm{RH}}}{dE} + \frac{d\Phi_{\mathrm{S}}}{dE} \right) \tag{2.21}$$

as well as the respective standard deviation,

$$\sigma_{d\Phi/dE} = \frac{1}{3} * \sqrt{\sum_i \left(\frac{d\Phi_i}{dE} - \langle\frac{d\Phi}{dE}\rangle\right)^2}, \tag{2.22}$$

where $i \in \{T, RB, RH, S\}$ denotes the four muon flux models. Analogously, we computed the mean and the standard deviation of the integrated flux models $\langle\Phi\rangle$, σ_Φ. The resulting plot for vertical muons (i.e. $\theta = 0°$) are shown in Fig. 2.3. Please refer to Appendix B (Ch. 2.8) for the respective plots of higher zenith angles ($\theta = 45°, 60°$). The 1σ-uncertainty on this mean flux has been calculated by

$$\varepsilon_{diff,\pm 1\sigma} = \frac{\langle\frac{d\Phi}{dE}\rangle \pm \sigma_{d\Phi/dE}}{\langle\frac{d\Phi}{dE}\rangle} \tag{2.23}$$

and

$$\varepsilon_{int,\pm 1\sigma} = \frac{\langle\Phi\rangle \pm \sigma_\Phi}{\langle\Phi\rangle}, \tag{2.24}$$

where the indices $diff$ and int refer to the differential and integrated flux, respectively.

If the scope is to attach an uncertainty to a flux model, the purple line in Figs. 2.3, 2.B1 and 2.B2 may be used. Muon tomography experiments for geological purposes usually operate in environments with material thicknesses of few $10\ m$ to $1\ km$ of rock, although $1\ km$ is already considered as a thick mass of rock. This corresponds to an energy range of about $10\ GeV$ to $1\ TeV$ (The origin of these numbers is explained separately in Ch. 2.3.3). Instead of using the precise value of the error envelope, we may also attribute a conservative error estimate to the flux of around $15\ \%$ (Hebbeker and Timmermans, 2002), which is a commonly used value in the community. This constant error simplifies the description of the uncertainties because it is now independent of the energy. There is also a specific reason for the conservative error estimate. We have computed the error based on four selected muon flux models only to get a rough overview. Accordingly, a conservative approach is reasonable in order not to exclude a higher variation due to other models.

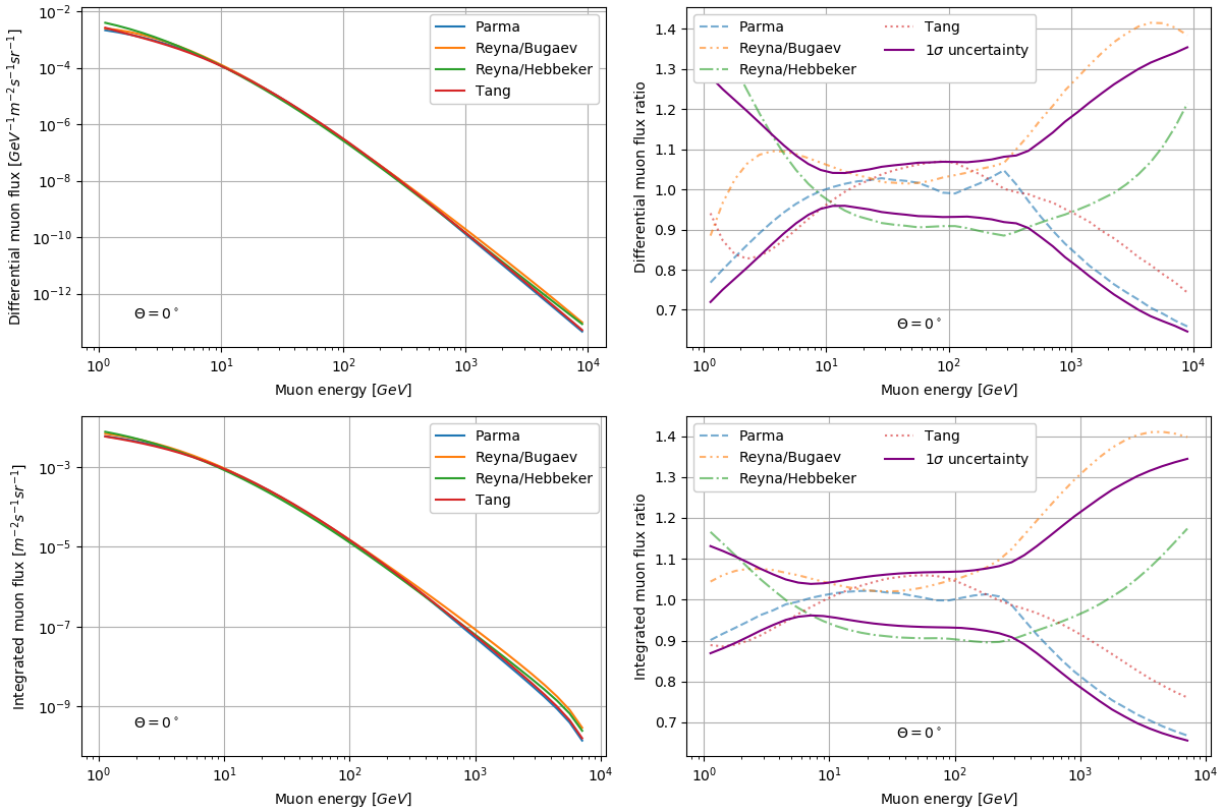

Figure 2.3: Comparison of the four muon flux models (Ch. 2.3.2.2 – 2.3.2.5) including an uncertainty estimate for a zenith angle of $\theta = 0°$. *Top left*: Differential muon flux as a function of energy. *Top right*: Differential muon flux ratio to the mean differential flux $\langle d\Phi/dE \rangle$ (see Eq. 2.21). *Bottom left*: Integrated muon flux as a function of the lower integration boundary (i.e. E_{cut} in Eq. 2.20). *Bottom right*: Integrated muon flux ration to the mean integrated flux $\langle \Phi \rangle$. The 1σ-uncertainty in the right-hand side plots has been calculated according to Eq. (2.23).

The above presented muon flux models are equally suitable for the use in experiments. They can also be easily exchanged as the different models lie within the 15 %-uncertainty boundary in the typical working energy range. We, however, found that the simple parametrisation by Reyna/Bugaev is a good starting point for the application in an experimental campaign. Of course different muon flux models should be tested during the experiment and the most suitable one should be chosen and employed.

2.3.2.7 Factors affecting the muon flux model

Apart from the different muon flux models, there are additional geophysical factors, such as the Earth's magnetic field or the weather conditions, that may affect the muon flux. This topic is discussed in Ch. 2.2 of Lesparre et al. (2010) in detail and we therefore limit ourselves to a short summary of that chapter.

The most important factor is the height of the measurement point. Any of the above-mentioned flux models may be scaled to another altitude by the relation (see for example Hebbeker & Timmermans, 2002)

$$\Phi_i(h) = \phi(0) * \exp\left(-\frac{h}{h_0}\right). \tag{2.25}$$

Here $h_0 = 4900 + 750\,p$ is in m and "p" denotes the muon's momentum. Users may find that another local scaling height, h_0, may be more appropriate to describe the local muon flux. This has for example

been done by Nishiyama et al. (2017), where $h_0 = 3400 + 1100\,p$, according to the results of a Monte Carlo simulation.

A second important effect concerns the atmospheric density variations over the cycle of the year. As temperature changes during the different seasons, so does the density of the air, which may impact the muon flux model. This factor is important if one desires to reconstruct a time dependent signal, which might, for example, be related to changes in a magma chamber of a volcano. Lesparre et al. (2010) show how the related effects may be corrected for.

2.3.3 Energy loss of muons in matter

In the preceding chapter we have presented how muons are produced in the outer atmosphere and how one can describe the amount of these particles showering down on Earth using a muon flux model. The next step in the journey of such a muon towards the detector, usually involves the penetration of a given amount of solid material. By various interactions with the electrons and nuclei within the matter, the muon (which is also a charged particle) loses energy as it traverses the solid body. We note here that the matter does not have to be in a solid state but may also be fluid or even gaseous. The processes of energy loss remain the same. However, in most practical muon tomography experiments the body in question is almost always a solid.

2.3.3.1 The energy loss equation

The processes of energy loss are well explained in Groom et al. (2001), and we gladly refer to this work and the references therein for detailed discussion of the involved particle physics. The resulting energy loss equation takes the form of a first order ordinary differential equation,

$$-\frac{dE}{dx} = \rho(x) * [a(x,E) + E * b(x,E)]\,, \tag{2.26}$$

where E is the energy of the muon, x its position along the path, $\rho(x)$ the density of the traversed matter and $a(x,E)$ & $b(x,E)$ the ionisation and radiative energy losses, respectively. By ionisation one refers to the excitation and/or ionisation of atomic electrons in the matter that were given some energy from the incident muon, whereas the radiation term encompasses bremsstrahlung, electron-positron pair production and photonuclear interactions. Important here is the fact that ρ, a & b are matter dependent properties. Groom et al. (2001) provide an energy loss list, where they tabulate the $-dE/dx$ for each element and selected compounds. Unfortunately, the only geologically relevant materials are SiO_2, $CaCO_3$ and an entity called "standard rock". An earlier work (Lechmann et al., 2018) addressed this problem and showed in which cases this standard rock is a valid approximation and when it should be exchanged with a more realistic rock model, that includes information on the composition. The Lechmann et al. (2018) study also provides energy loss calculations for several major rock types (i.e. granite, limestone, basalt) and developed a simple method to account for these different compositions. The result for a realistic rock model yields an energy loss formula in the same form as Eq. (2.26), i.e.

$$-\frac{dE}{dx} = \{\rho(x)\}_{rock} * [\{a(x,E)\}_{\text{rock}} + E * \{b(x,E)\}_{\text{rock}}] \,, \tag{2.27}$$

such that all subsequent calculations can be treated equally. In summary, one should consider a realistic rock model if the rock is either basalt or limestone and features an expected thickness of more than $300m$. If these criterions are not met one is usually fine using the standard rock approximation.

2.3.3.2 Solution of the energy loss equation

There are multiple ways to solve Eq. (2.27), all of which share one common first step. We have to assume that the physical parameters are homogeneously distributed throughout our material block. In this case, it is possible to represent the material with a set of constant parameters. If this can be reasonably achieved, the most straightforward method would be to program a numerical solver for Eq. (2.27). Usually for this kind of problem a Runge-Kutta integration scheme (e.g. Stoer and Bulirsch, 2013) is sufficient. Naturally, any higher order numerical scheme is also possible. However, in any case they have to be compared to already existing calculations, as the numerical errors in these solvers have not yet been investigated systematically when applied to the energy loss equation. Alternatively, it is possible to recast Eq. (2.27) as an integral,

$$L(E) = \int dx = \int_{E_0}^{E} \frac{1}{\rho * [a(E\prime) + E\prime * b(E\prime)]} dE' \,, \tag{2.28}$$

where E_0 "is sufficiently small that the result is insensitive to its exact value" (Groom et al., 2001). A good value can be chosen around several MeV. The range $10\ MeV - 100\ MeV$ is reasonable as muons in this energy range only penetrate a few centimetres into a material. Moreover, this range is also covered by the energy loss tables, which makes it easier to use if one does not want to implement a sophisticated solver. An example of such an energy loss table and information on where it may be retrieved can be found in Appendix C (Ch. 2.9). The parameter L in Eq. (2.28) denotes the penetration distance, which is in usually presented centimetres (depends on the units of a, b & ρ). Instead of L, however, the range R is often reported in physics literature. This quantity relates to the penetration distance as follows:

$$R(E) = L(E) * \rho = \int \rho(x)\, dx = \int_{E_0}^{E} \frac{1}{[a(E\prime) + E\prime * b(E\prime)]} dE' \,. \tag{2.29}$$

Equation (2.29) has the advantage that the results are better comparable if the equation is applied to different materials. Please note, that the second equality sign in Eq. (2.29) only holds for homogeneous media, where the material parameters do not change spatially. In applications with muon tomography, however, it is more convenient to use the penetration distance L of Eq. (2.28), even though these to equations convey the same information. In Table 2.C1 of Appendix C (Ch. 2.9) one can also verify, that the usual initial muon energies lie between $10\ GeV$ and $1\ TeV$ for penetration ranges L between $10\ m$ and $1\ km$.

As Groom et al. (2001) provide energy loss and range tables for selected materials it is useful to keep in mind the relation between $R(E)$ and $L(E)$, see Eq. (2.29). It is thus also possible to quickly adapt these

tables for a version where the densities are modified. Thus, a "standard rock" with modified density may be used in scenarios, where the actual rock density is not exactly $2.65\ g\ cm^{-3}$. This inherently assumes no variation in composition, as only density changes are considered. Please refer to Lechmann et al. (2018) for more information about how this can be meaningfully achieved in geological settings. In the aforementioned article, the reader may also find additional information on the exact geochemical and mineralogical composition of this "standard rock". These authors also discuss how to proceed if a more realistic rock model is required.

We conclude this section with a cautionary note. Even though Eqs. (2.28) & (2.29) may proof very useful, one has to consider that some part of the ionisation losses, $a(E)$, is dependent on the density, such that the right-hand side of the equation would change with different densities. If the modified densities are close (within ~5 %) the tabulated density (again for standard rock this is $2.65\ g\ cm^{-3}$) one should however be fine upon employing Eqs. (2.28) & (2.29). At this stage, we know of no publication where this possible bias has been systematically analysed within a geological context.

2.3.3.3 Multiple Scattering

The calculations listed above represent a good model, which should suit the needs for many applications. However, they carry an implicit assumption one has to be aware of. In particular, the solution to the energy loss equation assumes that muons penetrate the matter of interest along a straight path, i.e. a line. This does, however, not reflect reality. In fact, the muon is continuously deflected by small angles upon travelling through the material. These angles sum up, and upon leaving the material the muon may find itself within a cone, where the centre axis represents the perfect line path that is usually considered. Tanabashi et al. (2018) provide the following scheme (see Fig. 2.4) to illustrate the problem.

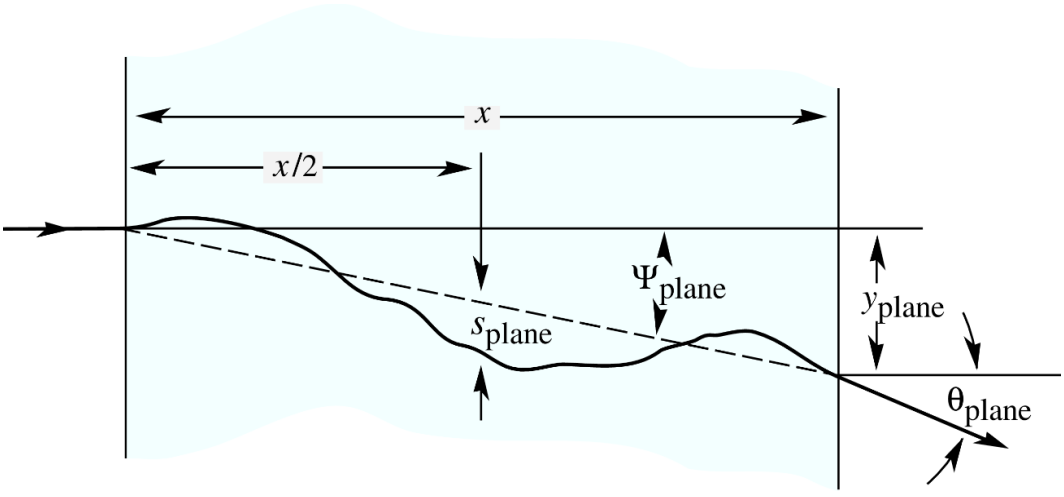

Figure 2.4: Scheme to illustrate multiple coulomb scattering of an incident particle (Figure 33.10 of Tanabashi et al. 2018, p. 452.). A particle hits a block of matter of thickness x and is continuously deflected. It exits this block with a mean angular deflection of θ_{plane} and an offset of y_{plane}. For the other quantities, which we do not need for further computations (i.e. Ψ_{plane}, s_{plane}) we refer the reader to the original source of this diagram.

In this context, we are mainly interested in the quantity θ_{plane}. This is a measure of the angular deviation of a muon after crossing a definite thickness of rock. The consideration of such a deviation is important

if the angular resolution of the detector is used as a reference. This then leaves the question of how to calculate θ_{plane}. For this purpose, we may use Highland's formula (see e.g. Lynch & Dahl, 1991)

$$\theta_{plane} = \frac{13.6}{\beta pc}\sqrt{\frac{\lambda}{\Lambda_0}}\left[1 + 0.088\log_{10}\left(\frac{\lambda}{\Lambda_0}\right)\right] , \tag{2.30}$$

where, p is the momentum of the muon, c is the speed of light, $\beta = v/c$ a relativistic parameter and λ is the thickness of the material in density length units (i.e. $[g\ cm^{-2}]$ can be obtained by $\lambda = \rho_{rhock} * x$, when x is the thickness in $[cm]$). Finally, Λ_0 is the radiation length of the material that can be obtained by the formula of Tasi (1974),

$$\frac{1}{\Lambda_0} = \frac{Z^2[L_{rad} - f(Z)] + ZL'_{rad}}{716.405\ A} . \tag{2.31}$$

The term $f(Z)$ in Eq. (2.34) may be calculated by

$$f(Z) = (\alpha Z)^2[(1 + (\alpha Z)^2)^{-1} + 0.20206 - 0.0369(\alpha Z)^2 + 0.0083(\alpha Z)^4 - 0.002(\alpha Z)^6] , \tag{2.32}$$

where Z is the atomic number of the element and $\alpha = 1/137$ is Sommerfeld's constant. The two auxiliary quantities L_{rad}, L'_{rad} on the other hand have to be chosen according to Table 2.1.

Unfortunately, it is often the case that we need to know Λ_0 not for a pure element, but for a rock, which is a mixture of elements. To solve this problem, we could conduct the aforementioned calculations for a standard rock, for example. Lesparre et al. (2010) as well as the PDG (Particle Data Group; https://pdg.lbl.gov) list the radiation length for standard rock as $\Lambda_{0,SR} = 26.54\ g\ cm^{-2}$.

Table 2.1: Key on how to calculate the quantities L_{rad} and L'_{rad} necessary for Eq. (2.31). Table 33.2 of Tanabashi et al. (2018, p. 452).

Element	Z	L_{rad}	L'_{rad}
H	1	5.31	6.144
He	2	4.79	5.621
Li	3	4.74	5.805
Be	4	4.71	5.924
Others	> 4	$\ln(184.15\ Z^{-1/3})$	$\ln(1194\ Z^{-2/3})$

But generally, we want to calculate the radiation length of a mixture of elements (Tanabashi et al., 2018) by

$$\langle\frac{1}{\Lambda_0}\rangle = \sum_j w_j \frac{1}{\Lambda_{0,j}} . \tag{2.33}$$

Here, w_j is the weight fraction of the j-th element in the compound and $\Lambda_{0,j}$ is the radiation length of the j-th element, respectively. We show in Appendix D (Ch. 2.10) how the user may derive a radiation length, given some XRF (X-ray fluorescence) measurements. The resulting radiation length for our exemplary "real" rock is $\Lambda_{0,rock} = 25.72\ g\ cm^{-2}$.

Please note, that even though the difference is ~3 % and thus very small considering the overall scheme, our host rock, that we measured had a rather granitic composition. As shown in Lechmann et al. (2018) granitic rocks tend to be well approximated by standard rock, while others may not. We recommend performing an analogous calculation as shown in Appendix D (Ch. 2.10) for every experiment, even if one has no XRF data at hand and has to rely on a rough (usually macroscopic) description of the lithology.

With this $\Lambda_{0,rock}$ it is now possible to calculate the scattering parameters from Fig. 2.4. Unfortunately, Eq. (2.31) is only valid for a relatively thin absorber, where the energy stays roughly constant, i.e. the energy loss is negligible. As Lesparre et al. (2010) state, we need a differential form of Eq. (2.30) to also account for the energy, which is lost during the passage through matter. Even though they do not provide the differential form, one might get an idea from the CERN report of Schwarz (2013), where the total deviation is calculated by adding the "thin slab"-contributions together in quadrature, taking into account the energy loss. Tailoring this idea to Eq. (2.30) yields

$$\theta_{plane} = 13.6 \left[1 + 0.088 \log_{10}\left(\frac{\lambda}{\Lambda_0}\right)\right]\left(\frac{\rho_{rock}}{\Lambda_{0,rock}}\int_0^D \left(\frac{1}{\beta pc}\right)^2 dx'\right)^{1/2} . \quad (2.34)$$

Note that this is already the integrated formula for a thick absorber such as a mass of rock. One would end up with a similar result when the original formula from Lesparre et al. (2010) would be used. The only difference lies in the integrand (i.e. $(\beta pc)^{-1}$ vs. E^{-1}). This may be explained by the high energy nature of the experiments in the field of muon tomography. Usually, these kinds of studies require muon energies on the GeV level. βpc may be expressed as $(\gamma - \gamma^{-1})m_\mu c^2$. When energies are high, then $\beta \rightarrow 1$ and $(\gamma - \gamma^{-1}) \rightarrow \gamma$, such that $\beta pc \rightarrow \gamma m_\mu c^2 = E$. For example, a $1.05\ GeV$ muon has roughly a $\gamma \approx 10$ and thus the difference between the two different formulae is 1 %. As $1\ GeV$ is rather a lower threshold, one should be fine in using the energy approximation

$$\theta_{plane} = 13.6 \left[1 + 0.088 \log_{10}\left(\frac{D\rho_{rock}}{\Lambda_0}\right)\right]\left(\frac{\rho_{rock}}{\Lambda_{0,rock}}\int_0^D \left(\frac{1}{E}\right)^2 dx'\right)^{1/2} . \quad (2.35)$$

Table 2.2 shows the calculations of θ_{plane} for standard rock for different thicknesses, D, and exit energies, E_{ex}, (i.e. energy of the muon after the thick absorber).

Table 2.2: Calculations of the mean angular deviation, θ_{plane}, for different absorber thicknesses, D, and different muon exit energies, E_{ex}.

D $[m]$	50	150	300
E_{ex} $[GeV]$	θ_{plane} $[mrad]$		
0.1	316.53	316.71	316.74
1	77.34	78.04	78.18
10	19.85	21.57	22.00
100	3.39	4.69	5.30

We note that θ_{plane} is only weakly dependent on the thickness of the absorber and more sensitive to the exit energy of the muon. This has a rather direct implication on how the detector needs to be constructed (we briefly address this issue in Ch. 2.3.4).

First, these θ_{plane} values are a lower threshold for the angular resolution that we may achieve, irrespective of the actual angular resolution of the detector. Second, according to Fig. 2.4, one would also expect that certain muons are deflected away from the detector, such that we may end up with an underestimation of our muon flux because these muons are not registered on the detector. We address this problem in Appendix E (Ch. 2.11) and show that usually, this does not affect our measurements in a significant way.

These two biases (but especially the first one) can be rather well mitigated by building the detector in a way that allows only allows to register those muons with a sufficiently high energy. Thus, one gains some control over this rather difficult problem. The possible bias that results from the sensitivity of the equations to is also discussed in Lesparre et al. (2010) and attributed to the fact that we integrate in Eq. (2.35) over $1/E^2$. This means that the muons are scattered more, the slower they become, i.e. during the very last part of their trajectories.

2.3.4 Detectors

In this chapter we present the detectors that are commonly used in a muon tomography experiment, so that the user may form an own idea which device may be suitable for his/her own research. As our own expertise lies with the application of nuclear emulsion films, we will portray the corresponding detector type in more detail. However, we will also present the other technologies, summarise them and redirect the user to studies for more information and/or applications. In general, muon detectors are passive detectors as they only record the naturally occurring cosmic ray muon flux at a position in a certain direction. The main difference of the following detector types lies in their deployment conditions, that are closer described in the respective sections.

2.3.4.1 Nuclear Emulsions

The concept of how nuclear emulsions work may probably be best described through a comparison to photographic films that were used decades ago. An overview of how we built our detectors and processed the data can be found in Ariga et al. (2018) and we limit our presentation here to the most important production and data processing steps.

Figure 2.5 shows a small sketch of how an emulsion film is built up and how it works. Even though the setup for one emulsion film looks rather straightforward, already their production is rather involved. A short overview over the different production steps can be found in Morishima et al. (2017). The result is a doubly layered emulsion film that is vacuum packed in a completely lightproof sleeve (see Fig 5. of Morishima et al., 2017). For visibility reasons, the sleeve has been omitted in our Fig. 2.5.

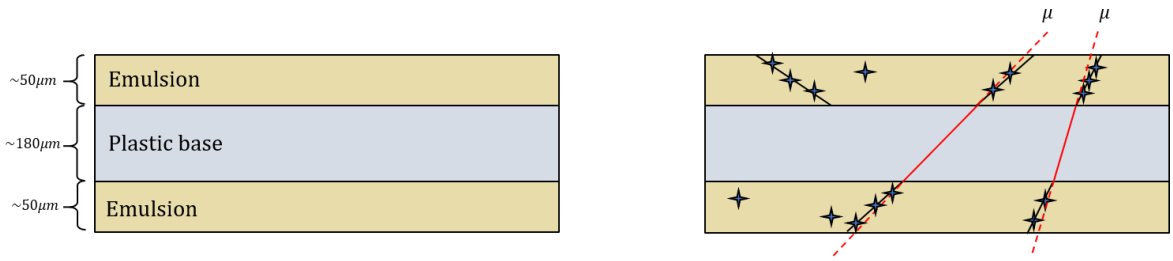

Figure 2.5: Structure and working principles of an emulsion film detector. *Left*: Structure of a single emulsion film. It consists of a plastic base ($\sim 180\ \mu m$) coated on both sided with a photosensitive (i.e. contains $AgBr$-crystals) emulsion ($\sim 50\ \mu m$). *Right*: Schematic view of the state of an emulsion film when it is developed after exposure to the cosmic ray muon flux. Stars indicate activated $AgBr$-crystals (i.e. clusters; they will show as dark grains). Black lines connecting clusters are reconstructed particle tracks. Muons are assumed to propagate straight through the detector. Dashed red lines denote the part of the muon track within the emulsion, whereas the solid red lines indicate the "basetrack", i.e. the unobserved muon track within the plastic base.

The right panel of Fig. 2.5 shows the principles of how emulsion films register incoming and outgoing muons. In particular, when muons hit the prepared muon film, then parts of the silver-bromide crystal are broken up into bromide and silver ions. The latter tend to aggregate on the surface of the crystal and form a latent image, which then show up as clusters (i.e. stars in Fig. 2.5) when the film is developed in the laboratory. In each emulsion layer a linear sequence of clusters can be assembled to a "microtrack" (see solid black lines in Fig. 2.5). Through the matching of microtracks from the top and the bottom layer on one film one may construct so called "basetracks" (i.e. tracks of muons that must have penetrated the whole film, including the plastic base; see solid red lines in Fig. 2.5). However, as this film also records tracks in the time span between the production and the deployment at the experimental site, one would have to deal with a hard signal-noise separation problem. One possible solution to this problem, is to build the emulsion detector in a ECC (emulsion cloud chamber) arrangement (Nishiyama et al., 2014, 2015).

The principle is to form a "sandwich" of single emulsion films interlaced with metal plates as depicted in Fig. 2.6. This arrangement of the detector has two big advantages. First, the ECC structure may assembled upon arrival at the experimental site, and one is sure to only record muon tracks from the study site. The trick lies in the fact that one only has to consider muon tracks that penetrate the whole detector. These tracks and their orientations may be reconstructed using the same logic (i.e. alignment of the different layers) as the processing step from microtracks to basetracks. Second, the addition of metal plates acts as an artificial threshold to filter out the low energy particles. This filtering occurs mainly through the deflection of low energy particles at a higher angle, such that they do not appear as straight tracks anymore. This means that also electrons that may produce a substantial bias, or even worse a background noise within the films, are filtered out and do not significantly contaminate the measurement (Nishiyama et al., 2015). Therefore, such a detector setup is better suited for geological purposes than an emulsion film detector that is made up of a to the blank single layer only, because it considerably facilitates the data processing afterwards. For an example image we refer to Fig. 2.7, where two of our deployed instruments are shown.

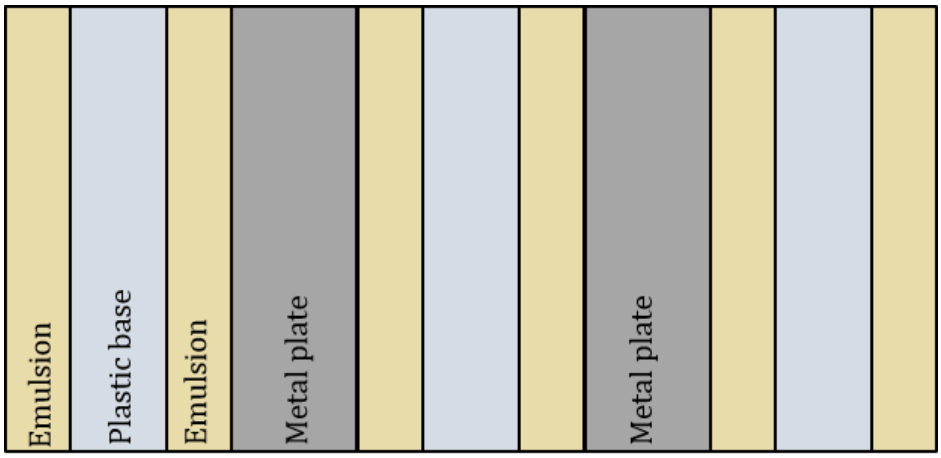

Figure 2.6: Emulsion cloud chamber (ECC) arrangement. This type of emulsion detector consists of alternating layers of emulsion film and metal plates.

Emulsion detectors are thus very versatile and, once packed in a lightproof sleeve, relatively easy to handle and transport. The most outstanding feature, however, is the fact that emulsion detectors do not need any form of electric power supply. They collect the data passively and continuously, which means that there is theoretically no dead time in the detector. This enables scientists to place these detectors in tunnels underground or other remote places in the mountains, without having to worry about excessive hauling or, as said, installing an equipment for power supply.

These advantages do not come without any significant drawbacks. In comparison to the other detectors, we sacrifice the ability to retrieve time resolved data. In particular, emulsion detectors record a time-integrated signal, and one has no chance of reconstructing, which track has been recorded at which moment and under what conditions. Additionally, emulsions require a rather long pre- and post-processing time. This means that the production of emulsion films, their development in the dark chamber as well as their scanning may take some time. Finally, emulsion detectors can lose their recorded signal ("fading") if the film is exposed for too long a time span (> 3-4 months). In addition, the equipment has to be kept always around the same temperature and humidity conditions, because any fluctuations of these parameters may favour the occurrence of premature fading.

Figure 2.7: Deployed ECC detector frames in two different formats. *Left:* Small scale detector consisting of two ECC pouches with a total detection area of $\sim 250\ cm^2$. *Right:* Large scale detector consisting of four ECC pouches with a total detection area of $\sim 1.2\ m^2$. Humans are included for scale.

2.3.4.2 Scintillators

A second type of detector, that has been widely employed in muon tomography studies are scintillators. Here the incoming charged particles excite the electrons of the scintillating material to higher energy levels. These electrons fall back into their ground state, thereby releasing energy in form of a photon. The latter is then often detected by a photomultiplier and converted into an electronic signal (see also Lesparre et al., 2010; Gibert et al., 2010; and Pla-Dalmau et al., 2001, for more information). The scintillation detectors are in a way the opposites of the emulsion detectors. The former need an external power supply, which is often provided by a photovoltaic panel (e.g. Gibert et al., 2010). Thus, much of the detector design is focused on the power consumption to render the detector energetically self-sufficient. By recording each particle live, it is possible to record the muon flux in real time, even if the flux will then be manually time integrated during the subsequent processing steps. Therefore, on the positive side, one may keep the control over the integration step, such that possible seasonal effects may be analysed. On the downside, scintillation detectors may consist of too many heavy parts, which make the transport and the installation difficult to organise. Furthermore, by using scintillation bars one often has to limit the angular resolution of the detector, as these bars cannot be made arbitrarily small. Another point to consider is the dead time of the detector (as with nearly every real time detector). Once the detector records a track, it needs to recharge and cannot record another track during this time. Ambrosino et al. (2015) report the dead time in the order of 20 % for their scintillation detector. For readers interested in how such a detector looks like, please see Figure 2.8.

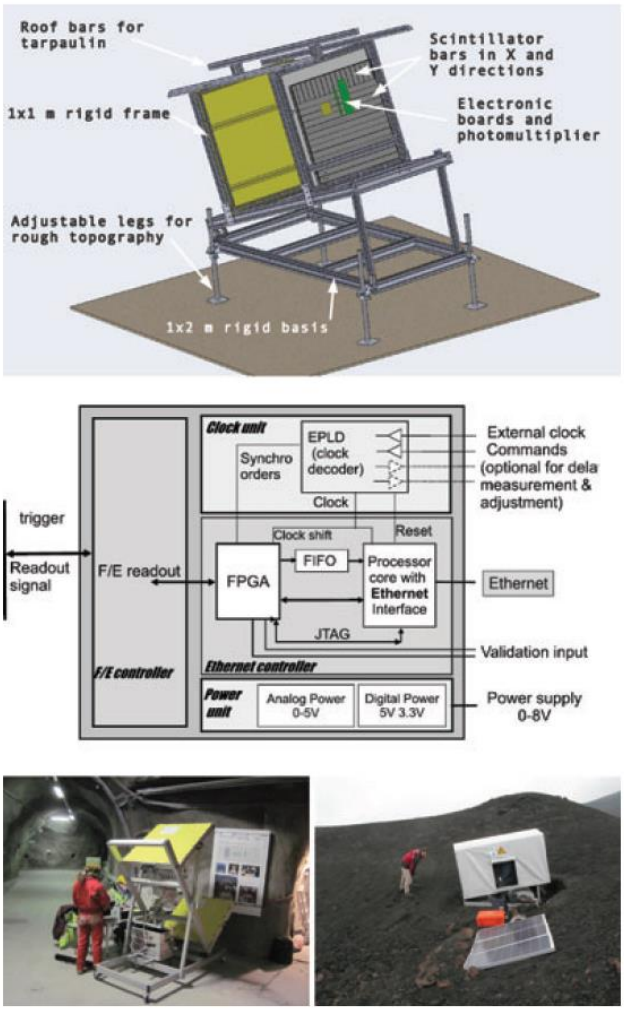

Figure 2.8: Example of a deployed scintillation detector. Fig. 5 from Lesparre et al. (2010). *Top*: Sketch of a muon detector consisting of horizonal and vertical scintillator bars. *Middle*: Electronics of the muon telescope. *Bottom*: Example of two muon detectors deployed in the field.

2.3.4.3 Gaseous detectors

A further type of detector uses a gas to record a charged particle's presence and movement (see Fig. 2.9). When a charged particle traverses the gas, then its electrons are ionised. As the gas is enclosed by an anode and a cathode, both of which maintain an electric field, the ionised electrons are accelerated towards the anode. This acceleration of the electrons initiates a chain reaction where further electrons are ionised thereby resulting in an electron avalanche. This, in turn, induces a signal in the electrodes, that can then be measured. The interested reader is referred to Asmundis et al. (2007) for further information on resistive plate chamber (RPC) detectors. Another similar detector type, that has been deployed for muon tomographic experiments, is the Mircomegas detector (see e.g. Giomataris et al., 1996). This is basically a variant of the RPC detector.

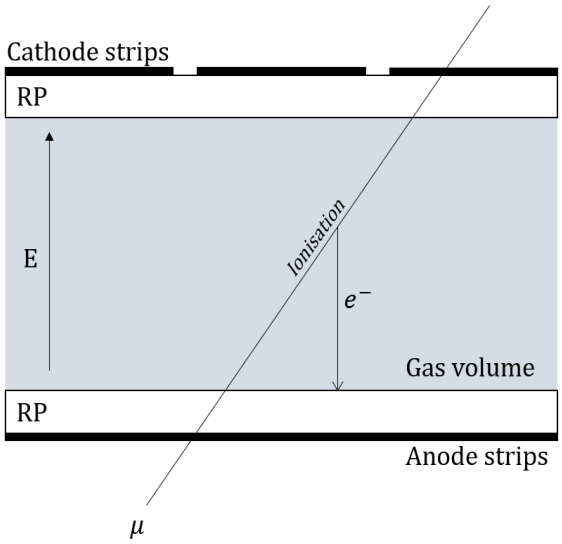

Figure 2.9: Basic structure and working principles of a gaseous detector. A charged particle (here a muon) crosses the gas volume and ionises electrons along its trajectory. Due to the presence of an electrical field (produced by the cathode/anode strips) the electron is accelerated towards the anode, producing an avalanche of even more electrons. The avalanche is usually large enough to induce a signal in the electrodes, that may be read out. The resistive plates (RP) damp the electron avalanche in order to reset the detector (such that it can record a new particle). A segmentation of the cathode/anode into strips enables localisation of the particle.

Figure 2.9 shows the concept of one single detector layer, which, however, is not suitable to detect the directionality of the incident particle. For this reason, RPCs usually are deployed as stacks of multiple RPCs on top of each other, an arrangement which is often called a "hodoscope". Accordingly, most particle detectors presented here fulfil the description of a hodoscope.

As a detector that records passing particles in real time, it features similar advantages and drawbacks as the scintillation detectors. The most important advantage is the time resolution of the recorded muon flux. The dead time in modern-day gaseous detectors is reported to be around 6 % (Ambrosino et al., 2015) and can be even lower than 1 % (Varga et al., 2020). On the negative side, the generation of an electrical field needs an external power supply, that may require more planning before an experiment.

2.3.4.4 Cherenkov detectors

The last instrument that we describe in this review is a rather niche detector. This type records the Cherenkov radiation that is emitted when a charged particle traverses a block of matter while exceeding the speed of light within the traversed matter. This may be best described by an analogy to the supersonic wave that is created when an object travels faster through the matter than its speed of sound, with the difference that the wave that is created in the Cherenkov process is an electromagnetic wave, i.e. a photon. We refer here to the study of Catalano et al. (2016) who deployed a Cherenkov detector to perform a muon radiography experiment at Mt. Etna in Sicily, Italy. These authors also describe how the detector works, and they provide illustrative photographs that nicely show the dimensions of this device. As a real time detector, it has very much the same advantages as the other real time detectors as well as the need for an external power source. Moreover, due to its sheer size, this detector is probably

more suited for a long-term, quasi-stationary observation ward (The mirror of the Cherenkov telescope in Catalano et al., 2016, has a diameter of roughly 4m).

There are also more recent developments that aim at reducing the size of the detector by hybridising with another detector type. For example Vesga-Ramírez et al. (2021) employed with their MuTe a hybrid telescope that uses two scintillator panels and a water Cherenkov detector.

2.3.5 Inversion schemes and tools

In this chapter we present several inversion techniques that are commonly utilised to invert results from muon tomography experiments. The selection of the corresponding approach mostly depends on the goal of the muon flux measurement, and the data analysis procedure is then often adapted accordingly. We also want to present a few tools, that may be useful when designing and implementing an own inversion procedure.

2.3.5.1 The Density-Length approach

This is by far the most used technique in muon tomography, mainly due to its simplicity. The idea comes from Eq. (2.29), where

$$\int \rho(x)\, dx = \Lambda\,, \tag{2.36}$$

and Λ, the "density-length" or opacity, can be calculated from the muon flux model and a material table (see Ch. 2.3.3) given some measurement results. From the expression in Eq. (2.36) one can construct a wide array of parametrisations, i.e.

$$L_1 * \rho_1 = \Lambda\,, \tag{2.37}$$

when only one material is present or

$$L_1 * \rho_1 + L_2 * \rho_2 = \Lambda\,, \tag{2.38}$$

for a stack of two different materials, etc. In any case Eqs. (2.37) & (2.38) are underdetermined and thus need additional information to resolve the involved parameters well. In case of Eq. (2.37) one usually knows the material thickness, L_1, and tries to draw inferences on the mean density, ρ_1. In many vulcanological applications this is the procedure, as one is mostly interested in mapping the density anomalies. Eq. (2.38) is an example which could be used for an interface detection, i.e. one is interested in L_1 and L_2. This can be solved by assuming that we know the densities ρ_1 & ρ_2 and the total material thickness $L_1 + L_2 = L_{tot}$. From this short discussion one sees that the growing number of parameters is countered with additional information, which is the only practicable way when facing an underdetermined problem. The popularity of this approach comes largely from its ease to use and the relatively robust result it produces.

The aforementioned approach is often formulated as a deterministic inverse problem, i.e. a least squares problem, that can be solved using a matrix equation. We refer here to Nishiyama et al. (2014) or Barnoud

et al. (2019) for an example on how this may be set up. In those studies, the authors have combined muon tomography measurements with gravimetric measurements (a reasonable choice, as will be discussed in Ch. 2.5).

2.3.5.2 Bayesian approaches

Even though Bayesian techniques provide a large arsenal of techniques to tackle the inverse problem, their use in muon tomography is far from ubiquitous. The reason for this circumstance lies most probably in the intricacies of design and solution of a probabilistic model. Despite these involved problems, Bayesian methods shine when information on parameters from various sources such as the results of laboratory measurements, literature data or even state-of-the art knowledge (on boundaries of parameter values, for example has to be incorporated. As the probabilistic formulation remains the same these different datasets can be integrated with ease. In this approach, the physical laws take the form of surfaces within the multidimensional data-model space in which each datum and each parameter has its own dimension. A comprehensive explanation of this line of thought can be found in the book of Tarantola (2005). Barnoud et al. (2019) as well as Lelièvre et al. (2019) provide an interesting example of how a Bayesian approach to merge gravimetric and muon tomographic inversion might look like. Other, muon tomographic stand-alone, studies were undertaken by Lesparre et al. (2012, 2017) and Vesga-Ramírez et al. (2021) by using a technique called simulated annealing. We refer the reader to Kirkpatrick et al. (1983) for the original paper on this technique or to Sivia and Skilling (2012, p.63, 203–208) for an easy introduction to the topic. Lechmann et al. (in prep) present an approach on how to construct the joint posterior, i.e. the central quantity in every Bayesian calculation, from a directed acyclic graph.

Even though we advocate in favour of Bayesian approaches, we have to stress that usually this comes at the price of having to solve the inverse problem by means of a Monte Carlo simulation, in order to properly sample the posterior probability density function. The aforementioned simulated annealing technique serves as a prime example. This is often associated with higher computational costs, and therefore the chosen algorithms have to be programmed carefully. For example, this does usually not allow for another Monte Carlo simulation to be performed within the Monte Carlo inversion. We think, however, that if care is taken in the design of the inversion, this should not pose a grave hindrance.

2.3.5.3 Tools

As the state of this technology is still very much in its beginnings, no commercial software and therefore no standardised way exists for data processing. Thus, for this last step in the whole data processing chain, one is often confronted with the situation, that some own code has to be written. Here we would like to compile a few tools that we think are useful if one desires to build an own application.

The first tool we refer to is GEANT4 (Agostinelli et al., 2003), an all-purpose toolkit to simulate particle transport through a variety of materials. In addition, with PUMAS, Niess et al. (2018) released a backward simulation modification, such that the Monte Carlo Simulation of the particles is sped up

considerably, by only considering muons that actually hit the detector. In light of its use in gravimetric inversion, pyGIMLi (Rücker et al., 2017) might also prove useful if one wants to invert joint measurements. Moreover, in another study a toolset, SMAUG (Lechmann et al., in prep), is provided that allows the user to perform a Bayesian inversion of muon flux data, with customisable materials.

2.4 Recent applications

In this chapter we will show an overview of the recent applications to redirect the reader to studies that might be useful or similar to one's own research. This is intended to provide the reader with a rough idea on how muon tomography can be applied in the specific contexts. We focus solely on geological contexts, as other reviews, that were listed in previous chapters, cover the other fields (mostly archaeology and civil engineering) in great detail.

In general, muon tomography can be applied in two main ways. First, this technology allows to detect regions of relatively high/low density. This is a feature, that is often used in volcanological contexts (e.g. Tanaka et al., 2005; Oláh et al., 2019) to visualise the conduit in the corona region of a volcano. The other possibility is to detect boundaries with a high density contrast. This has for example been performed on glaciers (e.g. Nishiyama et al., 2017) to detect the rock-ice interface or in a tunnel to detect the location of a (low-density) karstic network (see Lesparre et al., 2017). Most of the muon tomography studies fall into either of the two categories. We have compiled a list of recent application of muon tomography to tackle geoscientific questions in Table 2.3.

Table 2.3: Selected publications of muon tomography experiments in geoscientific contexts.

Volcanology	Muon detector	Location	Summary
Tanaka et al. (2005)	Plastic scintillator	Mt. West-Iwate, Honshu Japan	Muon tomographic and gravimetric data have been collected on two Volcanoes (Mt. Kurokura & Mt. Ubakura). Alongside a density estimation of the volcanic lithology, a time dependent change in muon intensity has been linked to volcanic activity. The observation lasted 1 year; the detector was designed to withstand also snowy weather conditions.
Tanaka et al. (2007)	ECC	Mt. Asama, Honshu, Japan	A survey in which muon tomography was used to depict lithological density differences in the top region of the volcano. Density anomalies were related to volcanological structures of previous eruptions (lava cap, magma conduits). The device recorded for 2 months.
Tanaka et al. (2009)	Plastic scintillator	Satsuma-Iojima, Osumi islands, Japan	Imaging of the magma head in the main conduit of the Mt. Io volcano is performed. Degassing processes were identified and characterised according to the muon measurements.
Lesparre et al. (2012)	Scintillator	La Soufrière, Guadeloupe, France	This work presents relative 2D density distributions, retrieved from muon measurements. These are compared to separate electric resistivity and gravimetric models. Volcanic features are identified with the different observed structures in the various density models. Data acquisition took around 82 days.
Nishiyama et al. (2014)	ECC	Mt. Usu region, Hokkaido, Japan	This study combined measurements of gravimetry and muon flux of the Showa-Shinzan lava dome (side peak of Mt. Usu). A joint inversion, i.e. a 3D structural density analysis of the volcanic complex is performed, i.e. horizontal cross-sections for various altitudes across the volcano. The muon data has been collected for 3 months.
Tanaka et al. (2014)	Plastic scintillator	Satsuma-Iojima, Osumi islands, Japan	The muon flux measurements have been used to depict a temporally resolved image of an eruption of the upper region of Mt. Io in 2013. The measurements have been aggregated to periods of 3 days over the course of a month.
Ambrosino et al. (2015)	Plastic scintillator (MU-RAY) Glass RPC (TOMUVOL)	Puy de Dôme, Auvergne, France	Comparison of two different detector types from two independent measurement campaigns used to unravel systematic errors that are invisible from only one measurement.
Rosas-Carbajal et al. (2017)	Scintillator	La Soufrière, Guadeloupe, France	Joint 3D inversion of gravity and muon flux data that are compared to a conductivity model, received from electric resistivity tomography. Identification of the volcanic hydrothermal system and its connection to the mechanical instabilities of the volcano's southern slope.
Oláh et al. (2019)	Multiwire proportional chamber (see Varga et al. 2016)	Sakurajima, Kyushu, Japan	This survey investigated the possible formation of a magma plug in the volcano's conduit and its relation to the eruption frequency of two neighbouring craters. 2D tomographic images have been produced to strengthen the empirical basis.
Tioukov et al. (2019)	ECC	Stromboli, Aeolian islands, Italy	A study that determines the internal structure of the crater region and the north-eastern flank of the volcano with 2D tomographic images. Links between eruption dynamics and volcano structure are investigated. The detector was operated for 5 months.
Lo Presti et al. (2020)	Plastic scintillator	Etna, Sicilly, Italy	2D tomographic images of the volcano's crater region are produced and used to monitor ongoing eruptions. Measurements were taken during 2017 (2 months) and 2018 (4-5 months). Changes in muon tomographic images could be linked to visually observable volcanic processes.

Table 2.3 (Continued)

Glaciology	Muon detector	Location	Summary
Nishiyama et al. (2017)	ECC	Jungfrau region, Bern, Switzerland	3D tomographic images of the bedrock-ice interface were produced and used to infer the stability of the rock mass above in light of the gradual melting of the glaciers. Observation duration was 3 months.
Nishiyama et al. (2019)	ECC	Jungfrau region, Bern, Switzerland	This survey took muon flux measurements during a total period of 6 months. A 3D model of the glacier bedrock was reconstructed, and its geometry was linked to possible erosion processes that dominate in upper glacial regions.
Caves			
Caffau et al. (1997)	RPC	Grotta Gigante, Trieste, Italy	The measurement of the atmospheric muon flux was used to determine the shape of the cave vault. For comparison, available gravity measurements and digital elevation models were considered. The data acquisition timeframe is stated to be at least 24 hours.
Oláh et al. (2012)	Closed cathode chamber (see Barnaföldi et al. 2012)	Various caves around Budapest, Hungary	This study presents a nice assembly of various test sites, where muon flux measurements have been performed. Another, projection-based, approach of 3D visualisation has been taken to present the results.
Fault zones			
Tanaka et al. (2011)	Scintillator	Itoigawa-Shizuoka Tectonic Line (ISTL), Itoigawa, Japan	Use of 2D muon tomographic imaging to locate a low-density, i.e. highly fractured, zone parallel to the ISTL and identification thereof as a possible new fault. A correlation between water content (i.e. rainfall) and muon attenuation has been observed to strengthen this implication.
Lesparre et al. (2017)	Scintillator	Tournemire, Aveyron, France	The authors present an approach to perform a 3D inversion based on a voxel parametrisation of a geologically well-known section. A low-density zone in one geologic unit is interpreted as a karstic network, that was able to form due to the presence of localised fault zones.
Borehole applications			
Oláh et al. (2018)	Closed cathode chamber (see Barnaföldi et al. 2012)	NEC Tamagawa Plant, Kanagawa, Japan	In this study the muon detector was deployed in a vertical borehole for the imaging of a near concrete pillar. Images were produced at different total measurement lengths (up to 2 weeks).
Bonneville et al. (2019)	Scintillator	Los Alamos Canyon, New Mexico, USA	A borehole detector (horizontal borehole) has been tested against a large-scale detector in a nearby tunnel. It was shown that small-scale borehole detectors may prove useful if accessibility below the target is not given.
Geophysical exploration			
Bryman et al. (2014)	Scintillator	Nyrstar Myra Falls mine, British Columbia, Canada	In this book chapter a case study is presented where the authors applied a muon detector inside a mine, where a known ore body is located between tunnel and surface. The collected muon data is compared to ample existing borehole data and a good agreement is found in the two different inversions.
Baccani et al. (2019)	Scintillator	San Silvestro Archaeo-Mining Park, Tuscany, Italy	A 53-day measurement campaign was conducted in an abandoned mine. There, a high-resolution image of the rock space above was made, thereby locating previously unknown cavities and a high-density vein.

2.5 Best practice guidelines

We would like to conclude our review with a rough guide on how a (geo)scientist who is interested in utilising this technology might proceed. In the subsequent paragraphs we define various criteria which, we think, a prospective user must ask him-/herself whilst preparing for a project. Even though the points we raise are also valid for many other geophysical methods one wishes to use, here, they are set in the context of muon tomography experiments. We split the basic planning steps in two. While Ch. 2.5.1 explains the basic planning steps before deciding on whether to use muon tomography or not, Ch. 2.5.2 focuses more on some technical questions regarding detector selection, exposure length and alternative methods.

2.5.1 Planning phase

In this chapter we quickly summarise three basic questions that should ideally be answered with "Yes" for muon tomography to be considered a serious alternative. These considerations can already be made in an early planning phase, where it is not already clear how the parameters of interest are supposed to be measured.

1) Applicability: *"Is the method sensitive to the parameter in question?"*

The first question a potential user must answer, concerns the general applicability of the method to the problem at hand. Muon tomography is mainly sensitive to material density and only slightly to material composition. However, state-of-the-art muon tomography is not capable of resolving compositions very well, due to the systematic errors in the cosmic ray flux models. Thus, if the research question requires information about a 3D density structure, then muon tomography is a valid option.

2) Alternatives: *"Is there another method that would yield more useful results?"*

Intricately linked to the previous point is the question whether muon tomography is the optimal method for the problem at hand. We advise the prospective user to inform themselves if there are other geophysical methods, that may provide better results. In this case one could ask if muon tomography is then a valid auxiliary method (seeing that nowadays many experimental field campaigns do rely on multiple geophysical measurements).

3) Accessibility (Location): *"Is there a suitable place to deploy a muon detector?"*

If the technology can be applied to the researcher's problem, the issue of accessibility has to be solved next. As the reader might have picked up, muon tomography requires the detector to be located underneath the study object. This is because, so far, one measures muons that originate from the natural

cosmic ray flux, i.e. from above. This implies that the study object must either be topographically distinct (like a volcano) or accessible from underneath (for example caves, mines and tunnels); a circumstance that might be considered one of the greatest limitations of muon tomography. As can be seen in Ch. 2.4, researchers have already begun to examine the possibilities of borehole muon detectors which might prove a potent solution for future applications. In every case one has to remember that muon tomography remains a shallow subsurface imaging technique, meaning that when the overburden is larger than ~1km, reliable results are difficult to obtain (see Ch. 2.5.2 for more details on this).

4) Accessibility (Technology): *"Is there a physics institute nearby that can provide detectors and know-how?"*

We stated earlier that the know-how of particle detection (i.e. detector construction and analysis) is still very much concentrated in the (particle) physics community. Unless this state of affairs changes, most prospective muon tomography experiments will typically require the collaboration with a particle physics institute. Thus, it is advantageous to enquire at the local university, as it facilitates the quick exchange of personnel, knowledge, and material.

2.5.2 Operation phase

Whereas Ch. 2.5.1 focused on the issues during the planning of an experimental campaign, we like to discuss here some central problems that appear once the decision has been taken to use muon tomography. Usually, these questions revolve around some technical aspects, that are nevertheless important to consider.

5) Detectors: *"Which detector should I use?"*

As explained in Ch. 2.3.4, there are a lot of muon detector variants to choose from. In reality, this choice is smaller due to the availability of the know-how and hardware at the collaborating physics institute (i.e. not every physics lab possesses a dedicated emulsion analysis infrastructure). Thus, it is a viable strategy to think about the deployment conditions and the instrumental specifics that a muon detector should encompass. For example, it would make no sense to deploy a detector inside a tunnel for a long time without any power supply or a nuclear emulsion in conditions that exhibit large temperature changes over the measurement period. As particle detectors are very often custom made, they can also be designed to operate in the desired environment. Therefore, one is best advised to discuss this matter within the collaboration and elaborate a roadmap.

6) Exposure: *"How long do I need to collect muons until I get useful results?"*

In the course of the experimental planning, it is of utmost importance to have a rough idea of how long the data acquisition will take until the processing of data can start, such that subsequent project steps can be meaningfully scheduled. In order to answer this, a back-of-the-envelope calculation is usually enough. We quickly show how this can be read of a chart that was singularly produced for this reason. Interested readers are also referred to Appendix F, where we elucidate the rationale behind this approach.

The aforementioned chart is depicted in Fig. 2.10 as a series of straight lines in a log-log plot. Every line denotes another relative spatial resolution (1 %, 5 %, 10 %, 20 %). Users usually haver already a target spatial resolution in mind before deciding on the exposure parameters (i.e. exposure time and detector area). The chart can be used by first deciding on which spatial resolution the experiment should have and then deciding on detector size (i.e. area) and exposure time. The resulting point in the graph should lie in the vicinity of the chosen spatial resolution line. This is nothing else as the trade-off between detector area and exposure time, i.e. the longer one records the muon flux, the smaller the detector can be, in order to record a muon flux of equal statistical significance.

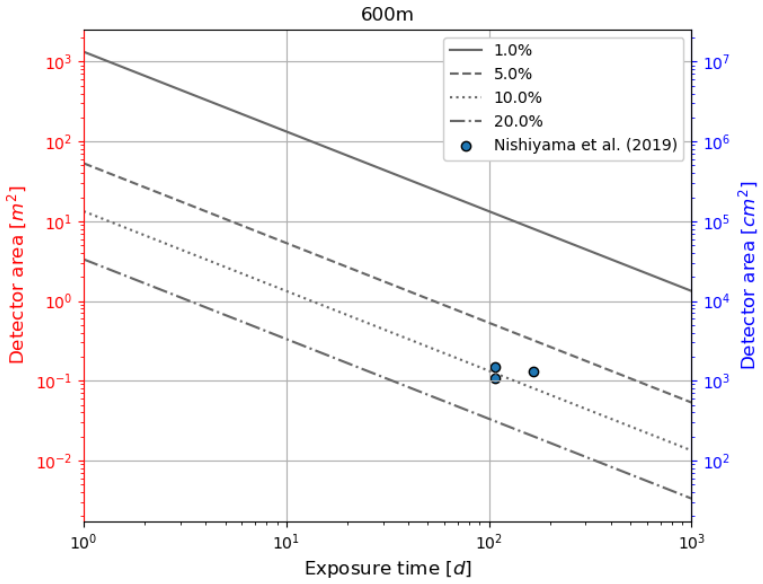

Figure 2.10: Decision help chart for the two experimental parameters detector size and exposure time in case of an overburden of around 600 m. Parallel lines indicate the amount of desired lateral precision one can achieve by using a corresponding area/time-point. The three blue dots represent an example from an earlier study performed on a glacier (Nishiyama et al., 2019).

As this sounds very technical, we included in Fig. 2.10 a small example from our own experimental campaign (Nishiyama et al., 2019). In that study we had three operating detector sites, that calculated from the digital elevation model an overburden of roughly 600 m (i.e. distance from the detector to the middle of the surface of the study object; in our case this was glacier). We were targeting a relative spatial resolution of 10 %, which corresponds to an absolute spatial resolution of around 60 m. Please note, that this value is the lateral spatial resolution (i.e. perpendicular to) and not along the viewing direction. This can also be understood as the bin size, that one plans on using during the data processing.

Limited by the total scanning throughput of our infrastructure, the $0.1\ m^2 - 0.2\ m^2$ were an upper boundary to the overall detector size. Thus, we settled with an exposure time of around $100\ d - 200\ d$.

In Appendix F, we provide the prospective user with similar plots as Fig. 2.10 but for different expected thicknesses of the overburden. Alternatively, the reader may use the respective formulae to plot his/her own version of this graph.

7) Placement: *"Where should I position my detectors?"*

This question relates somewhat to point 3 in the previous Ch. 2.5.1 where we discussed the physical accessibility of the measurement location. For one, it is still important that the detector is located below the target, in order to detect the natural cosmic ray muons. Another issue, that should be regarded from an experimental design point of view is the arrangement of different detectors with respect to each other. Frankly, if a 3D muon tomography is desired, one is advised to distribute the detectors as much as possible around the object in question. This could help prevent somewhat against an underdetermined inverse problem, where individual parameters cannot be resolved well because the detector geometry only allows to gain information on the correlation between the parameters and not their absolute values. A similar problem exists in seismology, where the detectors (i.e. seismographs) are preferably stationed around the earthquake to optimally resolve the earthquake source position.

8) Synergies: *"Can I improve my results by means of other geophysical methods?"*

This last issue ties strongly to point 2 from the previous Ch. 2.5.1. Namely, the question if other geophysical methods are better suited to fill the needs of the researcher. Here, we change the perspective on that question slightly and ask if there are other geophysical methods that may reinforce the muon tomography measurements. Many of the examples given in Ch. 2.4 are studies that utilise gravimetry in addition to muon tomography. This is a natural choice, as both methods are sensitive to the same physical parameter, i.e. material density. Additionally, both methods compensate many weaknesses of the respective other. This yields a superb synergy between these methods. It may at this point also be a good idea to consult fellow geoscientists who are experienced in geophysical imaging methods to get an idea if they are compatible with muon tomography.

2.6 Conclusions

Until now insights into the Earth's interior have mostly utilised well-established geophysical methods such as seismic tomography, electric resistivity tomography, ground penetrating radar etc. In recent years a new method originating from particle physics, muon tomography, was the longer the more used gain insights into shallow geological features. This new technology synergises well with the well-established geophysical methods as their advantages and drawbacks balance each other. Muon tomography brought to geology the possibility to measure structural properties (like the density distribution) within the object in question, while not having to go near dangerous or inaccessible places. Naturally, there are also scenarios where the established geophysical methods yield much better results.

To be able to make the decision whether this new technology could benefit one's research, well-founded knowledge on the possibilities and limitations of muon tomography are needed. However, due to originating from a particle physics environment the know-how is located mostly in particle physics laboratories around the globe. With this work, we present a starting point for prospective users with a geoscientific background to delve deeper into the matter of muon tomography. The summaries of important aspects should help interested readers to form a solid foothold. From there on the acquisition of new particle physics knowledge is hopefully facilitated. The aspects in the previous chapters are not meant to be exhaustive. They consist, however, of a few important cornerstones that we think are important to get a good idea on the whole topic of muon tomography. The guidelines are also intended to point the prospective users into the right direction. The showcase of different applications is thought to be an inspiration for readers. Knowing about the potential uses of muon tomography, one can employ this technology in their own research field. The possible applications of this technology are still far from exhausted.

2.7 Appendix A – Results from PARMA

Table 2.A1: Numerical results from PARMA (Sato, 2016) for the location of Bern, Switzerland (Lat: 46.94 °N, Lon: 7.44 °E) for an altitude of 0 m above sea level.

Total energy E $[GeV]$	Differential muon flux $\frac{d\Phi_S}{dE}$ $[GeV^{-1}m^{-2}s^{-1}sr^{-1}]$		
	$\theta = 0°$	$\theta = 45°$	$\theta = 60°$
1.13	2.12E-03	5.93E-04	2.39E-04
1.42	1.80E-03	5.36E-04	2.29E-04
1.79	1.49E-03	4.73E-04	2.15E-04
2.25	1.19E-03	4.05E-04	1.97E-04
2.84	9.23E-04	3.36E-04	1.74E-04
3.57	6.90E-04	2.69E-04	1.48E-04
4.50	4.97E-04	2.06E-04	1.21E-04
5.66	3.45E-04	1.52E-04	9.41E-05
7.13	2.31E-04	1.07E-04	6.98E-05
8.97	1.49E-04	7.25E-05	4.93E-05
11.29	9.30E-05	4.70E-05	3.31E-05
14.22	5.62E-05	3.10E-05	2.30E-05
17.90	3.30E-05	1.99E-05	1.55E-05
22.54	1.88E-05	1.24E-05	1.01E-05
28.37	1.05E-05	7.52E-06	6.32E-06
35.72	5.68E-06	4.42E-06	3.83E-06
44.97	3.01E-06	2.52E-06	2.25E-06
56.61	1.56E-06	1.40E-06	1.29E-06
71.26	7.91E-07	7.49E-07	7.12E-07
89.72	3.93E-07	3.93E-07	3.85E-07
112.94	1.95E-07	2.05E-07	2.07E-07
142.19	9.72E-08	1.07E-07	1.11E-07
179.01	4.80E-08	5.48E-08	5.93E-08
225.36	2.35E-08	2.79E-08	3.12E-08
283.71	1.14E-08	1.40E-08	1.63E-08
357.17	5.12E-09	6.42E-09	7.73E-09
449.65	2.26E-09	2.88E-09	3.58E-09
566.08	9.93E-10	1.28E-09	1.62E-09
712.64	4.35E-10	5.59E-10	7.25E-10
897.16	1.90E-10	2.42E-10	3.19E-10
1129.40	8.32E-11	1.05E-10	1.39E-10
1421.90	3.62E-11	4.56E-11	6.06E-11
1790.10	1.58E-11	1.99E-11	2.64E-11
2253.60	6.87E-12	8.64E-12	1.15E-11
2837.10	2.99E-12	3.76E-12	4.99E-12
3571.70	1.30E-12	1.63E-12	2.17E-12
4496.50	5.63E-13	7.09E-13	9.41E-13
5660.80	2.45E-13	3.08E-13	4.09E-13
7126.40	1.06E-13	1.34E-13	1.77E-13
8971.60	4.60E-14	5.80E-14	7.69E-14

2.8 Appendix B – Uncertainty estimates for muon flux

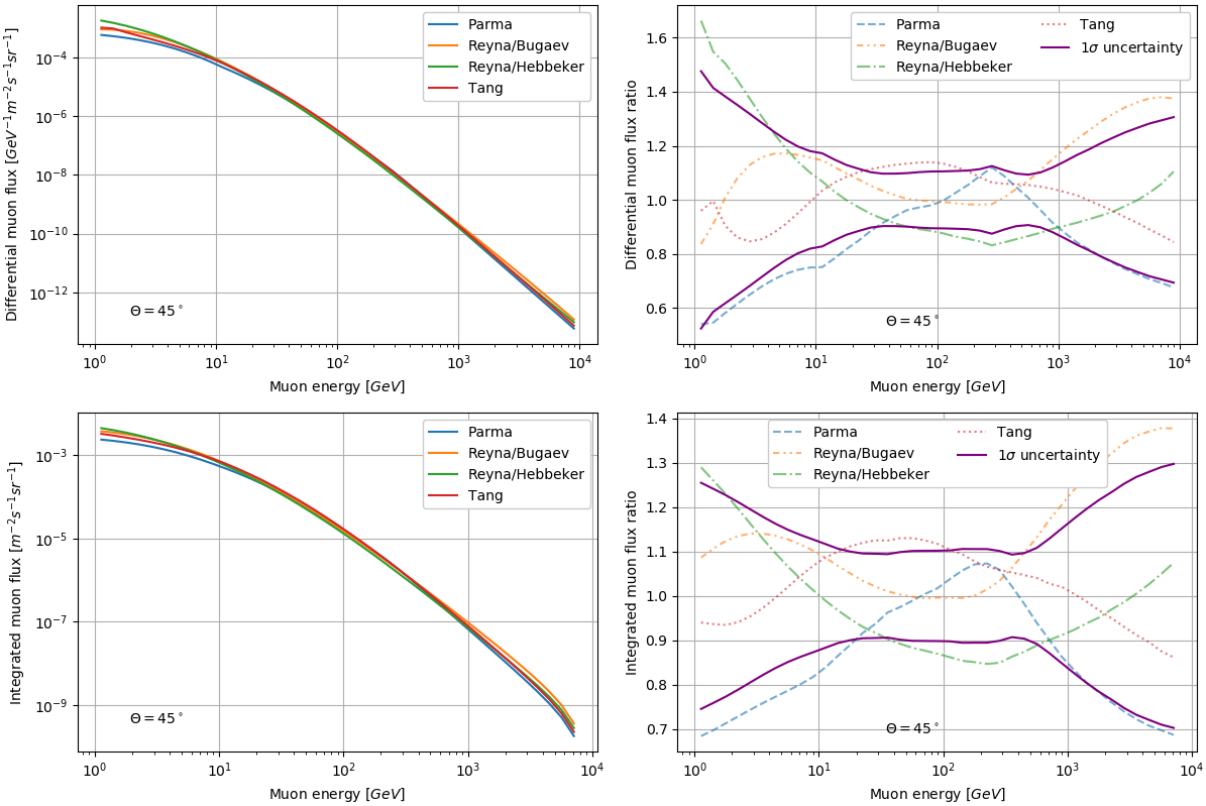

Figure 2.B1: Comparison of the four muon flux models (Ch. 2.3.2.2 – 2.3.2.5) including an uncertainty estimate for a zenith angle of $\theta = 45°$. *Top left*: Differential muon flux as a function of energy. *Top right*: Differential muon flux ratio to the mean differential flux $\langle d\Phi/dE \rangle$ (see Eq. 2.21). *Bottom left*: Integrated muon flux as a function of the lower integration boundary (i.e. E_{cut} in Eq. 2.20). *Bottom right*: Integrated muon flux ration to the mean integrated flux $\langle \Phi \rangle$. The 1σ-uncertainty in the right-hand side plots has been calculated according to Eq. (2.23).

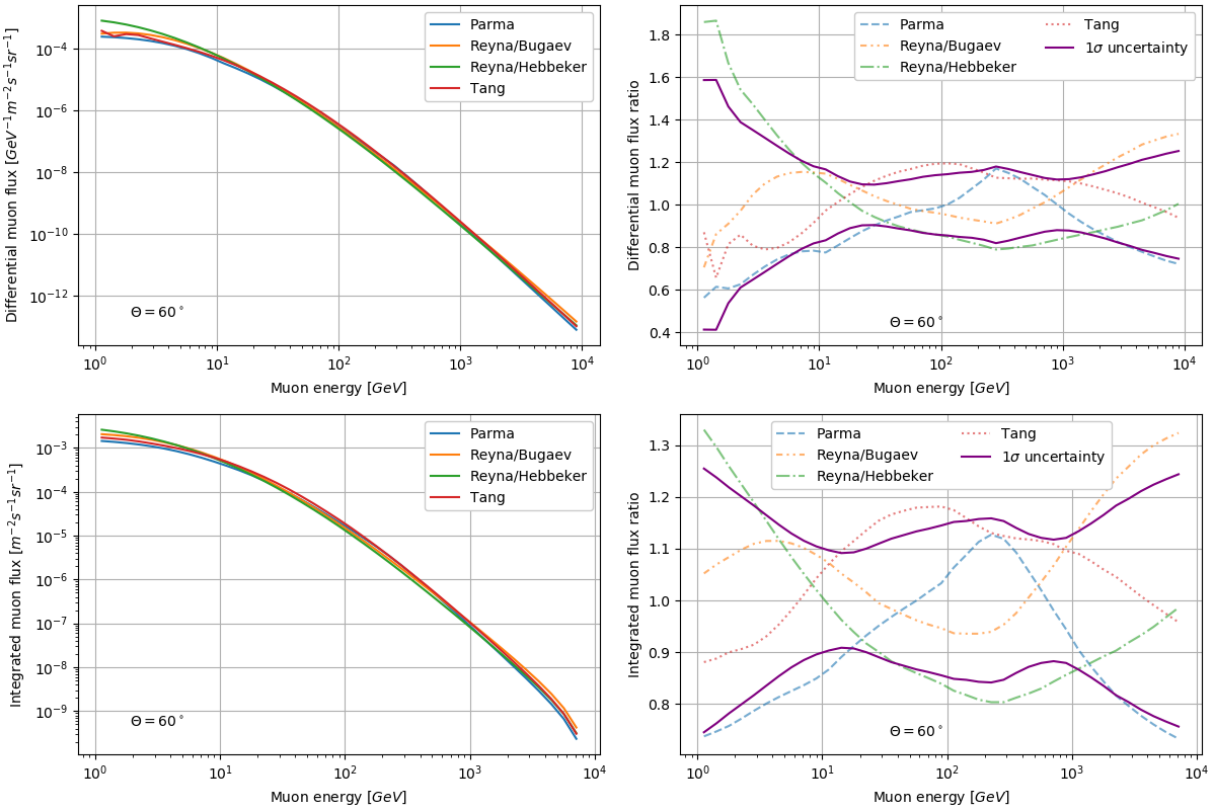

Figure 2.B2: Comparison of the four muon flux models (Ch. 2.2.2 – 2.2.5) including an uncertainty estimate for a zenith angle of $\theta = 60°$. *Top left*: Differential muon flux as a function of energy. *Top right*: Differential muon flux ratio to the mean differential flux $\langle d\Phi/dE \rangle$ (see Eq. 2.21). *Bottom left*: Integrated muon flux as a function of the lower integration boundary (i.e. E_{cut} in Eq. 2.20). *Bottom right*: Integrated muon flux ration to the mean integrated flux $\langle \Phi \rangle$. The 1σ-uncertainty in the right-hand side plots has been calculated according to Eq. (2.23).

2.9 Appendix C – Energy loss tables

The energy loss tables, as mentioned in Ch. 2.3.3.2 may be found on the website of the Particle Data Group, the international collaboration of particle physicists (https://pdg.lbl.gov/ → Atomic & Nuclear Properties). They offer energy loss tables for every pure element as well as for selected compounds. As an example, we present the table for "standard rock", reduced only to the most important information. Please note that in Table 2.C1 the indicated energy is the kinetic energy of the muon, T and not the total energy, E. They are however related by the formula

$$T = E - E_\mu \,, \tag{2.C1}$$

where $E_\mu = 105.7\ MeV$ is the rest mass of the muon. For $E \gg E_\mu$ we have $E \approx T$.

Table 2.C1: Excerpt from the energy loss table for standard rock between $1\ GeV - 900\ GeV$.

T $[MeV]$	dE/dx $[MeV\ cm^2\ g^{-1}]$	Range $[g\ cm^{-2}]$	T $[MeV]$	dE/dx $[MeV\ cm^2\ g^{-1}]$	Range $[g\ cm^{-2}]$
1.000E+03	1.808E+00	5.534E+02	1.000E+05	2.747E+00	4.084E+04
1.200E+03	1.837E+00	6.631E+02	1.200E+05	2.837E+00	4.800E+04
1.400E+03	1.862E+00	7.712E+02	1.400E+05	2.925E+00	5.495E+04
1.700E+03	1.895E+00	9.309E+02	1.700E+05	3.057E+00	6.498E+04
2.000E+03	1.922E+00	1.088E+03	2.000E+05	3.187E+00	7.459E+04
2.500E+03	1.960E+00	1.346E+03	2.500E+05	3.400E+00	8.977E+04
3.000E+03	1.990E+00	1.599E+03	3.000E+05	3.611E+00	1.040E+05
3.500E+03	2.016E+00	1.848E+03	3.500E+05	3.824E+00	1.175E+05
4.000E+03	2.038E+00	2.095E+03	4.000E+05	4.037E+00	1.302E+05
4.500E+03	2.058E+00	2.339E+03	4.500E+05	4.250E+00	1.423E+05
5.000E+03	2.075E+00	2.581E+03	5.000E+05	4.465E+00	1.538E+05
5.500E+03	2.091E+00	2.821E+03	5.500E+05	4.677E+00	1.647E+05
6.000E+03	2.105E+00	3.059E+03	6.000E+05	4.890E+00	1.752E+05
7.000E+03	2.130E+00	3.531E+03	7.000E+05	5.318E+00	1.948E+05
8.000E+03	2.152E+00	3.998E+03	8.000E+05	5.748E+00	2.129E+05
9.000E+03	2.171E+00	4.461E+03	9.000E+05	6.180E+00	2.296E+05
1.000E+04	2.188E+00	4.920E+03	1.000E+06	6.615E+00	2.453E+05
1.200E+04	2.218E+00	5.827E+03	1.200E+06	7.475E+00	2.737E+05
1.400E+04	2.244E+00	6.724E+03	1.400E+06	8.340E+00	2.990E+05
1.700E+04	2.277E+00	8.051E+03	1.700E+06	9.647E+00	3.324E+05
2.000E+04	2.306E+00	9.360E+03	2.000E+06	1.096E+01	3.616E+05
2.500E+04	2.347E+00	1.151E+04	2.500E+06	1.314E+01	4.032E+05
3.000E+04	2.383E+00	1.362E+04	3.000E+06	1.533E+01	4.384E+05
3.500E+04	2.416E+00	1.571E+04	3.500E+06	1.754E+01	4.688E+05
4.000E+04	2.447E+00	1.776E+04	4.000E+06	1.976E+01	4.957E+05
4.500E+04	2.476E+00	1.979E+04	4.500E+06	2.198E+01	5.197E+05
5.000E+04	2.503E+00	2.180E+04	5.000E+06	2.422E+01	5.413E+05
5.500E+04	2.530E+00	2.379E+04	5.500E+06	2.643E+01	5.611E+05
6.000E+04	2.556E+00	2.575E+04	6.000E+06	2.865E+01	5.792E+05
7.000E+04	2.606E+00	2.963E+04	7.000E+06	3.311E+01	6.117E+05
8.000E+04	2.654E+00	3.343E+04	8.000E+06	3.759E+01	6.400E+05
9.000E+04	2.701E+00	3.717E+04	9.000E+06	4.208E+01	6.651E+05

2.10 Appendix D – Radiation length of a real rock

In this chapter we guide the reader through an exemplary calculation from the raw XRF measurements to a radiation length.

We start off by showing the raw XRF data that was collected during our measurement campaign for Nishiyama et al. (2017) in Table 2.D1.

Table 2.D1: Raw XRF measurement data taken during the muon tomography measurement campaign of Nishiyama et al. (2017). Data in columns denote weight percent oxide fractions.

Sample	1	2	3	4	5	6	7	8	9	10	11	12	13
Oxide													
SiO2	0.6131	0.5981	0.6997	0.6139	0.6201	0.6401	0.5691	0.6555	0.7101	0.7181	0.6287	0.7593	0.6771
TiO2	0.0123	0.0067	0.0076	0.0094	0.0084	0.0088	0.0156	0.0089	0.0069	0.0065	0.0075	0.0055	0.0083
Al2O3	0.1567	0.1873	0.1481	0.1921	0.178	0.1736	0.1875	0.1719	0.1394	0.1455	0.1902	0.1142	0.147
Fe2O3	0.087	0.0791	0.0496	0.0686	0.065	0.0586	0.0833	0.0648	0.0486	0.0428	0.0683	0.0303	0.0558
MnO	0.001	0.0012	0.0009	0.0009	0.0008	0.0008	0.0011	0.0009	0.0007	0.0006	0.0009	0.0005	0.0009
MgO	0.0359	0.0285	0.0206	0.0288	0.0254	0.0246	0.0318	0.0215	0.0225	0.0192	0.0266	0.0139	0.0229
CaO	0.0202	0.0071	0.0201	0.0137	0.0147	0.0244	0.0325	0.0146	0.0168	0.0167	0.012	0.0161	0.0125
Na2O	0.0228	0.0248	0.0404	0.0323	0.0369	0.0372	0.0518	0.0442	0.0365	0.0378	0.0451	0.0264	0.0199
K2O	0.0343	0.0465	0.0287	0.0469	0.0465	0.0406	0.0315	0.0354	0.0233	0.0282	0.0452	0.0223	0.031
P2O5	0.0041	0.0029	0.0021	0.0027	0.0035	0.0064	0.0123	0.0014	0.0016	0.003	0.0014	0.0019	0.0009
Sum	0.9874	0.9822	1.0178	1.0093	0.9993	1.0151	1.0165	1.0191	1.0064	1.0184	1.0259	0.9904	0.9763

Following the methodology in Ch. 3.9.2 we may rearrange Table 2.D1 into pure element data by decomposing them into their elementary constituent weight fractions. This is shown in Table 2.D2.

Table 2.D2: Raw data from Table 2.D1 decomposed into elementary weight fractions.

Sample	1	2	3	4	5	6	7	8	9	10	11	12	13
Element													
Si	0.2866	0.2796	0.3271	0.2870	0.2899	0.2992	0.2660	0.3064	0.3319	0.3357	0.2939	0.3549	0.3165
Ti	0.0074	0.0040	0.0046	0.0056	0.0050	0.0053	0.0093	0.0053	0.0041	0.0039	0.0045	0.0033	0.0050
Al	0.0829	0.0991	0.0784	0.1017	0.0942	0.0919	0.0992	0.0910	0.0738	0.0770	0.1007	0.0604	0.0778
Fe	0.0609	0.0553	0.0347	0.0480	0.0455	0.0410	0.0583	0.0453	0.0340	0.0299	0.0478	0.0212	0.0390
Mn	0.0008	0.0009	0.0007	0.0007	0.0006	0.0006	0.0009	0.0007	0.0005	0.0005	0.0007	0.0004	0.0007
Mg	0.0216	0.0172	0.0124	0.0174	0.0153	0.0148	0.0192	0.0130	0.0136	0.0116	0.0160	0.0084	0.0138
Ca	0.0144	0.0051	0.0144	0.0098	0.0105	0.0174	0.0232	0.0104	0.0120	0.0119	0.0086	0.0115	0.0089
Na	0.0169	0.0184	0.0300	0.0240	0.0274	0.0276	0.0384	0.0328	0.0271	0.0280	0.0335	0.0196	0.0148
K	0.0285	0.0386	0.0238	0.0389	0.0386	0.0337	0.0261	0.0294	0.0193	0.0234	0.0375	0.0185	0.0257
P	0.0018	0.0013	0.0009	0.0012	0.0015	0.0028	0.0054	0.0006	0.0007	0.0013	0.0006	0.0008	0.0004
O	0.4656	0.4627	0.4909	0.4751	0.4708	0.4808	0.4704	0.4842	0.4893	0.4952	0.4822	0.4913	0.4737
Sum	0.9874	0.9822	1.0178	1.0093	0.9993	1.0151	1.0165	1.0191	1.0064	1.0184	1.0259	0.9904	0.9763

At this point we may normalise the data, i.e. rescale each data column to 1, as depicted in Table 2.D3.

Table 2.D3: Elementary weight fraction data from Table 2.D2 normalised to 1.

Sample	1	2	3	4	5	6	7	8	9	10	11	12	13
Element													
Si	0.2902	0.2846	0.3213	0.2843	0.2901	0.2948	0.2617	0.3007	0.3298	0.3296	0.2865	0.3584	0.3242
Ti	0.0075	0.0041	0.0045	0.0056	0.0050	0.0052	0.0092	0.0052	0.0041	0.0038	0.0044	0.0033	0.0051
Al	0.0840	0.1009	0.0770	0.1007	0.0943	0.0905	0.0976	0.0893	0.0733	0.0756	0.0981	0.0610	0.0797
Fe	0.0616	0.0563	0.0341	0.0475	0.0455	0.0404	0.0573	0.0445	0.0338	0.0294	0.0466	0.0214	0.0400
Mn	0.0008	0.0009	0.0007	0.0007	0.0006	0.0006	0.0008	0.0007	0.0005	0.0005	0.0007	0.0004	0.0007
Mg	0.0219	0.0175	0.0122	0.0172	0.0153	0.0146	0.0189	0.0127	0.0135	0.0114	0.0156	0.0085	0.0141
Ca	0.0146	0.0052	0.0141	0.0097	0.0105	0.0172	0.0229	0.0102	0.0119	0.0117	0.0084	0.0116	0.0092
Na	0.0171	0.0187	0.0294	0.0237	0.0274	0.0272	0.0378	0.0322	0.0269	0.0275	0.0326	0.0198	0.0151
K	0.0288	0.0393	0.0234	0.0386	0.0386	0.0332	0.0257	0.0288	0.0192	0.0230	0.0366	0.0187	0.0264
P	0.0018	0.0013	0.0009	0.0012	0.0015	0.0028	0.0053	0.0006	0.0007	0.0013	0.0006	0.0008	0.0004
O	0.4716	0.4711	0.4823	0.4707	0.4711	0.4736	0.4628	0.4751	0.4862	0.4862	0.4700	0.4961	0.4852
Sum	1.0000	1.0000	1.0000	1.0000	1.0000	1.0000	1.0000	1.0000	1.0000	1.0000	1.0000	1.0000	1.0000

The last step consists of forming so called log-ratios. This means that we divide our rows by one arbitrarily chosen row (we decided on the last row, i.e. oxygen) and take the natural logarithm of the resulting value. See Table 2.D4 for these results.

Table 2.D4: Log-ratios of the values given in Table 2.D3.

Sample	1	2	3	4	5	6	7	8	9	10	11	12	13
$\ln(Si/O)$	-0.4853	-0.5038	-0.4061	-0.5042	-0.4850	-0.4742	-0.5701	-0.4575	-0.3881	-0.3887	-0.4952	-0.3252	-0.4032
$\ln(Ti/O)$	-4.1457	-4.7469	-4.6800	-4.4348	-4.5381	-4.5125	-3.9183	-4.5083	-4.7734	-4.8450	-4.6753	-5.0043	-4.5561
$\ln(Al/O)$	-1.7253	-1.5406	-1.8346	-1.5418	-1.6089	-1.6549	-1.5561	-1.6718	-1.8920	-1.8610	-1.5665	-2.0955	-1.8063
$\ln(Fe/O)$	-2.0349	-2.1238	-2.6497	-2.2928	-2.3375	-2.4621	-2.0887	-2.3686	-2.6669	-2.8058	-2.3119	-3.1435	-2.4962
$\ln(Mn/O)$	-6.3989	-6.2103	-6.5572	-6.5245	-6.6331	-6.6541	-6.3139	-6.5434	-6.8053	-6.9713	-6.5393	-7.1459	-6.5214
$\ln(Mg/O)$	-3.0684	-3.2929	-3.6767	-3.3090	-3.4254	-3.4784	-3.1999	-3.6202	-3.5853	-3.7557	-3.4032	-4.0710	-3.5351
$\ln(Ca/O)$	-3.4736	-4.5129	-3.5314	-3.8821	-3.8025	-3.3167	-3.0083	-3.8373	-3.7076	-3.7254	-4.0293	-3.7542	-3.9707
$\ln(Na/O)$	-3.3152	-3.2248	-2.7960	-2.9871	-2.8448	-2.8577	-2.5048	-2.6923	-2.8943	-2.8711	-2.6680	-3.2224	-3.4684
$\ln(K/O)$	-2.7944	-2.4838	-3.0255	-2.5017	-2.5011	-2.6578	-2.8898	-2.8019	-3.2307	-3.0517	-2.5534	-3.2787	-2.9127
$\ln(P/O)$	-5.5615	-5.9015	-6.2834	-5.9995	-5.7308	-5.1482	-4.4732	-6.6751	-6.5522	-5.9354	-6.6710	-6.3844	-7.0950
$\ln(O/O)$	0.0000	0.0000	0.0000	0.0000	0.0000	0.0000	0.0000	0.0000	0.0000	0.0000	0.0000	0.0000	0.0000

As these log-ratios are usually statistically well-behaved, i.e. gaussian-like, we may form a meaningful mean log-ratio of our different samples. For an explanation why this works, the reader is referred to the textbook of Aitchison (1986). Normality plots of this data may additionally be found in Ch. 3.9.2.

Now we may calculate the mean of the data in Table 2.D4 (see Table 2.D5 for results).

Table 2.D5: Mean values of the 13 log-ratios given in Table 2.D4.

Log-ratio	Mean value
$\ln(Si/O)$	-0.4528
$\ln(Ti/O)$	-4.5645
$\ln(Al/O)$	-1.7197
$\ln(Fe/O)$	-2.4448
$\ln(Mn/O)$	-6.6014
$\ln(Mg/O)$	-3.4939
$\ln(Ca/O)$	-3.7348
$\ln(Na/O)$	-2.9498
$\ln(K/O)$	-2.8218
$\ln(P/O)$	-6.0316
$\ln(O/O)$	0.0000

Table 2.D6: Back-transformed mean values from Table 2.D5. Additionally, the inverse value of the radiation length is also shown. $1/\Lambda_0$ has been calculated according to Eqs. (2.34) & (2.35) and Table 2.1.

Element	Wt-mean	$1/\Lambda_0$ (rad. length) $[cm^2\ g^{-1}]$
Si	0.3054	0.0458
Ti	0.0050	0.0619
Al	0.0860	0.0416
Fe	0.0417	0.0723
Mn	0.0007	0.0683
Mg	0.0146	0.0399
Ca	0.0115	0.0619
Na	0.0251	0.0361
K	0.0286	0.0578
P	0.0012	0.0472
O	0.4803	0.0292

Using the back transformation from log-ratios to element weight fractions, i.e.

$$wt_{ele,i} = \frac{\exp(r_i)}{1+\sum_{j=1}^{N_{ele}-1}\exp(r_j)} \tag{2.D1}$$

for the numerator elements and

$$wt_{ele,N_{ele}} = \frac{1}{1+\sum_{j=1}^{N_{ele}-1}\exp(r_j)} \tag{2.D2}$$

for de denominator element (oxygen), we can transform these mean log-ratios from Table 2.D5 back to meaningful element weight fractions (see Table 2.D6). Once we have these weight fractions, we may perform a weighted average over the inverse values of the radiation length (see Eq. 2.36) to get the radiation length of our rock. We eventually end up with $1/\Lambda_{0,\mathrm{rock}} = 0.0389\ cm^2\ g^{-1}$ or equivalently, $\Lambda_{0,rock} = 25.72\ g\ cm^{-2}$.

With the log-ratio formalism it is theoretically also possible to calculate an error on this radiation length. As this however goes too far for the purpose of this calculation, we omit this step.

2.11 Appendix E – Treatment of multiple Coulomb scattering

In this appendix we try to illustrate how we can apply the concepts from Ch. 2.3.3.3 to an example experimental setup in order to understand how we can cope with the potential outscattering of particles. Following Tanabashi et al. (2018) we assume that our scattering can be well described by a 2D-Gaussian distribution around zero deviation with a "standard deviation" of $\sigma = \theta_{plane}$, i.e.

$$p(\theta_x, \theta_y) = \frac{1}{2\pi\theta_{plane}^2} \exp\left(-\frac{\theta_x^2+\theta_y^2}{2\theta_{plane}^2}\right). \tag{2.E1}$$

An example of how this looks like when this scattering cone hits a detector please see a) of Fig. 2.E1. We see that not all muons hit the detector. However, we also have to account for muons, that would not normally hit the detector and are scattered into the detector. We present here a conceptual approach for this non-trivial phenomenon. We may add some imaginary detectors around our real device, which then forms a sort of detector lattice, with one detector being a "unit cell". For every imaginary detector we can form also such a muon scattering cone, coming from the same direction as the original one (i.e. they are parallel to each other). Muons that would normally not hit this imaginary detector, will instead hit our real detector (at least on the side where real and imaginary detector touch). These particles are then scattered into our detector (see b) of Fig. 2.E1). This is valid for every point on our detector; c) & d) of Fig. 2.E1 depict the situation for a non-centred point on the detector.

One sees that out-scattering and in-scattering are always balanced and thus the measured muon flux can be reliably measured. One warning has to be made though. If we have to deal with in- and out-scattering, we actually lower the spatial resolution of our measurement. This can be explained by the fact, that if we have to rely on imaginary detectors to "catch" our stray muons, then we actively enlarge the effective detector area relative to the structures that we want to observe. In the example from Fig. 2.E1. we tripled the height and width of our detector, meaning that we cannot resolve structures below $\sim 3\ m$ anymore, as they tend to be "smoothed" out in our measurements. This effect is expected to become even more prominent with lower-energy (i.e. higher scattering angle) muons.

Luckily, as we usually do not use only muons from one energy, but from the whole flux (i.e. energy integrated), this "blurring"-effect is usually mitigated to an extent where the blurring is below the resolution one tries to achieve.

Note, that this is only a very rough sketch of the problem and we do not present a definitive solution, but only a way on how one might conceptualise this issue. Certainly, more research is needed in this area.

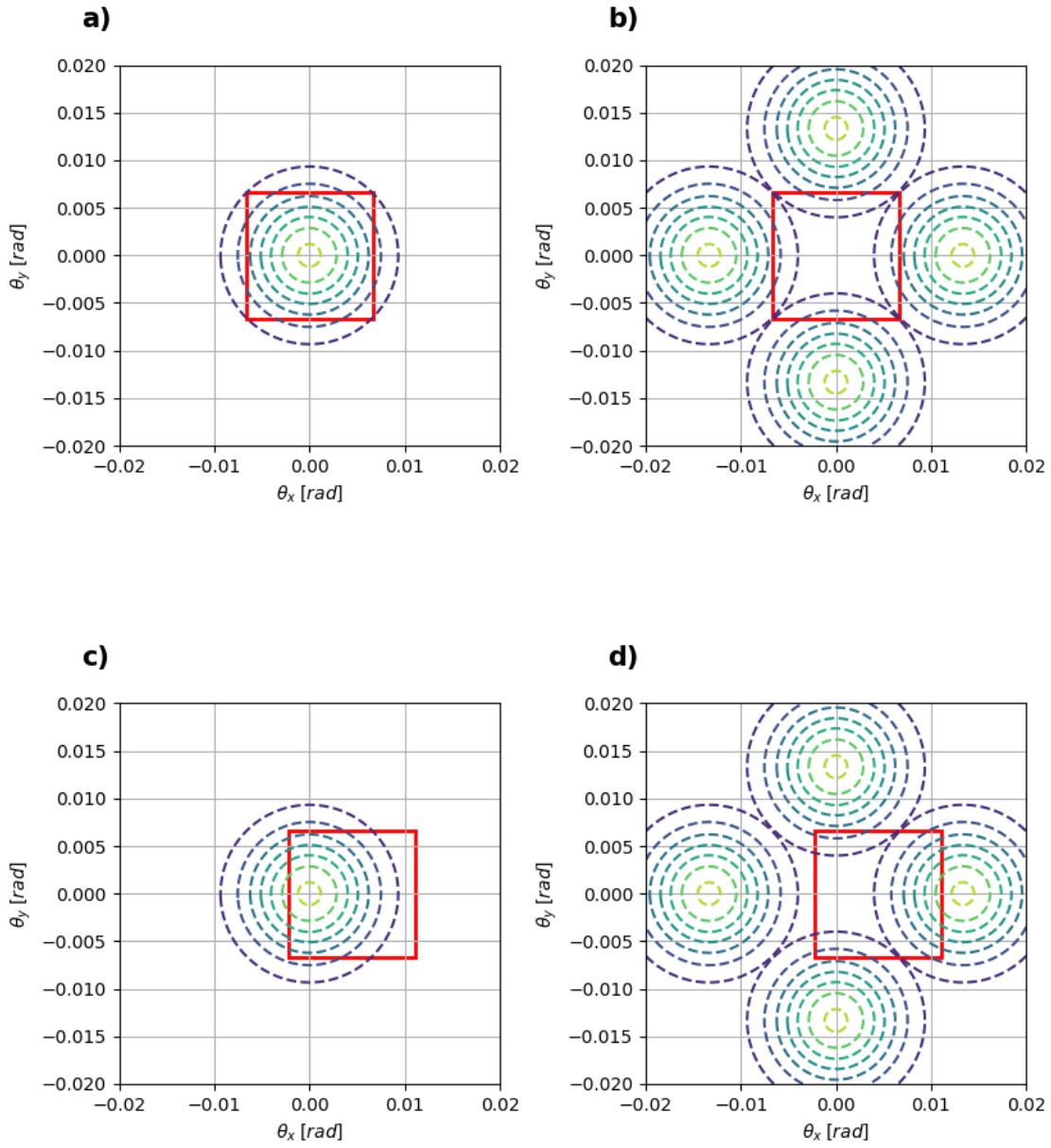

Figure 2.E1: Examples of out-scattering and in-scattering from different (adjacent) incident muon trajectories on a detector (red rectangle) with side lengths $l = 1\ m$. Dashed circles denote the isolines from a 2D Gaussian distribution (here with the parameters for $150\ m$ of standard rock and an exit energy of $100\ GeV$; this means $\theta_{plane} = 4.69\ mrad$ (see Table 2.2). *a)* A small part of the scattered muons does not hit the detector, i.e. they are scattered "out". *b)* Scattering-in of muons that would normally not hit the detector. *c)* & *d)* show the same phenomenon if we look at a decentral position on the detector. One can always find a periodic arrangement of detectors to balance in- and out-scattering.

2.12 Appendix F – Derivation of the exposure decision helper

The basis for this derivation is formed by Eq. (2.20), i.e. the formulation of the integrated flux. However, one does usually not measure the integrated flux directly, but a number of muons, N_μ, in a certain solid angle, $\Delta\Omega$, over a certain time, ΔT, on a detector with a definite size, ΔA. Given this description, the relation between the integrated flux and the number of muons becomes

$$\Phi(E_{cut}) = \frac{N_\mu}{\Delta A * \Delta T * \Delta\Omega}\,. \tag{2.F1}$$

One may also think of the number of recorded muons as the integral of the (integrated) flux over the detector area, the total exposure time and the covered solid angle. Eq. (2.F1) is consequently the reduced formulation if the integrated flux does not depend on the experimental parameters $\Delta A, \Delta T$ or $\Delta\Omega$. In contrast to the detector size where this is generally the case, the exposure time may be an integral over seasonal variations. However, if the experiment is short enough or if the seasonal variations are small in the energy range one is looking at, one is usually fine with this approximation. The solid angle on the other hand could potentially introduce a large bias if unaccounted for (the muon flux depends strongly on the zenith angle). One remedy to this problem is the introduction of small bins that do not cover a large zenith angle interval.

If we can assume that the errors on $\Delta A, \Delta T$ & $\Delta\Omega$ are well controllable and are thus negligible, the only real source of uncertainty is given by the counting statistics of N_μ. This can very well be modelled by a Poisson distribution, yielding a statistical error of

$$\varepsilon_{\mathrm{N}} = \sqrt{\Phi * \Delta A * \Delta T * \Delta\Omega}\,, \tag{2.F2}$$

or

$$\varepsilon_{\mathrm{N}} = \sqrt{\Phi * \Delta EXP}, \tag{2.F3}$$

where $\Delta EXP = \Delta A * \Delta T * \Delta\Omega$, is defined to be the "exposure". Performing a (gaussian) uncertainty propagation on the equation $\Phi = N_\mu / \Delta EXP$ yields an absolute error of

$$\varepsilon_\Phi = \sqrt{\frac{\Phi}{\Delta EXP}}\,, \tag{2.F4}$$

and a relative error of

$$\epsilon_\Phi = \frac{\varepsilon_\Phi}{\Phi} = \sqrt{\frac{1}{\Phi * \Delta EXP}}\,, \tag{2.F5}$$

respectively. Equation (2.F5) can now be rearranged for the exposure,

$$\Delta EXP = \frac{1}{\Phi * \epsilon_\Phi^2}\,. \tag{2.F6}$$

This formulation now allows for the calculation of the necessary exposure for a given flux and relative uncertainty. Recalling from Ch. 2.3.2.6 that the systematic error of the flux model is in the order of 15 %, or 0.15, we may use this value for ϵ_Φ as we want the statistical error of the number of muons to be smaller or equal compared to the systematic flux error.

With help from the equations of Ch. 2.4 we compiled a graph (see Fig. 2.F1) that shows how large the integrated muon flux after a certain thickness of rock is. Additionally, we put an equivalent graph next to it that converts the necessary exposure for a given rock thickness by using Eq. (2.F6) and $\epsilon_\Phi = 0.15$.

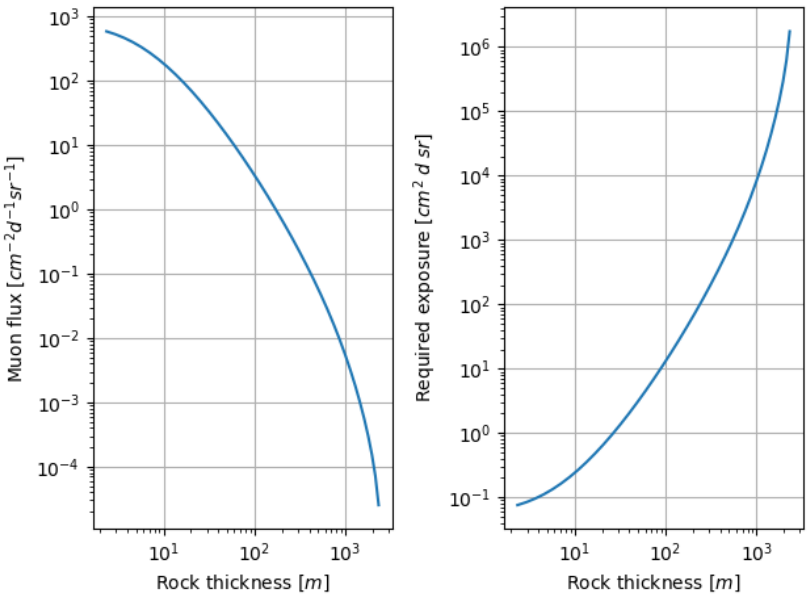

Figure 2.F1: Expected muon flux and required exposure as a function of rock thickness. *Left:* Integrated muon flux (Reyna-Bugaev model, see Ch. 2.3.2.3) as a function of rock thickness. *Right:* Required exposure to achieve a relative statistical error of 0.15 as a function of rock thickness (calculated with Eq. 2.F6).

We can use this newly gained information on what amount of exposure we need to construct a function that may help us visualise which combinations of exposure parameters (i.e. detector area, exposure time and solid angle) are feasible. We proceed in writing the equation for the exposure in a slightly different way,

$$\Delta A = \frac{\Delta EXP}{\Delta T * \Delta \Omega}\,. \tag{2.F7}$$

At this point we make use of the fact that the solid angle is often rather small, as researchers tend to bin the measured muons in directional bins. This way detailed directional information can be used for a much more precise tomography. The definition of the solid angle is given as the surface of the sphere at distance D within the bin margins divided by the radius of the sphere squared, D^2. At large distances this spherical surface can be approximated by the tangential surface, whose area is much easier to compute, i.e. $\Delta X * \Delta Y$, where X and Y are the width and the height of the tangential surface. The solid angle can thus be approximately calculated by

$$\Delta\Omega \approx \frac{\Delta X * \Delta Y}{D^2}\,. \tag{2.F8}$$

For computational convenience we assume a quadratic bin, such that Eq. (2.F8) can be recast into

$$\Delta\Omega = \frac{\Delta Res^2}{D^2}\,, \tag{2.F9}$$

where we substituted ΔX and ΔY each with ΔRes, the lateral resolution in a distance unit (usually metres).

Putting Eq. (2.F9) into Eq. (2.F7) gives

$$\Delta A = \frac{\Delta Exp * D^2}{\Delta T * \Delta Res^2}\,. \tag{2.F10}$$

This equation can be put in an even simpler form by taking the logarithm on both sides,

$$\log(\Delta A) = -\log(\Delta T) + \log\left(\frac{\Delta EXP * D^2}{\Delta Res^2}\right). \tag{2.F11}$$

Equation (2.F11) is a linear equation on a Log-Log plot where the exposure time is on the x-axis while the detector size is on the y-axis. For a given rock thickness, D, also the exposure is fixed (see Fig. 2.F1), this making the lateral spatial resolution, ΔRes, the last variable, that has to be chosen. A summary for different rock thicknesses can be seen in Fig 2.F2.

For computational simplicity, we display the detector size axis in two different colours indicating two different measurement units that are often used to describe the detector area. One sees also nicely that the variation of the lateral spatial resolution affects the linear relationship only as an offset.

A recipe and an example on how to choose valid exposure parameters can be found in Ch. 2.5.2.

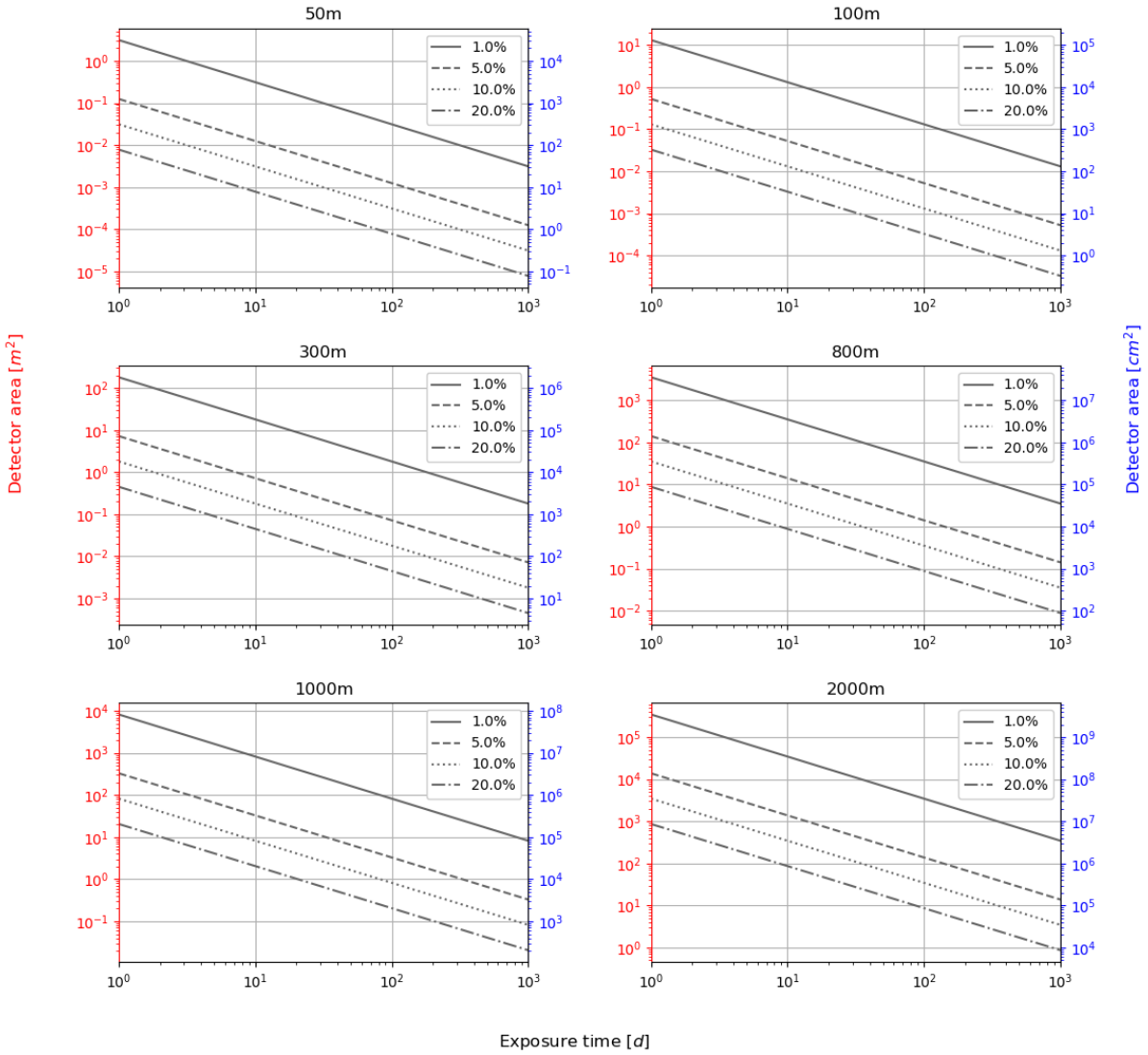

Figure 2.F2: Decision help chart for the two experimental parameters detector size and exposure time for various rock thicknesses. Parallel lines indicate the amount of desired lateral precision one can achieve by using a corresponding area/time-point.

2.13 Author contributions

AL, FS and AE designed the study

AA, TA, PS, RN and CP verified the outcome of the numerical experiments

AL wrote the text with contributions from all co-authors

AL designed the figures with contributions by DM

All co-authors contributed to the discussion and finally approved the manuscript

2.14 Competing interests

The authors declare that they have no conflict of interest.

2.15 Acknowledgements

We thank the Swiss National Science Foundation (project No 159299 awarded to F. Schlunegger and A. Ereditato) for their financial support of this research project.

2.16 References

Acquafredda, R., et al.: *The OPERA experiment in the CERN to Gran Sasso neutrino beam*, J. Inst., 4, P04018–P04018, https://doi.org/10.1088/1748-0221/4/04/P04018, 2009.

Agostinelli, S., et al.: *Geant4—a simulation toolkit*, Nuclear Instruments and Methods in Physics Research Section A: Accelerators, Spectrometers, Detectors and Associated Equipment, 506, 250–303, https://doi.org/10.1016/S0168-9002(03)01368-8, 2003.

Aitchison, J.: *The Statistical Analysis of Compositional Data*, Chapman and Hall Ltd, New York, 1986.

Alvarez, L. W., Anderson, J. A., El Bedwei, F., Burkhard, J., Fakhry, A., Girgis, A., Goneid, A., Hassan, F., Iverson, D., Lynch, G., Miligy, Z., Moussa, A. H., Mohammed-Sharkawi, and Yazolino, L.: *Search for Hidden Chambers in the Pyramids*, Science, 167, 832–839, 1970.

Ambrosino, F., Anastasio, A., Bross, A., Béné, S., Boivin, P., Bonechi, L., Cârloganu, C., Ciaranfi, R., Cimmino, L., Combaret, C., D'Alessandro, R., Durand, S., Fehr, F., Français, V., Garufi, F., Gailler, L., Labazuy, P., Laktineh, I., Lénat, J.-F., Masone, V., Miallier, D., Mirabito, L., Morel, L., Mori, N., Niess, V., Noli, P., Pla-Dalmau, A., Portal, A., Rubinov, P., Saracino, G., Scarlini, E., Strolin, P., and Vulpescu, B.: *Joint measurement of the atmospheric muon flux through the Puy de Dôme volcano with plastic scintillators and Resistive Plate Chambers detectors*, Journal of Geophysical Research Solid Earth, 120, 7290–7307, https://doi.org/10.1002/2015JB011969, 2015.

Anderson, C. D.: *The Apparent Existence of Easily Deflectable Positives*, Science, 76, 238–239, https://doi.org/10.1126/science.76.1967.238, 1932.

Ariga, A., Ariga, T., Ereditato, A., Käser, S., Lechmann, A., Mair, D., Nishiyama, R., Pistillo, C., Scampoli, P., Schlunegger, F., and Vladymyrov, M.: *A Nuclear Emulsion Detector for the Muon Radiography of a Glacier Structure*, Instruments, 2, 7, https://doi.org/10.3390/instruments2020007, 2018.

Asmundis, R. de, Avella, P., and Toglia, F.: *Using RPC Detectors as Cosmic Rays Monitor*, IEEE Transactions on Nuclear Science, 54, 670–676, https://doi.org/10.1109/TNS.2007.895505, 2007.

Athanassas, C. D.: *Muography for geological hazard assessment in the South Aegean active volcanic arc (SAAVA)*, Med. Geosc. Rev., https://doi.org/10.1007/s42990-020-00020-x, 2020.

Baccani, G., Bonechi, L., Bongi, M., Brocchini, D., Casagli, N., Ciaranfi, R., Cimmino, L., Ciulli, V., D'Alessandro, R., Del Ventisette, C., Dini, A., Gigli, G., Gonzi, S., Guideri, S., Lombardi, L., Melon, B., Mori, N., Nocentini, M., Noli, P., Saracino, G., and Viliani, L.: *Muon Radiography of Ancient Mines: The San Silvestro Archaeo-Mining Park (Campiglia Marittima, Tuscany)*, Universe, 5, 34, https://doi.org/10.3390/universe5010034, 2019.

Barnaföldi, G. G., Hamar, G., Melegh, H. G., Oláh, L., Surányi, G., and Varga, D.: *Portable cosmic muon telescope for environmental applications*, Nuclear Instruments and Methods in Physics Research Section A: Accelerators, Spectrometers, Detectors and Associated Equipment, 689, 60–69, https://doi.org/10.1016/j.nima.2012.06.015, 2012.

Barnoud, A., Cayol, V., Niess, V., Cârloganu, C., Lelièvre, P., Labazuy, P., and Le Ménédeu, E.: *Bayesian joint muographic and gravimetric inversion applied to volcanoes*, Geophys J Int, 218, 2179–2194, https://doi.org/10.1093/gji/ggz300, 2019.

Bettini, A.: *Introduction to elementary particle physics*, Second edition., Cambridge University Press, New York, 2014a.

Bettini, A.: *New underground laboratories: Europe, Asia and the Americas*, Physics of the Dark Universe, 4, 36–40, https://doi.org/10.1016/j.dark.2014.05.006, 2014b.

Bohr, N.: *On the Constitution of Atoms and Molecules*, Phil. Mag., 26, 1–25, 1913.

Bonechi, L., D'Alessandro, R., and Giammanco, A.: *Atmospheric muons as an imaging tool*, Reviews in Physics, 5, 100038, https://doi.org/10.1016/j.revip.2020.100038, 2020.

Bonneville, A., Kouzes, R., Yamaoka, J., Lintereur, A., Flygare, J., Varner, G. S., Mostafanezhad, I., Guardincerri, E., Rowe, C., and Mellors, R.: *Borehole muography of subsurface reservoirs*, Philosophical Transactions of the Royal Society A: Mathematical, Physical and Engineering Sciences, 377, 20180060, https://doi.org/10.1098/rsta.2018.0060, 2019.

Bryman, D., Bueno, J., Davis, K., Kaminski, V., Liu, Z., Oldenburg, D., Pilkington, M., and Sawyer, R.: *Muon Geotomography - Bringing New Physics to Orebody Imaging*, in: Building Exploration Capability for the 21st Century, edited by: Kelley, K. D. and Golden, H. C., Society of Economic Geologists, Inc., Littleton, 235–241, 2014.

Bugaev, E. V., Misaki, A., Naumov, V. A., Sinegovskaya, T. S., Sinegovsky, S. I., and Takahashi, N.: *Atmospheric Muon Flux at Sea Level, Underground, and Underwater*, Phys. Rev. D, 58, 054001, https://doi.org/10.1103/PhysRevD.58.054001, 1998.

Caffau, E., Coren, F., and Giannini, G.: *Underground cosmic-ray measurement for morphological reconstruction of the "Grotta Gigante" natural cave*, Nuclear Instruments and Methods in Physics Research Section A: Accelerators, Spectrometers, Detectors and Associated Equipment, 385, 480–488, https://doi.org/10.1016/S0168-9002(96)01041-8, 1997.

Catalano, O., Del Santo, M., Mineo, T., Cusumano, G., Maccarone, M. C., and Pareschi, G.: *Volcanoes muon imaging using Cherenkov telescopes*, Nuclear Instruments and Methods in Physics Research Section A: Accelerators, Spectrometers, Detectors and Associated Equipment, 807, 5–12, https://doi.org/10.1016/j.nima.2015.10.065, 2016.

Chadwick, J.: *The existence of a neutron*, Proc. R. Soc. Lond. A, 136, 692-708, https://doi.org/10.1098/rspa.1932.0112, 1932.

Gaisser, T. K., Engel, R., and Resconi, E.: *Cosmic rays and particle physics*, Second edition., Cambridge University Press, Cambridge, 2016.

George, E.: *Cosmic rays measure overburden of tunnel*, Commonwealth Engineer, 455-457, 1955.

Gibert, D., Beauducel, F., Déclais, Y., Lesparre, N., Marteau, J., Nicollin, F., and Tarantola, A.: *Muon tomography: Plans for observations in the Lesser Antilles*, Earth Planet Sp, 62, 153–165, https://doi.org/10.5047/eps.2009.07.003, 2010.

Giomataris, Y., Rebourgeard, Ph., Robert, J. P., and Charpak, G.: *MICROMEGAS: a high-granularity position-sensitive gaseous detector for high particle-flux environments*, Nuclear Instruments and Methods in Physics Research Section A: Accelerators, Spectrometers, Detectors and Associated Equipment, 376, 29–35, https://doi.org/10.1016/0168-9002(96)00175-1, 1996.

Gosse, J. C. and Phillips, F. M.: *Terrestrial in situ cosmogenic nuclides: theory and application*, Quaternary Science Reviews, 20, 1475–1560, https://doi.org/10.1016/S0277-3791(00)00171-2, 2001.

Groom, D. E., Mokhov, N. V., and Striganov, S. I.: *MUON STOPPING POWER AND RANGE TABLES 10 MeV–100 TeV*, Atomic Data and Nuclear Data Tables, 78, 183–356, https://doi.org/10.1006/adnd.2001.0861, 2001.

Harel, A. and Yaish, D.: *Lingacom muography*, Philosophical Transactions of the Royal Society A: Mathematical, Physical and Engineering Sciences, 377, 20180133, https://doi.org/10.1098/rsta.2018.0133, 2019.

Hebbeker, T. and Timmermans, C.: *A compilation of high energy atmospheric muon data at sea level*, Astroparticle Physics, 18, 107–127, https://doi.org/10.1016/S0927-6505(01)00180-3, 2002.

Heck, D., Knapp, J., Capdevielle, J. N., Schatz, G., and Thouw, T.: *CORSIKA: A Monte Carlo Code to Simulate Extensive Air Showers*, Forschungszentrum Karlsruhe GmbH, Karlsruhe, 1998.

Hess, V. F.: *Über Beobachtungen der durchdringenden Strahlung bei sieben Freiballonfahrten*, Physikalische Z., 13, 1084–1091, 1912.

Kaiser, R.: *Muography: overview and future directions*, Philosophical Transactions of the Royal Society A: Mathematical, Physical and Engineering Sciences, 377, 20180049, https://doi.org/10.1098/rsta.2018.0049, 2019.

Kajita, T., Koshiba, M., and Suzuki, A.: *On the origin of the Kamiokande experiment and neutrino astrophysics*, EPJ H, 37, 33–73, https://doi.org/10.1140/epjh/e2012-30007-y, 2012.

Kearey, P., Brooks, M., and Hill, I.: *An introduction to geophysical exploration*, 3rd ed., Blackwell Science, Malden, MA, 2002.

Kirkpatrick, S., Gelatt, C. D., and Vecchi, M. P.: *Optimization by Simulated Annealing*, Science, 220, 671–680, https://doi.org/10.1126/science.220.4598.671, 1983.

Lechmann, A., Mair, D., Ariga, A., Ariga, T., Ereditato, A., Nishiyama, R., Pistillo, C., Scampoli, P., Schlunegger, F., and Vladymyrov, M.: *The effect of rock composition on muon tomography measurements*, Solid Earth, 9, 1517–1533, https://doi.org/10.5194/se-9-1517-2018, 2018.

Lelièvre, P. G., Barnoud, A., Niess, V., Cârloganu, C., Cayol, V., and Farquharson, C. G.: *Joint inversion methods with relative density offset correction for muon tomography and gravity data, with application to volcano imaging*, Geophys J Int, 218, 1685–1701, https://doi.org/10.1093/gji/ggz251, 2019.

Lesparre, N., Gibert, D., Marteau, J., Déclais, Y., Carbone, D., and Galichet, E.: *Geophysical muon imaging: feasibility and limits*, Geophys J Int, 183, 1348–1361, https://doi.org/10.1111/j.1365-246X.2010.04790.x, 2010.

Lesparre, N., Gibert, D., Marteau, J., Komorowski, J.-C., Nicollin, F., and Coutant, O.: *Density muon radiography of La Soufrière of Guadeloupe volcano: comparison with geological, electrical resistivity and gravity data*, Geophys J Int, 190, 1008–1019, https://doi.org/10.1111/j.1365-246X.2012.05546.x, 2012.

Lesparre, N., Cabrera, J., and Marteau, J.: *3-D density imaging with muon flux measurements from underground galleries*, Geophys. J. Int., 208, 1579–1591, https://doi.org/10.1093/gji/ggw482, 2017.

Lo Presti, D., Riggi, F., Ferlito, C., Bonanno, D. L., Bonanno, G., Gallo, G., La Rocca, P., Reito, S., and Romeo, G.: *Muographic monitoring of the volcano-tectonic evolution of Mount Etna*, Scientific Reports, 10, 11351, https://doi.org/10.1038/s41598-020-68435-y, 2020.

Lynch, G. R. and Dahl, O. I.: *Approximations to multiple Coulomb scattering*, Nuclear Instruments and Methods in Physics Research Section B: Beam Interactions with Materials and Atoms, 58, 6–10, https://doi.org/10.1016/0168-583X(91)95671-Y, 1991.

Marteau, J., Gibert, D., Lesparre, N., Nicollin, F., Noli, P., and Giacoppo, F.: *Muons tomography applied to geosciences and volcanology*, Nuclear Instruments and Methods in Physics Research Section A: Accelerators, Spectrometers, Detectors and Associated Equipment, 695, 23–28, https://doi.org/10.1016/j.nima.2011.11.061, 2012.

Maurer, H., Curtis, A., and Boerner, D. E.: *Recent advances in optimized geophysical survey design*, GEOPHYSICS, 75, 75A177-75A194, https://doi.org/10.1190/1.3484194, 2010.

McDonough, W. F., Šrámek, O., and Wipperfurth, S. A.: *Radiogenic Power and Geoneutrino Luminosity of the Earth and Other Terrestrial Bodies Through Time*, Geochemistry, Geophysics, Geosystems, 21, e2019GC008865, https://doi.org/10.1029/2019GC008865, 2020.

Morishima, K., Nishio, A., Moto, M., Nakano, T., and Nakamura, M.: *Development of nuclear emulsion for muography*, Annals of Geophysics, 60, 0112, https://doi.org/10.4401/ag-7387, 2017.

Nagamine, K.: *Geo-tomographic Observation of Inner-structure of Volcano with Cosmic-ray Muons*, J. Geography, 104, 998–1007, https://doi.org/10.5026/jgeography.104.7_998, 1995.

Nagamine, K., Iwasaki, M., Shimomura, K., and Ishida, K.: *Method of probing inner-structure of geophysical substance with the horizontal cosmic-ray muons and possible application to volcanic eruption prediction*, Nuclear Instruments and Methods in Physics Research Section A: Accelerators, Spectrometers, Detectors and Associated Equipment, 356, 585–595, https://doi.org/10.1016/0168-9002(94)01169-9, 1995.

Neddermeyer, S. H. and Anderson, C. D.: *Note on the Nature of Cosmic-Ray Particles*, Physical Review, 51, 884–886, 1937.

Niess, V., Barnoud, A., Cârloganu, C., and Le Ménédeu, E.: *Backward Monte-Carlo applied to muon transport*, Computer Physics Communications, 229, 54–67, https://doi.org/10.1016/j.cpc.2018.04.001, 2018.

Nishiyama, R., Tanaka, Y., Okubo, S., Oshima, H., Tanaka, H. K. M., and Maekawa, T.: *Integrated processing of muon radiography and gravity anomaly data toward the realization of high-resolution 3-D density structural analysis of volcanoes: Case study of Showa-Shinzan lava dome, Usu*, Japan, Journal of Geophysical Research Solid Earth, 119, 699–710, https://doi.org/10.1002/2013JB010234, 2014.

Nishiyama, R., Miyamoto, S., and Naganawa, N.: *Application of Emulsion Cloud Chamber to cosmic-ray muon radiography*, Radiation Measurements, 83, 56–58, https://doi.org/10.1016/j.radmeas.2015.04.013, 2015.

Nishiyama, R., Ariga, A., Ariga, T., Käser, S., Lechmann, A., Mair, D., Scampoli, P., Vladymyrov, M., Ereditato, A., and Schlunegger, F.: *First measurement of ice-bedrock interface of alpine glaciers by cosmic muon radiography*, Geophysical Research Letters, 44, 6244–6251, https://doi.org/10.1002/2017GL073599, 2017.

Nishiyama, R., Ariga, A., Ariga, T., Lechmann, A., Mair, D., Pistillo, C., Scampoli, P., Valla, P. G., Vladymyrov, M., Ereditato, A., and Schlunegger, F.: *Bedrock sculpting under an active alpine glacier revealed from cosmic-ray muon radiography*, Scientific Reports, 9, 6970, https://doi.org/10.1038/s41598-019-43527-6, 2019.

Oláh, L., Barnaföldi, G. G., Hamar, G., Melegh, H. G., Surányi, G., and Varga, D.: *CCC-based muon telescope for examination of natural caves*, Geosci. Instrum. Method. Data Syst., 1, 229–234, https://doi.org/10.5194/gi-1-229-2012, 2012.

Oláh, L., Hamar, G., Miyamoto, S., Tanaka, H. K. M., and Varga, D.: *The first prototype of an MWPC-based borehole-detector and its application for muography of an underground pillar*, BUTSURI-TANSA(Geophysical Exploration), 71, 161–168, https://doi.org/10.3124/segj.71.161, 2018.

Oláh, L., Tanaka, H. K. M., Ohminato, T., Hamar, G., and Varga, D.: *Plug Formation Imaged Beneath the Active Craters of Sakurajima Volcano With Muography*, Geophysical Research Letters, 46, 10417–10424, https://doi.org/10.1029/2019GL084784, 2019.

Pacini, D.: *La radiazione penetrante alla superficie ed in seno alle acque*, Il Nuovo Cimento, 3, 93–100, 1912.

Pla-Dalmau, A., Bross, A. D., and Mellott, K. L.: *Low-cost extruded plastic scintillator*, Nuclear Instruments and Methods in Physics Research Section A: Accelerators, Spectrometers, Detectors and Associated Equipment, 466, 482–491, https://doi.org/10.1016/S0168-9002(01)00177-2, 2001.

Procureur, S.: Muon imaging: *Principles, technologies and applications*, Nuclear Instruments and Methods in Physics Research Section A: Accelerators, Spectrometers, Detectors and Associated Equipment, 878, 169–179, https://doi.org/10.1016/j.nima.2017.08.004, 2018.

Reichstein, M., Camps-Valls, G., Stevens, B., Jung, M., Denzler, J., Carvalhais, N., and Prabhat: *Deep learning and process understanding for data-driven Earth system science*, Nature, 566, 195–204, https://doi.org/10.1038/s41586-019-0912-1, 2019.

Reyna, D.: *A Simple Parameterization of the Cosmic-Ray Muon Momentum Spectra at the Surface as a Function of Zenith Angle*, arXiv Prepr. hep-ph/0604145 [online] Available from: http://arxiv.org/abs/hep-ph/0604145, 2006.

Rosas-Carbajal, M., Jourde, K., Marteau, J., Deroussi, S., Komorowski, J.-C., and Gibert, D.: *Three-dimensional density structure of La Soufrière de Guadeloupe lava dome from simultaneous muon radiographies and gravity data*, Geophysical Research Letters, 44, 6743–6751, https://doi.org/10.1002/2017GL074285, 2017.

Rücker, C., Günther, T., and Wagner, F. M.: pyGIMLi: *An open-source library for modelling and inversion in geophysics*, Computers & Geosciences, 109, 106–123, https://doi.org/10.1016/j.cageo.2017.07.011, 2017.

Rutherford, E.: LXXIX. *The Scattering of α and β Particles by Matter and the Structure of the Atom*, The London, Edinburgh, and Dublin Philosophical Magazine and Journal of Science, 21, 669–688, https://doi.org/10.1080/14786440508637080, 1911.

Rutherford, E.: LIV. *Collision of α particles with light atoms. IV. An anomalous effect in nitrogen*, The London, Edinburgh, and Dublin Philosophical Magazine and Journal of Science, 37, 31–37, https://doi.org/10.1080/14786440608635919, 1919.

Sato, T.: *Analytical Model for Estimating the Zenith Angle Dependence of Terrestrial Cosmic Ray Fluxes*, PLOS ONE, 11, e0160390, https://doi.org/10.1371/journal.pone.0160390, 2016.

Sato, T., Niita, K., Matsuda, N., Hashimoto, S., Iwamoto, Y., Noda, S., Ogawa, T., Iwase, H., Nakashima, H., Fukahori, T., Okumura, K., Kai, T., Chiba, S., Furuta, T., and Sihver, L.: *Particle and Heavy Ion Transport code System, PHITS, version 2.52*, Journal of Nuclear Science and Technology, 50, 913–923, https://doi.org/10.1080/00223131.2013.814553, 2013.

Schwarz, S.: *Validation of Geant4 Proton Scattering A Summer Student Project*, CERN, Geneva, 2013.

Sivia, D. S. and Skillings, J. H.: *Data analysis: a Bayesian tutorial*, Second Edition., Oxford Univ. Press, Oxford, 2012.

Šrámek, O., McDonough, W. F., Kite, E. S., Lekić, V., Dye, S. T., and Zhong, S.: *Geophysical and geochemical constraints on geoneutrino fluxes from Earth's mantle*, Earth and Planetary Science Letters, 361, 356–366, https://doi.org/10.1016/j.epsl.2012.11.001, 2013.

Stoer, J. and Bulirsch, R.: *Introduction to Numerical Analysis*, Springer Science & Business Media, New York, 2013.

Tanabashi, M., et al. (Particle Data Group): *Review of Particle Physics*, Phys. Rev. D, 98, 030001, https://doi.org/10.1103/PhysRevD.98.030001, 2018.

Tanaka, H., Nagamine, K., Kawamura, N., Nakamura, S. N., Ishida, K., and Shimomura, K.: *Development of the Cosmic-Ray Muon Detection System for Probing Internal-Structure of a Volcano*, Hyperfine Interactions, 138, 521–526, https://doi.org/10.1023/A:1020843100008, 2001.

Tanaka, H., Nagamine, K., Kawamura, N., Nakamura, S. N., Ishida, K., and Shimomura, K.: *Development of a two-fold segmented detection system for near horizontally cosmic-ray muons to probe the internal structure of a volcano*, Nuclear Instruments and Methods in Physics Research Section A: Accelerators, Spectrometers, Detectors and Associated Equipment, 507, 657–669, https://doi.org/10.1016/S0168-9002(03)01372-X, 2003.

Tanaka, H. K. M. and Oláh, L.: *Overview of muographers*, Philosophical Transactions of the Royal Society A: Mathematical, Physical and Engineering Sciences, 377, 20180143, https://doi.org/10.1098/rsta.2018.0143, 2019.

Tanaka, H. K. M., Nagamine, K., Nakamura, S. N., and Ishida, K.: *Radiographic measurements of the internal structure of Mt. West Iwate with near-horizontal cosmic-ray muons and future developments*, Nuclear Instruments and Methods in Physics Research Section A: Accelerators, Spectrometers, Detectors and Associated Equipment, 555, 164–172, https://doi.org/10.1016/j.nima.2005.08.099, 2005.

Tanaka, H. K. M., Nakano, T., Takahashi, S., Yoshida, J., Takeo, M., Oikawa, J., Ohminato, T., Aoki, Y., Koyama, E., Tsuji, H., and Niwa, K.: *High resolution imaging in the inhomogeneous crust with cosmic-ray muon radiography: The density structure below the volcanic crater floor of Mt. Asama*, Japan, Earth and Planetary Science Letters, 263, 104–113, https://doi.org/10.1016/j.epsl.2007.09.001, 2007.

Tanaka, H. K. M., Uchida, T., Tanaka, M., Shinohara, H., and Taira, H.: *Cosmic-ray muon imaging of magma in a conduit: Degassing process of Satsuma-Iwojima Volcano*, Japan, Geophysical Research Letters, 36, https://doi.org/10.1029/2008GL036451, 2009.

Tanaka, H. K. M., Miyajima, H., Kusagaya, T., Taketa, A., Uchida, T., and Tanaka, M.: *Cosmic muon imaging of hidden seismic fault zones: Rainwater permeation into the mechanical fractured zones in Itoigawa–Shizuoka Tectonic Line*, Japan, Earth and Planetary Science Letters, 306, 156–162, https://doi.org/10.1016/j.epsl.2011.03.036, 2011.

Tanaka, H. K. M., Kusagaya, T., and Shinohara, H.: *Radiographic visualization of magma dynamics in an erupting volcano*, Nature Communications, 5, 3381, https://doi.org/10.1038/ncomms4381, 2014.

Tang, A., Horton-Smith, G., Kudryavtsev, V. A., and Tonazzo, A.: *Muon Simulations for Super-Kamiokande, KamLAND and CHOOZ*, Phys. Rev. D, 74, 053007, https://doi.org/10.1103/PhysRevD.74.053007, 2006.

Tarantola, A.: *Inverse Problem Theory and Methods for Model Parameter Estimation*, 1st ed., siam, Philadelphia, 2005.

Tioukov, V., Alexandrov, A., Bozza, C., Consiglio, L., D'Ambrosio, N., De Lellis, G., De Sio, C., Giudicepietro, F., Macedonio, G., Miyamoto, S., Nishiyama, R., Orazi, M., Peluso, R., Sheshukov, A., Sirignano, C., Stellacci, S. M., Strolin, P., and Tanaka, H. K. M.: *First muography of Stromboli volcano*, Scientific Reports, 9, 6695, https://doi.org/10.1038/s41598-019-43131-8, 2019.

Tsai, Y.-S.: *Pair production and bremsstrahlung of charged leptons*, Rev. Mod. Phys., 46, 815–851, https://doi.org/10.1103/RevModPhys.46.815, 1974.

Varga, D., Nyitrai, G., Hamer, G., Oláh, L.: *High Efficiency Gaseous Tracking Detector for Cosmic Muon Radiography*, *Advances in High Energy Physics*, Article ID 1962317, 1-11, https://doi.org/10.1155/2016/1962317, 2016.

Varga, D., Nyitrai, G., Hamar, G., Galgóczi, G., Oláh, L., Tanaka, H. K. M., and Ohminato, T.: *Detector developments for high performance Muography applications*, Nuclear Instruments and Methods in Physics Research Section A: Accelerators, Spectrometers, Detectors and Associated Equipment, 958, 162236, https://doi.org/10.1016/j.nima.2019.05.077, 2020.

Vesga-Ramírez, A., Sanabria-Gómez, J. D., Sierra-Porta, D., Arana-Salinas, L., Asorey, H., Kudryavtsev, V. A., Calderón-Ardila, R., and Núñez, L. A.: *Simulated Annealing for volcano muography*, Journal of South American Earth Sciences, 109, 103248, https://doi.org/10.1016/j.jsames.2021.103248, 2021.

Wulf, T.: *About the radiation of high penetration capacity contained in the atmosphere*, Physikalische Zeitschrift, 5, 152–157, 1910.

Chapter 3

SMAUG v1.0 – a user-friendly muon simulator for transmission tomography of geological objects in 3D

Alessandro Lechmann[1], David Mair[1], Akitaka Ariga[2], Tomoko Ariga[3], Antonio Ereditato[2], Ryuichi Nishiyama[4], Ciro Pistillo[2], Paola Scampoli[2,5], Mykhailo Vladymyrov[2], and Fritz Schlunegger[1]

[1]Institute of Geological Sciences, University of Bern, Bern, CH-3012, Switzerland
[2]Albert Einstein Center for Fundamental Physics, Laboratory for High Energy Physics, University of Bern, Bern, CH-3012, Switzerland
[3]Faculty of Arts and Science, Kyushu University, Fukuoka, JP-819-0385, Japan
[4]Earthquake Research Institute, The University of Tokyo, Tokyo, JP-113-0032, Japan
[5]Physics Department "Ettore Pancini", University of Naples Federico II, Naples, IT-80126, Italy

Prepared for publication in: Geoscientific Model Development, EGU Open Access Journal

3.1 Abstract

Knowledge about muon tomography has spread in recent years in the geoscientific community and several collaborations between geologists and physicists have been founded. As the data analysis is still mostly done by particle physicists, we address the need of the geoscientific community to participate in the data analysis, while not having to worry too much about the particle physics equations in the background. The result hereof is SMAUG, a toolbox consisting of several modules that cover the various aspects of data analysis in a muon tomographic experiment. In this study we show how a comprehensive geophysical model can be built from basic physics equations. The emerging uncertainties are dealt with by a probabilistic formulation of the inverse problem, which is finally solved by a Monte Carlo Markov Chain algorithm. Finally, we benchmark the SMAUG results against a recent study and show that they reach identical results with the same level of accuracy and precision.

3.2 Introduction

Among the manifold geophysical imaging techniques, muon tomography has increasingly gained the interest of geoscientists during the course of the past years. Before its application in Earth sciences, it was initially used for archaeological purposes. Alvarez et al. (1970) used this method to search for hidden chambers in the pyramids of Giza, in Egypt; an experiment which was recently repeated by Morishima et al. (2017), as better technologies have continuously been developed. Other civil engineering applications include the monitoring of nuclear power plant operations (Takamatsu et al., 2015) and the search for nuclear waste repositories (Jonkmans et al., 2013) as well as the investigation of underground tunnels (e.g. Thompson et al., 2020; Guardincerri et al., 2017). A serious deployment of muon tomography in Earth sciences has only begun in the past decades. These undertakings mainly encompass the study of the interior of volcanoes in France (Ambrosino et al., 2015; Jourde et al., 2016; Noli et al., 2017; Rosas-Carbajal et al., 2017), Italy (Ambrosino et al., 2014; Lo Presti et al., 2018;

Tioukov et al., 2017) and Japan (Kusagaya and Tanaka, 2015; Nishiyama et al., 2014; Oláh et al., 2018; Tanaka, 2016). Other experiments have been performed in order to explore the geometry of karst cavities in Hungary (Barnaföldi et al., 2012) and Italy (Saracino et al., 2017). Further studies have been conducted by our group to recover the ice-bedrock interface of Alpine glaciers in central Switzerland (Nishiyama et al., 2017; 2019).

The core component of every geophysical exploration experiment is formed by the inversion, which might be better known to other communities as fitting or modelling. This is where the model parameters are found which best fit the observed data. Up until now, this central part has mostly been built specifically to meet the needs of the experimental campaign at hand. On the one hand this approach has the advantage of allowing for the peculiarities of particle detectors, their data processing chain and other models involved (e.g. the cosmic ray flux model). On the other hand, when every group builds a separate inversion, the reconstruction of the precise calculations performed in the data analysis procedure becomes a challenge. For a researcher who is not familiar with the intricacies of inversion, this might even be tougher. We thus see the need for a lightweight programme that incorporates a structured and modular approach to inversion, that also allows users with little inversion experience to familiarise themselves with this rather involved topic. This programme can be used to directly analyse experimental data in a stand-alone working environment, and the modules and theoretical foundations can be adapted, customised, and integrated into new programmes. For this reason, the code is built in the programming language Python as to facilitate exchange between researchers and to enhance modifiability. Moreover, the source code is freely available online (see code availability section below).

3.2.1 Inversion – a modular view

The goal of every muon tomography study is essentially to infer physical parameters of the radiographed object by a measurement of the cosmic ray muon flux and its absorption through that object. In geological applications these objects are almost always lithological underground structures such as magma chambers, cavities, or other interfaces with a high-density contrast. The reconstruction of the geometry of such structures can only be achieved if the measured muon data is compared to the results of a muon flux simulation. As stated earlier, this is the basic principle of the inversion procedure. However, the aforementioned “muon flux simulation” is not just a simple programme, but it consists of several physically independent models that act together. Taking a modular view, we will call those models “modules” from here on, as they will inevitably be part of a larger inversion code. We have visualised the components that are necessary to build an inversion in Fig. 3.1.

The first of the modules is the input module for the experiment results, which also considers the detectors that were used in the experiment. Typical detector setups include nuclear emulsion films (e.g. Ariga et al., (2018), cathode chambers (e.g. Oláh et al., 2013), scintillators (e.g. Anghel et al., 2015) or other hardware solutions. Although the detailed data processing chain may be comprehensive, the related output almost always comes in the form of a measured directional (i.e. from various incident angles)

muon flux, which will be the input to the inversion scheme. Here, we primarily work with the premise that the muon flux data and the associated errors are given. The corresponding errors can then be furnished to the code by means of an interface. The simulation module on the other hand, consists of four autonomous components (see Fig. 3.1). First, a cosmic ray muon flux model is necessary, which describes the muon abundance in the atmosphere, generally dependent on muon energy, incident angle and height. Lesparre et al. (2010) list and compare various muon flux models that may be incorporated into an extensive simulation. Second, it is necessary to model the spatial distribution of the detectors as well as the initial distribution of the lithologies. Related pre-existing software solutions mainly comprise GIS- and geological 3D-modelling applications, that excel at capturing and compiling geological information from various sources (e.g. field, maps, etc.) into a spatially organised database. Third, the lithologies consisting of different minerals have to be translated to a set of parameters, which are a necessary input for the subsequent physical simulation. This can be done by a rock model (e.g. Lechmann et al., 2018), which considers the effects of the mass density as well as the average atomic mass and charge of the rock as a function of its mineralogical composition. Lastly, the muon fluxes at the detector sites have to be simulated by means of a muon transportation model, which calculates all physical processes by which a muon loses kinetic energy while travelling through matter. The particle physics community has a great variety of particle simulators, the most prominent being GEANT4 (Agostinelli et al., 2003), a Monte Carlo based simulator. These have the advantage that stochastic processes resulting in energy loss are simulated according to their probabilistic occurrence - an upside that has to be traded off for longer computation times. In contrast to obtaining the full energy loss distribution, lightweight alternatives often resort to the calculation of only the mean energy loss. The solution of the resulting differential equation can even be tabulated, as has been done by Groom et al. (2001). The interplay of these four submodules allows for the simulation of muon fluxes at the detector sites that are mostly located in an underground environment.

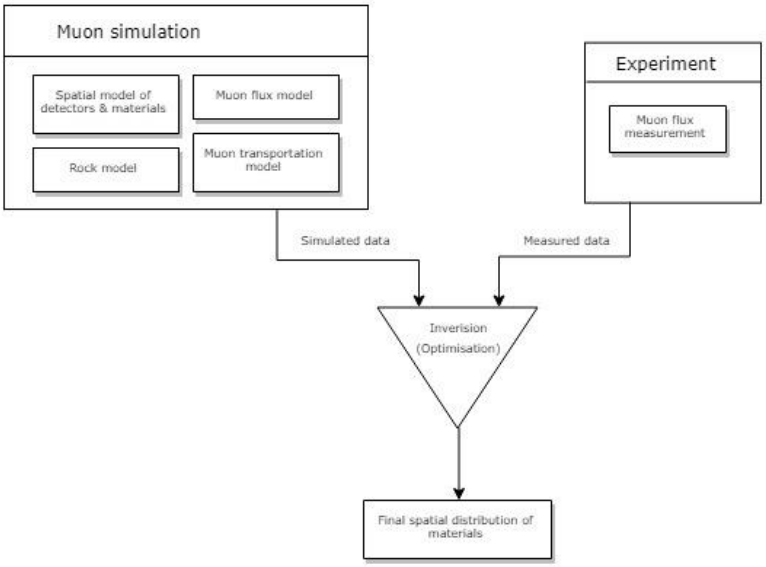

Figure 3.1: A schematic flowchart showing the different involved models in a muon tomographic experiment. The muon simulation consists of a model for rocks, detectors, the cosmic ray flux and a particle physical model on how muons lose energy upon travelling through rocks. These models allow for a synthetic data set to be computed, which will be compared to the actual measured data from the experiment. An optimisation problem then solves for the best set of parameters.

3.2.2 The need for a consistent inversion environment

The sole combination of the aforementioned four submodules does not fully justify the need for a new software, as cosmic ray flux models as well as rock model can also be programmed within existing Monte Carlo simulators such as GEANT4 (Agostinelli et al., 2003) or MUSIC (Kudryavtsev, 2009). Unfortunately, the application of such a Monte Carlo approach requires a rather good understanding of programming and nuclear physics processes. Thus, it might prove time-consuming to programme a specific code. Moreover, these codes are often written in a specialised programming language such as C++, which is already a rather specialised language. Third, the compatibility between different modules (e.g. cosmic ray flux and energy loss) may be severely hampered, if the programme interfaces are not taken into consideration. It might be even worse if the two modules are written in two different programming languages. In addition, one has to carefully evaluate the benefit of such an undertaking, especially if the resulting code will most likely be tailored only to a specific problem. We thus see the need for a versatile, user-friendly simulator, which allows users not only to quickly perform the necessary calculations, without the need of additional coding, but also tailor the individual models to custom needs. A new simulator can be more useful if an inversion functionality is already included. As can be seen in Fig. 3.1, the inversion compares the simulated flux data with the measured ones. It also attempts to reduce the discrepancy between measurements and simulations by optimising the parameters in the simulation, namely material density and the thickness distribution of the overlying materials. This results in a density- or structural rock model, which best reproduces the measured data. As the mathematical optimization in muon tomography generally is nonlinear, one has to employ nonlinear solvers or even Monte Carlo techniques. This circumstance encourages us to work with a lightweight

version of a muon transport simulator, because a nonlinear inversion of Monte Carlo simulations, although mathematically preferable, is computationally prohibitive. This allows us to make use of methods from the Bayesian realm, that thrive when measurements from different sources have to be combined into a single comprehensive model. With the code presented in this paper, we aspire to make muon tomography accessible to a broader geoscientific community, as the know-how in this field is mainly concentrated in particle physics laboratories. We want to provide the tools for Earth scientists, or users that are mainly focused on the application of the method, so that they can perform their own analyses.

In this contribution we present our new code, SMAUG (Simulation for Muons and their Applications UnderGround), that allows a broader scientific community to plan and analyse muon tomographic experiments more easily, by providing them with data analysis and inversion tools. Specifically, we describe the governing equations of the physical models, and the mathematical techniques that were used. Chapter 3.3 depicts how the muon flux simulation is conducted by its submodules and how a muon flux simulation is performed. Chapter 3.4 then dives into the inversion module and explains how the parameters of the inferred density/rock-model can be estimated based on measured data. This chapter includes a description of the model and data errors and an explanation on how a subsurface material boundary can be constructed. Chapter 3.5 provides a short overview of the program, explaining which functionality can be found in which source code. Chapter 3.6 discusses the model's performance based on the data that we collected in the framework of an earlier experimental campaign (see supplement of Nishiyama et al., 2017). Chapter 3.7 concludes this study by outlining a way of how this code can be developed further to fit the needs of the muon tomography and geology community.

3.3 The forward model: Muon flux simulation

In geophysical communities this part is generally known as the forward model, i.e. a mathematical model which calculates synthetic data for given "model" parameters. In muon tomography experiments this forward model consists of different physical models which are serially connected.

3.3.1 Cosmic ray flux model

The nature of the data used in muon tomography generally consists of several counts within a directional bin, defined by two polar and two azimuthal angles. Additionally, the measurement is taken over a defined period of time, as well as over a given extent within the detector area. The simulated number of muons, in the i-th bin, can be calculated by this integral,

$$N_{\mu,i}^{sim} = \int_{\mathrm{T}} \iint_{\Omega} \iint_{\mathrm{A}} \int_{E} \frac{dI}{dE} dE \; dA \; d\Omega \; dT \; . \tag{3.1}$$

Here, T denotes the exposure time interval, A the detector area, Ω the solid angle of the bin and E the energy range of the muons that were able to be registered by the detector. There are various differential muon flux models, also referred to as the integrand in Eq. (3.1), that can be employed at this stage. Lesparre et al. (2010) provide a good overview on the different flux models, which can broadly be

divided in two classes. On the one hand theoretical models exist, which capture the manifold production paths of muons and condense them in an analytical equation, e.g. the Tang et al., (2006) model. They contrast with empirical models that were generated by fitting formulae to the results of muon flux measurements. The model of Bugaev et al. (1998) falls into this category, with later adjustments for different zenith angles (Reyna, 2006) and altitude (Nishiyama et al., 2017), which are also utilised in this study. The details of the formula are explained in Appendix A (Ch. 3.8). The evaluation of Eq. (3.1) is rather cumbersome as strictly speaking several of the integration variables depend on each other. We may facilitate the calculation by considering that the differential muon flux model is only dependent on energy, E, and zenith angle, θ whereas the effective area, $\Delta A_{eff,i}$, is solely dependent on the orientation of the bin. This is the case because muons do not necessarily hit the detector perpendicularly, such that the effective target area is usually smaller. By averaging over the zenith angle and keeping the bin size reasonably small, we may approximate Eq. (3.1) by

$$N_{\mu,i}^{sim}(\mathrm{E_{cut,i}}) = \int_{E_{cut,i}}^{\infty} \frac{dI}{dE}\left(E, \widehat{\theta_i}\right) dE * \Delta T * \Delta A_{eff,i}(\widehat{\varphi_i}, \widehat{\theta_i}) * \Delta\Omega_i \,, \tag{3.2}$$

where ΔT is the exposure time and $\Delta A_{eff,i}$ is the effective detector area. $\Delta\Omega_i$ is the solid angle, $\widehat{\varphi_i}$ and $\widehat{\theta_i}$ are the mean azimuth and zenith angle of the i-th bin, respectively. $E_{cut,i}$ describes the energy needed for a muon to enter the detector. $\Delta A_{eff,i}$ has to be scaled by the cosine of the angle between bin direction and detector facing direction, which can be calculated using the formula for a scalar product,

$$\Delta A_{eff,i} = \Delta A * \frac{\vec{n} \cdot \vec{d}_\mu(\widehat{\varphi_i}, \widehat{\theta_i})}{\|\vec{n}\| \|\vec{d}_\mu(\widehat{\varphi_i}, \widehat{\theta_i})\|}, \tag{3.3}$$

where $\vec{n}$ is the normal vector to the detector surface and $\vec{d}_\mu\left(\widehat{\varphi_i}, \widehat{\theta_i}\right)$ is the mean vector of muon incidence within the i-th bin, both of which can be chosen to feature unit length. Evaluating the scalar product in spherical coordinates, Eq. (3.3) yields

$$\Delta A_{eff,i} = \Delta A * \left[\sin(\theta_d) \sin\left(\widehat{\theta_i}\right) \cos(\varphi_d - \widehat{\varphi_i}) + \cos(\theta_d) \cos\left(\widehat{\theta_i}\right)\right]. \tag{3.4}$$

Here, θ_d and φ_d are the zenith and azimuth angles of the detector facing direction. It is important to note that except for $E_{cut,i}$ all variables in Eq. (3.2) are predetermined by the experimental setup (ΔT, ΔA) as well as the data processing ($\widehat{\varphi_i}$, $\widehat{\theta_i}$), such that the number of muons $N_{\mu,i}^{sim}$ can be interpreted as a function of one variable, $E_{cut,i}$ only.

3.3.2 Muon transportation model

Since muons permanently lose energy when travelling through matter, they also need a certain amount of energy to enter the detector. This energy, $E_{cut,i}$, was introduced in Eq. (3.2) and is called the cutoff energy. If the detector is now positioned underground, the muons have to traverse more matter to reach the detector and consequently need a higher initial energy to reach the target. For this purpose, we introduce the new variable E_0, which refers to the energy needed to penetrate the detector, and we

reinterpret $E_{cut,i}$ as the minimum energy that is required to traverse the matter and to be registered at the detector. For the goal of studying the interactions between particles and matter, physicists regularly use energy loss models. We base our calculations in large parts on the equations of Groom et al. (2001), where the energy loss of a muon along its path is described by an ordinary differential equation of 1st order,

$$-\frac{dE}{dx} = \rho(x) * [a(x,E) + E * b(x,E)] \,. \tag{3.5}$$

In Eq. (3.5), ρ denotes the density of the traversed material, and a and b are the ionisation loss and radiation loss parameters respectively. The radiation loss parameter groups the effects related to bremsstrahlung, b_{brems}, pair-production, b_{pair}, and photonuclear interactions, b_{photo}, where

$$b(x,E) = b_{brems}(x,E) + b_{pair}(x,E) + b_{photo}(x,E). \tag{3.6}$$

Each of the radiative process is, in turn, calculated through

$$b_k = \frac{N_A}{A}\int_0^1 \nu \frac{d\sigma_k}{d\nu} d\nu \,, \tag{3.7}$$

where $k \in \widetilde{K} = \{$bremsstrahlung, pair-production, photonuclear$\}$ is the set of radiative processes, N_A is Avogadro's number, A is the atomic weight of the traversed material, ν is the fractional energy transfer and $d\sigma_k/d\nu$ the differential cross-section of the process. Eq. (3.7) becomes important when modelling errors have to be included (see Ch. 3.4). For a detailed discussion of the equations for a and b we refer to Groom et al. (2001). The only exception in Eq. (3.6) is b_{pair}, which is calculated after GEANT4 (Agostinelli et al., 2003). We selected the solution of these latter authors because it is computationally less time consuming. As the two results agree within 1 %, we deem it acceptable to exchange the two differential cross-sections.

Because Eq. (3.5) describes the energy loss in response to the interaction with a single-element material, certain modifications have to be made to make it also valid for rocks, which in this context represent a mixture of minerals and elements. In this case, the modified equation takes an equivalent form to Eq. (3.5) when replacing ρ, a, b with their mixture counterparts $\{\rho\}_{rock}, \{a\}_{rock}, \{b\}_{rock}$ (Lechmann et al., 2018), thus yielding

$$-\frac{dE}{dx} = \{\rho(x)\}_{rock} * [\{a(x,E)\}_{\mathrm{rock}} + E * \{b(x,E)\}_{\mathrm{rock}}] \,. \tag{3.8}$$

We show in Appendix B3 (Ch. 3.9.3) how the rock model (explained in Ch. 3.3.3) can be used to determine these quantities.

By applying a change of variables to Eq. (3.8), i.e. $x' = -x$, the energy loss equation can be transformed to an energy gain equation. This has the advantage of being much easier to solve than the "final value problem" in Eq. (3.8). We can reorganise Eq. (3.8) into an initial value problem by setting the initial energy to E_0,

$$\frac{dE}{dx} = \{\rho(x)\}_{rock} * [\{a(x,E)\}_{\mathrm{rock}} + E * \{b(x,E)\}_{\mathrm{rock}}] \tag{3.9}$$

$E(0) = E_0$.

In this context E_0 is the minimal energy needed for a muon to penetrate the detector, which can be influenced by the detector design. Equation (3.9) is a well-investigated problem that can be solved by numerous methods. In our work we employ a standard Runge-Kutta integration scheme (see for example Stoer and Bulirsch, 2013), with a step size of 10 cm. As a result, it is now possible to write the cut-off energy in functional form, where

$$E_{cut,i} = rk(\vec{x}_i, \vec{\rho}, \vec{c}) \; . \tag{3.10}$$

Here $rk(\cdot)$ is the function that returns the Runge-Kutta solution of Eq. (3.9) for defined thicknesses of materials, $\vec{x}_i$, with densities $\vec{\rho}$ and compositional parameters $\vec{c}$. Thickness and density are allowed to be vectors, as there may be more than just one material. In this case, the final energy, after the muon has passed through the first segment of materials, is the initial energy for the second segment, etc. In order to speed up the computations – especially the calculation of the pair production cross-section, which includes two nested integrations – a log-log table of muon energy vs. radiation loss parameters is produced, from which the b-values, see Eq. (3.7), can be interpolated. We justify this approach because the radiative losses are almost linear in a log-log plot, as can be seen in Fig. 33.1 of Tanabashi et al. (2018, p.447) for the example of copper. The general shape of the energy loss function remains the same for various materials even if the absolute values differ.

3.3.3 Rock model

Equation (3.10) shows, that for the calculation of the cut-off energy two types of material parameters are required, the material density $\vec{\rho}$ and its average composition $\vec{c}$. The pre-tabulated values from Groom et al. (2001), however, include only pure elements as well as certain compounds. To extract the relevant parameters in a geological setting, a realistic rock model is needed. In an earlier work (Lechmann et al., 2018) we have shown how an integrated rock model can be constructed and how the physical parameters for a realistic rock can be retrieved. In the present work we largely use the same approach, apart from a few aspects. First, we measured the average material density directly in the laboratory, using various techniques which are explained in detail in Appendix B1 (Ch. 3.9.1). Second, in order to be able to compare the results of this study with the previous Nishiyama et al. (2017) publication, we consider a rock composition that corresponds to a density modified standard rock. This is applicable, as the rock in the study region is mostly of granitic/gneissic origin, with thicknesses rarely larger than 200 m, such that the differences are negligible. However, as the inclusion of compositional data is a planned feature for a future version of our code, we decided to include the theoretical treatment in this work. Hence, all equations are tailored to include the statistical description of such data. Compositional data for whole rock samples which can be scaled to outcrop scale are usually presented in one of two forms, the first being measurements of X-Ray Diffraction (XRD). This kind of data yields the mineral phases within a

rock. Unfortunately, XRD is a rather time-consuming method. This is the reason why in muon tomographic experiments researchers often resort to a bulk chemical analysis of the rock, which is the second form of compositional data. This type of data is usually the output of dedicated X-Ray Fluorescence (XRF) measurements, describing the bulk rock composition by major oxide fractions. We note here that by the absence of information on the spatial distribution of mineral phases within a rock, we implicitly infer a homogeneous mixture of elements within the rock itself, which is thus different from our previous work (Lechmann et al., 2018). From a particle physics perspective this does not pose a real problem as the difference to a mixture of minerals is rather small. Nevertheless, we lose the power to obtain meaningful compositional inferences. As the present work aims to infer positions and uses material parameters as constraints, we can accept this circumstance. Details on how compositional parameters are constructed from XRF information, including an example, can be found in Appendix B2 (Ch. 3.9.2), and an explanation of their influence on the energy loss equation in Appendix B3 (Ch. 3.9.3).

3.3.4 Spatial models of detectors and materials

In addition to the above explained physical models, we may also utilise available spatial data for our purposes. In this context, the use of a digital elevation model (DEM) of the surface allows the visualisation of the position of the detectors relative to the surface, as well as the spatial extent of the bins, and it allows us to determine the location where they intersect with the topographic surface. As a first deliverable, we can draw conclusions on which bins consist of how many parameters. For example, if we know that the detector is located underground and that there is ice at the surface, we can already infer the existence of at least 2 materials (rock and ice). For this purpose, we wrote the script "modelbuilder.py", which allows the user to attach geographic and physical information to the selected bins. This process of building a coherent geophysical model is needed for the subsequent employment of the inversion algorithm to process all the data.

3.4 The inverse model: A Bayesian perspective

As stated in the Introduction, we solve the inversion by using Bayesian methods. This needs an explanation as to why we chose this way and not another. First, the equations in Ch. 3.3 enable us to calculate a synthetic dataset for fixed parameter values. There, one can see that the governing equations constitute a nonlinear relationship between parameter values and measured data. Despite this being of no particular interest in the forward model, the parameter estimation problem from measured data is rendered vastly more complicated. Among muon tomographers, linearised versions have been extensively used with deterministic approaches (e.g. Nishiyama et al., 2014; Rosas-Carbajal et al., 2017), which are successfully applicable when the only variables are the density or the intersection boundaries. When deterministic approaches are viable, they efficiently produce good results. Descent algorithms or, generally speaking, locally optimising algorithms, pose a valid alternative, as they could cope with the nonlinearity of the forward model, while including all desired parameters. Even though these algorithms suffer from possible non-uniqueness solutions (i.e. the solution depends heavily on the starting model,

yielding possibly multiple solutions), the main problem is the calculation of the derivatives of the forward model with respect to the parameter values. The analytical calculation of the derivatives is enormously tedious because the cut-off energy is the result of a numerical differential equation solver, as can be seen in Eq. (3.9) & (3.10). Unfortunately, numerical derivatives do not produce better results, because they might easily produce artefacts, which are hard to track down. This is especially true if the derivative has to be taken on a numerical result, which is always slightly noisy. In that case the differentiation amplifies the "noise", resulting in unreliable gradient estimates. A good overview over deterministic inversion methods can be found in Tarantola (2005).

The reasons stated above and our desire to include as much information on the parameters as possible nudge us towards probabilistic methods. Those approaches are also known as Bayesian methods. The main feature that distinguishes them from the deterministic methods described above is the consistent formulation of the equations and additional information in a probabilistic manner, i.e. as probability density functions (pdfs). This allows us to incorporate for example density values that were measured in the lab (including its error), set bounds on the location of the material interface or define a plausible range for the composition of the rock. All these changes act on the pdf of the respective parameter and does naturally integrate into the Bayesian inversion. Readers may find the book of Tarantola (2005) very resourceful for the explanation and illustration of probabilistic inversion. Several studies in the muon tomography community have already employed such methods with success (e.g. Lesparre et al., 2012; Barnoud et al., 2019).

The flexibility of being able to include as much information on the parameters as we desire comes at the price of having to solve the inversion in a probabilistic way. This can either be done using Bayes' Theorem and solving for the pdfs of the parameters of interest, or if the analytical way is not possible by employing Monte Carlo techniques. As the presence of a numerical solver renders the analytical solution impossible, we resort to the Monte Carlo approaches. In the following sections we guide the reader through the various stages of how such a probabilistic model can be set up, how probabilities may be assigned and how the inversion can finally be solved.

3.4.1 Probabilistic formulation of the forward model

The starting point for a probabilistic formulation is denoted by the equations that were elaborated in Ch. 3.3. These deterministic equations need to be upgraded into a probabilistic framework, where their attributed model and/or parameter uncertainties are inherently described. In the following paragraphs we describe how each model component can be expressed by a pdf before the entire model is composed at the end of this subchapter. The model is best visualised by a directed acyclic graph (DAG), i.e. see Kjaerulff and Madsen (2008), that depicts which variables enter the calculation at what point. For our muon tomography experiment this is visualised in Fig. 3.2. In the following the pdfs are denoted with the bold Greek letter $\boldsymbol{\pi}$, to differentiate them from normal parameters.

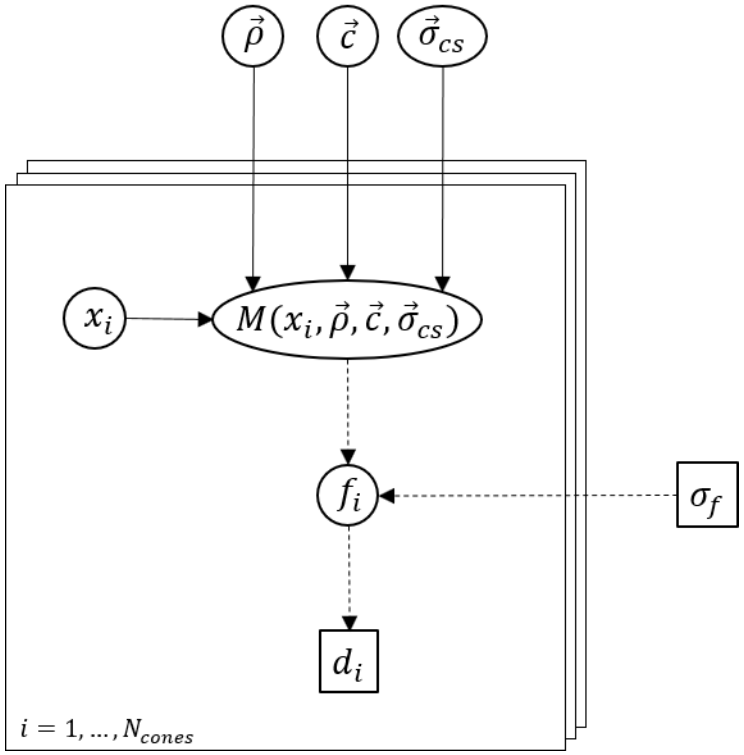

Figure 3.2: Directed acyclic graph (DAG) for the problem of muon tomography. Variables in a square (□) denote fixed, i.e. known values and variables in a circle/ellipse (○) are generally unknown and have to be represented by a pdf. Solid arrows (→) denote a deterministic relation, i.e. within a physical model, whereas dashed arrows (⇢) indicate a probabilistic relationship, i.e. a parameter within the statistical description of the variable. $\vec{\rho}, \vec{c}$ are the density and composition for different materials, whereas $\vec{\sigma}_{cs}$ contains the errors on the physical cross-sections in the energy-loss equation. σ_f describes the error on the cosmic-ray flux model. Within each cone, x_i is the position of the bedrock-ice interface, $M(x_i, \vec{\rho}, \vec{c}, \vec{\sigma}_{cs})$ is the calculated flux (i.e. energy-loss model and flux model combined), f_i the actual muon flux and d_i the observed number of muon tracks.

3.4.1.1 Muon data

The data in muon tomography experiments are usually count data, i.e. a certain number of measured tracks within a directional bin, which has been collected over a certain exposure time and detector area. As the measured number of muons is always an integer, we may model such data by a Poisson distribution,

$$\boldsymbol{\pi}(d_i|N_i) = \frac{N_i^{d_i} e^{-N_i}}{d_i!}, \tag{3.11}$$

where d_i denotes the measured number of muons in the i-th bin and N_i is the poisson parameter in the same bin, which can be interpreted as mean and variance of this distribution. Equation (3.11) may be rewritten in terms of a flux, f_i by

$$\boldsymbol{\pi}(d_i|f_i) = \frac{(f_i \Delta Ex_i)^{d_i} e^{-(f_i \Delta Ex_i)}}{d_i!}, \tag{3.12}$$

where f_i is the muon flux in the i-th bin and

$$\Delta Ex_i = \Delta A_{eff,i} * \Delta T * \Delta \Omega_{\mathrm{i}} \tag{3.13}$$

is the exposure, in which $\Delta A_{eff,i}$ is the effective total detector area from Eq. (3.4), ΔT is the exposure time and $\Delta\Omega_i$ is the solid angle.

3.4.1.2 Flux model

The next step is to set up a probabilistic model for the muon flux. First, we observe that "flux" is a purely positive parameter, i.e. $f_i \in [0, \infty)$. Thus, it is natural to model it by a lognormal probability distribution if estimates of mean and variance are readily available. The uncertainty on the muon flux is generally taken around 15% of the mean value. As it is possible, by Eq. (3.2), to calculate a flux for a given cut-off energy, which we interpret as the mean of the non-logarithmic values, the parameters of the lognormal distribution (i.e. $\mu_{f_i}, \sigma_{f_i}^2$) may be expressed by

$$\sigma_{f_i}^2 = \ln\left(1 + \left(\frac{F_i(E_{cut,i})*0.15}{F_i(E_{cut,i})}\right)^2\right) = \ln(1.0225) \tag{3.14}$$

and

$$\mu_{f_i} = \ln\big(F_i(E_{cut,i})\big) - \frac{\sigma_{f_i}^2}{2}, \tag{3.15}$$

which yield the probability density function for the flux, conditional on the cut-off energy

$$\boldsymbol{\pi}\big(f_i\big|\mu_{f_i}, \sigma_{f_i}^2\big) = \boldsymbol{\pi}\big(f_i\big|E_{cut,i}\big) = \frac{1}{\sqrt{2\pi} * f_i * \sigma_{f_i}} \exp\left(-\frac{1}{2}\left(\frac{\ln(f_i) - \mu_{f_i}}{\sigma_{f_i}}\right)^2\right). \tag{3.16}$$

3.4.1.3 Energy loss model

The energy loss model has multiple sources of error that have to be taken into account. Most notably, the relative errors on the different physical cross sections are given by Groom et al. (2001) as $\varepsilon_{ion} = 6\,\%, \varepsilon_{brems} = 1\,\%, \varepsilon_{pair} = 5\,\%, \varepsilon_{photonucl} = 30\,\%$. As it is not clearly stated as to what this error relates, i.e. one or more standard deviations, we interpret an error like $\varepsilon_{ion} = 6\,\%$ as: "within a factor of 1.06", which can be written as

$$\frac{\sigma_k}{(1+\varepsilon_k)} \leq \sigma_k \leq \sigma_k(1 + \varepsilon_k), \tag{3.17}$$

where $k \in K = \{\text{ionisation, bremsstrahlung, pair-production, photonuclear}\}$. Dividing this inequality by σ_k and taking the logarithm yields

$$-\ln(1 + \varepsilon_k) \leq 0 \leq \ln(1 + \varepsilon_k). \tag{3.18}$$

Thus, we may attribute a Gaussian pdf in the log-space for a "log-correction factor, $l\sigma_k$" by setting its mean to zero and its standard deviation to $\ln(1 + \varepsilon_k)$, i.e.

$$\boldsymbol{\pi}(\mathrm{l}\sigma_\mathrm{k}) = \frac{1}{\sqrt{2\pi} * \ln(1+\varepsilon_k)} \exp\left(-\frac{1}{2}\left(\frac{l\sigma_k}{\ln(1+\varepsilon_k)}\right)^2\right). \tag{3.19}$$

With a change of variables, using the Jacobian rule as explained in Tarantola (2005), we get

$$\boldsymbol{\pi}(\sigma_k) = \frac{1}{\sqrt{2\pi}*\sigma_k*\ln(1+\varepsilon_k)} \exp\left(-\frac{1}{2}\left(\frac{\ln(\sigma_k)}{\ln(1+\varepsilon_k)}\right)^2\right), \tag{3.20}$$

the lognormal pdf for the correction factor. The pdf for the cross-section uncertainty $\boldsymbol{\pi}(\vec{\sigma}_{cs})$ can now be written as a product of the four different pdfs described by Eq. (3.20)

$$\boldsymbol{\pi}(\vec{\sigma}_{cs}) = \prod_{k\in K} \boldsymbol{\pi}(\sigma_k), \tag{3.21}$$

as the errors of the physical cross-sections are stochastically independent from each other.

The calculated energy loss depends also on material parameters and subsequently on their uncertainties. However, these will be explained in detail in Ch. 3.4.1.4. A last error enters by the numerical solution of the ordinary differential equation, Eq. (3.9). We decided not to model this error, as its magnitude is directly controlled by the user (by setting a small enough step length in the Runge-Kutta algorithm) and thus can be made arbitrarily small. Lastly, we assume that all the errors in the energy loss model are explained by uncertainties in the cross sections as well as in the material parameters. Although this assumption is rather strong, as it excludes the possibility of a wrong model, we argue that this approach works as long as the variation in these parameters can explain the variation in the calculated cut-off energy. If this requirement is met, we may model the pdf for the energy loss model as a delta function,

$$\boldsymbol{\pi}\left(E_{cut,i}|\vec{\sigma}_{cs},\vec{\rho},\vec{c},x_i\right) = \boldsymbol{\delta}\left(E_{cut,i} - rk(\vec{\sigma}_{cs},\vec{\rho},\vec{c},x_i)\right), \tag{3.22}$$

where $\vec{\sigma}_{cs} = (\sigma_k)$, $\vec{\rho}$ is the vector of all material densities, $\vec{c}$ is the vector of all compositions and x_i is the vector of thicknesses of segments used in this cone. It is now already possible to eliminate $E_{cut,i}$ as a parameter by first multiplying Eqs. (3.16) & (3.22), which yields

$$\boldsymbol{\pi}(f_i, E_{cut,i}|\vec{\sigma}_{cs},\vec{\rho},\vec{c},x_i) = \boldsymbol{\pi}\left(f_i\middle|E_{cut,i}\right) * \boldsymbol{\pi}\left(E_{cut,i}|\vec{\sigma}_{cs},\vec{\rho},\vec{c},x_i\right). \tag{3.23}$$

From this expression it is possible to marginalise the parameter $E_{cut,i}$, by simply integrating over it, i.e.

$$\boldsymbol{\pi}(f_i|\vec{\sigma}_{cs},\vec{\rho},\vec{c},x_i) = \int \boldsymbol{\pi}(f_i, E_{cut,i}|\vec{\sigma}_{cs},\vec{\rho},\vec{c},x_i)\, dE_{cut,i}\ . \tag{3.24}$$

Due to the presence of the delta function in Eq. (3.22), this integral is solved analytically resulting in

$$\boldsymbol{\pi}(f_i|\vec{\sigma}_{cs},\vec{\rho}_i,\vec{c}_i,x_i) = \frac{1}{\sqrt{2\pi}*\mathrm{f_i}*\sigma_{f_i}} \exp\left(-\frac{1}{2}\left(\frac{\ln(f_i)-\mu_{f_i}}{\sigma_{f_i}}\right)^2\right), \tag{3.25}$$

where the parameters are given by

$$\sigma_{f_i}^2 = \ln\left(1+\left(\frac{M(\vec{\sigma}_{cs},\vec{\rho},\vec{c},x_i)*0.15}{\mathrm{M}(\vec{\sigma}_{cs},\vec{\rho},\vec{c},x_i)}\right)^2\right) = \ln(1.0225) \tag{3.26}$$

and

$$\mu_{f_i} = \ln(\mathrm{M}(\vec{\sigma}_{cs},\vec{\rho},\vec{c},x_i)) - \frac{\sigma_{f_i}^2}{2}\,. \tag{3.27}$$

Please note that $\mathrm{M}(\vec{\sigma}_{cs}, \vec{\rho}, \vec{c}, x_i) = F_i(rk(\vec{\sigma}_{cs}, \vec{\rho}, \vec{c}, x_i))$ describes the combined parts of the forward model that include the energy loss and the integrated flux calculation, which is basically a composition of functions.

3.4.1.4 Rock model

The density model can take different forms of probability densities (see Appendix B1, Ch. 3.9.1), such as fixed, normal, lognormal or even multimodal. For either form, it is possible to describe it by a generic function $\boldsymbol{\pi}(\vec{\rho})$, which is short for a multidimensional pdf, i.e. $\boldsymbol{\pi}(\rho_{ice}, \rho_{rock})$ if the i-th cone is known to consist of two segments with two specific densities. Equivalently, the pdf for the composition (see Appendix B2, Ch. 3.9.2) is either fixed or a multidimensional Gaussian distribution in the space of log-ratios. Thus $\boldsymbol{\pi}(\vec{c})$ can be split up to $\boldsymbol{\pi}(c_{ice}, c_{rock})$, like in the example above. Generally, we may assume that in our problem j different materials exist.

The situation for the thicknesses of the segments, $\boldsymbol{\pi}(x_i)$, within the i-th cone presents itself in a similar light as for the compositions. As the total thickness is known (detector position and a digital elevation model are given), the thickness parameter sub-space is endowed with the same mathematical structure as the composition parameter sub-space (i.e. one sum constraint), if the cone consists of more than just one segment. One can therefore safely assume that the thickness parameters live in a log-ratio space, within which we a-priori possess no information about the parameters. Thus, we attribute the thickness parameters a multidimensional uniform distribution on the log-ratio space.

3.4.1.5 The Joint probability density function

With the help of the DAG, introduced in Fig. 3.2, it is now straightforward to factorise the joint probability distribution for the whole problem, as their structure is equal. This results in

$$\boldsymbol{\pi}\left(\vec{d}, \vec{f}, \vec{\sigma}_{cs}, \vec{\rho}, \vec{c}, \vec{\mathrm{x}}\right) = \prod_{i=1}^{N_{cones}} \boldsymbol{\pi}(d_i|f_i)\boldsymbol{\pi}(f_i|\vec{\sigma}_{cs}, \vec{\rho}, \vec{c}, x_i)\boldsymbol{\pi}(x_i) * \prod_{j=1}^{N_{materials}} \boldsymbol{\pi}\left(\rho_j\right)\boldsymbol{\pi}\left(c_j\right) * \prod_{k\in K} \boldsymbol{\pi}(\sigma_k)\,, \tag{3.28}$$

or equivalently (and this will also be of much better use later on) the log joint pdf

$$\boldsymbol{l\pi}\left(\vec{d}, \vec{f}, \vec{\sigma}_{cs}, \vec{\rho}, \vec{c}, \vec{\mathrm{x}}\right) = \sum_{i=1}^{N_{cones}} \boldsymbol{l\pi}(d_i|f_i) + \boldsymbol{l\pi}(f_i|\vec{\sigma}_{cs}, \vec{\rho}, \vec{c}, x_i) + \boldsymbol{l\pi}(x_i) + \sum_{j=1}^{N_{materials}} \boldsymbol{l\pi}\left(\rho_j\right) + \boldsymbol{l\pi}\left(c_j\right) + \sum_{k\in K} \boldsymbol{l\pi}(\sigma_k), \tag{3.29}$$

where the prefix "$\boldsymbol{l}$" denotes the logarithm of the pdf. This has the benefit of reducing the size of numbers that the code has to cope with. Moreover, many computational statistics packages already have this feature included, which renders it easy to use.

Equation (3.28) depicts the full joint pdf. However, the relations between the parameters, as shown by the DAG (see Fig. 3.2), classify this model as a hierarchical model (Betancourt and Girolami, 2013). The key characteristic of such models is their tree-like parameter structure, i.e. the measured number of muons is related to the thickness or the density of the material only by the flux parameter, which "relays"

the information. A central problem of such models is the presence of a hierarchical "funnel" (see Fig. 2 & 3 of Betancourt and Girolami, 2013), which renders it very difficult for standard MCMC methods to adequately sample the model space. In high-dimensional parameter spaces this problem exacerbates even more.

Our aim to provide a simple and easy-to-use program somewhat contradicts this necessity of a sophisticated method (which inevitably requires the user to possess a strong statistical background). As the main problem is the rising number of parameters, it should be possible to mend the joint pdf by imposing thought-out simplifications.

We first get rid of the flux parameter, as for our problem it merely is a nuisance parameter. This is an official term for a parameter in the inversion which is of no particular interest but still has to be accounted for. Here specifically, we integrate over all possible values of the muon flux, $\vec{f}$ within its uncertainty, so that we can relate the results of the energy loss calculation (encoded in μ_{f_i}; see Eq. 3.27) directly to the measured number of muons, d_i. This effectively reduces the number of parameters and thus the number of dimensions of the model space. This can be achieved by marginalising the flux parameter out of the joint pdf,

$$\boldsymbol{\pi}\left(\vec{d}, \vec{\sigma}_{cs}, \vec{\rho}, \vec{c}, \vec{\mathrm{x}}\right) = \int \boldsymbol{\pi}\left(\vec{d}, \vec{f}, \vec{\sigma}_{cs}, \vec{\rho}, \vec{c}, \vec{\mathrm{x}}\right) d\vec{f}\,. \tag{3.30}$$

This effectively reduces to problem to the calculation of the new likelihoods (as d_i is given)

$$\boldsymbol{\pi}(d_i|\vec{\sigma}_{cs}, \vec{\rho}, \vec{c}, x_i) = \int \boldsymbol{\pi}(d_i|f_i)\boldsymbol{\pi}(f_i|\vec{\sigma}_{cs}, \vec{\rho}, \vec{c}, x_i)\, df_i, \tag{3.31}$$

or fully,

$$\boldsymbol{\pi}(d_i|\vec{\sigma}_{cs}, \vec{\rho}, \vec{c}, x_i) = \int_0^\infty \frac{(f_i \Delta E x_i)^{d_i} e^{-(f_i \Delta E x_i)}}{d_i!} \frac{1}{\sqrt{2\pi} * \mathrm{f_i} * \sigma_{f_i}} \exp\left(-\frac{1}{2}\left(\frac{\ln(f_i) - \mu_{f_i}}{\sigma_{f_i}}\right)^2\right) df_i\,, \tag{3.32}$$

where μ_{f_i} and σ_{f_i} are given by Eqs. (3.26) and (3.27), respectively. This integral is not solvable analytically but can be evaluated by numerical integration schemes. The likelihood has a maximum when the Poisson and the log-normal pdfs fully overlap. Interestingly, this directly shows the trade-off between the flux model and the data uncertainty. Usually, we want to measure enough muons that the statistical counting error is smaller than the systematic uncertainty of the flux model (i.e. the width of the Poisson pdf is smaller than the width of the log-normal pdf). This can be controlled directly by the exposure of the experiment, via larger detector area, coarser binning, or longer exposure time.

This marginalisation roughly halves the number of parameters, but there is still another simplification, which we may use. Many muon tomography applications deal with a two-material problem, while there may also be measurement directions where only one material is present. If we conceptually split those two problems and solve them independently, it is possible to further reduce the number of

simultaneously modelled parameters. In our study these two cases encompass bins where we measured only rock and others where we know there is ice and rock. The joint pdf for rock bins subsequently is

$$\boldsymbol{\pi}\left(\vec{d}, \vec{\sigma}_{cs}, \rho_{rock}, c_{\mathrm{rock}}\right) = \prod_{i=1}^{N_{cones}^{rock}} \boldsymbol{\pi}(d_i|\vec{\sigma}_{cs}, \rho_{rock}, c_{\mathrm{rock}}) * \boldsymbol{\pi}(\rho_{rock})\boldsymbol{\pi}(c_{rock}) * \prod_{k\in K} \boldsymbol{\pi}(\sigma_k), \quad (3.33)$$

which leaves the problem effectively with only a handful of parameters. Solving Eq. (3.33), for the rock density we retrieve $\widetilde{\boldsymbol{\pi}}(\rho_{rock})$, the posterior marginal pdf for the rock density. We refer the reader to Ch. 3.4.2 for the details of how to solve this inverse problem. Theoretically we could also retrieve $\widetilde{\boldsymbol{\pi}}(\rho_{ice})$, but this would require the detector to be positioned within the glacier, which poses more of a practical difficulty than a mathematical one.

For the second problem, we can interpret $\widetilde{\boldsymbol{\pi}}(\rho_{rock})$ as the new prior pdf for the rock density. At this point we employ one last simplification by assuming that the parameters between different cones are independent form each other. This is a rather strong presumption, which must be justified. The main problem mathematically lies in the hierarchical nature of the density parameter, which is the same for each cone, thus not independent in different cones. We, however, argue that in cones with two materials, there are more parameters than in bins with only rock, such that we may expect the posterior pdf of the rock density of these second kind of models to be less informative than the posterior rock density pdf of Eq. (33). This, in turn, means that the posterior rock density pdf of the two-material model largely equals the prior one if we select the posterior of the first kind of models as the prior of the second kind of models. The same is valid for the composition $\vec{c}_i$ and the cross-section error parameters $\vec{\sigma}_{cs}$. As long as this assumption is valid, we may decompose the joint pdf into independent joint pdfs for each cone

$$\boldsymbol{\pi}\left(d_i, \vec{\sigma}_{cs,i}, \vec{\rho}_i, \vec{c}_i, x_i\right) = \boldsymbol{\pi}\left(d_i\middle|\vec{\sigma}_{cs,i}, \vec{\rho}_i, \vec{c}_i, x_i\right)\boldsymbol{\pi}(x_i) \prod_{j=1}^{N_{materials}} \widetilde{\boldsymbol{\pi}}\left(\rho_{ij}\right)\widetilde{\boldsymbol{\pi}}\left(c_{ij}\right) * \prod_{k\in K} \widetilde{\boldsymbol{\pi}}(\sigma_{ik}). \quad (3.34)$$

Our inversion program enables the user to choose the type of model parametrisation. Either the full hierarchical model, which is given by Eqs. (3.28) & (3.29) or the simplified single-cone-bin inversion model ("Sicobi"-model), given by Eqs. (3.33) & (3.34) can be run.

3.4.2 Solution to the inverse problem

Usually in Bayesian inference, the goal is to calculate the posterior pdf, given the measured data, i.e. the quantity

$$\boldsymbol{\pi}\left(\vec{\sigma}_{cs}, \vec{\rho}, \vec{c}, \vec{\mathrm{x}}|\vec{d}\right) = \frac{\boldsymbol{\pi}\left(\vec{d}, \vec{\sigma}_{cs}, \vec{\rho}, \vec{c}, \vec{\mathrm{x}}\right)}{\boldsymbol{\pi}(\vec{d})}. \quad (3.35)$$

This can be interpreted as the inferences one may draw on the parameters in a model given measured data. The denominator on the right-hand side of Eq. (3.35), also called the "evidence", can be rewritten as the data marginal of the posterior, i.e.

$$\boldsymbol{\pi}\left(\vec{d}\right) = \int\int\int\int \boldsymbol{\pi}\left(\vec{d}, \vec{\sigma}_{cs}, \vec{\rho}, \vec{c}, \vec{\mathrm{x}}\right) d\vec{\sigma}_{cs}\, d\vec{\rho}\, d\vec{c}\, d\vec{x}\,. \quad (3.36)$$

As Eq. (3.36) basically describes an integration over the whole model parameter space, this may become such an extensive computation (especially when the number of model parameters is large), that it cannot be solved in meaningful time. However, as the evidence usually is a fixed value, the left- and right-hand side of Eq. (3.35) are merely scaled by a scalar and thus proportional to each other, i.e.

$$\boldsymbol{\pi}\left(\vec{\sigma}_{cs}, \vec{\rho}, \vec{c}, \vec{\mathrm{x}} | \vec{d}\right) \propto \boldsymbol{\pi}\left(\vec{d}, \vec{\sigma}_{cs}, \vec{\rho}, \vec{c}, \vec{\mathrm{x}}\right). \tag{3.37}$$

This is the starting point of Monte Carlo Markov Chain (MCMC) methods.

3.4.2.1 The Metropolis-Hastings algorithm

The basic MCMC algorithm, which we also use in this study is the Metropolis-Hastings (MH) algorithm (Hastings, 1970; Metropolis et al., 1953), which allows for the sampling of the joint pdf to obtain a quantitative sample. We note, however, that many different MCMC algorithms exist for various purposes and that the MH has no special status except for being comparatively simple to use and implement. An example of another MCMC algorithm in muon tomography can be found in Lesparre et al. (2017). The authors used a simulated annealing technique on the posterior pdf in order to extract the maximum a posteriori (MAP) model. As every simulated annealing algorithm has some type of MH-algorithm at its core, we directly use the MH-algorithm in its original form such that we not only retrieve a point estimate but a pdf for the posterior parameter distribution. The algorithm is explained in detail by Gelman (2014), such that we only provide a short pseudo-code description.

Algorithm 3.1 (Metropolis-Hastings):

(1) Draw a starting model, $\vec{m}_0 = (\vec{\sigma}_{cs,0}, \vec{\rho}_0, \vec{c}_0, \vec{\mathrm{x}}_0)$, by drawing $\vec{\sigma}_{cs,0}, \vec{\rho}_0, \vec{c}_0, \vec{\mathrm{x}}_0$ from their respective prior pdfs and determine the log-pdf value of this model

(2) Until convergence:

   a. Propose a new model according to $\vec{m}_{new} = \vec{m}_0 + J(0, c^2\Sigma)$, where Σ is the matrix of prior variances and $c = 2.4/\sqrt{D}$ and D is the number of parameters.

   b. Evaluate log-pdf value of $\vec{m}_{new}$ and calculate:
   $r = \exp(lp(\vec{m}_{new}) - lp(\vec{m}_0))$

   c. Evaluate the acceptance probability, $p_A = \min(1, r)$ and draw a number q from the uniform distribution U(0,1).

   d. If $q < p_A$: sample $\vec{m}_{new}$ & set $\vec{m}_{new} \rightarrow \vec{m}_0$,
   Else: sample $\vec{m}_0$

The advantage of this algorithm, compared to a "normal" sampling, lies in its efficiency. It is often not possible, or even reasonable, to probe the whole model space, as the largest part of the model space is "empty", where the pdf-value of the posterior is uninterestingly small. This fact that regions of high probability are scarce, and this becomes worse in high dimensional model spaces, is known as the "curse of dimensionality" (Bellman, 2016). MCMC algorithms (including the here presented MH-algorithm) allow the focus on regions of high probability, and therefore we are able to construct a reliable and

representative sample of the posterior pdf. We again refer to Gelman (2014) for a discussion why the MH-algorithm converges to the correct distribution and why we may use samples that were gained this way as estimate of the posterior probability density.

3.4.2.2 Assessing convergence, mixing, and retrieving the samples

The above stated advantages however, come at a price. First and foremost, we must ensure that the algorithm advances fast enough, but not too fast, through the model space. This is mainly controlled by the proposal distribution $J(0, c^2\Sigma)$, which is taken to be a multivariate Gaussian distribution. Ideally, the covariance matrix of the proposal distribution Σ is equal to the covariance structure of the posterior pdf. As at the start of the algorithm one generally has no idea what this looks like, but we assume that a combination of the prior variances is a reasonable starting point. After a certain number of steps, it is possible to approximate the covariance matrix of the proposal distribution with the samples taken up to this point.

A second crucial point is the presence of a warm-up period. The starting point, which usually lies in a region of high prior probability, does not necessarily also lie in a region of high posterior probability. The time it takes to move from the latter to the former is exactly this warm-up. This can usually be visualised by a trace plot, e.g. Fig. 3.3, in which the value of a parameter is plotted against the number of iterations. After this warm-up phase, the algorithm can be run in operational mode and "true" samples can be collected.

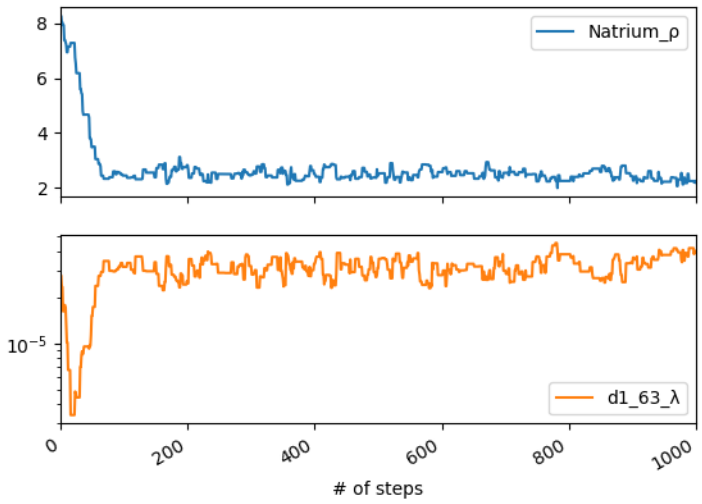

Figure 3.3: Example of a trace plot of a MH run with 1000 Draws. This plot shows the parameter value (y-axis) vs. # of steps (x-axis). This simplistic model consists of one cone with Sodium ("Natrium") as material. The only two parameters are the density of sodium (upper) and the flux within that cone (lower). The warm-up phase takes around 80-100 MH steps.

As in a Markov Chain the actual sample is dependent on the last one, we need a criterion to argue that the samples created in that way really represent "independent" samples. Qualitatively, we may say that if the Markov Chain forgets the past samples fast enough, then we may sooner treat them as independent

from each other. Gelman (2014) suggests that in order to assess this quantitatively, multiple MH-chains could be run in parallel and statistical quantities within and between each chain are analysed. For a detailed discussion thereof, we refer the reader to Appendix C (Ch. 3.10).

Once a satisfying number of samples has been drawn from the posterior pdf, marginalisation of nuisance parameters can be done by looking at the parameters of interest only. These samples may then be treated like counts in a histogram, i.e. distributional estimates, or simply the interesting statistical moments, such as mean and variance, can be obtained.

3.4.3 Construction of the bedrock-ice interface

The main analysis program allows us to export all parameters either as a full chain data, where every single draw is recorded, or as a statistical summary (i.e. mean and variance); both converted to point data, i.e. (x, y, z) – data. For the subsequent construction of the interface between rock and ice we only need the full-chain point-data. In the present study we restrict ourselves to a probabilistic description until the bedrock positions within a cone. It would also be possible to treat the bedrock construction within a Bayesian framework, however this would go beyond the scope of this study and is therefore left for a future adaption of the code. Nonetheless, in order to construct a surface, we rely on deterministic methods, which are explained in detail in what follows.

3.4.3.1 Interpolation to a grid

The "modelviewer.py" routine is able to read datasets from different detectors (which are saved as JSON-files) and computes for each cone the statistic, which the user is interested in (see "sigma" entry in program). Thus, it is possible to use the mean or, for example, the $+1\ \sigma$ position of each cone. From here onwards this point cloud is named H and contains one interface position (x, y & z coordinates) per cone. These are shown as triangles (▲) in Fig. 3.4.

As a second step, the program interpolates this point cloud in a bilinear way to a rectangular grid with a user specified cell size, Δ_{cs}. This grid can be described by a matrix $P \in \mathbb{R}^{r \times c}$, where r and c are the number of rows and columns (i.e. the number of y- and x-cells, needed to cover the whole grid). The procedure is similar to the bilinear interpolation of Lagrangian markers (that carry a physical property) to a (fixed) Eulerian grid in geodynamical modelling (see Gerya, 2010, p. 116), with the difference that our physical property is the height of the ice-bedrock interface.

We could also have fitted a surface through the resulting point cloud. However, by formulating this surface as a matrix we gain access to the whole machinery of linear algebra. Moreover, P can directly be interpreted as a rasterised DEM, which can be easily loaded and visualised in any GIS software. Thus, from a modular design perspective we think the matrix formulation has more advantages than drawbacks. The bilinear interpolation is shown in more detail in Fig. 3.4.

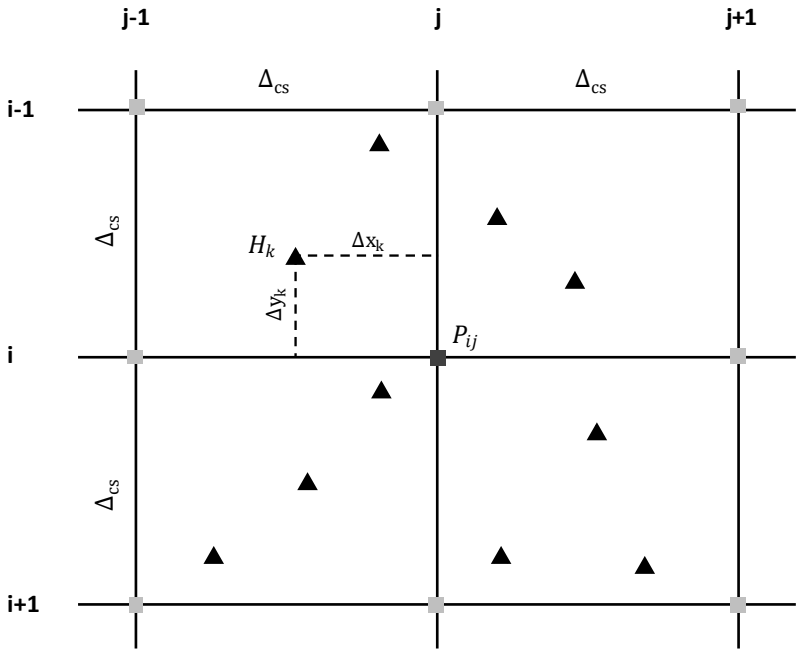

Figure 3.4: Example of a two-dimensional stencil. This is used to summarise the bilinear interpolation of interface positions within cones (H_k, ▲) to a fixed grid (P_{ij}, ■) with a user-defined cell size Δ_{cs}. Every interface position within a $\pm\Delta_{cs}$ interval contributes to the grid height P_{ij}.

In order to calculate the height at a grid point, P_{ij}, one has to form a weighted sum over all cone interface positions within a $\pm\Delta_{cs}$ interval, i.e.

$$P_{ij} = \frac{\sum_k w_k H_k}{\sum_l w_l}, \tag{3.38}$$

where the weights, w_k, are given by

$$w_k = \left(1 - \frac{\Delta x_k}{\Delta_{cs}}\right) * \left(1 - \frac{\Delta y_k}{\Delta_{cs}}\right). \tag{3.39}$$

3.4.3.2 Damping & Smoothing

The concept of damping usually revolves around the idea to force parameters to a certain value (e.g. in deterministic inversion by introducing a penalty term in the misfit function for deviations from that value). From a Bayesian viewpoint this would be accomplished by setting the prior mean to a specific value. In our code we implemented this idea by allowing the user to read a DEM and a "damping weight" to the code (see "fixed length group" in code). The program effectively computes a weighted average between the bedrock positions within the cones and a user defined DEM. The higher the chosen damping weight, the more the resulting interface will match the DEM, when pixels overlap.

The matrix formulation also enables us to use a further data processing technique without much tinkering. As geophysical data are often quite noisy, a standard procedure in nearly every geophysical inversion is a smoothing constraint. This effectively introduces a correlation between parameters and forces them to be similar to each other. From a Bayesian perspective, we could have achieved this correlation by defining a prior covariance matrix of the thickness parameters, such that neighbouring cones should

have similar thicknesses (which makes sense as we do except the bedrock-ice interface to be relatively continuous). As we work with independent cones in this study, we leave the exploration of this aspect open for a future study. Nevertheless, we offer the possibility in our code to use a smoothing on the final interpolated grid. This is achieved by a convolution of a smoothing kernel, K (see Appendix D, Ch. 3.11, for details), with the surface matrix P, which results in a smoothed surface matrix

$$P^S = K * P. \tag{3.40}$$

Please note that the $*$ operator in Eq. (3.40) denotes a convolution. In index notation the advantage of the linear algebra formalism becomes clear, as P^S can be expressed by

$$P_{ij}^S = \sum_{k=-s}^{s} \sum_{l=-s}^{s} K_{k+s+1,l+s+1} P_{i+k,j+l} \,. \tag{3.41}$$

The user is free to choose the number of neighbouring pixels, s, across which the program smooths over. As a smoothing matrix we use an approximation to a Gaussian kernel, which corresponds to a Gaussian blur in image processing. Whereas "smoothing" is a general term used in the geophysical community for the forced correlation of parameters, in our case where the parameters describe a surface, the convolution effectively smooths the surface, i.e. removes small scale variations.

Finally, we added a checkbox to our code to allow it to change the order of the damping and smoothing operations. Sometimes when a strong damping is necessary, this may result in rather unsmooth features at DEM boundaries, such that it makes sense to perform a smoothing only afterwards.

3.5 Main modules of SMAUG

Our toolbox, SMAUG, contains several subprograms, which are executed separately. This allows the user to inspect intermediate results without any difficulty. We also tried to keep the intermediate results as portable as possible, by using JSON-files, as often as possible. Here we explain, in logical order, the rational of the submodules (a detailed user manual is separately available):

MATERIALIZER.py

This subroutine allows the user to create their own material that will be used in the subsequent model builder. The user may choose a density (either from data or directly insert mean and standard deviation) and a composition (also either from data or from the list of Groom et al., 2001).

DATA_BINNING.py

As the name suggests, this subroutine is used to spatially bin the recorded track data. The bin data (i.e. the output hereof) is then fed to the model builder.

MODEL_BUILDER.py

The model builder takes the bin data and the materials as inputs and allows the user, with help of DEMs, to allocate data and materials to certain cones. This is basically the spatial setup of the model. The resulting model file is then provided to the inversion code.

INVERSION.py

This is the main module in SMAUG, providing the functionality to perform a MCMC algorithm on the probabilistic model created with MODEL_BUILDER.py. It also includes several analysis tools to assess MCMC performance.

MODEL_VIEWER.py

The model viewer allows us to visualise the interface results, obtained and exported by INVERSION.py. It also has the functionality to dampen and smooth the resulting surfaces.

3.6 Model verification

In this section we present examples of how the model can be employed, what it calculates and how the output is structured. We proceed by verifying, in a first step, that the physical models employed in this work yield results which are numerically consistent with the results of calculations from other studies. We will compare our results with reported values from literature in Ch. 3.6.1. We do this because we do not change the parameters of the flux model (except the height scaling, which has been verified by Nishiyama et al. (2017), and since the energy loss calculations is based on equations that stem from different frameworks.

In a second step, we will benchmark the results obtained by this code from real data against previously published results. For this purpose, we will reanalyse the raw data from Nishiyama et al. (2017). This is a study that was conducted in the Central Swiss Alps in a railway tunnel that featured a glacier (part of the Great Aletsch glacier) above. Our goal there was to estimate the thickness of the overlying glacier and thus the subsurface structure of the ice-bedrock interface. The respective calculation and discussion thereof are presented in Ch. 3.6.2.

3.6.1 Verification of energy loss calculations

The energy loss model, that we use in our code generally reproduces the literature values well (below 1%) across the different energy loss processes and relevant energies. In Fig. 3.5 we present the energy loss calculations for each energy loss process (i.e. ionisation, bremsstrahlung, pair-production and photonuclear interactions) across energies from 10 MeV to 100 TeV for silicon.

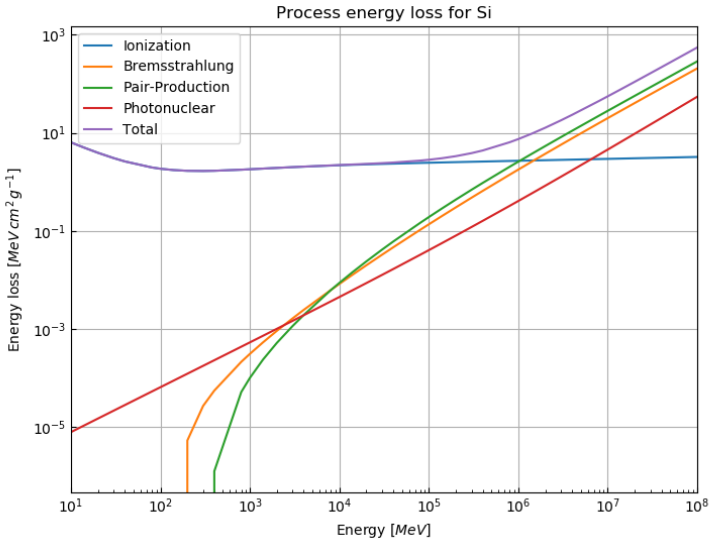

Figure 3.5: Log-log plot of the stopping power of the different energy loss processes for silicon. At ~ 10 GeV the radiative processes (i.e. bremsstrahlung, pair-production and photonuclear interactions) reach around 1 % of the total stopping power. At a few hundred GeV (at the so called "critical energy") the radiative processes start to become dominant over the ionisation losses.

The overall characteristics between different elements are the same with minor differences regarding the position of the critical energy and the 1 % - radiative point. In Fig. 3.6 we show the relative error of our calculations to the tabulated values from Groom et al. (2001) for the whole energy range.

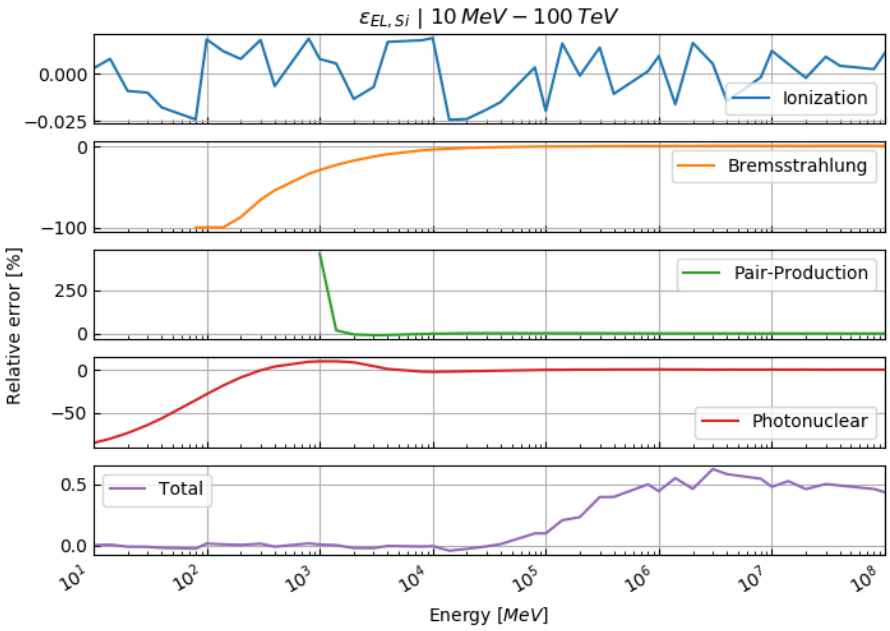

Figure 3.6: Relative error of our energy loss calculations compared to the tabulated values from Groom et al. (2001) for silicon. Ionisation losses agree very well with the literature values (within 0.025 %). At low energies the relative errors of the radiative processes are large and converge to a value close to 0 towards higher energies, resulting in a relative error on the total energy loss of around 0.5 % compared to literature.

We note that the energy losses by ionisation are reproduced very well over the entire energy range. We also note that the relative error on the radiative energy losses is rather large below 10 GeV. This does, however, not introduce a major bias, because below this energy, radiative energy losses are negligible compared to ionisation losses, as can be seen in Fig. 3.5. Furthermore, the related errors are in an acceptable range at the energy level at which radiative losses begin to become noticeable (i.e. around 100 GeV). This can be seen in Fig. 3.6, in the sense that the total relative error remains well bounded within 0.5 %. In the ionisation domain (i.e. below 100 GeV) the total relative error is dominated by the ionisation relative error, whereas above this energy level the relative errors on radiative losses start to prevail. A close-up of this energy range is given in Fig. 3.7.

There are different sources and circumstances that contribute to the error in the process energy losses. The scatter of the relative ionisation loss error around 0 with a rather small deviation can be viewed as simple rounding errors. The errors on the radiative processes, however, seem to be of a more systematic nature. We explain this behaviour through a different numerical integration scheme in Eq. (3.7), which tend to systematically under-/overestimate the true value, especially when the integrand comprises exponential functions. Whereas we used a Double Exponential Integration scheme (see Takahasi & Mori,

1974), the integration scheme from Groom et al. (2001) is not discernible. However, as the relative errors on the energy loss processes remain well within the theoretical uncertainties, (see Ch. 3.4.1.3), we consider, that our calculation accurately reproduces the literature values for elements.

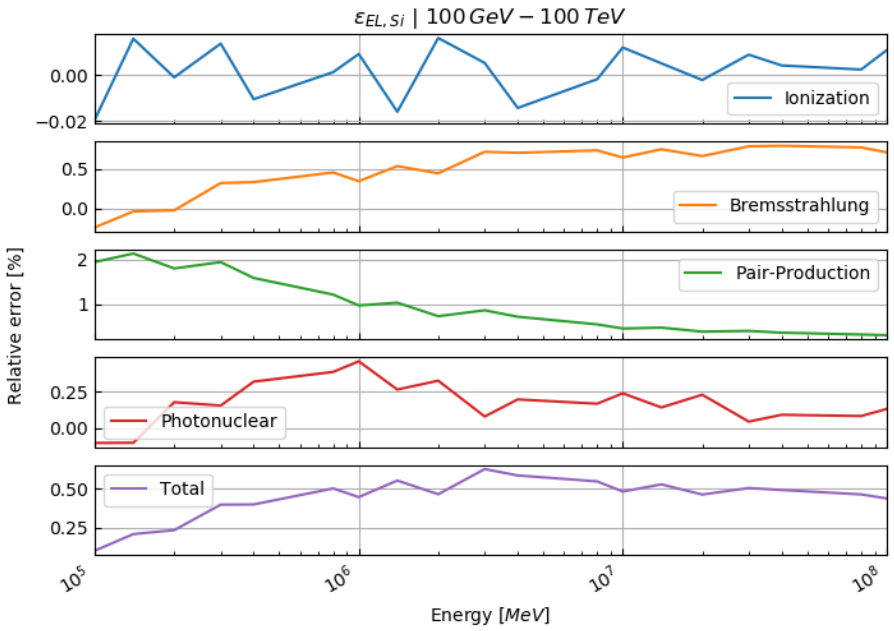

Figure 3.7: Relative error of our energy loss calculations for silicon compared to the tabulated values from Groom et al. (2001) at higher energies (100 GeV – 100 TeV). The relative errors remain bounded within their theoretical uncertainties (see Ch. 3.1.3).

The above calculations were performed for pure silicon. The respective figures for other four important elements in the Earth's crust (Al, Fe, Ca & O) can be found in Appendix E (Ch. 3.12). Those elements are, however, not representative for any real material encountered in geological applications. For this reason, we compiled the same computations for four selected, geologically important compounds (SiO2, CaCO3, Standard Rock, ice) that are also shown in Appendix E (Ch. 3.12). We summarise, that with the exception of Standard Rock, all calculations yield results that are similar to the silicon calculation above. The discrepancy for Standard Rock stems from its inconsistent definition, with respect to the different parameters. In particular, the "Standard Rock" according to Lohmann et al. (1985) has an atomic number Z of 11 (i.e. sodium) and an atomic weight A of 22, which yield the characteristic parameter values of $\langle Z/A \rangle = 0.5$ and $\langle Z^2/A \rangle = 5.5$ respectively. Groom et al. (2001), on the other hand, list sodium as the only constituent of a standard rock. However, this material cannot be modelled by any mixture of pure elements, as common sodium consists of one neutron more and thus has a higher atomic weight (i.e. $A_{Na} = 23$). Consequently, the use of standard sodium would lead to different characteristic parameter values, i.e. $\langle Z/A \rangle = 0.478$ and $\langle Z^2/A \rangle = 5.263$, thus leading to an inconsistency. This is often conveyed by the phrase that standard rock "is not-quite-sodium" (see Groom et al. 2001, p.203). In order to circumvent this problem, we advocate the exchange of ${}^{23}_{11}Na$ with its ${}^{22}_{11}Na$ isotope, that would lead

to the characteristic parameter values $\langle Z/A \rangle = 0.500$ and $\langle Z^2/A \rangle = 5.501$, which are much closer to the actual definition of standard rock. For this reason, we extended the element/compound-list, (which is available from http://pdg.lbl.gov/2019/AtomicNuclearProperties/expert.html) by the $^{22}_{11}Na$ isotope, assuming that all parameters are equal to the ones from $^{23}_{11}Na$. Additionally, we redefined the standard rock (i.e. material number 281 in the list) to consist only of $^{22}_{11}Na$. With this change, standard rock does not need any more special treatment and can be calculated in a way that is consistent to all other compounds.

Furthermore, the relative error between the tabulated values and our modified calculation falls in line with the calculations for the other compounds and elements (Figures 3.8 and 3.9).

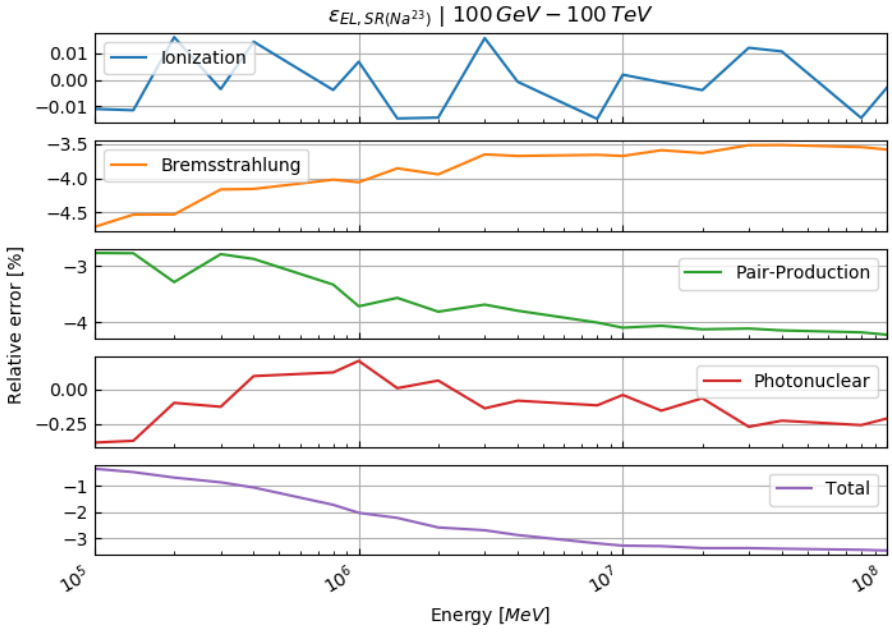

Figure 3.8: Relative error of our energy loss calculations for a standard rock consisting of $^{23}_{11}$Na, compared to the tabulated values from Groom et al. (2001) at higher energies (100 GeV – 100 TeV).

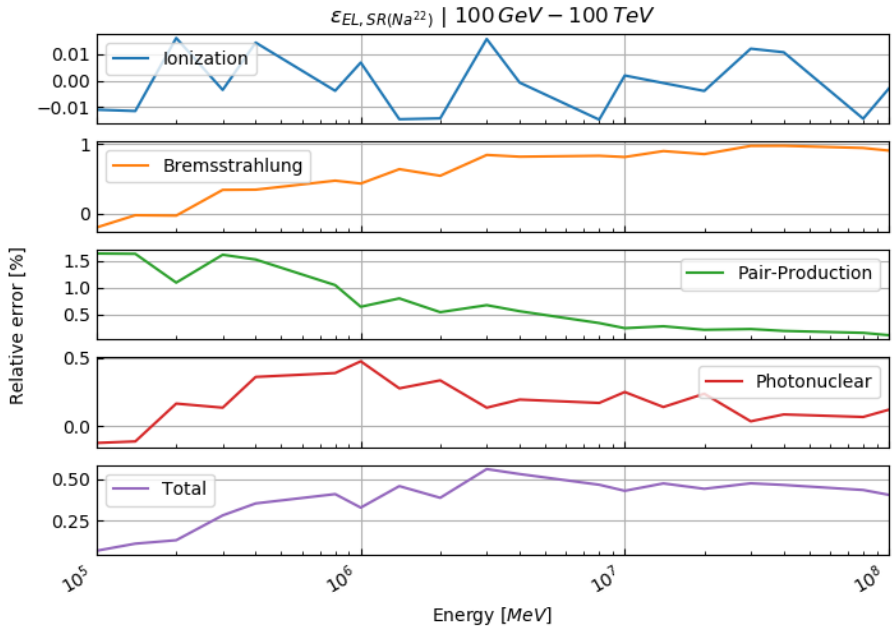

Figure 3.9: Relative error of our energy loss calculations for a standard rock consisting of $^{22}_{11}$Na, compared to the tabulated values from Groom et al. (2001) at higher energies (100 GeV – 100 TeV).

3.6.2 Verification of the bedrock-ice interface reconstruction

In this part we test the presented reconstruction algorithm on previously published data. For this purpose, we compare our calculations to the ones already published in the study by Nishiyama et al., (2017), where the goal was to measure the interface between the glacier and the rock, in order to determine the spatial distribution of the rock surface (also below the glacier). We could access the Railway Tunnel to install the muon detectors beneath the ice. A situation sketch is shown in Fig. 3.10.

The results shown below (Figs. 3.11 – 3.13) represent the bedrock-ice interface interpolated to an 8-metre grid, which was first damped (weight 8) and then smoothed (2 grid pixel). We assess the goodness of fit according to the three cross-sections (East, Central, West), that are shown in Fig. 3.10. The crosscuts are nearly perpendicular to the train tunnel and roughly 40 m apart from each other. Figures 3.11 to 3.13 show the three cross-sections in detail. In every plot, we also indicate the solution from Nishiyama et al. (2017). Please note that we added a systematic error of 2 m to the uncertainty planes, as the DEM we are working with has itself an uncertainty of $\pm$ 2 m. The dash-dotted lines mark thus the most conservative error estimate. Moreover, we highlighted the parts of the cross-section that had either been damped to the bedrock DEM or that have been solely resolved by the measurement (see "damping marker" in Fig. 3.10).

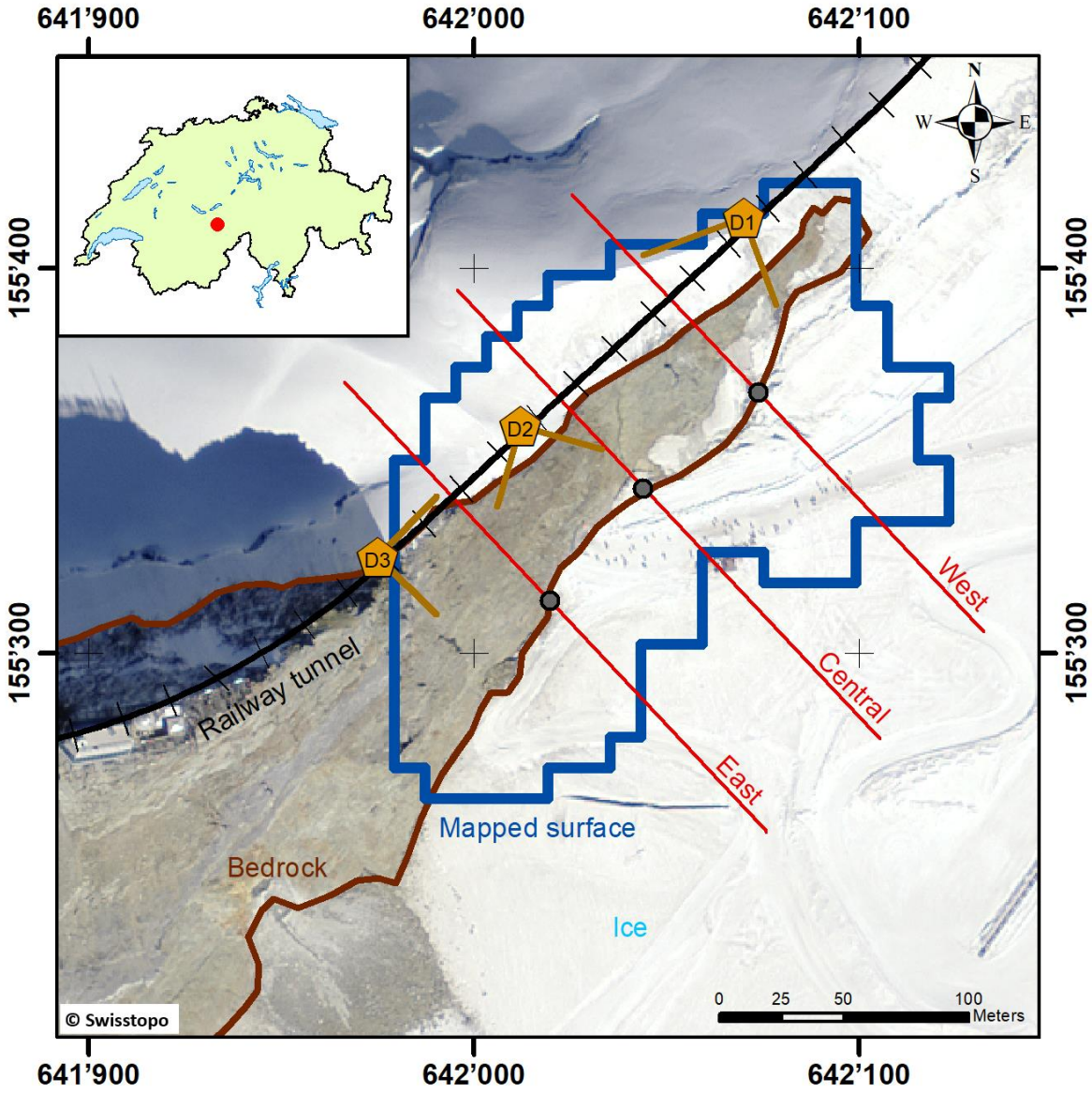

Figure 3.10: Overview map of the study area around Jungfraujoch. The brown line separates the visible bedrock in the DEM from the glacier part ("Ice"). The three profiles (East, Central & West) are depicted with a red line, on which the damping marker is shown by a grey point. The extent of the reconstructed bedrock-ice interface is shown by the blue area. Additionally, the three detector positions (D1, D2 & D3) are shown by orange pentagons, including their viewfield. Basemap: Orthophotomosaic Swissimage, © Federal Office of Topography swisstopo.

Figure 3.11 shows the western profile, where our bedrock-ice interface and the one from the previous study agree well and both lie within the given error margins. The lack of fit in areas where the steepness changes rapidly (i.e. around 40 m and 80 m) can be explained as a smoothing artefact. Towards the end of the profile, the decreasing data coverage becomes evident as the uncertainties rise. This effect can also be seen in the jagged behaviour of the interface curves around 100 m to 120 m, hinting at interpolations with few data.

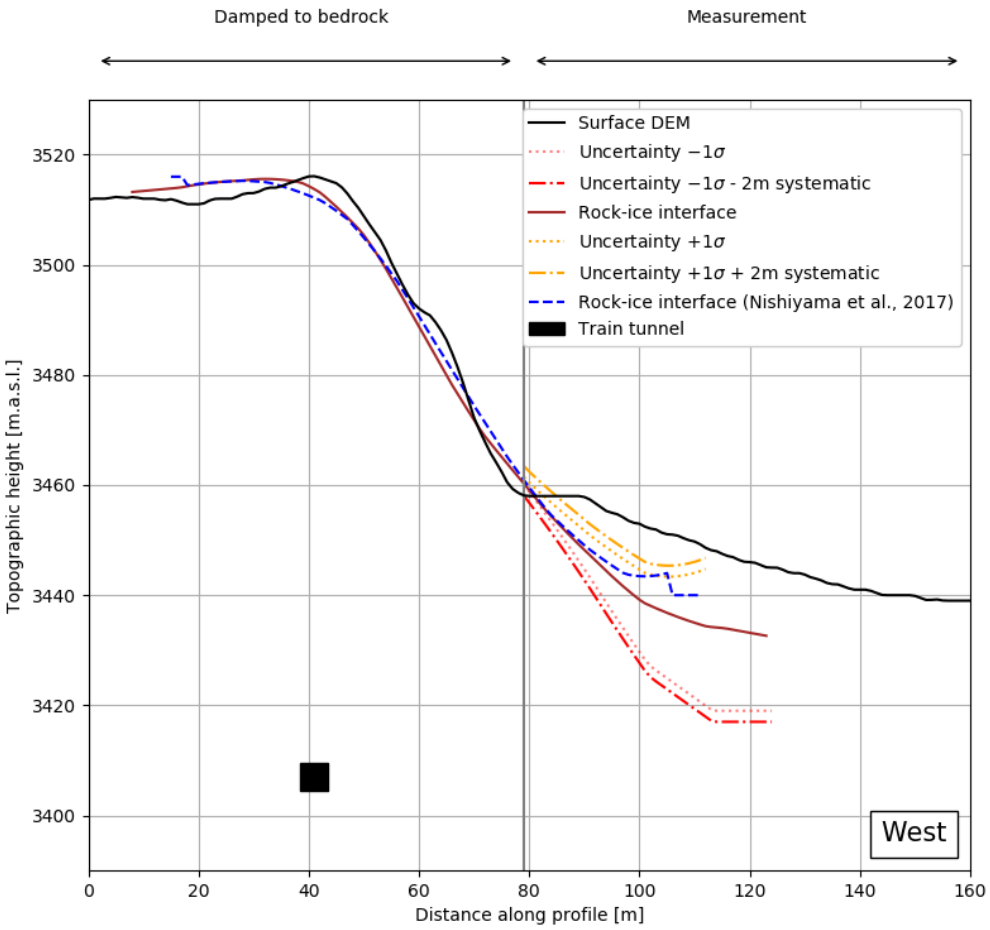

Figure 3.11: Western cross-section. The brown and dashed blue line indicate the ice-bedrock interface solutions of this study and the one from Nishiyama et al. (2017), respectively. 1 σ-error margins are shown in yellow (upper) and red (lower). The dotted margins encompass only the statistical variation of the interface position, whereas the dash-dotted include a ± 2 m systematic error which stems from the inherent DEM-uncertainty. For completeness we also show the position of the railway tunnel as a black square.

Figure 3.12 presents the central profile. Similar to the western profile (Fig. 3.11) the fits match quite well and are within the error margins. It may be possible that the point where the actual bedrock begins might be further down (i.e. $\sim 80m$ instead of 65 m). Here we used the same DEM and aerial photograph as the previous study. This means that newer versions might be available, that show more bedrock (due to the glacial retreat as a response to global warming).

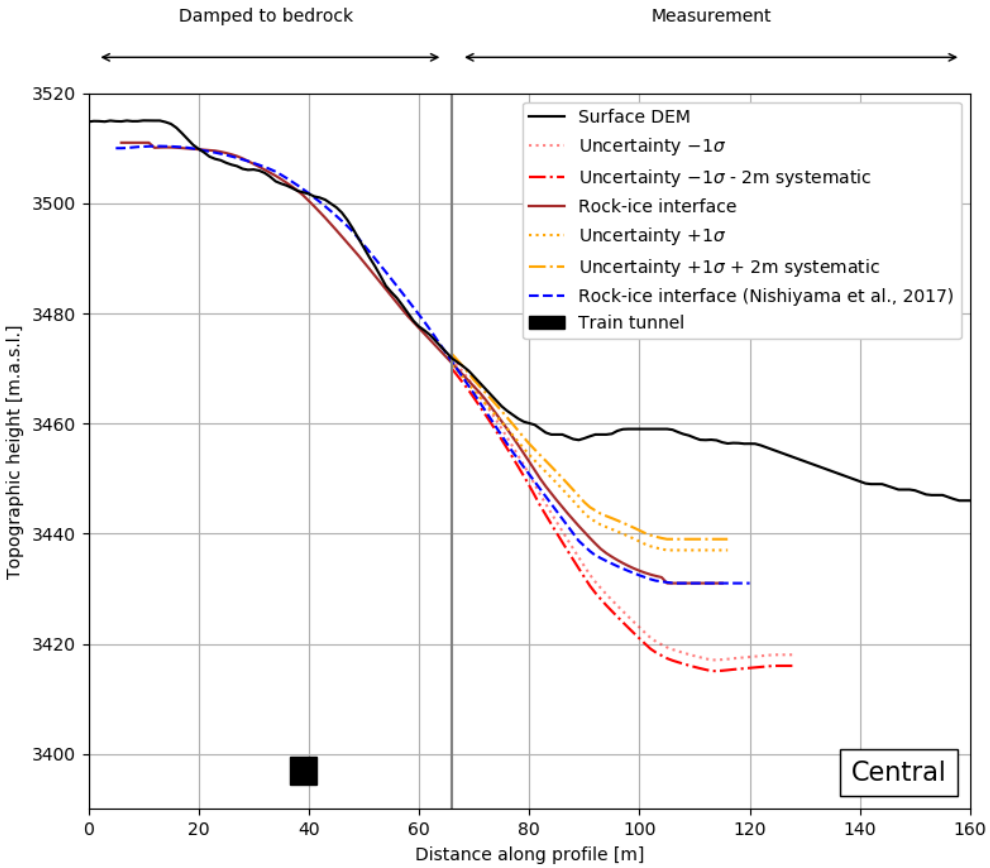

Figure 3.12: Central cross-section. The brown and dashed blue line indicate the ice-bedrock interface solutions of this study and the one from Nishiyama et al. (2017), respectively. 1 σ-error margins are shown in yellow (upper) and red (lower). The dotted margins encompass only the statistical variation of the interface position, whereas the dash-dotted include a $\pm 2\ m$ systematic error which stems from the inherent DEM-uncertainty. For completeness we also show the position of the railway tunnel as a black square.

The eastern profile is shown in Fig. 3.13. One sees that the results from this study are internally consistent. The surface from the previous study plunges down earlier with respect to the surfaces calculated here. This may in fact be a damping effect, as the bedrock-ice interface from Nishiyama et al. (2017) has not been constrained to the bedrock (via damping) and thus plunges down before the damping mark at $\sim 72\ m$. Still, the two surfaces agree within 5 m, which we consider as acceptable.

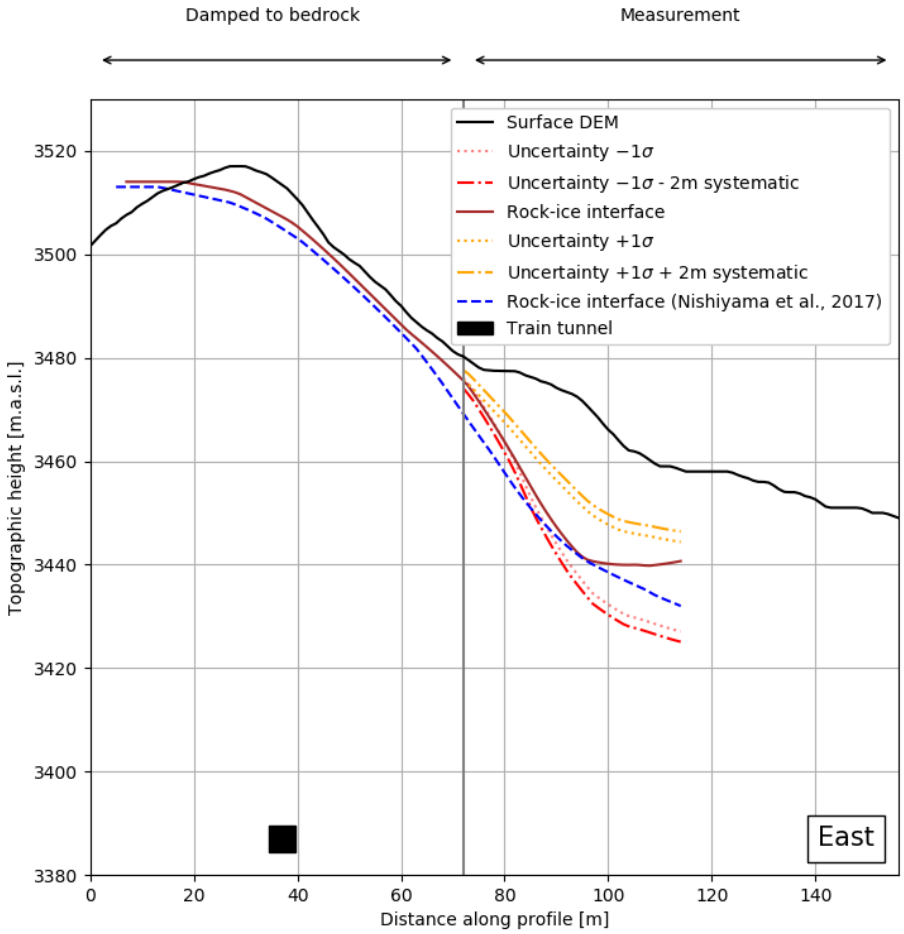

Figure 3.13: Eastern cross-section. The brown and dashed blue line indicate the ice-bedrock interface solutions of this study and the one from Nishiyama et al. (2017), respectively. 1 σ-error margins are shown in yellow (upper) and red (lower). The dotted margins encompass only the statistical variation of the interface position, whereas the dash-dotted include a $\pm 2\ m$ systematic error which stems from the inherent DEM-uncertainty. For completeness we also show the position of the railway tunnel as a black square.

All together the performance of the whole workflow, which is shown in this study, produces results, which are similar to the ones published in the previous study (Nishiyama et al., 2017). We use the results of this comparison to validate the base of our code.

3.7 Conclusions

In this study we have presented a model that allows us to integrate geological information into a muon tomography framework. The inherent parameter estimation problem has been formulated in a probabilistic way and solved accordingly. The propagation of uncertainties thus occurs automatically within this formalism. We also considered approaches including DAGs or the simplex subspace of compositions which could be helpful to the muon tomography community while tackling their own research. We condensed these approaches in a modular toolbox. This assortment of python programs allows the user to address the subproblems during the data analysis of a muon tomography experiment. The programs are modular in the sense that the user can always access the intermediate results, as the files are mostly in a portable format (JSON). Thus, it is perfectly possible to only use one submodule of the toolbox while working with an own codebase. As every “tool” is embedded in a GUI, the program is made accessible without the need to first read and consider several thousand code lines. Furthermore, we have shown that the results we obtain with our code are largely in good agreement with an earlier, already published experiment. The small deviations may be attributed to data analysis subtleties.

We would like to stress that this work is merely a foundation upon which many extensions can be built when it is used in other applications as well. Future content might for example include a realistic treatment of multiple scattering and the inclusion of compositional uncertainties in the inversion, for which we laid out the basis in this study.

3.8 Appendix A – Muon flux model

As many empirical muon flux models, the one that we employed consists of an energy spectrum for vertically incident muons at sea level at its core. An accepted instance is the energy spectrum of Bugaev et al. (1998), that takes the form

$$\Phi_B(p) = A_B p^{-\left(\alpha_3 \log_{10}^3(p) + \alpha_2 \log_{10}^2(p) + \alpha_1 \log_{10}(p) + \alpha_0\right)}, \tag{3.A1}$$

where p denotes the momentum of the incident muon in $GeV * c^{-1}$. The values of the α_i and A_B are, for example, listed in Lesparre et al. (2010). This model is an extended version of Renya (2006), to account for different incident angles,

$$\Phi_R(p, \theta) = \cos^3(\theta)\, \Phi_B(p \cos(\theta)), \tag{3.A2}$$

where θ is the zenith angle of the incident muon. It is important to note that the parameter values in Eq. (3.A1) are changed to $\alpha_0 = 0.2455$, $\alpha_1 = 1.288$, $\alpha_2 = -0.2555$, $\alpha_3 = 0.0209$ and $A_B = 0.00253$. In order to include height above sea level as an additional parameter, Hebbeker and Timmermans (2002) proposed to model the altitude dependence as an exponential decay, which modifies Eq. (3.A2) into

$$\Phi(p, \theta, h) = \Phi_R(p, \theta) * \exp\left(-\frac{h}{h_0}\right). \tag{3.A3}$$

The scaling height, h_0, is usually to be taken as $h_0 = 4900m + 750\, m\, c\, GeV^{-1} * p$, where p, is the momentum of the incident muon in $GeV * c^{-1}$. However, as this formula is only valid up to an altitude of 1000 m above sea level, Nishiyama et al. (2017) adapted it to $h_0 = 3400\, m + 1100\, m * c * GeV^{-1} * p * \cos(\theta)$. This was done in order to fit the energy spectrum up to 4000 m above sea level. This formula is now valid for momenta above 3 $GeV * c^{-1}$, zenith angles between 0° and 70° and an altitude below 4000 m above sea level.

3.9 Appendix B – Rock model

3.9.1 B1 – Density model

The density distribution of a lithology can be determined through various methods. In our work, we constructed a density model by analysing various rock samples from our study area in the laboratory. Two experimental setups were employed to gain insight into the grain, skeletal as well as the bulk density of the rocks. Grain and skeletal density were measured by means of the AccuPyc 1340 He-pycnometer, which is a standardised method that yields information on the volume. Bulk density values were then determined based on Archimedes' principle, where suspension of paraffin coated samples were suspended into water (ASTM C914-09, 2015; Blake and Hartge, 1986).

Every sample $j = 1, \dots, N$ (usually the size of a normal hand sample) has been split up into smaller subsamples $i = 1, \dots, S_j$, that were measured. The bulk density of the i-th subsample can be calculated by

$$\rho_{bulk,ij} = \frac{\rho_{H_2O} * m_{s,ij}}{(m_{s,ij}+m_{p,ij}+m_{t,ij}-m_{sus,ij})-\left(\frac{m_{p,ij}*\rho_{H_2O}}{\rho_p}\right)-(\frac{m_{t,ij}*\rho_{H_2O}}{\rho_T})}, \quad (3.B1)$$

where $\rho_{H_2O}, \rho_p, \rho_T$ denote the density of water, paraffin and the thread that was used to dip the sample into the liquid, respectively. $m_{s,ij}, m_{p,ij}, m_{t,ij}, m_{sus,ij}$ describe the mass of the sample, the paraffin coating, the thread and the apparent mass of all three components suspended in water. $m_{p,ij}, m_{t,ij}$ can then be simply obtained through

$$m_{p,ij} = m_{s,t,p,ij} - m_{s,t,ij}\ , \quad (3.B2)$$

as $m_{s,t,p,ij}$ denote the mass of the sample including thread and paraffin coating on one hand and $m_{s,t,ij}$ only the mass of the sample and the thread on the other hand. Further, the mass of the thread is given by

$$m_{t,ij} = m_{s,t,ij} - m_{s,ij}. \quad (3.B3)$$

The maximal precision of the reading is estimated at $\pm 5 * 10^{-5} g$, and the commonly ignored effects regarding buoyancy in air has been estimated to introduce an error on the order of $\pm 2 * 10^{-4} g$. This error has been attributed to all direct mass measurements. Moreover, because small pieces of material may detach from the sample upon attaching the thread to the sample and during the paraffin coating, we set an error of $\pm 2 * 10^{-2} g$ to all measurement results. The variables in Eq. (3.B1) are strictly positive values. Following Tarantola (2005) we model these "Jeffreys parameters" by lognormal distributions, as they inherently satisfy the positivity constraint. Because Eq. (3.B1) does not simply allow a standard uncertainty propagation, the script "subsample_analysis.py" performs a Monte Carlo simulation for each subsample and attributes a final lognormal probability density function to the resulting histogram. Figure 3.B1 illustrates such an example, where the calculation has been performed for subsample JT-20-1.

We have found 10'000 draws per subsample to be sufficient to retrieve a solid lognormal distribution. However, this parameter can easily be changed in the script, depending on the user's preference of precision/speed.

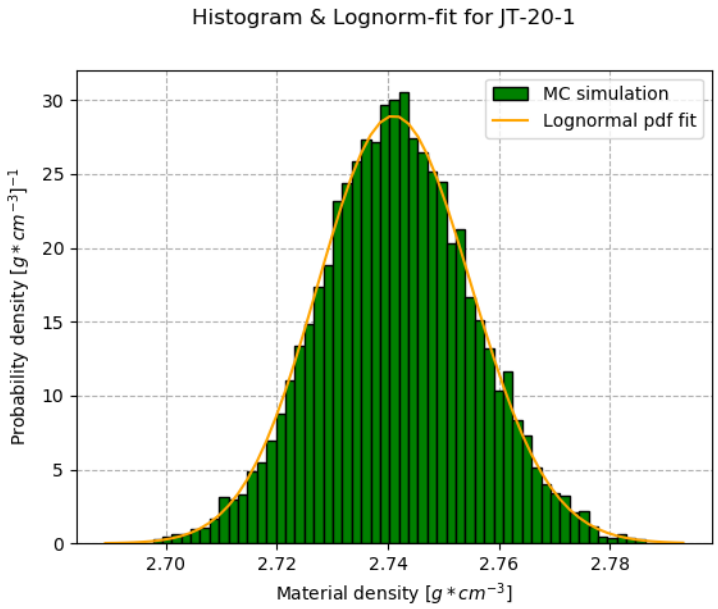

Figure 3.B1: Example output of "subsample_analysis.py" for a bulk density measurement of subsample JT-20-1 (see supplementary information for data). Green bars represent the histogram of 10'000 monte carlo simulation draws. The orange curve indicates the fitted lognormal probability density function.

The determination of the grain and skeletal densities is simpler than the bulk density measurements, because the corresponding method consists of a mass and a volume measurement, respectively. The density formula

$$\rho_{skeletal/grain,ij} = \frac{m_{ij}}{V_{ij}} \tag{3.B4}$$

can be transformed by taking logarithms on both sides, which yields

$$\ln(\rho_{\mathrm{skeletal/grain,ij}}) = \ln(m_{ij}) - \ln(V_{ij}) \,. \tag{3.B5}$$

As the logarithms of lognormally distributed parameters follow a normal distribution, the uncertainty propagation in Eq. (3.B5) can be treated by standard gaussian uncertainty propagation. An example output for this calculation can be found in Fig. 3.B2, for a grain density measurement of subsample SX-03-1.

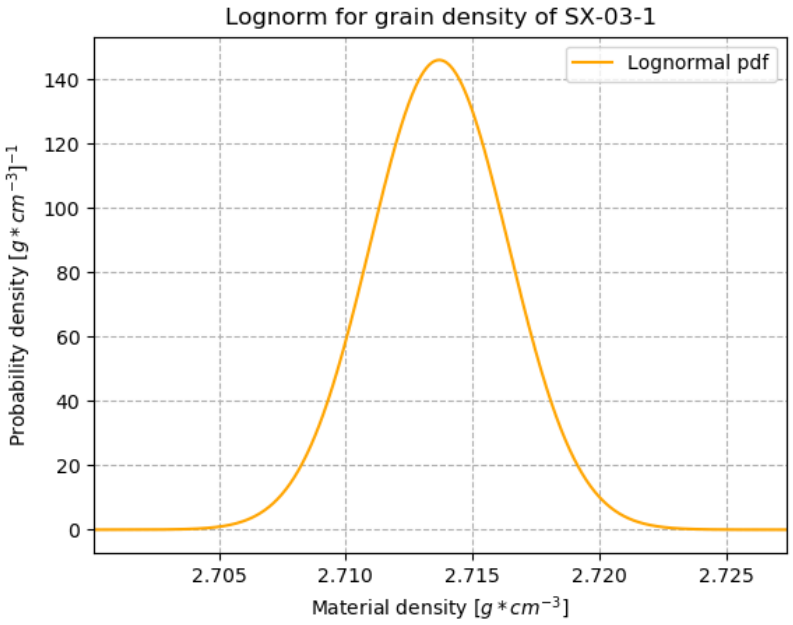

Figure 3.B2: Example output of "subsample_analysis.py" for a grain density measurement of subsample SX-03-1 (see supplementary information for data). The orange curve indicates the lognormal probability density function of $\rho_{grain,1,SX-03}$.

Uncertainties on the primary parameters (such as V_{ij} in Eq. 3.B5 or $m_{sus,ij}$ in Eq. 3.B1) can be translated to lognormal parameters. This is achieved by reinterpreting the expression $V_{ij} \pm \varepsilon_{V_{ij}}$ as the first plus/minus the square root of the second statistical moment, i.e. the mean and the variance (var) of the lognormal distribution. A transformation to the location and scale parameters of the lognormal distribution (μ, σ^2) can then be achieved by the following formulae:

$$\mu = \ln\left(\frac{mean}{\sqrt{1+\frac{var}{mean^2}}}\right), \qquad \sigma^2 = \ln\left(1+\frac{var}{mean}\right) . \tag{3.B6}$$

The script "sample_analysis.py" performs this conversion for each subsample measurement and combines the resulting pdfs to a sample pdf. This is done by a disjunction of the subsample pdfs (Tarantola, 2005),

$$p_j(\rho) = \frac{1}{S_j}\sum_{i=1}^{S_j} p_{ij}(\rho) , \tag{3.B7}$$

where $p_{ij}(\rho)$ is the lognormal probability density, that has been calculated during the subsample analysis (see Fig. 3.B1 and Fig. 3.B2). Fig. 3.B3 shows these disjunctions for all samples of dataset with bulk density values. As the number of subsamples per sample is small, the disjunction might not be representative of the sample distribution. We therefore implemented a fitted lognormal pdf to the disjunction to gain insight into this discrepancy.

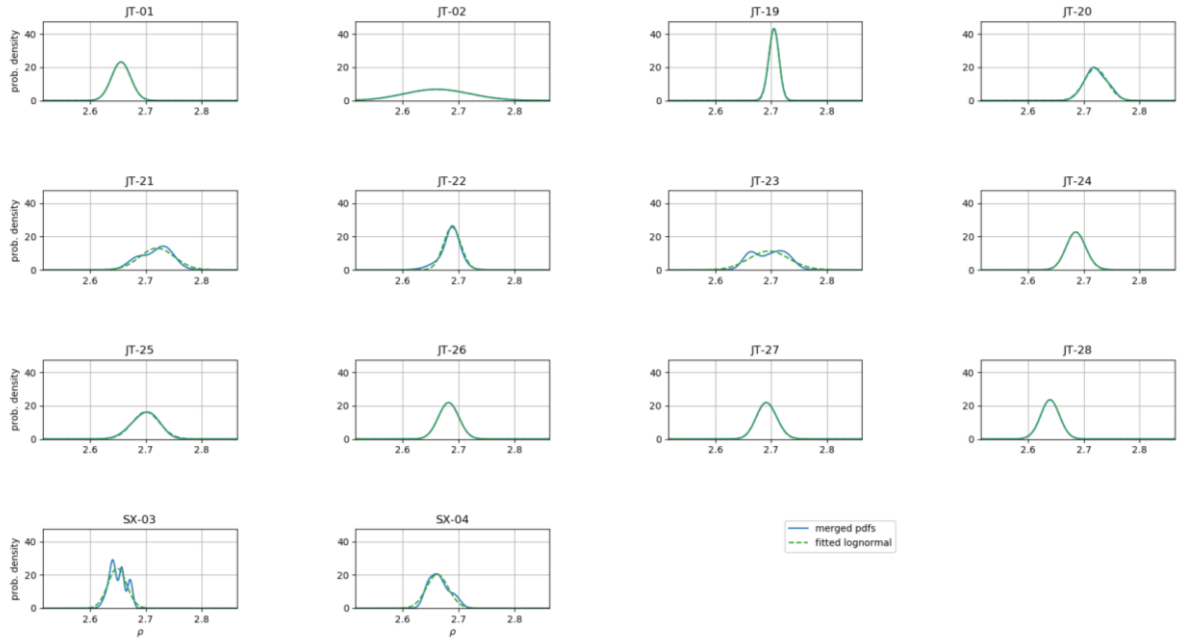

Figure 3.B3: Disjunction of subsample to sample pdfs for bulk density measurements, according to Eq. (3.B7). The dashed green line in each subplot denotes a fitted lognormal pdf to the disjunction (solid blue line).

As illustrated in Fig. 3.B3, the density of samples JT-21, JT-23 and SX-03 do not completely comply with a lognormal distribution. Severe discrepancies might hint at a problem during the sample preparation and/or measurements process, leading to samples being excluded from the analysis. However, as the difference between disjunction and fitted lognormal in these samples are still in an acceptable range, the data can be used for further analyses without problems.

In a second step the script performs another disjunction of the sample pdfs (from Fig. 3.B3) to a lithology pdf according to

$$p_{litho}(\rho) = \frac{1}{\mathrm{N}} \sum_{i=1}^{\mathrm{N}} p_j(\rho) \, . \tag{3.B8}$$

Fig. 3.B4 shows the result of Eq. (3.B7) together with a fitted lognormal pdf and their respective 25%, 50% and 75%-quantiles. The user is free to use both pdfs in the main code as a constraint on material density, because the code produces a disjunction pdf and a fitted lognormal output file.

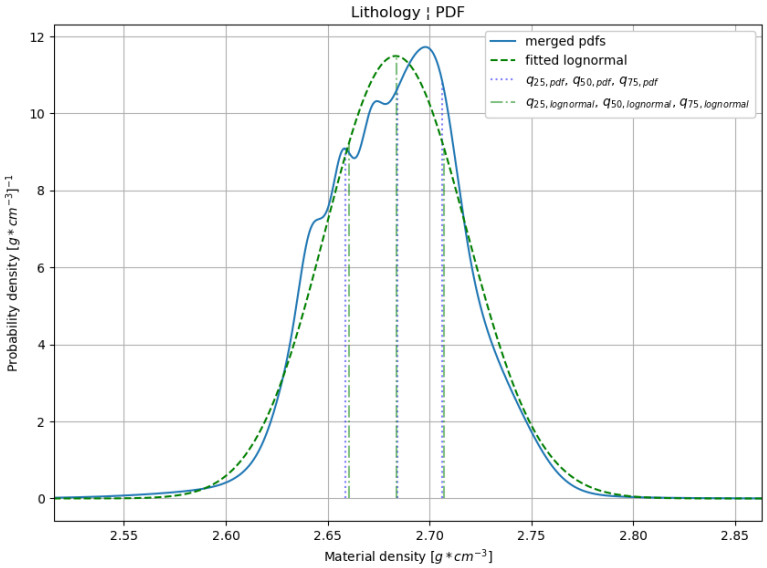

Figure 3.B4: Disjunction of sample pdfs to a lithology pdf for bulk density measurements, according to Eq. (3.B8).

3.9.2 B2 – Composition model

We have seen in Eq. (3.9) that the material density parameter enters the energy loss calculations rather directly. Contrariwise, the compositional model affects the energy loss equations much more subtly through average $\{Z/A\}_{rock}$ and $\{Z^2/A\}_{rock}$ values and mean excitation energies that need to be calculated for the entire lithology. Likewise, information on the weight percentages of the main elements within the rock is required for the quantification of the radiation loss term.

Although a modal mineral analysis (e.g. the quantitative determination of mineral volumes) is preferable and can be treated according to Lechmann et al. (2018), its execution is a rather time-consuming effort. This is the reason why compositional data in muon tomography experiments predominantly consist of XRF-data, which show the abundance of major oxides within the rock. We describe here a method to incorporate such type of information in a probabilistic way thereby following Aitchison (1986). Compositional data are usually available in the form of Table 3.B1, which presents an excerpt of four samples for illustration purposes. We refer to the supplementary material of this work for the full data.

Table 3.B1: Excerpt of XRF data for four samples. Data in column denote weight percentages of major oxides within the rock samples.

Sample	JT01	JT02	JT19	JT20
Oxides				
SiO2	0.6131	0.5981	0.6997	0.6139
TiO2	0.0123	0.0067	0.0076	0.0094
Al2O3	0.1567	0.1873	0.1481	0.1921
Fe2O3	0.087	0.0791	0.0496	0.0686
MnO	0.001	0.0012	0.0009	0.0009
MgO	0.0359	0.0285	0.0206	0.0288
CaO	0.0202	0.0071	0.0201	0.0137
Na2O	0.0228	0.0248	0.0404	0.0323
K2O	0.0343	0.0465	0.0287	0.0469
P2O5	0.0041	0.0029	0.0021	0.0027
Sum	0.9874	0.9822	1.0178	1.0093

There are several challenges to this kind of data. First, the parameters (i.e. the oxide percentages) can take a value between 0 and 1. This means that normal as well as lognormal distributions are not suitable to describe these parameters. Second, the requirement that the sum of all parameters has to ideally equal 1 poses a constraint on this parameter space, which effectively reduces the number of independent parameters by one. Third, due to measurement uncertainties, this sum is never exactly one.

Spaces, which have this unit sum condition can be viewed as a simplex, e.g. if we had three compositional parameters, the simplex would be a 2-dimensional surface (i.e. a subspace) in this 3-dimensional parameter space. The last issue, of not summing up exactly to 1, can be remedied by projecting each sample dataset back to the simplex (Aitchison, 1986, p. 257-261). This works only if the measurement imprecisions are not too large, which works well for the examples in Table 3.B1. With respect to the energy loss calculation, it is preferable to decompose the oxides into elements, which can be done by following formula

$$wt_{ele,i} = \sum_{j \in \{oxides\}} wt_j * \frac{n_{ij} m_i}{m_j}, \tag{3.B8}$$

where m_i and m_j denote the molar mass mass of the i-th element and the j-th oxide, wt_j is the j-th datum in the column and n_{ij} is the number of atoms of the i-th element within the j-th oxide. The two transformations are visualised in Table 3.B2.

Table 3.B2: Element weight percent data. Transformed from oxide weight percent data with use of Eq. (3.B8). All data has additionally been scaled to satisfy the unit sum constraint.

Sample	JT01	JT02	JT19	JT20
Elements				
Si	0.2902	0.2846	0.3213	0.2843
Ti	0.0075	0.0041	0.0045	0.0056
Al	0.0840	0.1009	0.0770	0.1007
Fe	0.0616	0.0563	0.0341	0.0475
Mn	0.0008	0.0009	0.0007	0.0007
Mg	0.0219	0.0175	0.0122	0.0172
Ca	0.0146	0.0052	0.0141	0.0097
Na	0.0171	0.0187	0.0294	0.0237
K	0.0288	0.0393	0.0234	0.0386
P	0.0018	0.0013	0.0009	0.0012
O	0.4716	0.4711	0.4823	0.4707
Sum	1	1	1	1

In order for the data to be in a statistically convenient form, Aitchison (1986) suggests to further transform the data in Table 3.B2 by first forming a ratio with an arbitrary element (in the list) and then taking the logarithm. For the exemplary dataset this is shown in Table 3.B3.

Table 3.B3: Log-ratio of element weight percentages, with respect to oxygen-wt%.

Sample	JT01	JT02	JT19	JT20
Elements				
ln(Si/O)	-0.48531565	-0.50379579	-0.40607778	-0.5042219
ln(Ti/O)	-4.14567399	-4.74687577	-4.68001075	-4.43477381
ln(Al/O)	-1.72531	-1.54064159	-1.83464118	-1.54183733
ln(Fe/O)	-2.03494223	-2.12384752	-2.64974526	-2.29276806
ln(Mn/O)	-6.39894857	-6.21033707	-6.55719484	-6.52451934
ln(Mg/O)	-3.06839321	-3.29293646	-3.67672517	-3.30896536
ln(Ca/O)	-3.47357746	-4.51287533	-3.53142599	-3.88207448
ln(Na/O)	-3.31519303	-3.22481996	-2.79600952	-2.98709658
ln(K/O)	-2.79436382	-2.48376691	-3.0254978	-2.50170175
ln(P/O)	-5.56150947	-5.90149576	-6.28344485	-5.99945492
ln(O/O)	0	0	0	0

The rationale behind this transformation is as follows. The division by an arbitrarily present element effectively transforms the space into an N-1-dimensional open space, where the parameters (i.e. ratios) may have values between 0 and ∞. The subsequent application of the logarithm further changes the space, such that the new parameters can have values between $-\infty$ and ∞. This results in so-called log-ratios, which should ideally be following a multivariate normal distribution. As a consequence, we can calculate the mean log-ratio vector across all samples as well as its corresponding covariance matrix, which completely describes the multivariate normal distribution. In addition to these statistical parameters, the script "compo_analysis.py" outputs a graph, that plots for all samples an order statistic,

z_r, (see Aitchison, 1986). This enables us to visualise how different the data is from a multivariate normal distribution. If equal, they should fall on the red line, shown in Fig. 3.B5.

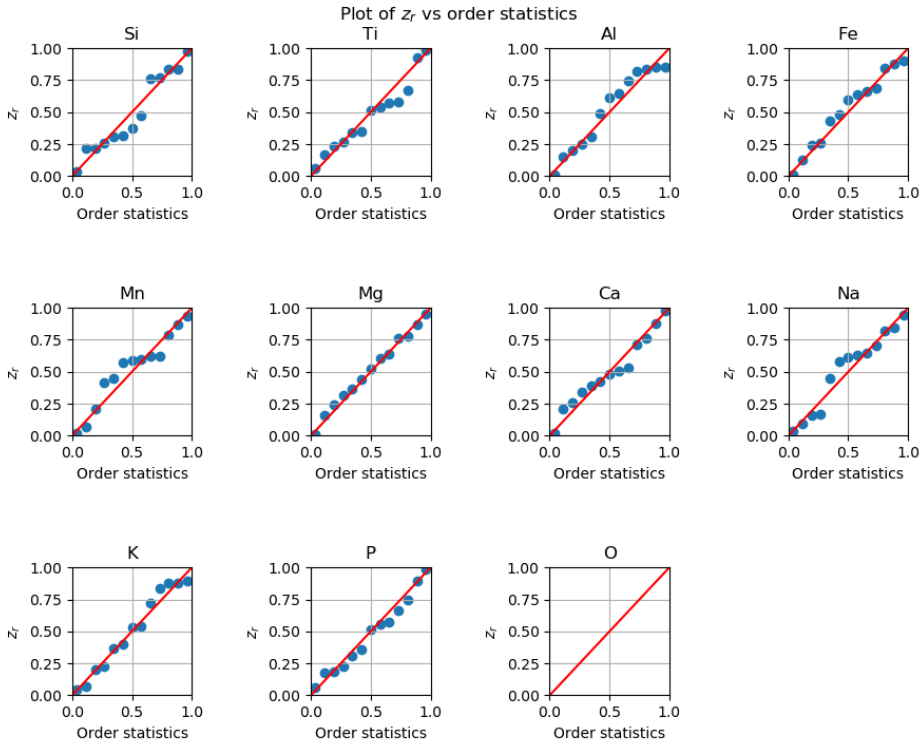

Figure 3.B5: Visual test for multivariate normality of the log-ratio data from Table 3.B3 (This plot shows the full dataset, of which Table 3.B3 is only an excerpt). Each subplot checks for marginal normality. Oxygen is the denominator variable (arbitrarily chosen) and does thus not appear in the plot.

With a graph like Fig. 3.B5 it is possible to check if the multivariate normal distribution is an appropriate model to describe the elemental composition data. For our example that we show in Fig. 3.B5 this looks acceptable, with only slight deviations for silicon, aluminium, manganese and sodium). Once the normality has been verified it is possible to generate random samples from this distribution. For every drawn sample it is then possible to calculate the weight percentages of the single elements by using the inverse formula to the log-ratio transformations

$$wt_{ele,i} = \frac{\exp(r_i)}{1-\sum_{j=1}^{N_{ele}-1}\exp(r_j)}, \tag{3.B9}$$

for all numerator elements and

$$wt_{ele,N_{ele}} = \frac{1}{1-\sum_{j=1}^{N_{ele}-1}\exp(r_j)} \tag{3.B10}$$

for the denominator element (here oxygen). In Eqs. (3.B9) and (3.B10) the r_i denote the log-ratios from Table 3.B3 and N_{ele} is the total number of elements (in Table 3.B2).

3.9.3 B3 – Energy loss equation for rocks

As stated in Eq. (3.7) the energy loss equation for rocks needs parameters that differ from the ones for pure elements. First, the expression for density can directly be exchanged according to the density model (see Appendix B1). Second, it is possible to generate an expression for the average ionisation loss within a rock by exchanging three parameters. Density values that also enter within $\{a\}_{rock}$, can again be directly changed. The average $\{Z/A\}_{rock}$ may be exchanged with the elemental Z/A by using

$$\{Z/A\}_{rock} = \sum_{i=1}^{N_{ele}} wt_{ele,i} * \frac{Z_i}{A_i} . \tag{3.B11}$$

$wt_{ele,i}$ are the weight fractions from Eqs. (3.B9) & (3.B10). Lastly, the mean excitation energy for the rock can be computed by

$$\ln\{I\}_{rock} = \frac{\sum_{i=1}^{N_{ele}} wt_{ele,i} * \frac{Z_i}{A_i} * \ln I_i}{\{Z/A\}_{rock}} . \tag{3.B12}$$

The radiation loss term, however, must be calculated as a weighted radiation energy loss over all elements. This means that the average can be written in a rather concise form,

$$\{\mathrm{b}\}_{\mathrm{rock}} = \sum_{i=1}^{N_{ele}} wt_{ele,i} * b_{ele,i} . \tag{3.B13}$$

3.10 Appendix C – Metropolis Hastings technicalities

This appendix chapter is a short summary of Gelman (2014, p. 284 – 287) and we refer to these pages for a detailed discussion of the calculations. This work presents a concept of how to assess the quality of a MCMC run. In particular, the aforementioned author proposes to analyse two quantities, the potential scale reduction factor $\hat{R}$ and the effective number of simulation draws $\hat{n}_{eff}$ for every parameter of interest. For every chain of a parameter the variance between different chains and within one chain is calculated. The posterior variance of the parameter is then estimated as a weighted average of these two types of variances. Finally, $\hat{R}$ is the quadratic ration between the posterior variance and the variance within one chain. This quantity shows if the various chains have mixed or not, i.e. it explored the same region of the model space. If the posterior variance is much larger than the variances of the single chains, then the chains have not sufficiently explored the same region. Gelman (2014) propose to employ a threshold of 1.1 as a rule of thumb, below which the value of $\hat{R}$ would lie.

One problem that arises in MCMC algorithms is the inherent dependence of one simulation on the one before (this is the definition of a Markov chain). One considers that such a dependence does not introduce a bias if enough samples are drawn. However, this also means, that the effective, independent sample size is much smaller than the number of simulations. Therefore, Gelman (2014) proposes to calculate the effective number of simulation draws, $\hat{n}_{eff}$ in order to assess if one has enough independent samples The underlying idea here is to evaluate the correlations within the chains. An accepted threshold value for this parameter is $5m$, where m is the number of sub-chains. For the calculation of $\hat{R}$ and $\hat{n}_{eff}$ the chains may be cut in half to generate more chains. Note, however, that $\hat{n}_{eff}$ can also be larger, which only means that the simulation standard error decreases. In our example we performed the calculations with two chains and a subdivision of 2, which means that our target quantity is around $20\ (= 5 * 4)$. Most of our thickness parameters have, in fact, a $\hat{n}_{eff} > 100$, with only a few below.

3.11 Appendix D – Construction of the smoothing kernel

As stated in the main text, the user specifies the number of neighbouring pixels s to smooth over. The main idea is to construct a roughly Gaussian smoothing kernel by approximating it with a binomial distribution. With help of the binomial coefficient we can construct a vector of weights with $L = (2 * s + 1)$ entries. The weight vector is then given by

$$w_i = \frac{1}{2^{2*s}}\binom{L-1}{i}, \tag{3.D1}$$

with $i \in \{0, .., L-1\}$. It is now possible to create a matrix by forming the dyadic product of $\vec{w}$ with itself, i.e.

$$K = \vec{w} \otimes \vec{w}, \tag{3.D2}$$

or in index notation,

$$K_{ij} = w_i * w_j . \tag{3.D3}$$

As an example, we show how a smoothing kernel that smooths over two neighbouring pixels (i.e. $s = 2$) is constructed. This is incidentally also the smoothing kernel we used to construct our ice-bedrock interface. The weight vector in this case is given by

$$\vec{w} = \frac{1}{16} * (1 \quad 4 \quad 6 \quad 4 \quad 1) . \tag{3.D4}$$

The weight vectors are, in fact, only the odd rows from Pascal's triangle, interpreted as vectors and normalised by a L1 norm. The smoothing matrix then takes the form

$$K = \frac{1}{256}\begin{pmatrix} 1 & 4 & 6 & 4 & 1 \\ 4 & 16 & 24 & 16 & 4 \\ 6 & 24 & 36 & 24 & 6 \\ 4 & 16 & 24 & 16 & 4 \\ 1 & 4 & 6 & 4 & 1 \end{pmatrix}. \tag{3.D5}$$

3.12 Appendix E – Energy loss calculations for various materials

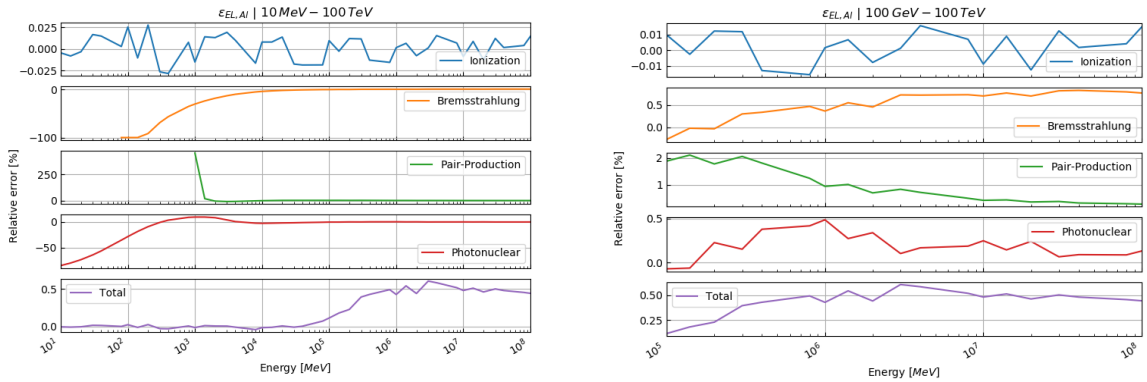

Figure 3.E1: Relative error of our energy loss calculations compared to the tabulated values from Groom et al. (2001) for aluminium in the energy ranges: (left) 10 MeV – 100 TeV, (right) 100 GeV – 100 TeV.

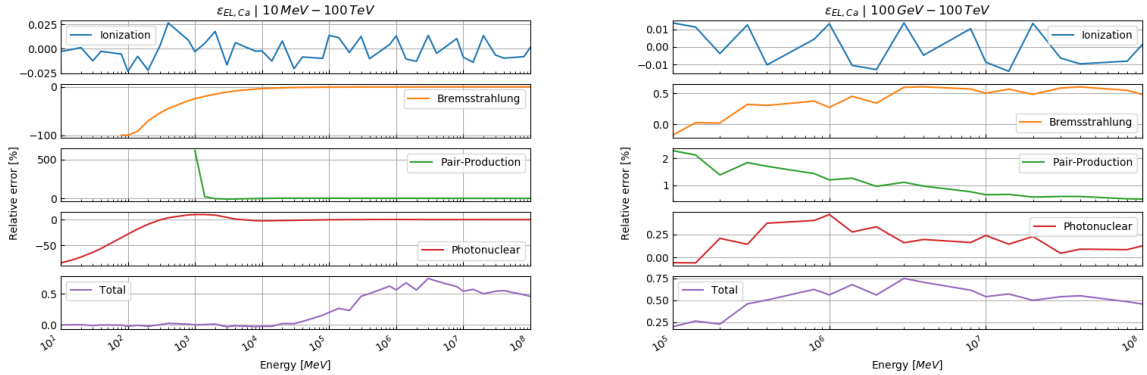

Figure 3.E2: Relative error of our energy loss calculations compared to the tabulated values from Groom et al. (2001) for calcium in the energy ranges: (left) 10 MeV – 100 TeV, (right) 100 GeV – 100 TeV.

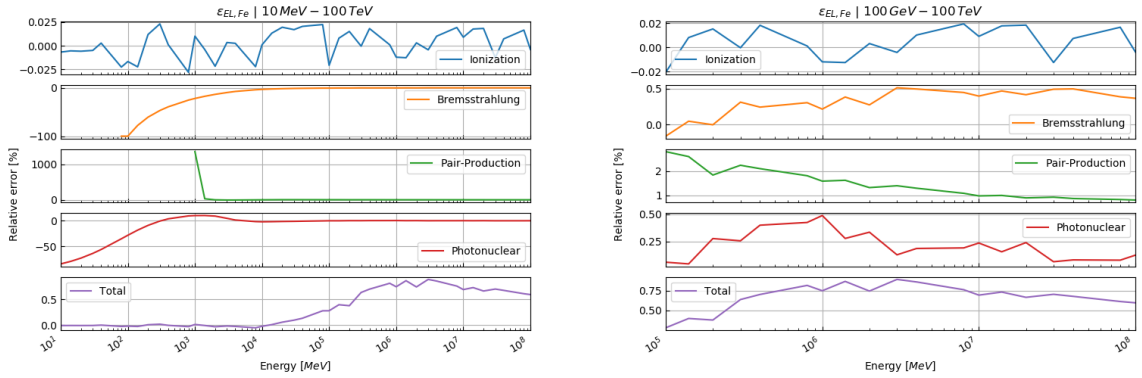

Figure 3.E3: Relative error of our energy loss calculations compared to the tabulated values from Groom et al. (2001) for iron in the energy ranges: (left) 10 MeV – 100 TeV, (right) 100 GeV – 100 TeV.

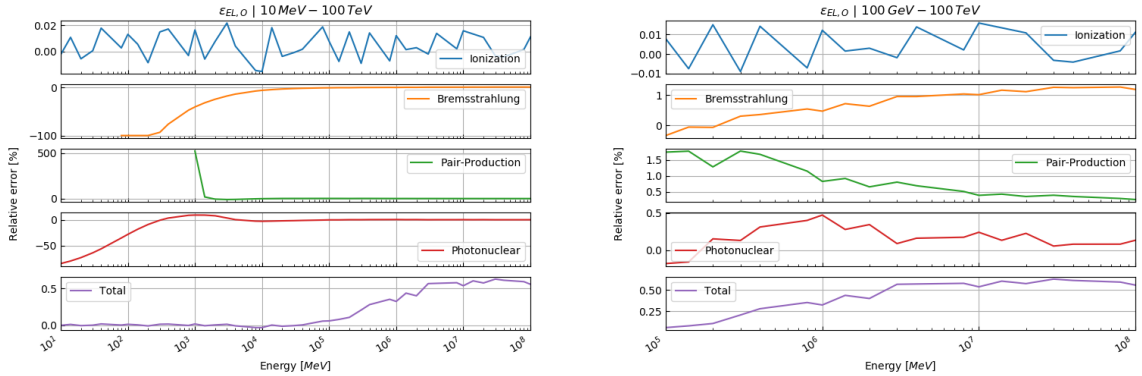

Figure 3.E4: Relative error of our energy loss calculations compared to the tabulated values from Groom et al. (2001) for oxygen in the energy ranges: (left) 10 MeV – 100 TeV, (right) 100 GeV – 100 TeV.

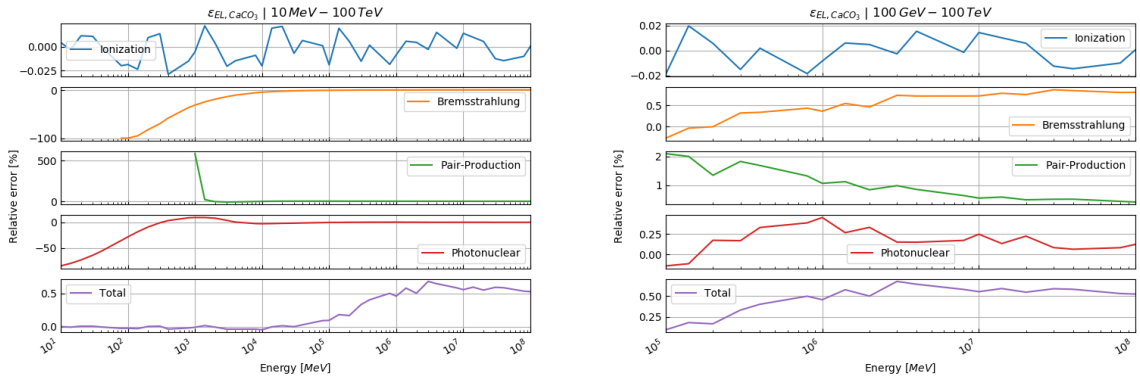

Figure 3.E5: Relative error of our energy loss calculations compared to the tabulated values from Groom et al. (2001) for calcium carbonate (calcite) in the energy ranges: (left) 10 MeV – 100 TeV, (right) 100 GeV – 100 TeV.

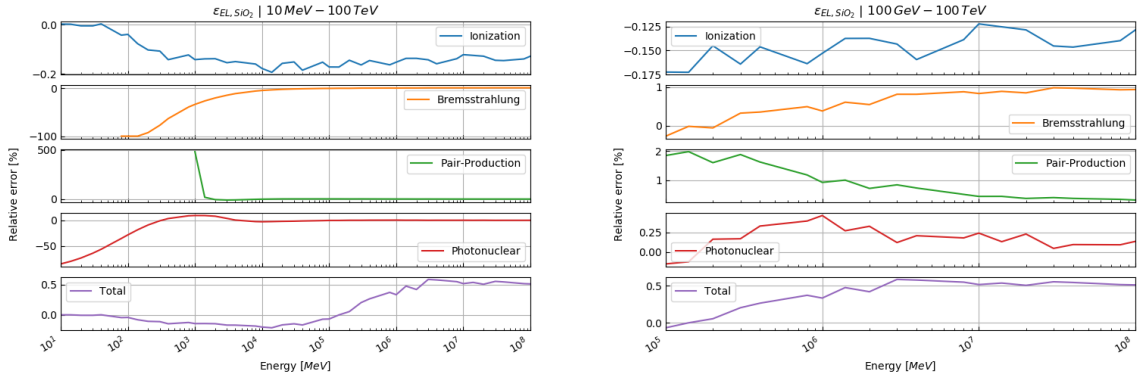

Figure 3.E6: Relative error of our energy loss calculations compared to the tabulated values from Groom et al. (2001) for silicon dioxide (quartz) in the energy ranges: (left) 10 MeV – 100 TeV, (right) 100 GeV – 100 TeV.

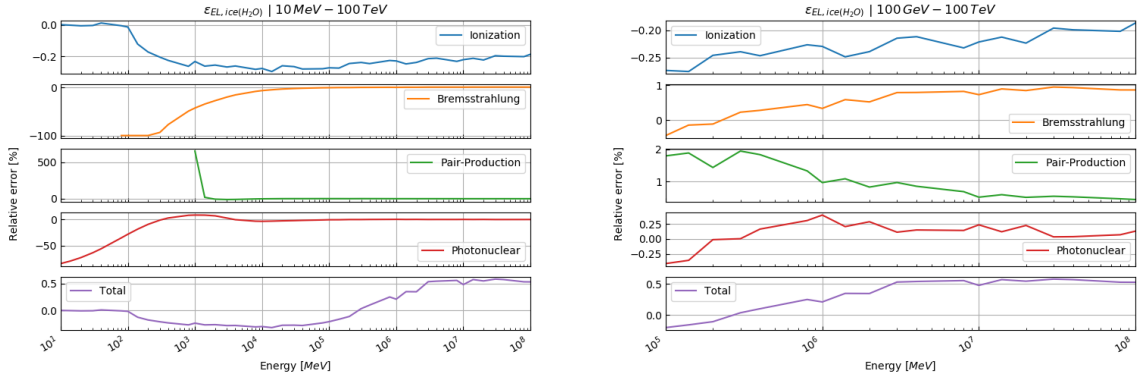

Figure 3.E7: Relative error of our energy loss calculations compared to the tabulated values from Groom et al. (2001) for ice in the energy ranges: (left) 10 MeV – 100 TeV, (right) 100 GeV – 100 TeV.

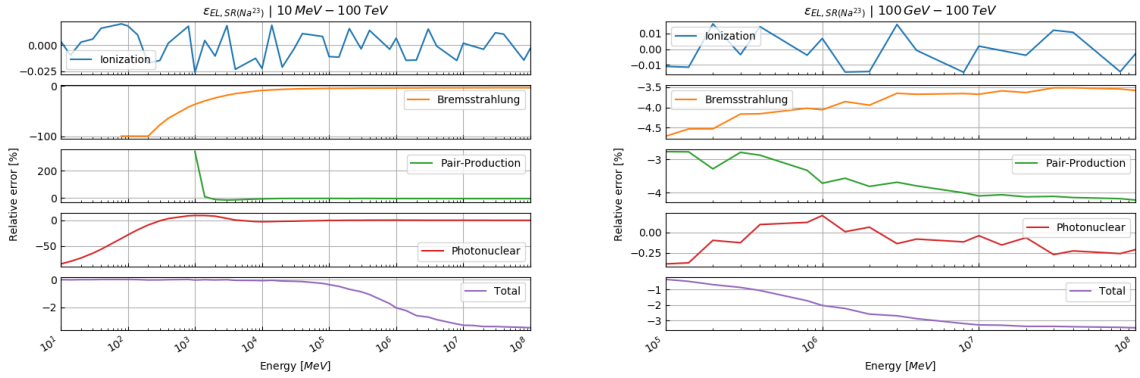

Figure 3.E8: Relative error of our energy loss calculations compared to the tabulated values from Groom et al. (2001) for standard rock ($^{23}_{11}$Na) in the energy ranges: (left) 10 MeV – 100 TeV, (right) 100 GeV – 100 TeV.

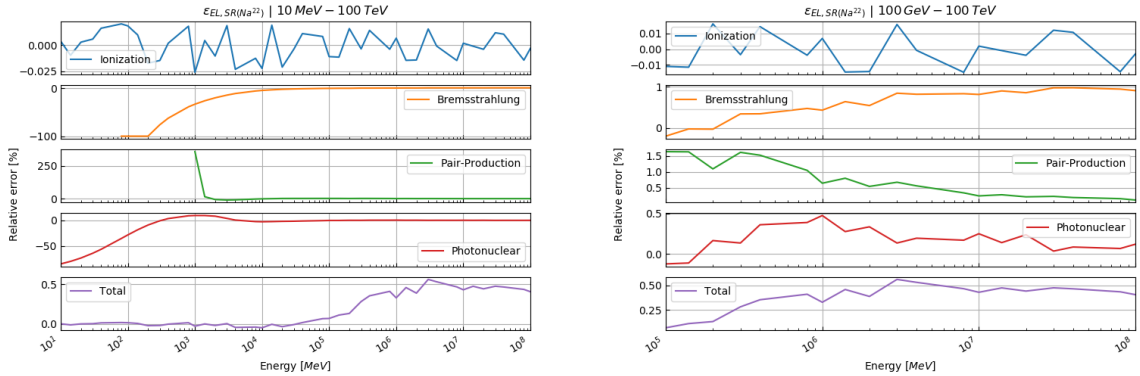

Figure 3.E9: Relative error of our energy loss calculations compared to the tabulated values from Groom et al. (2001) for standard rock ($^{22}_{11}$Na) in the energy ranges: (left) 10 MeV – 100 TeV, (right) 100 GeV – 100 TeV.

3.13 Code availability

The source code of SMAUG 1.0 is publicly and freely available on *https://github.com/ArcticSaru/SMAUG*.

3.14 Data availability

The data for the density and XRF measurements is available on *https://github.com/ArcticSaru/SMAUG.* The raw data from the Nishiyama et al. (2017) paper is publicly and freely available from the publisher's website (Open access).

3.15 Author contributions

AL, FS and AE designed the study

AL developed the code with contributions by MV, CP and RN

AL performed the numerical experiments with support by RN

DM and AL compiled geological data

AA, TA, PS, RN and CP verified the outcome of the numerical experiments

AL wrote the text with contributions from all co-authors

AL designed the figures with contributions by DM

All co-authors contributed to the discussion and finally approved the manuscript

3.16 Competing interests

The authors declare that they have no conflict of interest.

3.17 Acknowledgements

We thank the Swiss National Science Foundation (project No 159299 awarded to F. Schlunegger and A. Ereditato) for their financial support of this research project. Further, we want to thank the Jungfrau Railway Company for their continuing logistic support during our fieldwork in the central Swiss Alps. Finally, we want also to thank the High-Altitude Research Stations Jungfraujoch & Gornergrat for providing us with access to their research facilities and accommodation.

3.18 References

Agostinelli, S., et al.: *Geant4—a simulation toolkit*, Nucl. Instrum. Methods Phys. Res. Sect. Accel. Spectrometers Detect. Assoc. Equip., 506, 250–303, https://doi.org/10.1016/S0168-9002(03)01368-8, 2003.

Aitchison, J.: *The Statistical Analysis of Compositional Data*, Chapman and Hall Ltd, New York, 1986.

Alvarez, L. W., Anderson, J. A., El Bedwei, F., Burkhard, J., Fakhry, A., Girgis, A., Goneid, A., Hassan, F., Iverson, D., Lynch, G., Miligy, Z., Moussa, A. H., Mohammed-Sharkawi, and Yazolino, L.: *Search for Hidden Chambers in the Pyramids*, Science, 167, 832–839, 1970.

Ambrosino, F., Anastasio, A., Basta, D., Bonechi, L., Brianzi, M., Bross, A., Callier, S., Caputo, A., Ciaranfi, R., Cimmino, L., D'Alessandro, R., D'Auria, L., Taille, C. de L., Energico, S., Garufi, F., Giudicepietro, F., Lauria, A., Macedonio, G., Martini, M., Masone, V., Mattone, C., Montesi, M. C., Noli, P., Orazi, M., Passeggio, G., Peluso, R., Pla-Dalmau, A., Raux, L., Rubinov, P., Saracino, G., Scarlini, E., Scarpato, G., Sekhniaidze, G., Starodubtsev, O., Strolin, P., Taketa, A., Tanaka, H. K. M., Vanzanella, A., and Viliani, L.: *The MU-RAY project: detector technology and first data from Mt. Vesuvius*, J. Instrum., 9, C02029–C02029, https://doi.org/10.1088/1748-0221/9/02/C02029, 2014.

Ambrosino, F., Anastasio, A., Bross, A., Béné, S., Boivin, P., Bonechi, L., Cârloganu, C., Ciaranfi, R., Cimmino, L., Combaret, C., D'Alessandro, R., Durand, S., Fehr, F., Français, V., Garufi, F., Gailler, L., Labazuy, P., Laktineh, I., Lénat, J.-F., Masone, V., Miallier, D., Mirabito, L., Morel, L., Mori, N., Niess, V., Noli, P., Pla-Dalmau, A., Portal, A., Rubinov, P., Saracino, G., Scarlini, E., Strolin, P., and Vulpescu, B.: *Joint measurement of the atmospheric muon flux through the Puy de Dôme volcano with plastic scintillators and Resistive Plate Chambers detectors*, J. Geophys. Res. Solid Earth, 120, 7290–7307, https://doi.org/10.1002/2015JB011969, 2015.

Anghel, V., Armitage, J., Baig, F., Boniface, K., Boudjemline, K., Bueno, J., Charles, E., Drouin, P.-L., Erlandson, A., Gallant, G., Gazit, R., Godin, D., Golovko, V. V., Howard, C., Hydomako, R., Jewett, C., Jonkmans, G., Liu, Z., Robichaud, A., Stocki, T. J., Thompson, M., and Waller, D.: *A plastic scintillator-based muon tomography system with an integrated muon spectrometer*, Nucl. Instrum. Methods Phys. Res. Sect. Accel. Spectrometers Detect. Assoc. Equip., 798, 12–23, https://doi.org/10.1016/j.nima.2015.06.054, 2015.

Ariga, A., Ariga, T., Ereditato, A., Käser, S., Lechmann, A., Mair, D., Nishiyama, R., Pistillo, C., Scampoli, P., Schlunegger, F., and Vladymyrov, M.: *A Nuclear Emulsion Detector for the Muon Radiography of a Glacier Structure*, Instruments, 2, 7, https://doi.org/10.3390/instruments2020007, 2018.

ASTM C914-09: *Standard test method for bulk density and volume of solid refractories by wax immersion*, https://doi.org/10.1520/C0914-09R15, 2015.

Barnaföldi, G. G., Hamar, G., Melegh, H. G., Oláh, L., Surányi, G., and Varga, D.: *Portable cosmic muon telescope for environmental applications*, Nucl. Instrum. Methods Phys. Res. Sect. Accel. Spectrometers Detect. Assoc. Equip., 689, 60–69, https://doi.org/10.1016/j.nima.2012.06.015, 2012.

Barnoud, A., Cayol, V., Niess, V., Cârloganu, C., Lelièvre, P., Labazuy, P., and Le Ménédeu, E.: *Bayesian joint muographic and gravimetric inversion applied to volcanoes*, Geophys. J. Int., 218, 2179–2194, https://doi.org/10.1093/gji/ggz300, 2019.

Bellman, R. E.: *Adaptive Control Processes A Guided Tour*, Princeton University Press, Princeton, 2016.

Betancourt, M. J. and Girolami, M.: *Hamiltonian Monte Carlo for Hierarchical Models*, ArXiv13120906 Stat, 2013.

Blake, G. R. and Hartge, K. H.: *Bulk Density*, in: Methods of Soil Analysis: Part 1—Physical and Mineralogical Methods, vol. 9, edited by: Klute, A., American Society of Agronomy and Soil Science Society of America, Madison, 363–375, 1986.

Bugaev, E. V., Misaki, A., Naumov, V. A., Sinegovskaya, T. S., Sinegovsky, S. I., and Takahashi, N.: *Atmospheric Muon Flux at Sea Level, Underground, and Underwater*, Phys. Rev. D, 58, 054001, https://doi.org/10.1103/PhysRevD.58.054001, 1998.

Gelman, A.: *Bayesian data analysis*, Third edition., CRC Press, Boca Raton, 2014.

Gerya, T.: *Introduction to numerical geodynamic modelling*, Cambridge University Press, Cambridge, New York, 2010.

Groom, D. E., Mokhov, N. V., and Striganov, S. I.: *MUON STOPPING POWER AND RANGE TABLES 10 MeV–100 TeV*, At. Data Nucl. Data Tables, 78, 183–356, https://doi.org/10.1006/adnd.2001.0861, 2001.

Guardincerri, E., Rowe, C., Schultz-Fellenz, E., Roy, M., George, N., Morris, C., Bacon, J., Durham, M., Morley, D., Plaud-Ramos, K., Poulson, D., Baker, D., Bonneville, A., and Kouzes, R.: *3D Cosmic Ray Muon Tomography from an Underground Tunnel*, Pure Appl. Geophys., 174, 2133–2141, https://doi.org/10.1007/s00024-017-1526-x, 2017.

Hastings, W. K.: *Monte Carlo sampling methods using Markov chains and their applications*, Biometrika, 57, 97–109, https://doi.org/10.1093/biomet/57.1.97, 1970.

Hebbeker, T. and Timmermans, C.: *A Compilation of High Energy Atmospheric Muon Data at Sea Level*, Astropart. Phys., 18, 107–127, https://doi.org/10.1016/S0927-6505(01)00180-3, 2002.

Jonkmans, G., Anghel, V. N. P., Jewett, C., and Thompson, M.: *Nuclear waste imaging and spent fuel verification by muon tomography*, Ann. Nucl. Energy, 53, 267–273, https://doi.org/10.1016/j.anucene.2012.09.011, 2013.

Jourde, K., Gibert, D., Marteau, J., de Bremond d'Ars, J., and Komorowski, J.-C.: *Muon dynamic radiography of density changes induced by hydrothermal activity at the La Soufrière of Guadeloupe volcano*, Sci. Rep., 6, 33406, https://doi.org/10.1038/srep33406, 2016.

Kjaerulff, U. B. and Madsen, A. L.: *Bayesian Networks and Influence Diagrams: A Guide to Construction and Analysis*, Springer, New York, 2008.

Kudryavtsev, V. A.: *Muon simulation codes MUSIC and MUSUN for underground physics*, Comput. Phys. Commun., 180, 339–346, https://doi.org/10.1016/j.cpc.2008.10.013, 2009.

Kusagaya, T. and Tanaka, H. K. M.: *Development of the very long-range cosmic-ray muon radiographic imaging technique to explore the internal structure of an erupting volcano*, Shinmoe-dake, Japan, Geosci. Instrum. Methods Data Syst., 4, 215–226, https://doi.org/10.5194/gi-4-215-2015, 2015.

Lechmann, A., Mair, D., Ariga, A., Ariga, T., Ereditato, A., Nishiyama, R., Pistillo, C., Scampoli, P., Schlunegger, F., and Vladymyrov, M.: *The effect of rock composition on muon tomography measurements*, Solid Earth, 9, 1517–1533, https://doi.org/10.5194/se-9-1517-2018, 2018.

Lesparre, N., Gibert, D., Marteau, J., Déclais, Y., Carbone, D., and Galichet, E.: *Geophysical muon imaging: feasibility and limits*, Geophys. J. Int., 183, 1348–1361, https://doi.org/10.1111/j.1365-246X.2010.04790.x, 2010.

Lesparre, N., Gibert, D., and Marteau, J.: *Bayesian dual inversion of experimental telescope acceptance and integrated flux for geophysical muon tomography*, Geophys. J. Int., 188, 490–497, https://doi.org/10.1111/j.1365-246X.2011.05268.x, 2012.

Lesparre, N., Cabrera, J., and Marteau, J.: *3-D density imaging with muon flux measurements from underground galleries*, Geophys. J. Int., 208, 1579–1591, https://doi.org/10.1093/gji/ggw482, 2017.

Lo Presti, D., Gallo, G., Bonanno, D. L., Bonanno, G., Bongiovanni, D. G., Carbone, D., Ferlito, C., Immè, J., La Rocca, P., Longhitano, F., Messina, A., Reito, S., Riggi, F., Russo, G., and Zuccarello, L.: *The MEV project: Design and testing of a new high-resolution telescope for muography of Etna Volcano*, Nucl. Instrum. Methods Phys. Res. Sect. Accel. Spectrometers Detect. Assoc. Equip., 904, 195–201, https://doi.org/10.1016/j.nima.2018.07.048, 2018.

Lohmann, W., Kopp, R., and Voss, R.: *Energy Loss of Muons in the Energy Range 1-10000 GeV*, CERN, Geneva, 1985.

Metropolis, N., Rosenbluth, A. W., Rosenbluth, M. N., Teller, A. H., and Teller, E.: *Equation of State Calculations by Fast Computing Machines*, J. Chem. Phys., 21, 1087–1092, https://doi.org/10.1063/1.1699114, 1953.

Morishima, K., Kuno, M., Nishio, A., Kitagawa, N., Manabe, Y., Moto, M., Takasaki, F., Fujii, H., Satoh, K., Kodama, H., Hayashi, K., Odaka, S., Procureur, S., Attié, D., Bouteille, S., Calvet, D., Filosa, C., Magnier, P., Mandjavidze, I., Riallot, M., Marini, B., Gable, P., Date, Y., Sugiura, M., Elshayeb, Y., Elnady, T., Ezzy, M., Guerriero, E., Steiger, V., Serikoff, N., Mouret, J.-B., Charlès, B., Helal, H., and Tayoubi, M.: *Discovery of a big void in Khufu's Pyramid by observation of cosmic-ray muons*, Nature, 552, 386–390, https://doi.org/10.1038/nature24647, 2017.

Nishiyama, R., Tanaka, Y., Okubo, S., Oshima, H., Tanaka, H. K. M., and Maekawa, T.: *Integrated processing of muon radiography and gravity anomaly data toward the realization of high-resolution 3-D density structural analysis of volcanoes: Case study of Showa-Shinzan lava dome, Usu*, Japan, J. Geophys. Res. Solid Earth, 119, 699–710, https://doi.org/10.1002/2013JB010234, 2014.

Nishiyama, R., Ariga, A., Ariga, T., Käser, S., Lechmann, A., Mair, D., Scampoli, P., Vladymyrov, M., Ereditato, A., and Schlunegger, F.: *First measurement of ice-bedrock interface of alpine glaciers by cosmic muon radiography*, Geophys. Res. Lett., 44, 6244–6251, https://doi.org/10.1002/2017GL073599, 2017.

Nishiyama, R., Ariga, A., Ariga, T., Lechmann, A., Mair, D., Pistillo, C., Scampoli, P., Valla, P. G., Vladymyrov, M., Ereditato, A., and Schlunegger, F.: *Bedrock sculpting under an active alpine glacier revealed from cosmic-ray muon radiography*, Sci. Rep., 9, 6970, https://doi.org/10.1038/s41598-019-43527-6, 2019.

Noli, P., Ambrosino, F., Bonechi, L., Bross, A., Cimmino, L., D'Alessandro, R., Masone, V., Mori, N., Passeggio, G., Pla-Dalmau, A., Saracino, G., Scarlini, E., and Strolin, P.: *Muography of the Puy de Dôme*, Ann. Geophys., 60, https://doi.org/10.4401/ag-7380, 2017.

Oláh, L., Barnaföldi, G. G., Hamar, G., Melegh, H. G., Surányi, G., and Varga, D.: *Cosmic Muon Detection for Geophysical Applications*, Advances in High Energy Physics, https://doi.org/10.1155/2013/560192, 2013.

Oláh, L., Tanaka, H. K. M., Ohminato, T., and Varga, D.: *High-definition and low-noise muography of the Sakurajima volcano with gaseous tracking detectors*, Sci. Rep., 8, 3207, https://doi.org/10.1038/s41598-018-21423-9, 2018.

Reyna, D.: *A Simple Parameterization of the Cosmic-Ray Muon Momentum Spectra at the Surface as a Function of Zenith Angle*, arXiv Prepr. hep-ph/0604145 [online] Available from: http://arxiv.org/abs/hep-ph/0604145, 2006.

Rosas-Carbajal, M., Jourde, K., Marteau, J., Deroussi, S., Komorowski, J.-C., and Gibert, D.: *Three-dimensional density structure of La Soufrière de Guadeloupe lava dome from simultaneous muon radiographies and gravity data: 3-D MUON TOMOGRAPHY OF LA SOUFRIÈRE*, Geophys. Res. Lett., 44, 6743–6751, https://doi.org/10.1002/2017GL074285, 2017.

Saracino, G., Amato, L., Ambrosino, F., Antonucci, G., Bonechi, L., Cimmino, L., Consiglio, L., Alessandro, R. D. ', Luzio, E. D., Minin, G., Noli, P., Scognamiglio, L., Strolin, P., and Varriale, A.: *Imaging of underground cavities with cosmic-ray muons from observations at Mt. Echia (Naples)*, Sci. Rep., 7, 1181, https://doi.org/10.1038/s41598-017-01277-3, 2017.

Stoer, J. and Bulirsch, R.: *Introduction to Numerical Analysis*, Springer Science & Business Media, New York, 2013.

Takahasi, H. and Mori, M.: *Double Exponential Formulas for Numerical Integration*, Publ. Res. Inst. Math. Sci., 9, 721–741, https://doi.org/10.2977/prims/1195192451, 1974.

Takamatsu, K., Takegami, H., Ito, C., Suzuki, K., Ohnuma, H., Hino, R., and Okumura, T.: *Cosmic-ray muon radiography for reactor core observation*, Ann. Nucl. Energy, 78, 166–175, https://doi.org/10.1016/j.anucene.2014.12.017, 2015.

Tanabashi, M., et al. (Particle Data Group): *Review of Particle Physics*, Phys. Rev. D, 98, 030001, https://doi.org/10.1103/PhysRevD.98.030001, 2018.

Tanaka, H. K. M.: *Instant snapshot of the internal structure of Unzen lava dome, Japan with airborne muography*, Sci. Rep., 6, 39741, https://doi.org/10.1038/srep39741, 2016.

Tang, A., Horton-Smith, G., Kudryavtsev, V. A., and Tonazzo, A.: *Muon Simulations for Super-Kamiokande, KamLAND and CHOOZ*, Phys. Rev. D, 74, 053007, https://doi.org/10.1103/PhysRevD.74.053007, 2006.

Tarantola, A.: *Inverse Problem Theory and Methods for Model Parameter Estimation*, 1st ed., siam, Philadelphia, 2005.

Thompson, L. F., Stowell, J. P., Fargher, S. J., Steer, C. A., Loughney, K. L., O'Sullivan, E. M., Gluyas, J. G., Blaney, S. W., and Pidcock, R. J.: *Muon tomography for railway tunnel imaging*, Phys. Rev. Res., 2, 023017, https://doi.org/10.1103/PhysRevResearch.2.023017, 2020.

Tioukov, V., Lellis, G. D., Strolin, P., Consiglio, L., Sheshukov, A., Orazi, M., Peluso, R., Bozza, C., Sio, C. D., Stellacci, S. M., Sirignano, C., D'Ambrosio, N., Miyamoto, S., Nishiyama, R., and Tanaka, H. K. M.: *Muography with nuclear emulsions - Stromboli and other projects*, Ann. Geophys., 60, 0111, https://doi.org/10.4401/ag-7386, 2017.

Chapter 4

The effect of rock composition on muon tomography measurements

Alessandro Lechmann[1], David Mair[1], Akitaka Ariga[2], Tomoko Ariga[3], Antonio Ereditato[2], Ryuichi Nishiyama[2], Ciro Pistillo[2], Paola Scampoli[2,4], Mykhailo Vladymyrov[2], and Fritz Schlunegger[1]

[1]Institute of Geological Sciences, University of Bern, Bern, CH-3012, Switzerland
[2]Albert Einstein Center for Fundamental Physics, Laboratory for High Energy Physics, University of Bern, Bern, CH-3012, Switzerland
[3]Faculty of Arts and Science, Kyushu University, Fukuoka, J-812-8582, Japan
[4]Dipartimento di Fisica "E.Pancini", Università di Napoli Federico II, Napoli, I-80126, Italy

Published in: Solid Earth, 9, 1517-1533, https://doi.org/10.5194/se-9-1517-2018, 2018.

4.1 Abstract

In recent years, the use of radiographic inspection with cosmic-ray muons has spread into multiple research and industrial fields. This technique is based on the high-penetration power of cosmogenic muons. Specifically, it allows the resolution of internal density structures of large scale, geological objects through precise measurements of the muon absorption rate. So far, in many previous works, this muon absorption rate has been considered to depend solely on the density of traversed material (under the assumption of a standard rock) but the variation in chemical composition has not been taken seriously into account. However, from our experience with muon tomography in Alpine environments we find that this assumption causes a substantial bias on the muon flux calculation, particularly where the target consists of high $\{Z^2/A\}$ rocks (like basalts and limestones) and where the material thickness exceeds 300 metres. In this paper, we derive an energy loss equation for different minerals and we additionally derive a related equation for mineral assemblages that can be used for any rock type on which mineralogical data are available. Thus, for muon tomography experiments in which high $\{Z^2/A\}$ rock thicknesses can be expected, it is advisable to plan an accompanying geological field campaign to determine a realistic rock model.

4.2 Introduction

The discovery of the muon (Neddermeyer and Anderson, 1937) entailed experiments to characterise its propagation through different materials. The fact that muons lose energy proportionally to the mass density of the traversed matter (see Olive et al., 2014) inspired the idea of using their attenuation to retrieve information on the traversed material. This was first done by George (1955) for the estimation of the overburden upon building of a tunnel, and then later by Alvarez et al. (1970) to search for hidden chambers in the pyramids at Giza (Egypt). In a related study, Fujii et al. (2013) employed this technology to locate the reactor of a nuclear power plant. Recently, Morishima et al. (2017) successfully accomplished quest of Alvarez' team in the Egyptian Pyramids.

Besides these applications, which have mainly been designed for archaeological and civil engineering purposes, scientists have begun to deploy particle detectors to investigate and map geological structures. In recent years this has been done for various volcanoes in Japan (Nishiyama et al., 2014; Tanaka et al., 2005, 2014), including Shinmoe-dake volcano (Kusagaya and Tanaka, 2015), the lava dome at Unzen (Tanaka, 2016) and most recently Sakurajima volcano (Oláh et al., 2018). Further experiments have been conducted in the Caribbean, in France (Ambrosino et al., 2015; Jourde et al., 2013, 2015; Lesparre et al., 2012; Marteau et al., 2015) and in Italy on Etna (Lo Presti et al., 2018) and Stromboli (Tioukov et al., 2017). Recently, Barnaföldi et al. (2012) used this technology to examine karstic caves in the Hungarian mountains. Our group is presently carrying out an experimental campaign in the Central Swiss Alps for the purpose of imagining glacier-bedrock interfaces (Nishiyama et al., 2017).

Inferences about subsurface structures from observed muon flux (i.e. the number of recorded muons normalised by the exposure time and the detector acceptance) necessitate a comparison of the measurement data with muon flux simulations for structures with various densities. Such a simulation consists of a cosmic-ray muon energy spectrum model and a subsequent transportation of these muons through matter. The former describes the abundance of cosmic-ray muons for different energies and zenith angles at the surface of the earth. This has been well documented in literature (see for example Lesparre et al., 2010). The differences between models and experimental data, hence the systematic model uncertainty, can be as large as 15 % for vertical muons (Hebbeker and Timmermans, 2002). On the other hand, the attenuation of the muon flux is assumed to depend only on the density of the traversed material. In this context, however, potential effects of its chemical composition have not been taken into account specifically. Instead, previous works employ a certain representative rock, so-called “standard rock”, for which the rate of muon energy loss has been tabulated (e.g. Groom et al., 2001).

The origin of this peculiar rock type can be traced back to Hayman et al. (1963), Miyake et al. (1964), Mandò and Ronchi (1952) and George (1952), who gave slightly different definitions of its physical parameters (mass density ρ, atomic weight A and atomic number Z). A comprehensive compilation thereof can be found in Table 1 of Higashi et al. (1966). Various corrections to the energy loss equation were then added in the framework of following-up studies, which particularly includes a density effect correction (see for example Sternheimer et al., 1984). Richard-Serre (1971) listed data relevant for muon attenuation for: (i) soil from the CERN (European Organization for Nuclear Research) premises near Geneva (Switzerland), (ii) Molasse-type material (e.g. Matter et al., 1980) and (iii) a “rock” that equals the one from Hayman et al. (1963). These latter authors assigned additional energy loss parameters to this particular rock type, which were similar to those of pure quartz. Lohmann et al. (1985) then adjusted these parameters to energy loss variables for calcium carbonate (i.e. calcite) and gave the standard rock its present shape. In summary, this fictitious material consists of a density of crystalline quartz (i.e. $\rho_{qtz} = 2.65\ g\ cm^{-3}$), a Z and A of 11 and 22, respectively (which is almost sodium), and density effect parameters that have been measured on calcium carbonate.

However, when the material's Z and A differ greatly from standard rock parameters as for carbonates, basalts or peridotites, a substantial bias would be introduced to the calculation of the muon flux. Such a situation is easily encountered in geological settings such as the European Alps where igneous intrusions, thrusted and folded sedimentary covers and recent Quaternary deposits are found in close vicinity (e.g. Schmid et al., 1996). Currently, our collaboration is performing a muon tomography experiment in the Jungfrau region, in the Central Swiss Alps aiming at imaging the glacier-bedrock interface (Ariga et al., 2018; Nishiyama et al., 2017). There, we face a variety of lithologies ranging from gneissic to carbonatic rocks that have a thickness larger than 500 m (Mair et al., 2018). In this context, it turned out that the analyses based on the standard rock assumption might cause an over- or an underestimation of the bedrock position in the related experiment. Such an uncertainty arising from the chemical composition of the actual rock has to be reduced at least to the level of the statistical uncertainty inherent in the measurement as well as in the systematic uncertainty of the muon energy spectrum model.

To achieve this, we investigate how different rock types potentially influence the results of a muon tomographic experiment. We particularly compare the lithologic effect on simulated data with standard rock data to estimate a systematic error that is solely induced by a too simplistic assumption on the composition of the bedrock.

4.3 Methods

4.3.1 Rock types

In this study, we chose 10 different rock types that cover the largest range of natural lithologies, spanning the entire range from igneous to sedimentary rocks. The simplest rocks have a massive fabric in the sense that they do not exhibit any planar or porphyric texture. Typical lithologies with these characteristics are igneous rocks or massive limestones (not sandstones as they might have a planar fabric such as laminations and ripples). Exemplary thin sections of a granite and a limestone are shown in Fig. 4.1. Note that rocks featuring strong heterogenic, metamorphic textures are not treated in the framework of this study for simplicity purposes and will be subject of future research. Also, for simplicity purposes, we do not consider spatial variations in crystal sizes in our calculations (i.e. a porphyric texture). We justify this approach because a related inhomogeneity is likely to be averaged out if one considers a several metre-thick rock column. Additionally, the rock is considered to consist only of crystalline components, i.e. glassy materials such as obsidian have to be treated separately. Porous media can be approximated by assigning one of the constituents as air or (in the case of a pore fluid) water. This is explicitly done for the case of arkoses (10% air) and arenites (11% air).

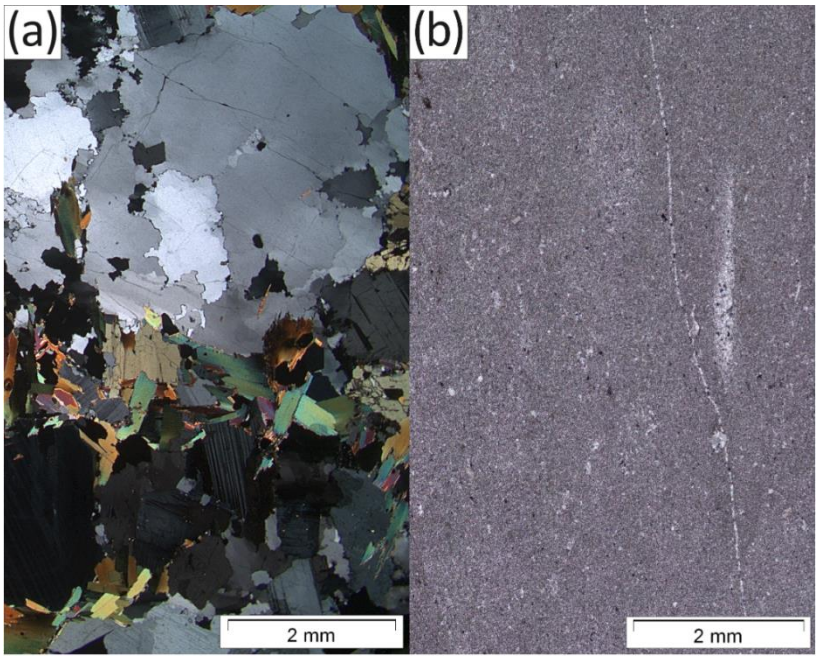

Figure 4.1: Thin-sections of two representative types of rock in crossed polarised light: (a) Granite, (b) Limestone. The crystal sizes are generally below 4 mm - 5 mm and a few orders of magnitude smaller in the limestone.

We compare the energy loss of muons in these rocks and hence the resultant muon flux attenuation depending on depth with those of the standard rock. The analysed lithologies, together with their relevant physical parameters, are listed in Table 4.1. Among these parameters, $\{Z/A\}$ and $\{Z^2/A\}$, i.e. the ratio of the atomic number (and its square) to the mass number averaged over the entire rock, are most relevant to the energy loss of muons (Groom et al., 2001). The former is almost proportional to the ionisation energy loss that occurs predominantly at low energies, whereas the latter is mostly proportional to the radiation energy loss, that becomes dominant for muons faster than their critical energy at around $600\ GeV$. The volumetric mineral fractions of these ten rocks can be found in Appendix A (Ch. 4.6).

Table 4.1: Physical parameters of the ten studied rock types and of standard rock.

Rock	Density $[g\ cm^{-3}]$	{Z/A}	$\{Z^2/A\}$	$\{Z^2/A\}/\{Z/A\}$	{I} $[eV]$
Standard rock	2.650	0.5000	5.500	11.0	136.40
Igneous rocks					
Granite/Rhyolite	2.650	0.4968	5.615	11.30	145.09
Andesite/Diorite	2.812	0.4960	5.803	11.70	147.77
Gabbro/Basalt	3.156	0.4945	6.258	12.66	154.91
Peridotite	3.340	0.4955	5.788	11.68	149.98
Sedimentary rocks					
Arkose	2.347	0.4980	5.563	11.17	143.73
Arenite (Sandstone)	2.357	0.4993	5.392	10.80	141.04
Shale	2.512	0.4993	5.384	10.78	139.09
Limestone	2.711	0.4996	6.275	12.56	136.40
Dolomite	2.859	0.4989	5.423	10.87	127.65
Aragonite	2.939	0.4996	6.275	12.56	136.40

4.3.2 Cosmic ray flux model

We perform our calculations with the muon energy spectrum model proposed by Reyna (2006), at sea level and for vertical incident muons. This model describes the kinetic energy distribution of the muons before they enter the rock. The calculation of the integrated muon flux after having crossed a certain amount of material is done in two steps. First, the minimum energy required for muons to penetrate a given thickness of rock is calculated considering the chemical composition effects (see Sect. 4.2.3). Afterwards, the energy spectrum model, dF/dE, is integrated above the obtained minimum energy (which we call from here on "cut-off energy", E_{cut}) to infinity, i.e.

$$F_{calc} = \int_{E_{cut}}^{\infty} \frac{dF(E)}{dE}\, dE\ . \tag{4.1}$$

The integration is necessary as most detectors, which have been used for muon tomography, record only the integrated muon flux. As already stated in the introduction, we attribute a systematic uncertainty of $\pm$ 15 % to the integrand dF/dE. All the calculations in this work have been verified with another flux model (Tang et al., 2006) and are presented in the supplementary material.

4.3.3 Muon propagation in rocks

As soon as muons penetrate a material, they start to interact with the material's electrons and nuclei and lose part of their kinetic energy. The occurring processes can be categorised into an ionisation process, i.e. a continuous interaction with the material's electrons, and radiative interactions with the material's nuclei (i.e. bremsstrahlung, electron-positron pair production and photonuclear processes), which are of a stochastic nature. All these processes are governed by the material density ρ and the atomic number Z and atomic weight A (see Groom et al., 2001 for details). Our general strategy for the calculation of the energy loss in a rock is to use its decomposition into energy losses for the corresponding minerals. Accordingly, the energy loss of muons travelling a unit length, dE/dx, in a rock can be described by a volumetrically averaged energy loss through its mineral constituents

$$\left\{\frac{dE_{rock}}{dx}\right\} = \sum_j \varphi_j \left\langle \frac{dE_{mineral,j}}{dx} \right\rangle , \tag{4.2}$$

where φ_j is the volumetric fraction of the j-th mineral within the rock. The derivation of Eq. (4.2) can be found in Appendix B (Ch. 4.7).

In order to exploit this abstraction efficiently we have to assume a homogeneous mineral distribution within the rock. This is a strong simplification, considering for example effects related to a local intrusion, tectonic processes like folding and thrusting, or spatial differences in sedimentation patterns. These concerns can be addressed through averaging over a large enough volume. Figure 4.1 shows two typical thin-sections from rock samples of our experimental site that exhibit crystal sizes well below 4 mm - 5 mm. As muon tomography for geological purposes generally operates at scales of 10 m - 1000 m it is safe to assume that small-scale variations are averaged out. Thus, the term on the right-hand side of Eq. (4.2), i.e. the energy loss across each mineral, can be written as

$$-\langle\frac{dE_{mineral}}{dx}\rangle = \rho_{mineral} * (\langle a\rangle + E * \langle b\rangle)\,, \tag{4.3}$$

where $\langle a\rangle$ and $\langle b\rangle$ are the ionisation and radiative energy losses across a given mineral, respectively. These two parameters are in turn calculated by averaging the contribution of each element (i.e. atom) constituting the mineral by their mass (see Eq. (4.B5) to Eq. (4.B15) in Appendix B (Ch. 4.7) for details). The density of the minerals, ρ_{mineral}, is estimated from its crystal structures (see Appendix A (Ch. 4.6) for more detailed instructions). Once the energy losses are obtained for all minerals, each contribution is summed up according to Eq. (4.2). The energy loss within the rock can then be expressed in a similar way, as in Eq. (4.3), (for a detailed discussion we refer to Appendix B, Ch. 4.7):

$$-\left\{\frac{dE_{rock}}{dx}\right\} = \rho_{rock} * (\{a\} + E * \{b\})\,. \tag{4.4}$$

Again, the values $\{a\}$ and $\{b\}$ indicate the averaged ionisation and radiative energy losses across the whole rock, respectively. Equation (4.4), an ordinary nonlinear differential equation, is usually given as a final value problem, i.e. we know that the muon, after having passed through the rock column, still needs some energy to penetrate the detector, E_{det}. This can be turned into an initial value problem, by reversing the sign of Eq. (4.4) and defining the detector energy threshold as initial condition.

$$\left\{\frac{dE_{rock}}{dx}\right\} = \rho_{rock} * (\{a\} + E * \{b\}) \tag{4.5}$$

$$E(x = 0) = E_{det}$$

The problem has been transformed into the one of finding the final energy, the cut-off energy, E_{cut}, after a predefined thickness of rock. This is a well investigated problem, for which a great variety of numerical solvers are available. In this work we employ a standard Runge-Kutta integration scheme (see for example Stoer and Bulirsh, 2002).

The energy loss equations are subject to systematic uncertainties, mainly because the experimentally determined interaction cross sections have an attributed error. According to Groom et al., (2001), the error on ionisation losses is "mostly smaller than 1 % and hardly ever greater than 2 %". These authors also state, that in the case of compounds the uncertainties might be thrice as large. Therefore, we considered an ionisation loss uncertainty of $\pm$ 6 % as appropriate for our calculations. The errors on the cross sections of bremsstrahlung, pair-production and photonuclear interactions are $\pm$ 1 %, $\pm$ 5 % and $\pm$ 30 %, respectively. Appendix C (Ch. 4.8) shows in detail how we propagated these errors to the cut-off energy, E_{cut}.

4.4 Results

Figures 4.2 and 4.3 show the muon flux simulations as a function of rock thicknesses up to 2 km for igneous and sedimentary rocks, respectively. The depth-intensity relation is described by a power law, as it is the integration of the differential energy spectrum of muons, which also follows a power law.

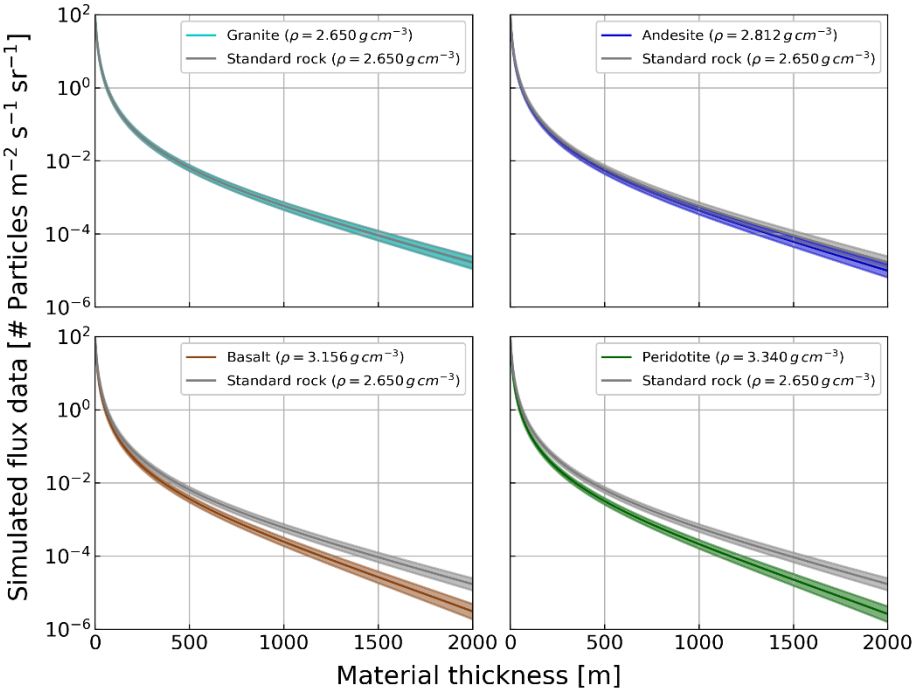

Figure 4.2: Simulated muon intensity vs. thickness of the four igneous rocks from Table 4.1 and standard rock. The mean flux is indicated by a bold line and 1 σ bounds are indicated by the shaded area.

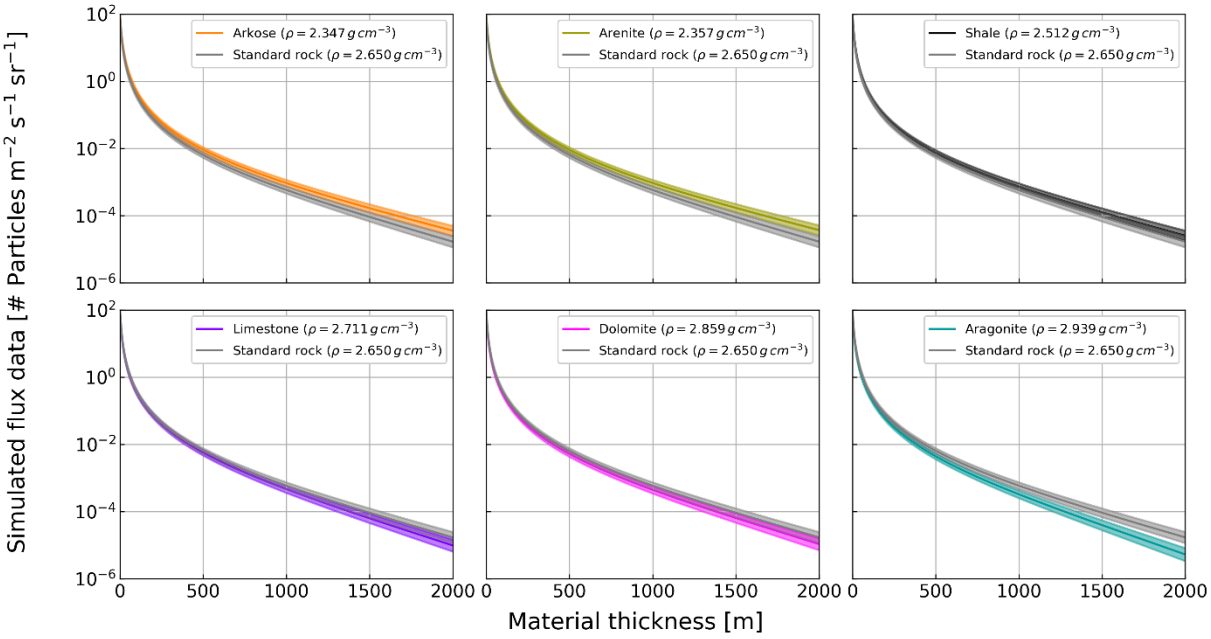

Figure 4.3: Simulated muon intensity vs. thickness of the six sedimentary rocks from Table 4.1 and standard rock. The mean flux is indicated by a bold line and 1 σ bounds are indicated by the shaded area.

To better visualise the difference between the fluxes after having passed these ten rock types and the standard rock, we report the ratio between fluxes calculated after the different materials and that after the standard rock in Fig. 4.4:

$$fr_{rock} = \frac{F_{calc,rock}}{F_{calc,SR}}. \quad (4.6)$$

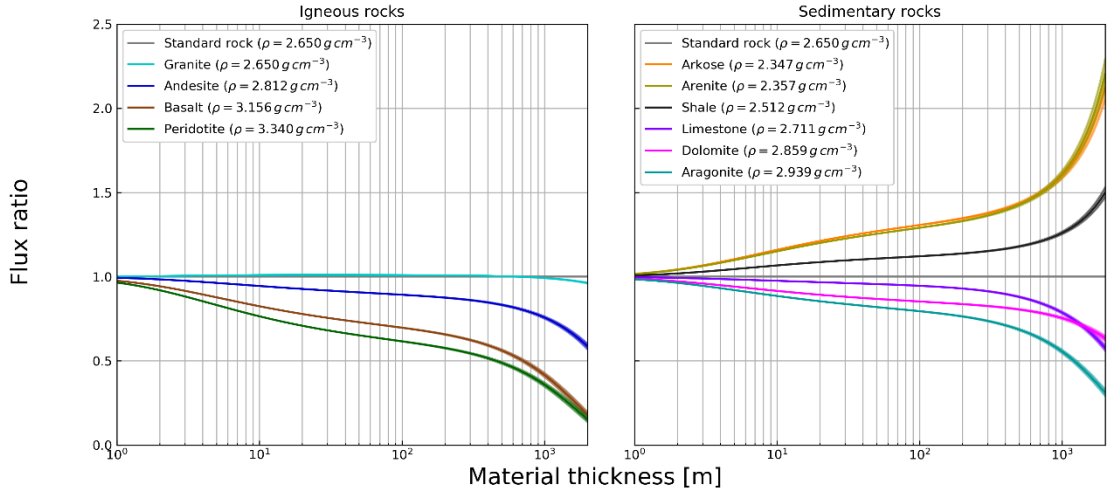

Figure 4.4: Ratio of the calculated rock fluxes to a standard rock ($\rho_{SR} = 2.650\ g\ cm^{-3}$) muon flux for the rocks reported in Table 4.1 as a function of rock thickness.

in Figs. 4.2 to 4.4. Rocks exhibiting a high material density result in a larger muon flux attenuation than lithologies with a lower density. This however, only depicts the overall differences, including density and compositional variations, between real and standard rock. In this regard, Groom et al. (2001) apply an explicit treatment of density variations of known materials. Thus, the flux data can be simulated for a standard rock with the exact density as its real counterpart. Such a density normalisation enables us to isolate the compositional influence on the computed data. Figures 4.5 and 4.6 show the muon flux simulations for each rock compared to a density normalised standard rock and Fig. 4.7 summarises this information by representing the ratio between muon fluxes after passing through real rocks and the muon flux after passing through a density normalised standard rock. It is important to note that the standard rock muon flux in each flux ratio has been normalised with respect to the density of the original rock (i.e. the peridotite is compared to a standard rock of density ρ = 3.340 $g\ cm^{-3}$, the limestone is comparted to a standard rock of density ρ = 2.711 $g\ cm^{-3}$, etc.).

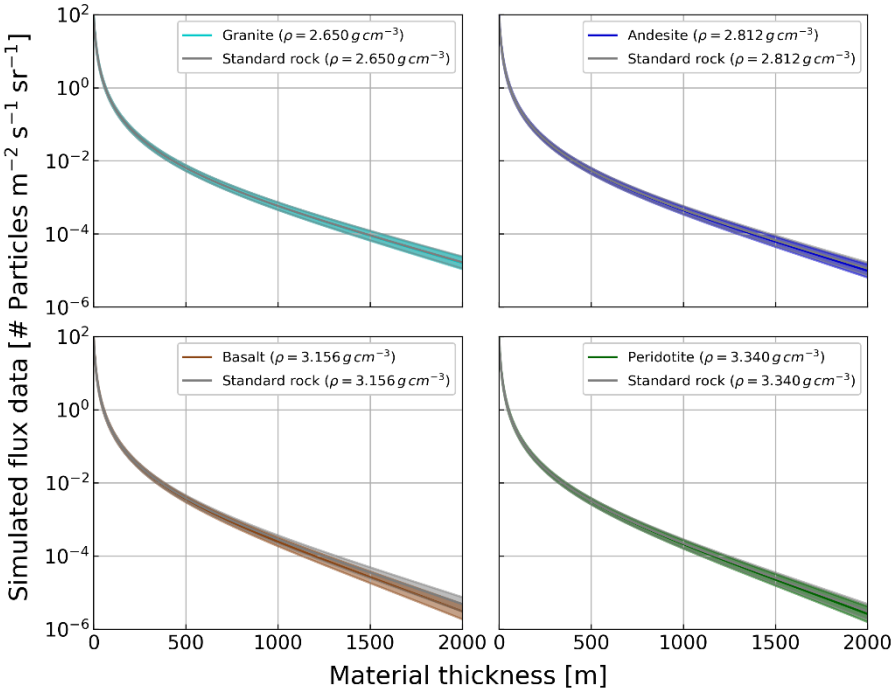

Figure 4.5: Simulated muon intensity vs. thickness of the four igneous rocks from Table 4.1 and a density modified standard rock. The mean flux is indicated by a bold line and 1 σ bounds are indicated by the shaded area.

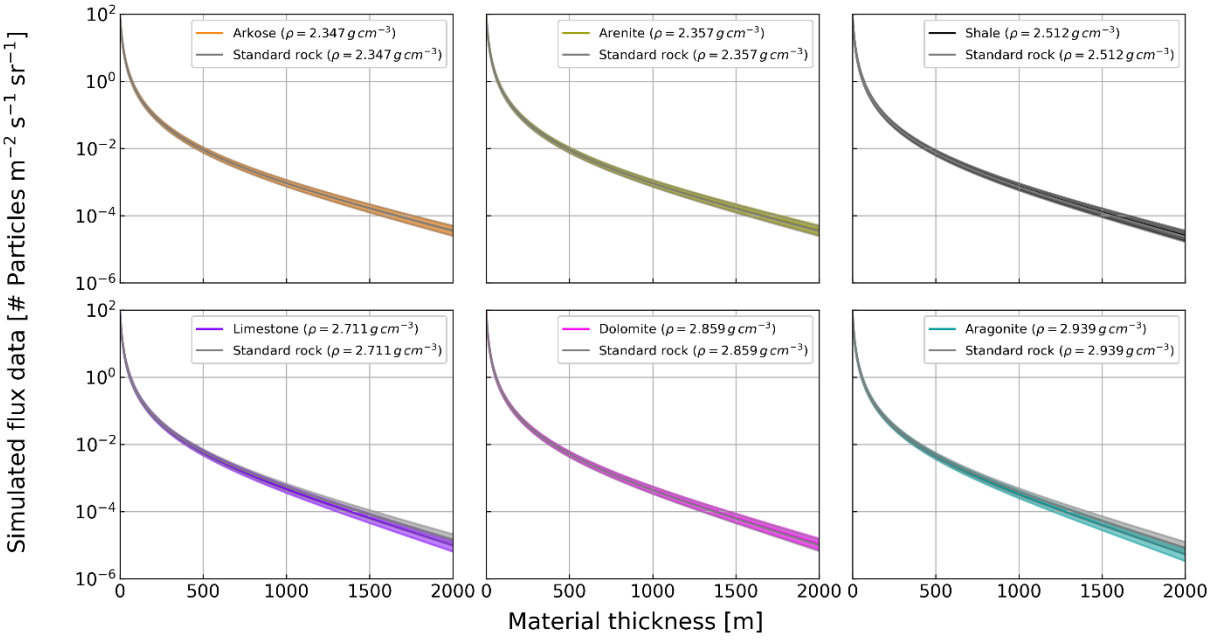

Figure 4.6: Simulated muon intensity vs. thickness of the six sedimentary rocks from Table 4.1 and a density modified standard rock. The mean flux is indicated by a bold line and 1 σ bounds are indicated by the shaded area.

One notices that the flux ratios are rather close together, mainly within 2.5 % of the standard rock flux, before they start to diverge towards larger (dolomite, shale and arenite) and smaller (igneous rocks, arkose, limestone and aragonite) flux ratios beyond 300 m thickness of penetrated rock. Even though the errors on the fluxes are relatively large and sometimes even overlap with the standard rock fluxes, the propagated errors on the flux ratios remain well bounded near their means. This effect is due to the correlation of the errors in the numerator and the denominator in Eq. (4.6). A detailed discussion of how uncertainties have been propagated is presented in Appendix C (Ch. 4.8).

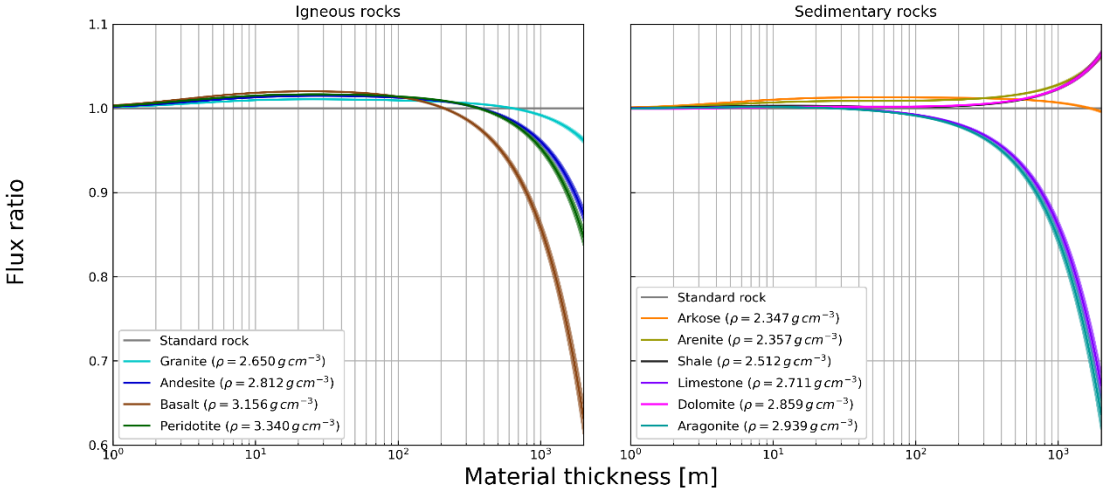

Figure 4.7: Ratio of the simulated rock fluxes to a standard rock muon flux with the same density as the rock ($\rho_{SR} = \rho_{Rock}$) for all the lithologies in Table 4.1 as a function of rock thickness.

4.5 Discussion

The differences in the calculated muon flux illustrated in Figs. 4.2 and 4.3 become even more pronounced in Fig. 4.4, where the fluxes are compared to the case where cosmic fluxes are attenuated by a standard rock. One notices a direct correlation with material density. This is reinforced by the fact that the granite (Fig. 4.2) has the same density as the standard rock, 2.650 $g\ cm^{-3}$, and shows an overall similar flux magnitude as the standard rock, i.e. a flux ratio of 1. This can be explained by Eq. (4.4), as the energy loss is almost directly proportional to the density, while the presence of density in the ionisation loss term (i.e. $\{a(E, \rho, A, Z)\}$) is negligible compared to this factor. Thus, if the rock flux data are compared to a standard rock with equal density, this effect should be removed, and one is left with the composition difference only.

A closer look at Fig. 4.7 reveals that the muon fluxes for every rock below 300 m do not depart more than 2.5 % from their respective density modified standard rock flux. The chemical composition effect can thus be considered negligible when compared to the systematic uncertainty originating from the muon flux model. We explain this through the dominance of the ionisation energy loss in this thickness region. Muons that penetrate down to 300 m of rock are still slow enough to predominantly lose their kinetic energy for the ionisation of the rock's electrons. As the number of electrons per unit volume is given by the product: $\rho_{rock} * \{Z/A\}$, ionisation losses are proportional to this term. When comparing a

density normalised standard rock with a real rock, the only difference can emerge from the second part, i.e. $\{Z/A\}$. According to Table 4.1, these values do not change more than 1 % with respect to each other.

When the rock thicknesses become larger than 300 m, the flux ratios start to exceed $\pm$ 2.5 % and the ratio patterns diverge. This corresponds to the point where radiative losses start to become the dominant energy loss processes. The latter are interactions of the muon with the nuclei of the atoms within the rock and its cross section is mainly proportional to the square of the nucleus' charge (i.e. $\{Z^2/A\}$). Hence, rocks that exhibit a lower $\{Z^2/A\}$-value than a standard rock (e.g. dolomite, arenite and shale) attenuate the muon flux less (i.e. flux ratio > 1), while all igneous rocks as well as limestone, aragonite and arkose, that have a higher $\{Z^2/A\}$-value attenuate the muon flux more, which results in a lower flux ratio.

The above results reflect only the most striking connections to the chemical composition of a rock. In reality however, the nature of muonic energy loss processes is much more complex than the shape of the flux ratios in Fig. 4.4 below 300 m suggests. The actual ionisation energy loss, Eq. (4.B27), is an interplay of the mean excitation energy $\{I\}$, i.e. the mean energy needed to ionise a material's electrons, the material density ρ_{rock} , $\{Z/A\}$ and various correction terms that depend on these parameters. These additional factors are also responsible for the non-linear behaviour of the flux ratios between 100 m and around 600 m, as effects from radiative losses start to become significant. However, as the resulting differences due to these processes remain smaller than 2.5%, a detailed discussion of these matters falls beyond the scope of this paper.

As we see above, the muon flux calculation is significantly biased when one employs the standard rock assumption and thus neglects the effect of the chemical composition, especially when the thickness of the rock is beyond 300 m. This systematic error would then later turn into an over- or an underestimation in the assessment of density structures. We can roughly estimate the error on a thickness estimation of a certain structure, by employing the following formula

$$\varepsilon_d\big(x_{ro}(F)\big) = \frac{x_{SR}(F) - x_{Ro}(F)}{x_{Ro}(F)}\,. \tag{4.7}$$

Here, $x_{SR}(F)$ and $x_{Ro}(F)$ denote the thickness of standard rock and a real rock respectively, needed to attenuate the cosmic ray muon flux to F. This is possible because the flux, as a function of rock thickness, is a strictly decreasing function. The domain of this function ranges from zero to infinite thickness, where its image takes the values from the initial flux, F_0, to zero. On these two sets the function is a bijection and therefore an inverse function, $x(F)$, exists. Although its functional form might be unknown, it is still possible to interpolate between the simulated points. For our rocks, this is shown in Fig. 4.8.

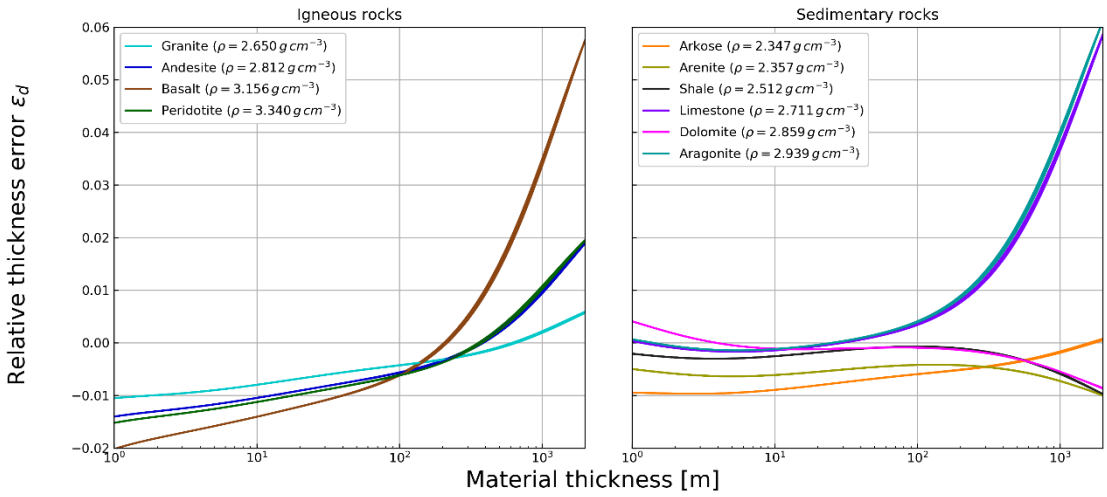

Figure 4.8: Relative error, which is made in the thickness estimation of a block of rock by assuming a density modified standard rock versus the actual rock thickness.

As an example, in case where the target is 600 m thick and made of limestone ($\rho = 2.711\ g\ cm^{-3}$), the standard rock assumption underestimates the flux by 7 % – 8 % and thus overestimates the thickness by around 15 m or 2.5 %. The same is valid for basalt and aragonite.

The above discussion concentrates on calculations of the mean values of model parameters. A full description encloses also the propagation of their uncertainties. The rather large error bounds on single flux calculations stems from the uncertainties in the flux model and in the interaction cross-sections. However, by taking a ratio, i.e. Eq. (4.6), of quantities with correlated errors, the resulting uncertainty on the ratio tends to cancel out. If the errors were propagated by linear operations, they would even cancel out perfectly. The small error-bars which are still present in Figs. 4.4, 4.7 and 4.8 can be seen as effects of the nonlinearity in the differential equation, Eq. (4.5).

Because this is a pure sensitivity study, we cannot offer distinct measurements to verify our predictions. The reason for this is mainly because dedicated experimental campaigns have not yet been conducted and thus such data are not available. We suggest that future studies in this field will address the composition issue and try to experimentally constrain this theoretical model. Nevertheless, our inferences are based on the same conceptual framework that has already been used for other materials, including standard rock. As a result of this, we find significant differences if the rock parameters are changed, especially for rock thicknesses larger than 300 m.

4.6 Conclusions

Our results suggest that it is safe to use the standard rock approximation for all rock types up to thicknesses of ~300 m, as the flux ratio will mainly remain within 2.5 % of the standard rock flux, which generally lies within the cosmic ray flux model error. However, we also find that beyond these thicknesses the use of the standard rock approximation and its density-modified version could lead to a serious bias. This mainly concerns basaltic and carbonate rocks. The flux error for these rock types increases with growing material thickness. It can be extrapolated, that the errors grow even further beyond 600 m of material thickness up to a point where any inference based upon this approximation becomes difficult. This is, however, a thickness range where muon tomography becomes increasingly hard to perform, as lower fluxes have to be counterbalanced by larger detectors and longer exposure times.

In order to account for the composition of rock, it is advisable to undertake a geological study of the region alongside the muon tomography measurements, especially when faced with basaltic rocks or carbonates, which includes at the least the analysis of local rock samples. Auxiliary data could comprise rock density measurements (i.e. He-pycnometer or buoyancy experiments), chemical composition, and mineralogical information (i.e. X-Ray diffractometry/fluorescence measurements) as well as microfabric analyses (i.e. mineral and fabric identification on thin sections). This additional information may help to constrain solutions of a subsequent inversion to a potentially smaller set. The use of additional information, such as spatial information in the form of a geological map or a 3D model of the geologic architecture, is strongly encouraged, because it might greatly improve the state of knowledge about the physical parameters that are to be unravelled.

4.7 Appendix A – Rock compositions

To estimate the mineral density, we assume that it can be calculated by dividing the mass of the atoms within the crystal unit cell by the volume of the latter (see for example Borchart-Ott, 2009):

$$\rho_{mineral} = \frac{Q*M}{N_A*V_{Unit\ Cell}} . \tag{4.A1}$$

In this equation, M is the total molar mass of one mineral "formula unit", Q is the number of formula units per unit cell and $V_{Unit\ Cell}$ is the volume of the unit cell. The latter is calculated by the volume formula of a parallelepiped:

$$V_{Unit\ Cell} = \left\| \vec{a} \cdot \left(\vec{b} \times \vec{c} \right) \right\| . \tag{4.A2}$$

Eq. (4.A2) can be rewritten as

$$V_{Unit\ Cell} = \|\vec{a}\| \left\|\vec{b}\right\| \|\vec{c}\| \sqrt{1 + 2\cos(\alpha)\cos(\beta)\cos(\gamma) - \cos^2(\alpha) - \cos^2(\beta) - \cos^2(\gamma)} . \tag{4.A3}$$

Here, $\vec{a}, \vec{b}, \vec{c}$ denote the unit cell vectors, their lengths, $\| \cdot \|$ is measured in Ångströms, i.e. $10^{-10}\ m$, whereas α, β, γ are the internal angles between those vectors. These six parameters can be looked up for each mineral in the crystallographic literature (e.g. Strunz and Nickel, 2001).

Table 4.A1: Volumetric percentages of the rock forming minerals within six sedimentary rocks. Qtz: Quartz, Or: Orthoclase, Ab: Albite, An: Anorthite, Cal: Calcite, Dol: Dolomite, Kln: Kaolonite, Mnt: Montmorillonite, Ill: Illite, Clc: Clinochlore

Mineral	Arkose	Arenite	Shale	Limestone	Dolomite	Aragonite
Qtz	56.0	89.0	17.0			
Or	34.0		2.5			
Ab			1.8			
An			0.7			
Cal				100.0		100.0
Dol					100.0	
Kln			1.7			
Mnt			52.7			
Ill			22.2			
Clc			1.4			
Air	10.0	11.0				

Table 4.A2: Volumetric percentages of the rock forming minerals within four igneous rocks. Qtz: Quartz, Or: Orthoclase, Ab: Albite, An: Anorthite, Phl: Phlogopite, Ann: Annite, Mg-Hbl: Magnesium hornblende, Fe-Hbl: Iron hornblende, Aug: Augite, En: Enstatite, Fs: Ferrosilite, Fo: Forsterite, Fa: Fayalite, Jd: Jadeite, Hd: Hedenbergite, Di: Diopside, Spl: Spinel, Hc: Hercynite

Mineral	Granite	Andesite	Basalt	Peridotite
Qtz	36.1	11.7		
Or	28.2			
Ab	27.3	37.7	17.7	
An		25.3	24.6	
Phl	2.95	4.5		
Ann	2.95	2.1		
Mg-Hbl	2.25	4.2		
Fe-Hbl	2.25	6.4		
Aug		8.1	33.8	
En			11.4	18.4
Fs			11.1	2.0
Fo			0.6	60.4
Fa			0.8	7.9
Jd				1.8
Hd				0.3
Di				8.0
Spl				0.9
Hc				0.3

The volumetric percentages of the minerals that constitute the 10 investigated rock types are shown in Table 4.A1 and Table 4.A2. They were chosen as a reasonable compromise from literature values (e.g. Best, 2003; Tuttle and Bowen, 1958; Folk, 1980).

4.8 Appendix B – Energy loss in geological materials

4.8.1 Energy loss in elements

The average spatial differential energy loss can be written in a rather simple form (Barrett et al., 1952):

$$-\left(\frac{dE(\rho,A,Z)}{dx}\right) = \rho * \big(a(E,\rho,A,Z) + E * b(E,A,Z)\big) . \quad (4.B1)$$

Here, ρ, A, Z denote the mass density, atomic weight and atomic number of the penetrated material, while E is the kinetic energy of the penetrating, charged particle and x is the position coordinate. The function $a(E,\rho,A,Z)$ in Eq. (4.B1) is the differential ionisation energy loss that accounts for the ionisation of electrons of the penetrated material. In the case of incident muons (i.e. electric charge $q_\mu = -1\ C$ and mass $m_\mu = 105.7\ MeV/c^2$), the relationship expressed in Eq. (4.B1) takes the form:

$$a(E,\rho,A,Z) = K\frac{Z}{A}\frac{1}{\beta^2}\left[\frac{1}{2}ln\left(\frac{2m_e c^2\beta^2\gamma^2 Q_{max}(E)}{I(Z)^2}\right) - \beta^2 - \frac{\delta(\rho,Z,A)}{2} + \frac{1}{8}\frac{Q^2_{max}(E)}{\left(\gamma m_\mu c^2\right)^2}\right] + \Delta\left|\frac{dE}{dX}\right|(Z,A) . \quad (4.B2)$$

In this equation, β, γ are the relativistic factors and are, therefore, a function of the kinetic energy E. The constant m_e denotes the mass of the electron and c is the speed of light. Q_{max} is the highest possible kinetic recoil energy of scattered electrons in the medium, while K is a constant incorporating information about the electron density. The function $\delta(\rho,Z,A)$ is a correction factor, which considers the mechanisms where the material becomes polarised at higher muon energies, with the consequence that the energy loss is weaker (Sternheimer, 1952). The last term in Eq. (4.B2) is another correction factor, which considers bremsstrahlung from atomic electrons (not the incident muon, which would be the term in Eq. 4.3) that also appears at higher muon energies. A more detailed explanation of this equation and its parameters can for example be found in Olive et al., 2014. In contrast to Eq. (4.B2), the function $b(E,A,Z)$ describes all the radiative processes that become dominant at higher velocities (above $\sim 600\ GeV\ c^{-1}$ for muons). This term includes energy losses due to bremsstrahlung, electron-positron pair production as well as photonuclear interactions. These different contributions can be written independently from each other:

$$b(E,A,Z) = b_{brems}(E,A,Z) + b_{pair}(E,A,Z) + b_{photonucl}(E,A,Z) . \quad (4.B3)$$

Each process in Eq. (4.B3) is computed by integrating its differential cross-section with respect to every possible amount of transferred energy:

$$b_{process} = \frac{N_A}{A}\int_0^1 \frac{d\sigma_{process}}{d\nu}\,d\nu . \quad (4.B4)$$

Here, N_A is the Avogadro number and $\nu = \varepsilon/E$ the fractional energy loss (whereas ε is the absolute energy loss) for this process. Specific cross-sections for bremsstrahlung (Kelner et al., 1995, 1997), photonuclear (Bezrukov and Bugaev, 1981) and pair-production (Nikishov, 1978) energy losses are used by Groom et al. (2001) for the calculations of their tables. As this pair-production cross-section involves the calculation of many computationally extensive dilogarithms, an equivalent cross-section (Kelner,

1998; Kokoulin and Petrukhin, 1969, 1971), which is used in GEANT4 (Agostinelli et al., 2003) by default, is used in our study.

4.8.2 Energy loss in minerals

Since the above equations are valid for pure elements, adjustments are needed for compounds (e.g. minerals) and mixtures thereof (e.g. rocks). Generally, it is advised to use the physical parameters for materials that have already been measured (see Seltzer and Berger, 1982 for a compilation). However, except for calcium carbonate (i.e., calcite) and silicon dioxide (i.e. quartz), no other minerals have been investigated. This also means that there is no standard approach available for considering natural rocks. Fortunately, for such materials a theoretical framework has been proposed (see for example Appendix A of Groom et al., 2001). The basic idea is to consider the compound as a single "weighted average"-material and the energy loss therein as a mass weighted average of its constituents' energy loss:

$$\langle\frac{dE_{mineral}}{d\chi}\rangle = \sum_i w_i \left(\frac{dE_{element,i}}{d\chi}\right). \tag{4.B5}$$

The weights w_i are calculated according to the atomic weights A_i of the elements

$$w_i = \frac{n_i A_i}{\sum_k n_k A_k} = \frac{m_{element,i}}{m_{mineral}}, \tag{4.B6}$$

and can then be used to calculate an average $\langle Z/A\rangle$ value

$$\langle\frac{Z}{A}\rangle = \sum_i w_i \frac{Z_i}{A_i}. \tag{4.B7}$$

Equivalently, the average $\langle Z^2/A\rangle$ value can be calculated according to

$$\langle\frac{Z^2}{A}\rangle = \sum_i w_i \frac{Z_i^2}{A_i}. \tag{4.B8}$$

One more change must be made to the ionisation loss Eq. (4.B2) in order to appropriately account for the change in the atomic structure that emerged due to chemical bonding of the elementary constituents. This is reflected in a modified mean excitation energy $\langle I\rangle$, which can be calculated by taking the exponential of the function

$$ln\langle I\rangle = \frac{\sum_i w_i \frac{Z_i}{A_i} ln(I_i)}{\sum_j w_j \frac{Z_j}{A_j}}, \tag{4.B9}$$

which is basically a weighted geometric average of the elementary mean excitation energies

$$\langle I\rangle = \sqrt[\sum_j w_j \frac{Z_j}{A_j}]{\prod_i I_i^{w_i \frac{Z_i}{A_i}}}. \tag{4.B10}$$

One has to pay attention that the mean excitation energies for some elements, I_i, can change quite significantly when they are part of a chemical bond. A guideline to address this issue can be found in

Seltzer and Berger (1982). Equations (4.B7) to (4.B10) are still a consequence of Eq. (4.B5). However, there is one term in the function $\delta(\rho, Z/A)$ in Eq. (B2) that is calculated differently from Eq. (4.B5). This concerns the logarithm of the plasma energy of the compound, which for an element is given by (e.g. Olive et al., 2014):

$$ln(\hbar\omega_p) = ln\left(28.816 * \sqrt{\rho \frac{Z}{A}}\right). \tag{4.B11}$$

According to Eq. (4.B5) the plasma energy for a compound should be calculated the same way as the mean excitation energy in Eq. (4.B9). However, Sternheimer et al. (1982) and Fano (1963) explicitly advise us to use the arithmetic mean within the logarithm when dealing with an atomic mixture (i.e. a molecule), yielding

$$ln\langle\hbar\omega_p\rangle = ln\left(28.816\sqrt{\rho_{mineral}\,\langle\frac{Z}{A}\rangle}\right). \tag{4.B12}$$

This results in the modified ionisation energy loss:

$$\langle a(E, \rho_{mineral}, A, Z)\rangle = K\,\langle\frac{Z}{A}\rangle\frac{1}{\beta^2}\left[\frac{1}{2}ln\left(\frac{2m_e c^2\beta^2\gamma^2 Q_{max}(E)}{\langle I(Z)\rangle^2}\right) - \beta^2 - \frac{\delta\left(\rho_{mineral}, \langle\frac{Z}{A}\rangle\right)}{2} + \frac{1}{8}\frac{Q_{max}^2(E)}{\left(\gamma m_\mu c^2\right)^2}\right] + \Delta\left|\frac{dE}{dX}\right|\left(\langle\frac{Z}{A}\rangle\right) . \tag{4.B13}$$

The radiation loss for the compound, on the other hand, is only a linear combination of the radiation losses of its elementary constituents, Eq. (4.B3), yielding:

$$\langle b\rangle = \sum_i w_i b_i . \tag{4.B14}$$

The resulting Eq. (4.B15)

$$-\langle\frac{dE_{mineral}}{dx}\rangle = \rho_{mineral} * (\langle a\rangle + E * \langle b\rangle), \tag{4.B15}$$

has now the same form as the energy loss Eq. (4.B1) for elements and can be solved accordingly.

4.8.3 Energy loss in rocks

To obtain an energy loss equation for rocks, a similar procedure as for forming minerals through the assembly of elements can be applied. Starting from Eq. (4.B5) we consider the energy loss for a rock as mass weighted average of the energy losses of its mineral constituents

$$\left\{\frac{dE_{rock}}{d\chi}\right\} = \sum_j q_j\,\langle\frac{dE_{mineral,j}}{d\chi}\rangle, \tag{4.B16}$$

where q_j are the mass fractions of the j-th mineral within the rock, analogous to Eq. (4.B6),

$$q_j = \frac{n_j A_j}{\sum_l n_l A_l} = \frac{m_{mineral,j}}{m_{rock}} . \tag{4.B17}$$

Using $d\chi = \rho * dx$, Eq. (4.B16) then takes the following form:

$$\frac{1}{\rho_{rock}}\left\{\frac{dE_{rock}}{dx}\right\} = \sum_j \frac{q_j}{\rho_{mineral,j}} \langle \frac{dE_{mineral,j}}{dx} \rangle \,. \tag{4.B18}$$

By inserting Eq. (4.B17) into Eq. (4.B18), one obtains

$$\frac{1}{\rho_{rock}}\left\{\frac{dE_{rock}}{dx}\right\} = \frac{1}{m_{rock}} \sum_j \frac{m_{mineral,j}}{\rho_{mineral,j}} \langle \frac{dE_{mineral,j}}{dx} \rangle \,. \tag{4.B19}$$

Multiplying both sides with ρ_{rock} and applying the definition of the density, $\rho = m/v$, that can also be written as $v = m/\rho$, Eq. (4.B19) becomes

$$\left\{\frac{dE_{rock}}{dx}\right\} = \frac{1}{v_{rock}} \sum_j v_{mineral,j} \langle \frac{dE_{mineral,j}}{dx} \rangle \,. \tag{4.B20}$$

If one sets $\varphi_j = v_{mineral,j}/v_{rock}$, the volumetric fraction of the j-th mineral within the rock, Eq. (4.B20) transforms into the compound equation for rocks

$$\left\{\frac{dE_{rock}}{dx}\right\} = \sum_j \varphi_j \langle \frac{dE_{mineral,j}}{dx} \rangle \,. \tag{4.B21}$$

Analogue to the mineral case we can now define new average energy loss parameters for the rock, beginning with its overall density

$$\rho_{rock} = \sum_j \varphi_j \rho_{mineral,j} \,. \tag{4.B22}$$

The average $\{Z/A\}$ is given by

$$\left\{\frac{Z}{A}\right\} = \sum_j \frac{\rho_{mineral,j}}{\rho_{rock}} \varphi_j \langle \frac{Z}{A} \rangle_j \tag{4.B23}$$

and similarly, the average $\{Z^2/A\}$ can be calculated according to

$$\left\{\frac{Z^2}{A}\right\} = \sum_j \frac{\rho_{mineral,j}}{\rho_{rock}} \varphi_j \langle \frac{Z^2}{A} \rangle_j \,. \tag{4.B24}$$

The rock's mean excitation energy is

$$ln\{I\} = \frac{\sum_j \frac{\rho_{mineral,j}}{\rho_{rock}} \varphi_j \langle \frac{Z}{A} \rangle_j ln\langle I \rangle_j}{\sum_l \frac{\rho_{mineral,l}}{\rho_{rock}} \varphi_l \langle \frac{Z}{A} \rangle_l} \,. \tag{4.B25}$$

The only difference between the rock calculation and the mineral calculation enters in the calculation of the plasma energy. While in the mineral case we were advised to use Eq. (4.B11) instead of what would naturally follow from the weighted average in Eq. (4.B5), we prefer to use the weighted average, Eq. (4.B21),

$$ln\{\hbar\omega_p\} = \frac{\sum_j \frac{\rho_{mineral,j}}{\rho_{rock}} \varphi_j \langle \frac{Z}{A} \rangle_j ln\langle \hbar\omega_p \rangle_j}{\sum_l \frac{\rho_{mineral,l}}{\rho_{rock}} \varphi_l \langle \frac{Z}{A} \rangle_l} \tag{4.B26}$$

for the case of rocks. The reason for this lies in the fact that the density effect operates on a nanometric scale, whereas minerals, have generally sizes between several micrometres and a few centimetres. In the case of a mineral compound, the molecular structure comprises also a nanometric scale.

These parameters can then be rearranged into an ionisation loss term for a rock

$$\{a(E,\rho_{rock},A,Z)\} = K\left\{\frac{Z}{A}\right\}\frac{1}{\beta^2}\left[\frac{1}{2}ln\left(\frac{2m_e c^2\beta^2\gamma^2 Q_{max}(E)}{\{I(Z)\}^2}\right) - \beta^2 - \frac{\delta\left(\rho_{rock},\left\{\frac{Z}{A}\right\}\right)}{2} + \frac{1}{8}\frac{Q_{max}^2(E)}{\left(\gamma m_\mu c^2\right)^2}\right] + \Delta\left|\frac{dE}{dX}\right|\left(\left\{\frac{Z}{A}\right\}\right). \quad (4.B27)$$

Like Eq. (4.B14) the radiative losses can be rewritten as a weighted average of the mineral radiative losses

$$\{b\} = \sum_j \frac{\rho_{mineral,j}}{\rho_{rock}}\varphi_j\langle b\rangle_j \,. \quad (4.B28)$$

Equations. (4.B27) and (4.B28) can then be joined together to form again a similar term to Eqs. (4.B1) and (4.B15),

$$-\left\{\frac{dE_{rock}}{dx}\right\} = \rho_{rock} * (\{a\} + E * \{b\}) \,, \quad (4.B29)$$

the energy loss equation for rocks.

We want to stress that the starting point of the derivation of the energy loss equation for rocks is a mass averaging of mineral energy losses. Therefore, the mass averaging approach is inherently included in this approach. In fact, mass averaging and volumetric averaging are two equivalent descriptions of the same problem. For the mass averaged formulae we refer to the supplementary material to this manuscript.

4.9 Appendix C – Uncertainty propagation

The first step in our uncertainty treatment includes a propagation of the interaction cross section errors ($\sigma_a = \pm 6\,\%, \sigma_{b_{brems}} = \pm 1\,\%, \sigma_{b_{pair}} = \pm 5\,\%, \sigma_{b_{photonucl}} = \pm 30\,\%$) to the cut-off energy, i.e. by solving the differential equation Eq. (4.5). Generally, a higher cross section yields a higher cut-off energy, as the muon needs more initial kinetic energy, which it then loses on the way and vice-versa. In order to estimate a lower and an upper error bound on the cut-off energy, E_{cut}, we use a conservative approach. This means that the lower cut-off energy error bound is calculated by setting all cross sections to their lower 1 σ bound and running the simulation with these modified values. The upper error bound is calculated accordingly. Of course, this overestimates the effective error, however if our calculations remain valid within this conservative error, then they can also be trusted with a conventional error.

The second step is the estimation of the error regarding the integrated flux. Here we need to propagate the errors through Eq. (4.1) to the simulated flux. There are two different errors present at this stage. The first one includes the error on the lower integration boundary, i.e. E_{cut}, which has just been calculated above. The second error addresses the integrand, i.e. the flux model. Figure 4.C1 visualises the concept behind the propagation of these two errors. The simulated flux error is equivalent to the error, which is made by calculating the area under the graphs. We estimate the lower error bound on the simulated flux (i.e. smallest area), by taking the upper error bound on E_{cut} and the lower error bound on dF/dE. Similarly, the upper error bound on the simulated flux (i.e. largest area) is calculated by setting E_{cut} to its lower error bound and dF/dE to its upper error bound. Again, this is a conservative approach, which we justify with the same rationale as above.

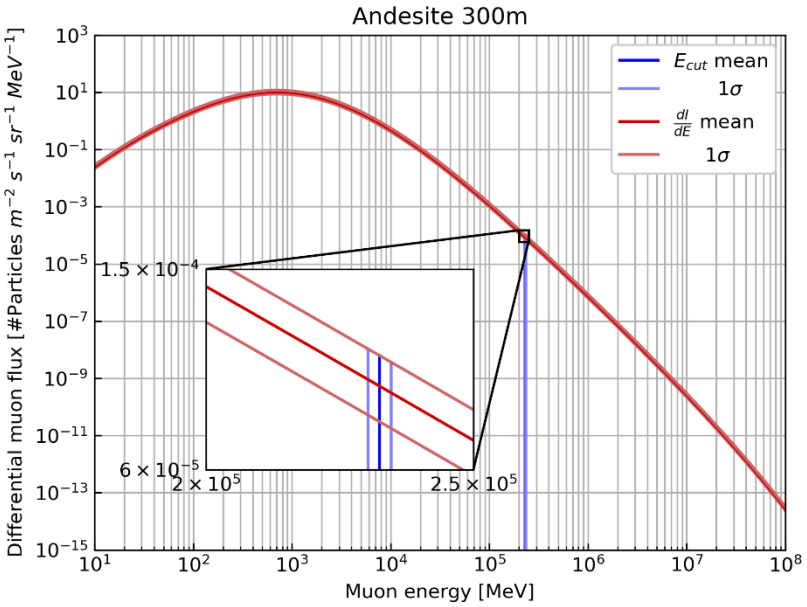

Figure 4.C1: Differential muon flux as a function of muon kinetic energy. Blue lines indicate the simulated cut-off energy for 300 m of Andesite and its respective propagated error bounds. Red lines show the flux model and its 1 σ error bounds.

The last step addresses the propagation of the simulated flux errors to the flux ratio in Eq. (4.6). Here we can make use of the fact that the errors in both simulations are perfectly correlated. In other words, if we knew the errors on all affected quantities in one simulation, we would instantaneously know the corresponding values for any other simulation. This allows us, for example, to calculate the upper error bound on the flux ratio by dividing the upper error bound of the simulated flux in the numerator by the upper error bound of the simulated flux in the denominator. The same is valid for any other constellation of errors, including the lower error bound and the mean.

4.10 Acknowledgements

We thank the Jungfrau Railway Company for their continuing logistic support during our fieldwork in the central Swiss Alps. We want also to thank the High-Altitude Research Stations Jungfraujoch & Gornergrat for providing us with access to their research facilities and accommodation. Furthermore, we thank the Swiss National Science Foundation (project No 159299 awarded to F. Schlunegger and A. Ereditato) for their financial support of this research project.

4.11 Author contributions

AL, FS and AE designed the study

AL developed the code with contributions by MV

AL performed the numerical experiments with support by RN

DM and AL compiled geological data

AA, TA, PS, RN and CP verified the outcome of the numerical experiments

AL wrote the text with contributions from all co-authors

AL designed the figures with contributions by DM

All co-authors contributed to the discussion and finally approved the manuscript

4.12 References

Agostinelli, S., et al.: GEANT4 - *A simulation toolkit*, Nucl. Instruments Methods Phys. Res. Sect. A Accel. Spectrometers, Detect. Assoc. Equip., 506, 250–303, doi:10.1016/S0168-9002(03)01368-8, 2003.

Alvarez, L. W., Anderson, J. A., Bedwei, F. E., Burkhard, J., Fakhry, A., Girgis, A., Goneid, A., Hassan, F., Iverson, D., Lynch, G., Miligy, Z., Moussa, A. H., Sharkawi, M. and Yazolino, L.: *Search for Hidden Chambers in the Pyramids*, Science, 167, 832–839, doi:10.1126/science.167.3919.832, 1970.

Ambrosino, F., Anastasio, A., Bross, A., Béné, S., Boivin, P., Bonechi, L., Cârloganu, C., Ciaranfi, R., Cimmino, L., Combaret, C., D'Alessandro, R., Durand, S., Fehr, F., Français, V., Garufi, F., Gailler, L., Labazuy, P., Laktineh, I., Lénat, J.-F., Masone, V., Miallier, D., Mirabito, L., Morel, L., Mori, N., Niess, V., Noli, P., Pla-Dalmau, A., Portal, A., Rubinov, P., Saracino, G., Scarlini, E., Strolin, P. and Vulpescu, B.: *Joint measurement of the atmospheric muon flux through the Puy de Dôme volcano with plastic scintillators and Resistive Plate Chambers detectors*, J. Geophys. Res. Solid Earth, 120, 1–18, doi:10.1002/2015JB011969, 2015.

Ariga, A., Ariga, T., Ereditato, A., Käser, S., Lechmann, A., Mair, D., Nishiyama, R., Pistillo, C., Scampoli, P., Schlunegger, F. and Vladymyrov, M.: *A Nuclear Emulsion Detector for the Muon Radiography of a Glacier Structure*, Instruments, 2, 1–13, doi:10.3390/instruments2020007, 2018.

Barnaföldi, G. G., Hamar, G., Melegh, H. G., Oláh, L., Surányi, G. and Varga, D.: *Portable cosmic muon telescope for environmental applications*, Nucl. Instruments Methods Phys. Res. Sect. A Accel. Spectrometers, Detect. Assoc. Equip., 689, 60–69, doi:10.1016/j.nima.2012.06.015, 2012.

Barrett, P. H., Bollinger, L. M., Cocconi, G., Eisenberg, Y. and Greisen, K.: *Interpretation of cosmic-ray measurements far underground*, Rev. Mod. Phys., 24, 133–178, doi:10.1103/RevModPhys.24.133, 1952.

Best, M. G.: *Igneous and metamorphic petrology*, 2nd ed., Blackwell Science Ltd, Malden MA., 2003.

Bezrukov, L. B. and Bugaev, E. V.: *Nucleon shadowing effects in photonuclear interaction*, Sov. J. Nucl. Phys., 33, 635–641, 1981.

Borchardt-Ott, W.: *Kristallographie*, Springer Berlin Heidelberg, Berlin, Heidelberg., 2009.

Fano, U.: *Penetration of protons, alpha particles, and mesons*, Annu. Rev. Nucl. Sci., 13, 1–66, 1963.

Folk, R. L.: *Petrology of the sedimentary rocks*, Hemphill Publishing Company, Austin TX., 1980.

Fujii, H., Hara, K., Hashimoto, S., Ito, F., Kakuno, H., Kim, S. H., Kochiyama, M., Nagamine, K., Suzuki, A., Takada, Y., Takahashi, Y., Takasaki, F. and Yamashita, S.: *Performance of a remotely located muon radiography system to identify the inner structure of a nuclear plant*, Prog. Theor. Exp. Phys., 2013, 073C01, doi:10.1093/ptep/ptt046, 2013.

George, E. P.: *Observations of cosmic rays underground and their interpretation*, in Process in Cosmic Ray Physics, vol. 1, pp. 395–451., 1952.

George, E. P.: *Cosmic rays measure overburden of tunnel*, Commonw. Eng., 455, 1955.

Groom, D. E., Mokhov, N. V. and Striganov, S. I.: *MUON STOPPING POWER AND RANGE TABLES 10 MeV–100 TeV*, At. Data Nucl. Data Tables, 78, 183–356, doi:10.1006/adnd.2001.0861, 2001.

Hayman, P. J., Palmer, N. S. and Wolfendale, A. W.: *The Rate of Energy Loss of High-Energy Cosmic Ray Muons*, Proc. R. Soc. A Math. Phys. Eng. Sci., 275, 391–410, doi:10.1098/rspa.1963.0176, 1963.

Hebbeker, T. and Timmermans, C.: *A compilation of high energy atmospheric muon data at sea level*, Astropart. Phys., 18, 107–127, doi:10.1016/S0927-6505(01)00180-3, 2002.

Higashi, S., Kitamura, T., Miyamoto, S., Mishima, Y., Takahashi, T. and Watase, Y.: *Cosmic-ray intensities under sea-water at depths down to 1400 m*, Nuovo Cim. A Ser. 10, 43, 334–346, doi:10.1007/BF02752862, 1966.

Jourde, K., Gibert, D., Marteau, J., de Bremond d'Ars, J., Gardien, S., Girerd, C., Ianigro, J.-C. and Carbone, D.: *Experimental detection of upward going cosmic particles and consequences for correction of density radiography of volcanoes*, Geophys. Res. Lett., 40, 6334–6339, doi:10.1002/2013GL058357, 2013.

Jourde, K., Gibert, D. and Marteau, J.: *Improvement of density models of geological structures by fusion of gravity data and cosmic muon radiographies*, Geosci. Instrumentation, Methods Data Syst. Discuss., 5, 83–116, doi:10.5194/gid-5-83-2015, 2015.

Kelner, S. R.: *Pair Production in Collisions between Muons and Atomic Electrons*, Phys. At. Nucl., 61, 448–456, 1998.

Kelner, S. R., Kokoulin, R. P. and Petrukhin, A. A.: *About Cross Section for High-Energy Muon Bremsstrahlung*, Prepr. Moscow Eng. Phys. Inst., 1–32, 1995.

Kelner, S. R., Kokoulin, R. P. and Petrukhin, A. A.: *Bremsstrahlung from Muons Scattered by Atomic Electrons*, Phys. At. Nucl., 60, 576–583, 1997.

Kokoulin, R. P. and Petrukhin, A. A.: *Analysis of the Cross-Section of Direct Pair Production by Fast Muons*, in Proceedings of the 11th Conference on Cosmic Rays, p. 277, Budapest., 1969.

Kokoulin, R. P. and Petrukhin, A. A.: *Influence of the Nuclear Formfactor on the Cross-Section of Electron Pair Production by High Energy Muons*, in Proceedings of the 12th International Conference on Cosmic Rays, pp. 2436–2445, Hobart, Australia., 1971.

Kusagaya, T. and Tanaka, H. K. M.: *Development of the very long-range cosmic-ray muon radiographic imaging technique to explore the internal structure of an erupting volcano , Shinmoe-dake , Japan*, Geosci. Instrum. Method. Data Syst., 4, 215–226, doi:10.5194/gi-4-215-2015, 2015.

Lesparre, N., Gibert, D., Marteau, J., Déclais, Y., Carbone, D. and Galichet, E.: *Geophysical muon imaging: feasibility and limits*, Geophys. J. Int., 183, 1348–1361, doi:10.1111/j.1365-246X.2010.04790.x, 2010.

Lesparre, N., Gibert, D., Marteau, J., Komorowski, J.-C., Nicollin, F. and Coutant, O.: *Density muon radiography of La Soufrière of Guadeloupe volcano: comparison with geological, electrical resistivity and gravity data*, Geophys. J. Int., 190, 1008–1019, doi:10.1111/j.1365-246X.2012.05546.x, 2012.

Lohmann, W., Kopp, R. and Voss, R.: *Energy Loss of Muons in the Range of 1-10000 GeV.*, 1985.

Mair, D., Lechmann, A., Herwegh, M., Nibourel, L. and Schlunegger, F.: *Linking Alpine deformation in the Aar Massif basement and its cover units – the case of the Jungfrau–Eiger mountains (Central Alps, Switzerland)*, Solid Earth, 9, 1099–1122, doi:10.5194/se-9-1099-2018, 2018.

Mando, M. and Ronchi, L.: *On the Energy Range Relation for fast Muons in Rock*, Nuovo Cim., 9, 517–529, doi:10.1007/BF02784646, 1952.

Marteau, J., Carlus, B., Gibert, D., Ianigro, J.-C., Jourde, K., Kergosien, B. and Rolland, P.: *Muon tomography applied to active volcanoes, in International Conference on New Photo-detectors*, PhotoDet2015, pp. 1–7, Moscow. [online] Available from: http://arxiv.org/abs/1510.05292, 2015.

Matter, A., Homewood, P., Caron, C., Rigassi, D., Stuijvenberg, J., Weidmann, M. and Winkler, W.: *Flysch and molasse of western and central Switzerland*, in Geology of Switzerland, a guide book: Schweiz Geologica Kommissione, pp. 261–292, Wepf., 1980.

Miyake, S., Narasimham, V. S. and Ramana Murthy, P. V.: *Cosmic-ray intensity measurements deep undergound at depths of (800÷8400) m.w.e.*, Nuovo Cim., 32, 1505–1523, doi:10.1007/BF02732788, 1964.

Morishima, K., Kuno, M., Nishio, A., Kitagawa, N., Manabe, Y., Moto, M., Takasaki, F., Fujii, H., Satoh, K., Kodama, H., Hayashi, K., Odaka, S., Procureur, S., Attié, D., Bouteille, S., Calvet, D., Filosa, C., Magnier, P., Mandjavidze, I., Riallot, M., Marini, B., Gable, P., Date, Y., Sugiura, M., Elshayeb, Y., Elnady, T., Ezzy, M., Guerriero, E., Steiger, V., Serikoff, N., Mouret, J.-B., Charlès, B., Helal, H. and Tayoubi, M.: *Discovery of a big void in Khufu's Pyramid by observation of cosmic-ray muons*, Nature, 552, 386–390, doi:10.1038/nature24647, 2017.

Neddermeyer, S. H. and Anderson, C. D.: *Note on the Nature of Cosmic-Ray Particles*, Phys. Rev., 51, 884–886, doi:10.1103/PhysRev.51.884, 1937.

Nikishov, A. I.: *Energy spectrum of e+e- pairs produced in the collision of a muon with an atom*, Sov. J. Nucl. Phys., 27, 677–681, 1978.

Nishiyama, R., Tanaka, Y., Okubo, S., Oshima, H., Tanaka, H. K. M. and Maekawa, T.: *Integrated processing of muon radiography and gravity anomaly data toward the realization of high-resolution 3-D density structural analysis of volcanoes: Case study of Showa-Shinzan lava dome, Usu*, Japan, J. Geophys. Res. Solid Earth, 119, 699–710, doi:10.1002/2013JB010234, 2014.

Nishiyama, R., Ariga, A., Ariga, T., Käser, S., Lechmann, A., Mair, D., Scampoli, P., Vladymyrov, M., Ereditato, A. and Schlunegger, F.: *First measurement of ice-bedrock interface of alpine glaciers by cosmic muon radiography*, Geophys. Res. Lett., 44, 6244–6251, doi:10.1002/2017GL073599, 2017.

Oláh, L., Tanaka, H. K. M., Ohminato, T. and Varga, D.: *High-definition and low-noise muography of the Sakurajima volcano with gaseous tracking detectors*, Sci. Rep., 8, 3207, doi:10.1038/s41598-018-21423-9, 2018.

Olive, K. A.: *Review of Particle Physics*, Chinese Phys. C, 38, 090001, doi:10.1088/1674-1137/38/9/090001, 2014.

Lo Presti, D., Gallo, G., Bonanno, D. L., Bonanno, G., Bongiovanni, D. G., Carbone, D., Ferlito, C., Immè, J., La Rocca, P., Longhitano, F., Messina, A., Reito, S., Riggi, F., Russo, G. and Zuccarello, L.: *The MEV project : Design and testing of a new high-resolution telescope for muography of Etna Volcano*, Nucl. Inst. Methods Phys. Res. A, 904, 195–201, doi:10.1016/j.nima.2018.07.048, 2018.

Reyna, D.: *A Simple Parameterization of the Cosmic-Ray Muon Momentum Spectra at the Surface as a Function of Zenith Angle*, arXiv Prepr. hep-ph/0604145 [online] Available from: http://arxiv.org/abs/hep-ph/0604145, 2006.

Richard-Serre, C.: *Evaluation de la perte d'energie unitaire et du parcours pour des muons de 2 à 600 GeV dans un absorbant quelconque*, 1971.

Seltzer, S. M. and Berger, M. J.: *Evaluation of the collision stopping power of elements and compounds for electrons and positrons*, Int. J. Appl. Radiat. Isot., 33, 1189–1218, doi:10.1016/0020-708X(82)90244-7, 1982.

Sternheimer, R. M.: *The density effect for the ionization loss in various materials*, Phys. Rev., 88, 851–859, doi:10.1103/PhysRev.88.851, 1952.

Sternheimer, R. M., Seltzer, S. M. and Berger, M. J.: *Density effect for the ionization loss of charged particles in various substances*, Phys. Rev. B, 26, 6067–6076, doi:10.1103/PhysRevB.26.6067, 1982.

Sternheimer, R. M., Berger, M. J. and Seltzer, S. M.: *Density effect for the ionization loss of charged particles in various substances*, At. Data Nucl. Data Tables, 30, 261–271, doi:10.1016/0092-640X(84)90002-0, 1984.

Stoer, J. and Bulirsch, R.: *Introduction to Numerical Analysis*, Springer New York, New York, NY., 2002.

Strunz, H. and Nickel, E.: *Strunz Mineralogical Tables*. Ninth Edition, Schweizerbart Science Publishers, Stuttgart, Germany., 2001.

Tanaka, H. K. M.: *Instant snapshot of the internal structure of Unzen lava dome, Japan with airborne muography*, Sci. Rep., 6, 39741, doi:10.1038/srep39741, 2016.

Tanaka, H. K. M., Nagamine, K., Nakamura, S. N. and Ishida, K.: *Radiographic measurements of the internal structure of Mt. West Iwate with near-horizontal cosmic-ray muons and future developments*, Nucl. Instruments Methods Phys. Res. Sect. A Accel. Spectrometers, Detect. Assoc. Equip., 555, 164–172, doi:10.1016/j.nima.2005.08.099, 2005.

Tanaka, H. K. M., Kusagaya, T. and Shinohara, H.: *Radiographic visualization of magma dynamics in an erupting volcano*, Nat. Commun., 5, 1–9, doi:10.1038/ncomms4381, 2014.

Tang, A., Horton-Smith, G., Kudryavtsev, V. A. and Tonazzo, A.: *Muon simulations for Super-Kamiokande, KamLAND, and CHOOZ*, Phys. Rev. D - Part. Fields, Gravit. Cosmol., 74, 1–34, doi:10.1103/PhysRevD.74.053007, 2006.

Tioukov, V., De Lellis, G., Strolin, P., Consiglio, L., Sheshukov, A., Orazi, M., Peluso, R., Bozza, C., De Sio, C., Stellacci, S. M., Sirignano, C., D'Ambrosio, N., Miyamoto, S., Nishiyama, R. and Tanaka, H.: *Muography with nuclear emulsions - Stromboli and other projects*, Ann. Geophys., 60, doi:10.4401/ag-7386, 2017.

Tuttle, O. F. and Bowen, N. L.: *Origin of granite in the light of experimental studies in the system NaAlSi3O8-KAlSi3O8-SiO2-H2O*, Geol. Soc. Am. Mem., 74, 1–146, 1958.

Chapter 5
Conclusion

5.1 Research conclusions

The studies that are presented in this thesis can be understood twofold. The first is as a contribution to render this technology more accessible to end-users such as geoscientists (Ch. 2). The second aspect concerns the exploration of new methods (the inversion; Ch. 3) and the exploitation of to date unused model parameters (rock composition; Ch. 4) in the framework of muon tomography. I briefly summarise the purpose and major conclusions of each study.

Chapter 2 was designed to be a tutorial for muon tomography novices. It presents a short introduction to the most important physical equations and redirects the reader to the important sources of continuative literature if more detail is needed. Moreover, readers may find examples of muon tomography experiments that were applied to tackle a geoscientific research question. This is intended to provide the prospective users with an idea of how this technology could be applied. It may even serve as a source of inspiration for the development of a completely new application avenue. To round this tutorial off, this contribution provides the reader with a guide to best practice in the form of addressing central questions. These issues will guide the user while planning and undertaking a muon tomography experiment.

In Ch. 3 an inversion framework was developed that allows for substantial geological information to be included. This information can be laboratory measurements of rock density and/or composition or even an assessment of these quantities from experience in the absence of any real data. This is always possible if they can be described by a probability density function. The Bayesian method that was used to construct this framework includes any type of a probabilistic statement on these parameters with ease. Furthermore, a systematic approach is presented that allows users to create their own Bayesian framework using a directed acyclic graph to visualise the joint probability density function. The resulting inversion has been proven to yield results that are consistent with literature values.

The issue of how much changes in rock composition affect the muon tomography measurements has been addressed in Ch. 4. I investigated with a numerical model by how much the muon flux measurements change if a realistic rock model is employed instead of the “standard rock” which is predominantly used in the community. I showed that there is a noticeable bias when the rock is either limestone or basalt and over 300m thick. For peridotites the effect is slightly less visible and for granitic rocks the standard rock approximation is generally fine. This result implies two points. First, researchers should be aware of lithological boundary conditions of an experiment to appropriately account for this lithology-dependent chemical composition effect. The second aspect is much more intricate in the sense

that muon tomographic measurements are sensitive to the composition of the material to a measurable extent. This could be used for example to infer compositions in a dedicated experiment.

These developments are not supposed to replace the conventional approaches that are widely applied in the community but serve to provide researchers with more tools to tackle their problems. It is my strong conviction that a technology can only thrive and evolve through a diverse methodological toolbox that is constantly expanded and improved. This is also true for the question of who drives the development of the technology. At a certain point in a technological development, end-users have to make requests to the developers as to what features should be included in the technology. I think the analogy to software design is well applicable, where the final product is often shaped by the users' needs, even though in the early stages the developers shape the technology.

5.2 Project conclusions

This project has performed two distinct measurement campaigns on two glaciers in the Jungfrau region in the central Swiss Alps. As a team, we could show that it is feasible to apply this technology in high alpine regions (see Nishiyama et al., 2017, 2019; Ch. 6 & 7), that has hitherto been used to investigate mostly volcanoes. The inital goals for the subdisciplines have also been met. From the geological perspective, a structural-geological 3D-model was built (Mair et al., 2018), which shows the rather intricate lithological architecture of that region. In the laboratory, field samples were analysed and combined to yield a valid representation of the necessary physical parameters (density & composition) of the encountered lithology. The physics aspect of the project also achieved the goal of adapting the infrastructure that was indispensable for a reasonably productive chain for the production and analysis of emulsion films (Ariga et al., 2018). Finally, from a geophysical perspective, we were able to build an inversion code (Lechmann et al., in prep.; Ch. 3), that was able to reconstruct the ice-bedrock interface below these two glaciers. Based on these advancements, I conclude, that even though this technology is not suitable to detect real-time changes on glaciers to a significant degree, the time-integrated image is of particularly good quality and is suitable for the analyses of glacial structure or erosional processes.

I critically refer to several aspects that should be addressed in future studies. First, the installation or upgrade of an emulsion film production and scanning facility is a massive undertaking that requires a lot of time, manpower and financial resources. Such an investment should only be made if further projects are planned. Second, the use of this technology for glaciers is mainly limited by the accessibility to a measurement location. This position must sit below the glacier and should not have too much material (> 1km) between the detector and the glacier. We were fortunate that we could access the train tunnel that runs below the glacier but in general, those spots are unfortunately quite rare.

5.3 Outlook

In this final chapter I present some possible routes that muon tomography, including the application to glaciers, can take.

A development, that has only just begun and is gaining quite some popularity, is the transition to industrially produced detectors. There are already a few companies that have specialised in constructing and vending such devices. Once such equipment becomes available to a wider geoscientific community, the application of muon tomography in a geophysical measurement array may become more visible.

The detector and analysis technologies are basically improved in parallel. Physicists are constantly tinkering with better muon flux detectors for related experimental constraints. In a few years it is possible that some kind of "standard" detector design will be established for muon tomography measurements. This would also facilitate the commercial production of the detectors. Most probably, however, this development will not be solely advanced by either academia or industry but a back and forth between the two domains. Additionally, geophysicists will also continue to establish inversion methods for the most popular applications such as interface reconstruction or density estimation.

A further development concerns borehole detectors. Such devices can be placed inside a borehole (hence the name) and allow to evaluate the overlying material in the vicinity. This has two particularly important implications. One, the borehole information, which is usually only a point information in space, can be coupled with a 3D measurement around the drill hole. This represents a qualitative improvement of the boreholes. Second and probably more important, this development erases the need of having a pre-existing measurement location that is situated below the target. One can now construct an own measurement location at points where they are most needed. In the context of glaciers this might be a tricky undertaking, as the borehole then should penetrate both an ice layer and a rock layer. The recuperation of the detector would probably be a difficult operation. Alternatively, one could think of drilling an oblique borehole from the side underneath the target. However, none of these approaches have been tried in practice for glaciers yet.

As muon tomography strongly relies on physical models for energy losses and cosmic ray fluxes, another angle can be taken to improve the related knowledge and technology. This consists of improving the aforementioned physical models by making them more exact, i.e. reducing their error-bars. Alas, the energy loss models have not been updated since the great developments of the 80s and 90s, as they have been deemed exact enough for most practical purposes. This is true; however, it would be nice to see also new theoretical models for the related physical effects, as theoretical physics has advanced quite a bit compared to 30-40 years ago. The cosmic ray flux community on the other hand, is involved in several other research domains, such as cosmogenic nuclide dating in geology. This means that there is a constant push to improve their muon flux models. The muon tomography community can also profit from this wide-spread use and constant improvement of the cosmic ray flux models. This is because the dominating limiting factor in muon tomography studies is still the precision of the muon flux models.

Somewhat tied to the improvement of the cosmic ray flux models is a rather far-fetched possible development. This concerns the way of how muons are generated. Until now, we still use muons that are created from naturally occurring cosmic rays. If it were possible to create muons by ourselves, via a particle accelerator or any other suitable device, this would greatly improve our uncertainty on the input flux. This is similar to using controlled source seismology instead of naturally occurring earthquakes. Another, more practical, way to approach this issue could be based on the measurement results of pure absorption. Here a detector could be placed behind the target, recording the undisturbed muon flux. Of course, this has its own difficulties (mainly technical), but one could create a proper, local muon flux model. Either way the model uncertainties in the cosmic ray flux model would be replaced either by a known error from the hypothetical particle generator or by an error related to the measurement of the undisturbed flux. The user has then a better control on this important experimental parameter.

5.4 References

Ariga, A., Ariga, T., Ereditato, A., Käser, S., Lechmann, A., Mair, D., Nishiyama, R., Pistillo, C., Scampoli, P., Schlunegger, F., and Vladymyrov, M.: *A Nuclear Emulsion Detector for the Muon Radiography of a Glacier Structure*, Instruments, 2, 7, https://doi.org/10.3390/instruments2020007, 2018.

Mair, D., Lechmann, A., Herwegh, M., Nibourel, L., and Schlunegger, F.: *Linking Alpine deformation in the Aar Massif basement and its cover units – the case of the Jungfrau–Eiger mountains (Central Alps, Switzerland)*, Solid Earth, 9, 1099–1122. https://doi.org/10.5194/se-9-1099-2018, 2018.

Nishiyama, R., Ariga, A., Ariga, T., Käser, S., Lechmann, A., Mair, D., Scampoli, P., Vladymyrov, M., Ereditato, A., and Schlunegger, F.: *First measurement of ice-bedrock interface of alpine glaciers by cosmic muon radiography*. Geophysical Research Letters, 44, 6244–6251. https://doi.org/10.1002/2017GL073599, 2017.

Nishiyama, R., Ariga, A., Ariga, T., Lechmann, A., Mair, D., Pistillo, C., Scampoli, P., Valla, P. G., Vladymyrov, M., Ereditato, A., and Schlunegger, F.: *Bedrock sculpting under an active alpine glacier revealed from cosmic-ray muon radiography*. Scientific Reports, 9, 6970. https://doi.org/10.1038/s41598-019-43527-6, 2019.

Appendix I

First measurement of ice-bedrock interface of alpine glaciers by cosmic muon radiography

R. Nishiyama[1], A. Ariga[1], T. Ariga[1], S. Käser[1], A. Lechmann[2], D. Mair[2], P. Scampoli[1,3], M. Vladymyrov[1], A. Ereditato[1], and F. Schlunegger[2]

[1]Albert Einstein Center for Fundamental Physics, Laboratory for High Energy Physics, University of Bern, Bern, Switzerland,
[2]Institute for Geological Sciences, University of Bern, Bern, Switzerland,
[3]Department of Physics "E. Pancini", University of Naples Federico II, Naples, Italy

Published in: Geophysical Research Letters, 44, 6244-6251, https://doi.org/10.1002/2017GL073599, 2017.

I.1 Abstract

The shape of the bedrock underneath alpine glaciers bears vital information on the erosional mechanism related to the flow of ice. So far, several geophysical exploration methods have been proposed to map the bedrock topography though with limited accuracy. Here we illustrate the first results from a technology, called cosmic ray muon radiography, newly applied in glacial geology to investigate the bedrock geometry beneath the Aletsch Glacier situated in the Central Swiss Alps. For this purpose we installed new cosmic muon detectors made of emulsion films at three sites along the Jungfrau railway tunnel and measured the shape of the bedrock under the uppermost part of Aletsch Glacier (Jungfraufirn). Our results constrain the continuation of the bedrock-ice interface up to a depth of 50 m below the surface, where the bedrock underneath the glacier strikes NE-SW and dips at 45° ± 5°. This documents the first successful application of this technology to a glaciated environment.

I.2 Introduction

In mountainous landscapes such as the Central Alps of Europe the bedrock topography is one of the most prominent surfaces as it separates the geological substratum—the bedrock—from the overlying unconsolidated units, which are commonly assigned to the Quaternary (Preusser et al., 2010). In low-elevated regions this surface has been sculpted by glaciers during past glaciations (e.g., Horberg and Anderson, 1956). In the highly elevated regions of the European Alps, however, glacial processes are still actively modulating the bedrock topography mainly above the Equilibrium Line Altitude. Accordingly, the geometry of the bedrock topography sets tight constraints on the erosional mechanisms at work underneath a glacier (e.g., Cook and Swift, 2012). This is the major motivation why several efforts have been undertaken toward exploring the bedrock topography surrounding formerly and still actively glaciated areas using drilling (Dürst Stucki and Schlunegger, 2013) and several geophysical

techniques, including seismic surveys and multibeam bathymetry (Duchesne et al., 2010; Dürst Stucki et al., 2012), gravity measurements (Adams and Hinze, 1990; Barnaba et al., 2010), and radio-echo soundings (Fisher et al., 1989; Shean and Marchant, 2010). Despite the progress achieved through the application of these geophysical surveys, the accuracy of bedrock maps varies greatly because of the assumption on which the reconstruction relies. For instance, bedrock surfaces with steep slopes and/or an overlying medium with a high fluid pressure ratio lower the resolution of seismic and radar surveys and set limits to the penetration depth of the related waves (Murray et al., 2007; Schrott and Sass, 2008). In addition, most of the previous investigations have been conducted either on landscapes where glaciers have disappeared after the termination of the last glacial epoch circa 20,000 years ago or on active glaciers where the surrounding landscape is flat.

In this paper we introduce a technology referred to as emulsion film muon radiography to investigate the bedrock geometry beneath active glaciers in a steep alpine environment. This detector technique relies on the high-penetration power of muon components in natural cosmic rays, where the attenuation rate of the intensity of muons mainly depends on the density of the crossed material. Accordingly, this method provides a suitable alternative to other approaches because of the large-density contrasts between the bedrock and the overlying glacier. In addition, the passive nature of the detecting device, not requiring electric power, computing support or radio data transmission, is an added value to the currently available geophysical tools. We demonstrated the performance of muon radiography through an experiment in the Jungfrau region, Switzerland. We benefit from the railway tunnel of the Jungfraubahn situated in the Jungfrau region. This tunnel crosses the bedrock at typically 50 m depth from the uppermost part of Aletsch Glacier (Jungfraufirn). We installed emulsion films at three sites along this tunnel and mapped the shape of the bedrock under the glacier. We then used the patterns of detected muons to map the orientation of the bedrock underneath this glacier, thereby documenting the first successful application of muon radiography in a steep and glaciated environment.

I.3 Muon radiography

Muon radiography is a technology that has been developed to investigate the internal density structures of geological targets. It relies on the high-penetration power of the muon particles, a component of the natural cosmic rays (Patrignani et al., 2016). The absorption rate of the muon flux can be used to derive the density length, i.e., the density integrated along the muon trajectories. This technique has been applied for noninvasive inspection purposes where the survey targets were volcanoes (Tanaka et al., 2007; Lesparre et al., 2010; Carbone et al., 2014; Ambrosino et al., 2015; Jourde et al., 2016), nuclear reactors (Fujii et al., 2013), seismic faults (Tanaka et al., 2011), and caves (Oláh et al., 2013). One requirement is that muon detectors must be placed at altitudes lower than survey targets because of downward going nature of cosmic ray muons. At sites where the interface between a glacier and the bedrock is the survey target, the muon radiography technology bears the potential to return the related densities as a result. Accordingly, because of the anticipated large-density contrasts in such an

environment, this technology provides information pertinent for mapping the shape of the bedrock at high resolution.

There are several types of particle detectors suitable for muon radiography, such as scintillation trackers (e.g., Lesparre et al., 2010; Anastasio et al., 2013), gaseous chambers (e.g., Cârloganu et al., 2013; Oláh et al., 2013), and emulsion films (e.g., Tanaka et al., 2007; Nishiyama et al., 2017). We adopt emulsion films for the observations of glaciers. Emulsion films are special photographic films, which record trajectories of charged particles (Ereditato, 2013; De Lellis et al., 2011). The microscope analysis of these trajectories then allows to measure the position and direction of incident muons with the unbeatable resolutions. The spatial and angular resolutions are 1 μm and a few milliradians, respectively. Contrary to other types of particle detectors, emulsion films are suitable for exposure in remote and harsh environments because they do not require power supply or any electronic device for operation.

I.4 Setting

The Aletsch Glacier, situated in the Central Alps of Switzerland, is the largest glacier in the Central Swiss Alps. It has a length of 23 km, a volume of 15 km^3, and covers an area of 81 km^2 (Figure I.1). The glacier is fed by three tributary glaciers (Ewigschneefeld, Jungfraufirn, and Grosser Aletschfirn). The target region of our observation is the uppermost part of Jungfraufirn, which sits on the southeastern flank of Mount Jungfrau (4158 m above sea level (asl)) and Mount Moench (4107 m asl). It has a length of 4 km and a width of about 2 km.

The Aletsch Glacier has shortened by about 5 km during the past 100 years in response to global warming (Hock et al., 1999; Huss et al., 2008). In the target region a rapid drop of the ice surface in the order of several meters per year has been reported by the local authorities, which is ultimately linked with the shrinkage of the Aletsch Glacier. As the Jungfraujoch, which represents the pass between the Mönch and the Jungfrau, hosts infrastructure buildings (train and research stations, communication, and tourist facilities) that were constructed on top of the bedrock above the Jungfraufirn (Figure I.1a), a shrinking of the ice volume and the related drop of the ice surface have large consequences on the mechanical stability of the bedrock underlying these constructions. Accordingly, attention has been paid by local authorities for predicting potential collapse failures of the bedrock, where the vanishing ice decreases the stability of the bedrock. A precise understanding of the shape of the bedrock beneath the glacier would thus help to predict future potential risks for the occurrence of those events.

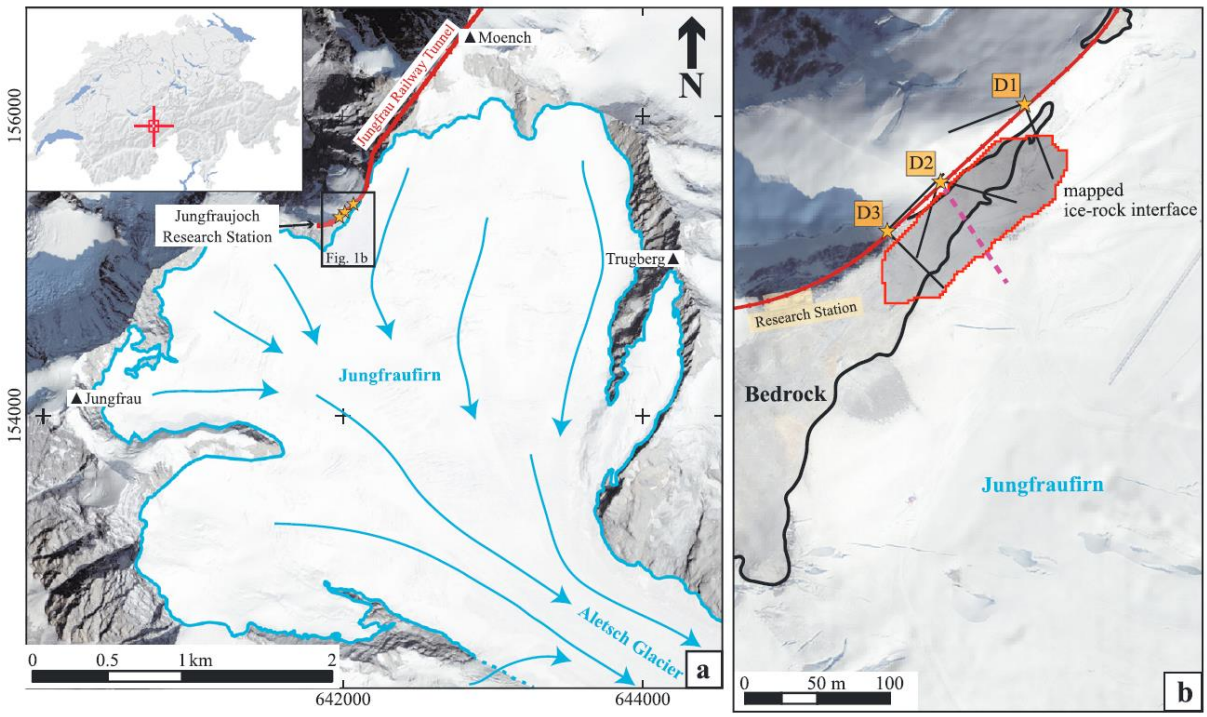

Figure I.1. (a) The uppermost part of Aletsch Glacier (Jungfraufirn). The blue arrows indicate the direction of glacier flow. (b) View of the survey region. The detectors were installed along the Jungfrau railway (stars D1, D2, and D3). The solid black lines from the detector indicate the view range of each detector. Basemap: SWISSIMAGE (digital color orthophotomosaic, 0.25 m ground pixel size) draped with a semitransparent hillshade based on SwissAlti3D reproduced by permission of swisstopo (BA17061).

I.5 Experimental design and methods

The muon detectors were installed at three sites along the Jungfrau railway tunnel facing the Aletsch Glacier. Installation took place on 16 February 2016 and removal on 4 April 2016, thereby collecting data during 47 days. The sites (D1-D3) are located ~100 m apart from each other (Figure I.1b) at altitudes of 3381 m asl for D1, 3401 m asl for D2, and 3414 m asl for D3. The individual detector (Figure I.2a) consists of a stack of eight layers of emulsion films with 1 mm thick lead plates between each one (Figure I.2b). The emulsion film is made of a 200 μm thick plastic base and a 50 μm thick sensitive gel poured on both sides. The gel production and assembling have been done at Nagoya University, Japan (Nishio et al., 2015), and at the University of Bern, respectively. This design yields to a total effective detection area of 250 cm^2 for each site.

After completion of the measurements, the films were chemically developed and automatically scanned at the University of Bern by means of optical microscopes. The microscope scanning facility consists of commercially available optics and stages (Arrabito et al., 2006) that are complemented with algorithms for image processing and track recognition that we developed for these purposes (Ariga and Ariga, 2014). Tracks that are straightly aligned in consecutive films are identified as muon trajectories, here defined by at least four tracks within the total of eight films. This selection assures a detection efficiency > 97% and a low contamination of low-energy background particles (< ~1 GeV/c; see Nishiyama et al. (2016) for details). We scanned 13% of the total detection area (32 cm^2 × eight consecutive layers for each detector site). The number of detected muons were then counted for each bin in a polar coordinate

histogram (Figure I.3a) and converted into the particle flux (cm^{-2} s^{-1} sr^{-1}, Figure I.3b) by normalizing with respect to the scanned area (32 cm^2), the exposure time (4.12×10^6 s), and the solid angle.

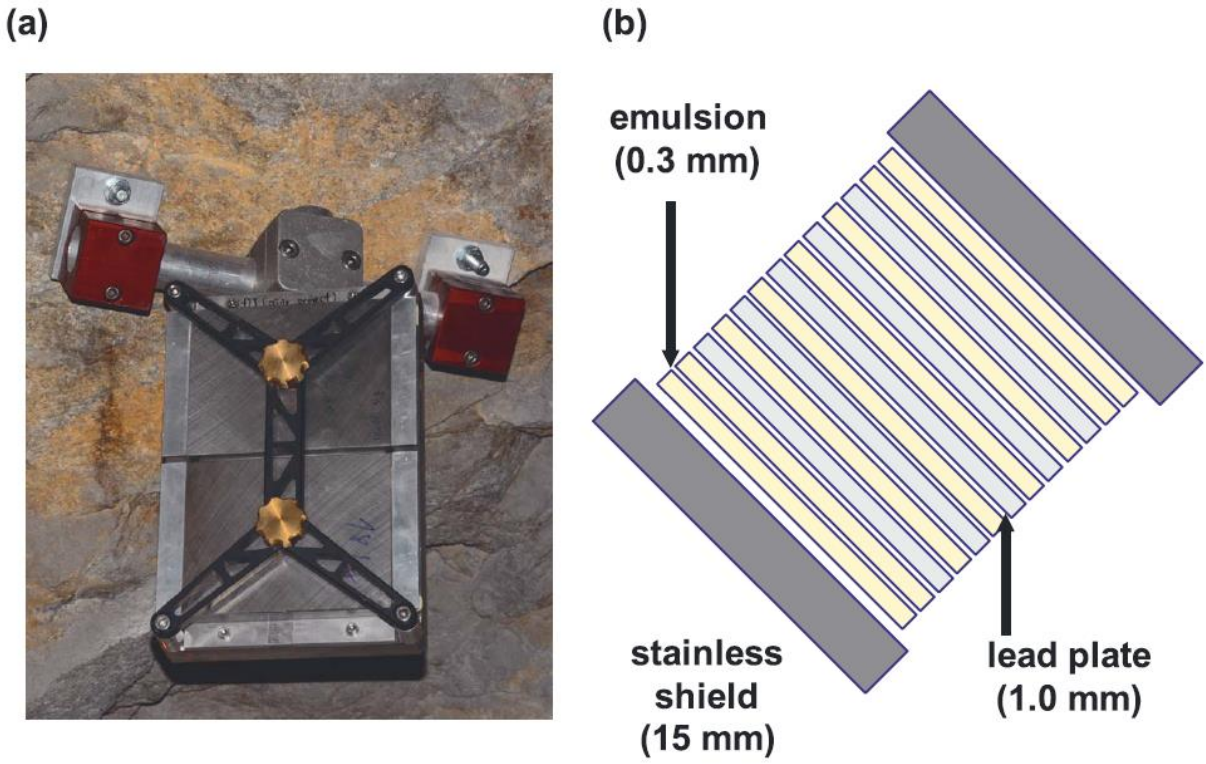

Figure I.2. (a) The detector frame is fixed on the wall of the Jungfrau railway tunnel, inclined 45° with respect to the zenith. (b) The detector consists of eight emulsion films interleaved with 1 mm thick lead plates. It is covered by ~15 mm thick stainless plates to shield environmental radioactive particles.

The comparison of the observed muon flux F^{obs} and the simulated one for various densities $F^{sim}(\rho)$ returns a density value that gives the best agreement. The simulated flux is calculated by using the muon energy spectrum and the digital elevation models (supporting information, Ch. I.10.2). The agreement between the observed and simulated flux is assessed with a chi-square test:

$$\chi^2(\rho) \equiv \sum_i^{bins} \frac{\left|F_i^{obs} - F_i^{sim}(\rho)\right|^2}{\sigma_i^2}, \quad \text{(I.1)}$$

where the error σ_i is a combination of the statistical fluctuations and the systematic errors with flux simulation (15%; see supporting information, Ch. I.10.2).

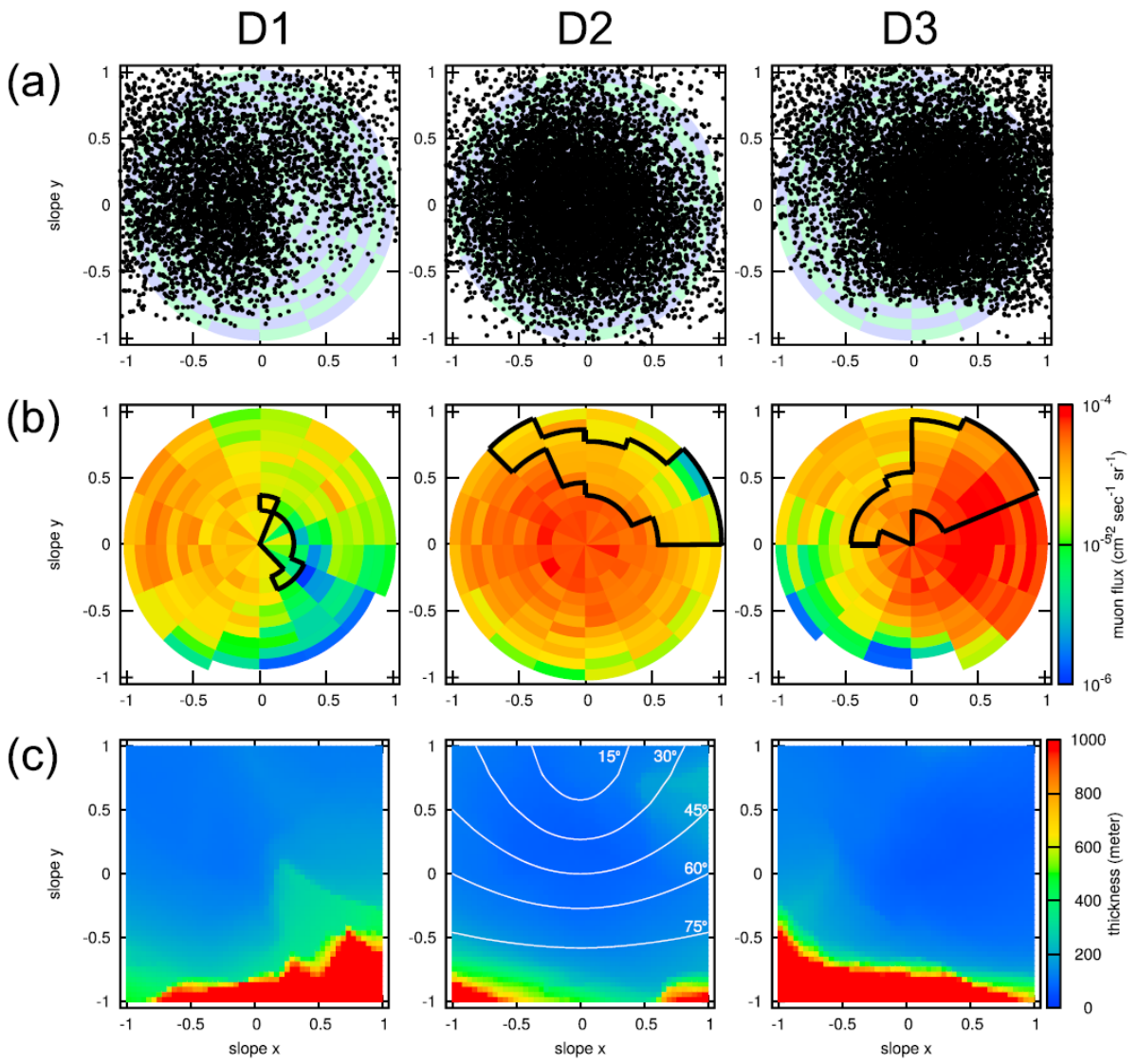

Figure I.3. (a) Angular distribution of muons detected in 47 days at D1 (left), D2 (middle), and D3 (right). Each dot corresponds to a single muon event. (b) Muon flux converted for each polar bin by normalizing the number of muon events with respect to the detector size, solid angle, and exposure time. The regions enclosed by the black solid lines are not covered with ice and used for estimation of bedrock density. (c) Obstacle thicknesses (rock + ice), traversed by muons before reaching the detectors. The muon intensity is clearly anticorrelated with the thickness. The white contour curves in the middle plot indicate the zenith angle of incoming muons.

Finally, we mapped the shape of the bedrock using all not empty bins of flux data. We determined the fraction of rock x from the average density values $< \rho >$ estimated for each bin (Figure I.4a). Considering the bulk density of bedrock component ρ_{rock} = 2.68 g/cm^3 (see next section) and that of ice component ρ_{ice}= 0.85 g/cm^3 (Huss, 2013), x is determined via a relationship:

$$< \rho > = \rho_{rock+}\rho_{ice} \cdot (1 - x). \quad \text{(I.2)}$$

Once x is obtained for each bin, the boundary position can be plotted at a distance Lx from the detector position (L is the total thickness of overlying material including bedrock and ice). We only considered those muons within a zenith angle between 0° and 70° because the systematic uncertainty affecting the flux simulation is larger than the statistical fluctuation for nearly horizontal muons (see supporting information, Ch. I.10.2). The bedrock shape estimated from muon flux analysis was displayed using the

Environmental Systems Research Institute ArcScene software licensed to the Institute of Geological Sciences of University of Bern.

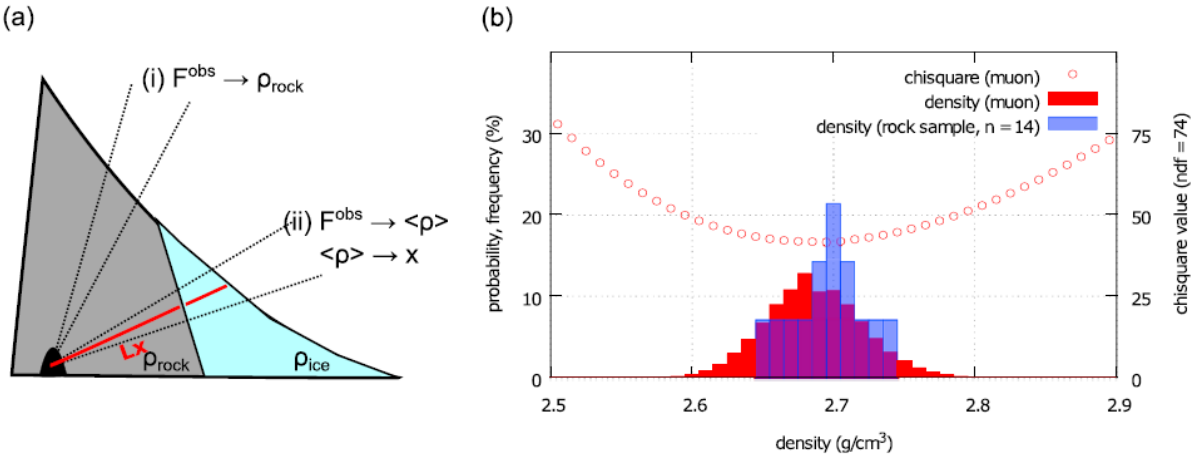

Figure I.4. (a) Schematic illustration of (i) bedrock density analysis and (ii) bedrock shape analysis. (b) The χ^2 statistics test is performed to determine the rock density. A total of 74 bins covering the hillslope are used for the test, which are indicated by the black solid lines in Figure I.3b. The minimum value of the chi-square is 41.68 (open red circles), giving the best bulk density of 2.68 ± 0.04 (g/cm^3, 1σ, red boxes). It agrees with the bulk density measured for rock samples taken near the detectors along the Jungfrau railway tunnel (blue boxes).

I.6 Results and discussion

Figure I.3a shows the angular distribution of muon events reconstructed in a 32 cm^2 area of the three detectors. Each dot in the plot corresponds to a detected muon. During 47 days of exposure we observed a total of 4655 (D1), 9348 (D2), and 10606 muons (D3) within the viewing range. The intensity of muon events is clearly anticorrelated with the thickness of the obstacles (rock + ice) along the muon trajectories (Figure I.3c). For instance, the shadows of muons where the dots are sparsely distributed coincide with the regions where the bedrock thicknesses are greater than 1 km. This indicates that most of the muons in these directions were absorbed in the thick bedrock edifices of the Jungfrau and the Mönch Mountains.

Figure I.4b illustrates the resultant $\chi 2(\rho)$ function for 74 bins covering the rock part (5 bins from D1, 31 from D2, and 38 from D3, indicated by the black solid lines in Figure I.3b). The minimum $\chi 2$ value of 41.68 yields the best density value of 2.68 ± 0.04 (g/cm3, 1σ). This estimation is in good agreement with the bulk density independently measured for rock samples taken near the detectors along the Jungfrau railway tunnel and on the surface (2.65 – 2.74 g/cm^3, Figure I.4b; see also supporting information, Ch. I.10.3). We thus applied a uniform density ρ_{rock} = 2.68 g/cm^3 for the calculation of the bedrock shape. Figure I.5a shows the position of the bedrock reconstructed from each bin of muon flux data. For visualization, we rasterized these point data using 2 m × 2 m grids (Figure I.5b). The reconstructed bedrock can be approximated as a plane with a strike angle of 225°N and a dip angle of 45° up to 50 m depth below the glacier's surface. The cross-sectional view from the middle detector (D2) is represented in Figure I.5c. The bedrock shapes reconstructed for two extreme ice densities (0.50 and 0.90 g/cm^3) are also displayed. Taking into account the uncertainty on the bulk density of ice, the

dip angle has a systematic error of ± 5°. This uncertainty is mainly related to (i) the selection of the muon energy spectrum model, (ii) unknown density variations of ice, and (iii) seasonal variations of the ice surface. As a first major source of errors, the calculation of muon flux has a systematic uncertainty of 15%. This results in a density estimation error of ~5%. The second source of errors, related to the poorly constrained depth dependence of ice density, is addressed here through the use of two mentioned extreme ice density values, thereby considering these as systematic uncertainties and thus deviations from a mean ice density value of 0.85 g/cm^3 that we applied as default for the calculation of the bedrock-ice interface illustrated in Figure I.5c. The implementation of a more realistic depth dependency of ice densities would significantly reduce the uncertainties of the inferred bedrock orientation. The third factor, i.e., the seasonal variation of the ice surface represented here through a digital elevation model (DEM), is not a problem for the present work because the DEM used in the analysis was recently taken and the annual snow accumulation at the research site is merely a few meters.

I.7 Conclusions

We demonstrated a successful application of muon radiography performed with emulsion film detectors. The results suggest that the uppermost part of Aletsch Glacier (Jungfraufirn) is underlain by a bedrock with a steep flank that dips at 45° ± 5° and strikes at 225°N. These values have been measured up to a depth of 50 m below the ice surface. The parallel orientation of the bedrock with respect to the glaciers' flow direction implies that the ice has passively on the bedrock without sculpting it. Muon radiography can be a complementary method for determination of the bedrock topography in a steep glaciated environment if underneath tunnels or suitable detector sites are available.

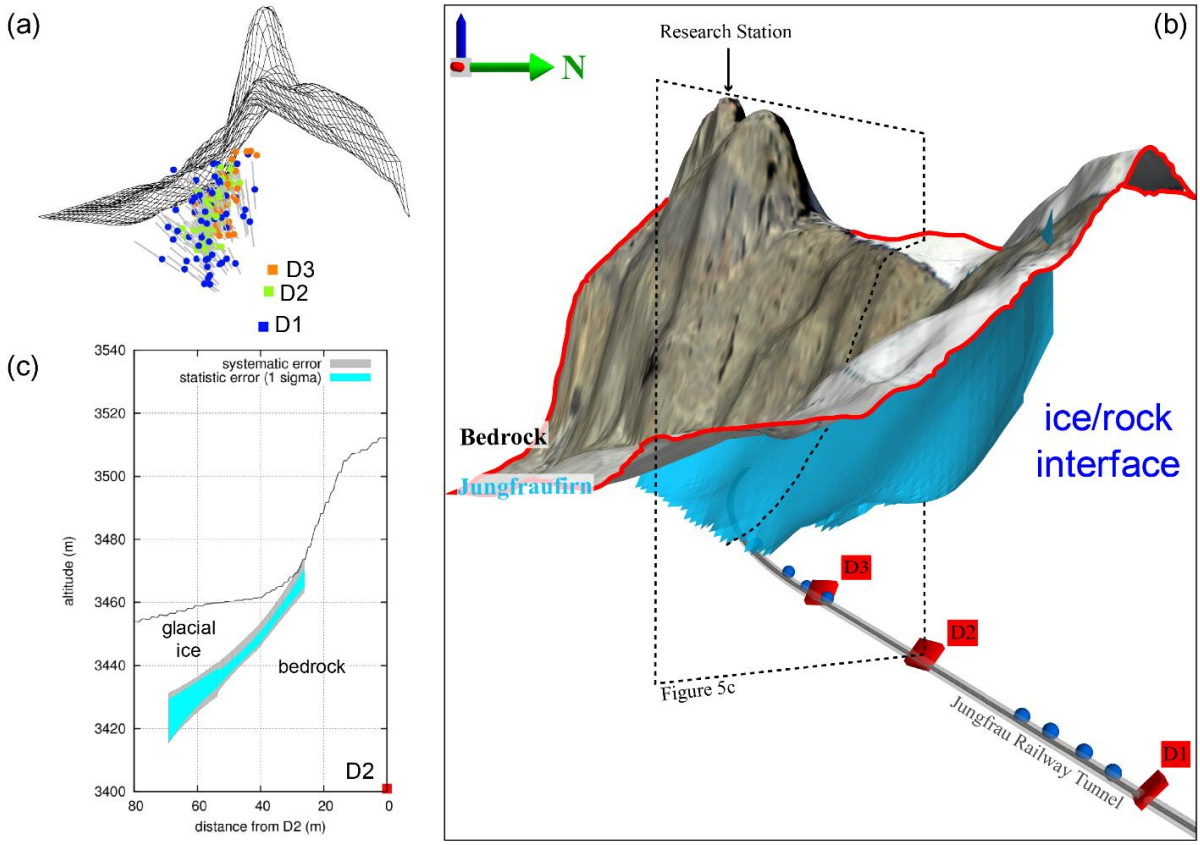

Figure I.5. (a) The three-dimensional reconstructed bedrock points under the surface, determined from muon flux attenua- tion analysis. (b) The point data are rasterized with 2 m × 2 m grids into the bedrock surface. The locations of rock sampling are also indicated with blue points along the railway tunnel. Basemap: SWISSIMAGE (digital color orthophotomosaic, 0.25 m ground pixel size) reproduced by permission of swisstopo (BA17061). (c) The cross-sectional view from the middle detector site (D2) along the steepest direction of the bedrock. The blue and grey bands are the 68% confidence level due to statistical fluctuations and the systematic uncertainty due ice density ambiguity.

I.8 Acknowledgments

This project is financially supported by Swiss National Science Foundation as an interdisciplinary research project (159299). We also benefited from the emulsion films R&D project supported by Swiss National Science Foundation Ambizione grant PZ00P2_154833. We warmly acknowledge M. Nakamura and his colleagues from F - lab, Nagoya University. We would like to express our gratitude to Jungfraubahn for the enormous help with the detector installation. The digital elevation model of the Jungfrau region was provided by Swisstopo. We would like to acknowledge the precious contributions of the technical staff from the LHEP and the Institute for Geological Science of the University of Bern. We would like to thank two anonymous reviewers for their useful suggestions that helped us to improve the manuscript. The original data used in the analysis and the details of the methods are available from the supporting information.

I.9 References

Adams, J. M., and Hinze, W. J.: *The gravity-geologic technique of mapping buried bedrock topography*, Soc. Explor. Geophys., 3, 99–106, doi:10.1190/1.9781560802785.3.ch7, 1990.

Abrecht, J.: *Geologic units of the Aarmassif and their pre-Alpine rock associations: A critical review*, Schweizerische Mineralogische Und Petrographische Mitteilungen, 74, 5–27, doi:10.5169/seals-56328, 1994.

Allkofer, O. C., Bella G., Dau W. D., Jokisch H., Klemke G., Oren Y., and Uhr R.: *Cosmic ray muon spectra at sea-level up to 10 TeV*, Nuclear Physics B, 259, 1–18, doi:10.1016/0550-3213(85)90294-9, 1985.

Ambrosino, F., et al.: *Joint measurement of the atmospheric muon flux through the Puy de Dôme volcano with plastic scintillators and Resistive Plate Chambers detectors*, J. Geophys. Res. Solid Earth, 120, 7290–7307, doi:10.1002/2015JB011969, 2015.

Anastasio, A., et al.: *The MU-RAY experiment. An application of SiPM technology to the understanding of volcanic phenomena*, Nucl. Instrum. Methods Phys. Res., Sect. A, 718, 134–137, doi:10.1016/j.nima.2012.08.065, 2013.

Ariga, A., and Ariga, T.: *Fast 4π track reconstruction in nuclear emulsion detectors based on GPU technology*, J. Instrum., 9, P04002, doi:10.1088/1748-0221/9/04/P04002, 2014.

Arrabito, L., et al.: *Hardware performance of a scanning system for high speed analysis of nuclear emulsions*, Nucl. Instrum. Methods Phys. Res., Sect. A, 568, 578–587, doi:10.1016/j.nima.2006.06.072, 2006.

ASTM C914-09: *Standard Test Method for Bulk Density and Volume of Solid Refractories by Wax Immersion*, ASTM International, West Conshohocken, PA, doi:10.1520/C0914-09R15; www.astm.org, 2015.

Barnaba, C., Marello, L., Vuan, A., Palmieri, F., Romanelli, M., Priolo, E., and Braitenberg, C.: *The buried shape of an alpine valley from gravity surveys, seismic and ambient noise analysis*, Geophys. J. Int., 180, 715–733, doi:10.1111/j.1365-246X.2009.04428.x, 2010.

Blake, G. R., and Hartge, K. H.: *Bulk Density*, in *Methods of Soil Analysis: Part 1*, Agron. Monogr. 9, 2nd ed., edited by A. Klute, pp. 363–375, American Society of Agronomy and Soil Science Society of America, Madison, 1986.

Carbone, D., Gibert, D., Marteau, J., Diament, M., Zuccarello, L., and Galichet, E.: *An experiment of muon radiography at Mt Etna (Italy)*, Geophys. J. Int., 196, 633–643, doi:10.1093/gji/ggt403, 2014.

Cârloganu, C., et al.: *Towards a muon radiography of the Puy de Dôme*, Geosci. Instrum. Method. Data Syst., 2, 55–60, doi:10.5194/ gi-2-55-2013, 2013.

Cook, S. J., and Swift, D. A.: *Subglacial basins: Their origin and importance in glacial systems and landscapes*, Earth Sci. Rev., 115, 332–372, doi:10.1016/j.earscirev.2012.09.009, 2012.

De Lellis, G., Ereditato, A., Nuclear Emulsions Niwa, K., Fabjan, C. W., and Schopper, H. (Eds.): *Springer Materials—Landolt-Bönstein Database*, pp. 109–118, Springer, Berlin, doi:10.1007/978-3-642-03606-4_9, 2011.

Duchesne, M. J., Pinet, N., Bédard, K., St-Onge, G., Lajeunesse, P., Campell, D. C., and Bolduc, A.: *Role of the bedrock topography in the Quaternary filling of a giant estuarine basin: The Lower St. Lawrence Estuary, Eastern Canada*, Basin Research, 22, 933–951, doi:10.1111/ j.1365-2117.2009.00457.x, 2010.

Dürst Stucki, M., and Schlunegger, F.: *Identification of erosional mechanisms during past glaciations based on a bedrock surface model of the central European Alps*, Earth Planet. Sci. Lett., 384, 57–70, doi:10.1016/j.epsl.2013.10.009, 2013.

Dürst Stucki, M., Schlunegger, F., Christener, F., Otto, J.-C., and Götzb, J. : *Deepening of inner gorges through subglacial meltwalter—An example from the UNESCO Entlebuch area, Switzerland*, Geomorphology, 139–140, 506–517, doi:10.1016/j.geomorph.2011.11.016, 2012.

Ereditato, A.: The study of neutrino oscillations with emulsion detectors, Adv. High Energy Phys., 2013, 382172, doi:10.1155/2013/ 382172, 2013.

Fisher, E., McMechan, G. A., Gorman, M. R., Cooper, A. P. R., Aiken, C. L. V., Ander, M. E., and Zumberge, M. A.: *Determination of bedrock topography beneath the Greenland ice sheet by three-dimensional imaging of radar sounding data*, J. Geophys. Res., 94, 2874–2882, doi:10.1029/JB094iB03p02874, 1989.

Fujii, H., et al.: *Performance of a remotely located muon radiography system to identify the inner structure of a nuclear plant*, Prog. Theor. Exp. Phys., 2013, 073C01, doi:10.1093/ptep/ptt046, 2013.

Groom, D. E., Mokhov, N. V., and Striganov, S. I.: *Muon stopping power and range tables 10 MeV–100 TeV*, At. Data Nucl. Data Tables, 78, 183–356, doi:10.1006/adnd.2001.0861, 2001.

Haino, S., et al.: *Measurements of primary and atmospheric cosmic-ray spectra with the BESS-TeV spectrometer*, Phys. Lett. B, 594, 35–46, doi:10.1016/j.physletb.2004.05.019, 2004.

Hebbeker, T., and Timmermans, C.: *A compilation of high energy atmospheric muon data at sea level*, Astroparticle Physics, 18, 107–127, doi:10.1016/S0927-6505(01)00180-3, 2002.

Hock, R., Iken, A., and Wangler, A.: *Tracer experiments and borehole observations in the overdeepening of Aletschgletscher, Switzerland*, Ann. Glaciol., 28, 253–260, 1999.

Horberg, L., and Anderson, R. C.: *Bedrock topography and Pleistocene glacial lobes in central United States*, J. Geol., 64, 101–116, doi:10.1086/626328, 1956.

Huss, M., Bauder, A., Funk, M., and Hock, R.: *Determination of the seasonal mass balance of four Alpine glaciers since 1865*, J. Geophys. Res., 113, F01015, doi:10.1029/2007JF000803, 2008.

Huss, M.: *Density assumptions for converting geodetic glacier volume change to mass change*, The Cryosphere, 7, 877–887, doi:10.5194/tc-7-877-2013, 2013.

Jourde, K., Gibert, D., Marteau, J., de Bremond d'Ars, J., and Komorowski, J.: *Muon dynamic radiography of density changes induced by hydrothermal activity at the La Soufrière of Guadeloupe volcano*, Sci. Rep., 6, 33406, doi:10.1038/srep33406, 2016.

Kremer, J., et al.: *Measurements of ground-level muons at two geomagnetic locations*, Phys. Rev. Lett., 83, 4241–4244, doi:10.1103/PhysRevLett.83.4241, 1999.

Lesparre, N., Gibert, D., Marteau, J., Déclais, Y., Carbone, D., and Galichet, E.: *Geophysical muon imaging: Feasibility and limits*, Geophys. J. Int., 183, 1348–1361, doi:10.1111/j.1365-246X.2010.04790.x, 2010.

Murray, T., Booth, A., and Rippin, D. M.: *Water-content of glacier-ice: Limitations on estimates from velocity analysis of surface ground-penetrating radar surveys*, J. Environ. Eng. Geophys., 12, 87–99, 2007.

Nishio, A., Morishima, K., Kuwabara, K., and Nakamura, M.: *Development of nuclear emulsion detector for muon radiography*, Physics Procedia, 80, 74–77, doi:10.1016/j.phpro.2015.11.084, 2015.

Nishiyama, R., Taketa, A., Miyamoto, S., and Kasahara, K.: *Monte Carlo simulation for background study of geophysical inspection with cosmic-ray muons*, Geophys. J. Int., 206, 1039–1050, doi:10.1093/gji/ggw191, 2016.

Nishiyama, R., Miyamoto, S., Okubo, S., Oshima, H., and Maekawa, T.: *3D density modeling with gravity and muon-radiographic observations in Showa-Shinzan lava dome, Usu, Japan*, Pure Appl. Geophys., 174, 1061, doi:10.1007/s00024-016-1430-9, 2017.

I.10 Supporting information

I.10.1 Introduction

This document explains the details of the muon flux simulation (Ch. I.10.2) and the rock bulk density measurements (Ch. I.10.3 and Table I.SI.1). As supporting information, the angular distribution of muon data (Data Set S1) and the bedrock shape reconstructed from muon absorption analysis (Data Set S2) are online provided as separate files (*https://doi.org/10.1002/2017GL073599)*.

Data Set S1. The direction data of all the muons observed at the three detectors (D1-3) are listed. The position of the detector is given in the Swiss coordinate system (CH1903). The detector orientation is described by an azimuth angle (measured clockwise from a north base line) and an inclination angle. The effective area and the exposure time are given for each detector. The direction of the each detected muon is described as "slope x" and "slope y". These are original data used to produce Figure I.3a.

Data Set S2. The positions of the bedrock-ice boundary reconstructed for each bin are given in the Swiss coordinate system (CH1903). The first three columns show the best fit position, the next three the lower limit of 1 sigma (68 %) confidence level and the last three the upper limit.

I.10.2 Muon flux simulation

The muon simulated flux F^{sim}, to be compared with the observed flux F^{obs}, is calculated following the methods summarized in Lesparre et al. (2010). Here the crucial and modified parts are described.

To calculate the flux of penetrated muons, the energy spectrum $\Phi(p, \theta, h)$ must be precisely evaluated at a given momentum p, arrival direction (zenith angle θ) and altitude h. We employ the model proposed by Reyna et al. (2006), which predicts the muon energy spectrum $\Phi(p, \theta, h = 0\ m)$ at the sea level. Since our observation is performed at a high altitude (~ 3500 m), the flux altitude dependence due to muon decay (muons are unstable particles with a lifetime of 2.2 μs) must be properly taken into account. The altitude dependence can be described as $\Phi(p, \theta, h) = \Phi(p, \theta, 0) \exp(h/L)$ where $L = 4900\ m + 750\ m \cdot p\ (GeV/c)$ (Hebbeker & Timmermans, 2002). This formula is only valid up to 1000 m a.s.l. For our purposes, we adapted this formula to $L = 3400\ m + 1100\ m \cdot p\ (GeV/c) \cdot \cos\theta$ to fit the energy spectra up to 4000 m a.s.l. in the Monte Carlo simulation by COSMOS simulator (see Nishiyama et al., 2016b for details). This new formula is valid for a wider momentum range (p > 3 GeV/c), a zenith angle range ($0° \leq \theta \leq 70°$) and an altitude (h < 4000 m).

If the density (ρ) is given, the amount of obstacles (often referred to as density-length or opacity in literature) is calculated by multiplying the length of the obstacle along the muon trajectory (L) as $X = \rho L$ (unit: g cm^{-2}). The minimum momentum (p_{min}) values of muons to penetrate the thickness X of standard rock were tabulated by Groom et al (2001). The standard rock (<A> = 22, <Z> = 11) is a virtual material commonly used to estimate the muon flux in undergrounds. Furthermore, we should consider the effect of glacial ice on muon energy loss, but, in this observation, its contribution is negligible because the minimum momentum for muons to pass through 100 m of rock is merely ~ 50 GeV/c. At

this momentum value, the continuous (ionizing) muon energy loss is still dominant compared to the stochastic loss such as Bremsstrahlung. The contribution of stochastic loss has only to be considered for a thickness > 1 km.

The flux of muons after passing through material is calculated by integrating the energy spectrum $\Phi(\mathrm{p}, \theta, \mathrm{h})$ above $\mathrm{p}_{\mathrm{min}}$ to infinity. $\mathrm{F}^{\mathrm{sim}}$ is obtained as the average of the simulated flux in one hundred bins (10 x 10) to cope with the rough surface topography of the mountains and the glacier. The uncertainty on the simulated flux arises mainly from that of the spectrum model. Comparisons between our modified Reyna model and the observed energy spectra reported by several independent experiments (Kremer et al., 1999; Haino et al., 2004; Allkofer et al., 1985) suggest that the systematic uncertainty on the flux simulation is less than 15 % within a thickness of 150 m.w.e. (equivalent to 30 GeV/c) and a zenith angle range from $0°$ to $70°$.

I.10.3 Rock bulk density measurements

The bedrock in our observation field consists of a migmatitic, granitic gneiss of the Innertkirchner-Lauterbrunnen Complex (Abrecht, 1994; Schaltegger, 1993). In total 14 samples were taken both in the railway tunnel and along the surface (see Figure I.5c for sample locations). Sample sites were selected to cover the entire range of encountered bedrock types and to avoid sites with structural weaknesses (such as brittle fault zones, open joints) or secondary formed minerals (e.g. joint fillings) as the collected samples must be representative for the whole rock volume. The collected sample were heavier than 1.5 kg, which yielded sufficient material to prepare spare samples, where we have split the original material into at least 3 sub-samples maintaining representativeness. Additionally, we explored the material for the grain size distributions and microstructures through thin section analyses, and we measured bulk mineral compositions on crushed and powdered samples using X-Ray Powder Diffraction (XRPD), thereby applying the Rietveld structural refinement method (Rietveld, 1969).

The bulk density (ρ_{bulk}) of rocks depends on (1) the mineral composition (densities and volume fractions), (2) the porosity (pores, fractures) and (3) the density of possible pore fillings. Bulk density is therefore given by $\rho_{bulk} = (1 - \phi) * \rho_{grain} + \phi * \rho_{fill}$ with $\rho_{grain} = \sum_i^n \rho_i * V_i$ where ρ_i is the density, V_i is the corresponding volume fraction and ϕ the total porosity, which is the sum of volumes related pores, fractures and their infill (Schön, 2015). Bulk densities were determined through volume measurements based on Archimedes' principle by suspending samples coated with paraffin wax into water (Blake & Hartge, 1986; ASTM C914-09, 2015). Coating was necessary due to presence of connected porosity and the resulting degassing of the samples in different auxiliary liquids (e.g. different paraffin oils). The paraffin for coating was heated to 45-50°C to prevent degassing and exploiting the immediate solidification on the sample surface due to the cooling effect of the lower tempered sample (~22°C). Paraffin density was obtained by measuring the buoyancy of cubes that were cut from the separated wax, that we used for coating upon immersion in water. Additionally, the grain density was measured on the powdered sample using an AccuPyc 1340 He-pycnometer. Values given in table I.SI.1

are averages of at least 5 individual measurements (3 for bulk density) and given uncertainties (1 sigma) are propagated errors that account both for accuracy and precision.

Table I.SI.1. Measured sample averages for the 14 rock samples taken along the tunnel and on the surface. ρ_{grain}: grain density in g cm^{-3}, ρ_{bulk}: bulk density in g cm^{-3}, av. ϕ: average porosity calculated under the assumption of air filled pores using the relation described in Section SI.2, sample coordinates were converted to WGS84 from Swiss Coordinate system (CH1903).

Sample	ρ_{grain}	± 1 σ	ρ_{bulk}	± 1 σ	av. ϕ	Sample Location (WGS84)
JT-01	2.71	0.007	2.66	0.014	2.07%	7.98544E 46.54766N Elev. 3478 m
JT-02	2.76	0.013	2.68	0.032	3.56%	7.98764E 46.54895N Elev. 3422 m
JT-19	2.73	0.004	2.71	0.011	1.11%	7.98743E 46.54884N Elev. 3427 m
JT-20	2.79	0.004	2.73	0.020	2.23%	7.98735E 46.54880N Elev. 3429 m
JT-21	2.77	0.003	2.74	0.017	1.74%	7.98708E 46.54862N Elev. 3436 m
JT-22	2.74	0.004	2.70	0.015	1.09%	7.98699E 46.54857N Elev. 3438 m
JT-23	2.79	0.004	2.72	0.023	1.22%	7.98688E 46.54850N Elev. 3441 m
JT-24	2.75	0.004	2.69	0.016	2.01%	7.98679E 46.54844N Elev. 3443 m
JT-25	2.73	0.004	2.71	0.020	0.92%	7.98596E 46.54792N Elev. 3466 m
JT-26	2.74	0.004	2.69	0.016	1.49%	7.98584E 46.54785N Elev. 3468 m
JT-27	2.74	0.017	2.70	0.016	1.02%	7.98573E 46.54779N Elev. 3471 m
JT-28	2.75	0.004	2.65	0.016	3.42%	7.98543E 46.54766N Elev. 3478 m
SX-03	2.71	0.003	2.67	0.013	0.72%	7.98350E 46.54687N Elev. 3512 m
SX-04	2.75	0.003	2.70	0.024	1.86%	7.98350E 46.54687N Elev. 3512 m

I.10.4 References

Abrecht, J.: *Geologic units of the Aarmassif and their pre-Alpine rock associations: A critical review*, Schweizerische Mineralogische Und Petrographische Mitteilungen, 74, 5–27, doi:10.5169/seals-56328, 1994.

Allkofer, O. C., Bella, G., Dau, W. D., Jokisch, H., Klemke, G., Oren, Y., and Uhr, R.: *Cosmic ray muon spectra at sea-level up to 10 TeV*, Nuclear Physics B, 259, 1–18, doi:10.1016/0550-3213(85)90294-9, 1985.

ASTM C914-09: *Standard Test Method for Bulk Density and Volume of Solid Refractories by Wax Immersion*, ASTM International, West Conshohocken, PA, doi:10.1520/C0914-09R15; www.astm.org, 2015.

Blake, G. R., and Hartge, K. H.: *Bulk Density*, in *Methods of Soil Analysis: Part 1*, Agron. Monogr. 9, 2nd ed., edited by A. Klute, pp. 363–375, American Society of Agronomy and Soil Science Society of America, Madison, 1986.

Groom, D. E., Mokhov, N. V., and Striganov, S. I.: *Muon stopping power and range tables 10 MeV–100 TeV*, At. Data Nucl. Data Tables, 78, 183–356, doi:10.1006/adnd.2001.0861, 2001.

Haino, S., et al.: *Measurements of primary and atmospheric cosmic-ray spectra with the BESS-TeV spectrometer*, Phys. Lett. B, 594, 35–46, doi:10.1016/j.physletb.2004.05.019, 2004.

Hebbeker, T., and Timmermans, C.: *A compilation of high energy atmospheric muon data at sea level*, Astroparticle Physics, 18, 107–127, doi:10.1016/S0927-6505(01)00180-3, 2002.

Kremer, J., et al.: *Measurements of ground-level muons at two geomagnetic locations*, Phys. Rev. Lett., 83, 4241–4244, doi:10.1103/PhysRevLett.83.4241, 1999.

Reyna, D.: *A simple parameterization of the cosmic-ray muon momentum spectra at the surface as a function of zenith angle*, arXiv:hep-ph/0604145, 2006.

Rietveld, H. M.: *A profile refinement method for nuclear and magnetic structures*, J. Appl. Crystallogr., 2, 65–71, doi:10.1107/S0021889869006558, 1969.

Schaltegger, U.: *The evolution of the polymetamorphic basement in the Central Alps unravelled by precise U-Pb zircon dating*, Contrib. Mineral. Petrol., 113, 466–478, doi:10.1007/BF00698316, 1993.

Schön, J.: *Physical properties of rocks: Fundamentals and principles of petrophysics*, in Developments in Petroleum Science, vol. 65, 2nd ed., 109-118, edited by J. Cubitt, Amsterdam Netherland, Elsevier, 2015.

Appendix II

Bedrock sculpting under an active alpine glacier revealed from cosmicray muon radiography

R. Nishiyama[1,2], A. Ariga[1], T. Ariga[3], A. Lechmann[4], D. Mair[4], C. Pistillo[1], P. Scampoli[1,5], M. Vladymyrov[1], P. G. Valla[6], A. Ereditato[1], and F. Schlunegger[4]

[1]Albert Einstein Center for Fundamental Physics, Laboratory for High-Energy Physics, University of Bern, Bern, Switzerland
[2]Earthquake Research Institute, The University of Tokyo, Tokyo, Japan
[3]Faculty of Arts and Science, Kyushu University, Fukuoka, Japan
[4]Institute for Geological Sciences, University of Bern, Bern, Switzerland
[5]Dipartimento di Fisica "E.Pancini", Università di Napoli Federico II, Naples, Italy
[6]Institut des Sciences de la terre – CNRS, Université Grenoble Alpes, Grenoble, France

Published in: Scientific Reports, 9, 6970, https://doi.org/10.1038/s41598-019-43527-6, 2019.

II.1 Abstract

Mountain glaciers form landscapes with U-shaped valleys, roche moutonées and overdeepenings through bedrock erosion. However, little evidence for active glacial carving has been provided particularly for areas above the Equilibrium Line Altitude (ELA) where glaciers originate. This is mainly due to our lack of information about the shape of the bedrock underneath active glaciers in highly elevated areas. In the past years, the bedrock morphology underneath active glaciers has been studied by geophysical methods in order to infer the subglacial mechanisms of bedrock erosion. However, these comprise surveys on the glaciers' surface, from where it has been difficult to investigate the lateral boundary between the ice and the bedrock with sufficient resolution. Here we perform a muon-radiographic inspection of the Eiger glacier (Switzerland, European Alps) with the aid of cosmic-ray muon attenuation. We find a reach (600 × 300 m) within the accumulation area where strong lateral glacial erosion has cut nearly vertically into the underlying bedrock. This suggests that the Eiger glacier has profoundly sculpted its bedrock in its accumulation area. This also reveals that the cosmic-ray muon radiography is an ideal technology to reconstruct the shape of the bedrock underneath an active glacier.

II.2 Introduction

Glaciers play an important role in limiting the height of mountain ranges and in shaping alpine-type landscapes, which are commonly characterized by U-shaped valleys, cirques and steep-edged ridges along their thalwegs (Hallet, 1979, 1996; Brocklehurst and Whipple, 2002; Egholm et al., 2009). Glaciers deepen and widen pre-existing valleys through processes referred to as abrasion and quarrying/plucking (Hallet, 1979, 1996). Theory and observations predict that glacial erosion is proportional to the sliding velocity raised to some power (Pederson and Egholm, 2013; Herman, 2015).

In addition, the sliding velocity has been considered to depend on both the basal shear stresses and the fluid pressure ratio, where higher values result in either an increase (shear stress) or a decrease (fluid pressure) in the erosion rates (Bindschadler, 1983; Herman et al. 2011). Modern erosion rates under glaciers have been studied from sediment yields and provenance tracing of material in subglacial streams (Godon et al., 2013; Herman, 2015). The erosional efficiency of glaciers is known to vary greatly depending on location, climate, strength of the bedrock, energy gradient and ice thickness (Hallet, 1979, 1996; Hallet et al., 1996; Brocklehurst and Whipple, 2002; Egholm et al., 2009; Herman et al., 2011; Pederson and Egholm, 2013; Herman, 2015). In this context, a major question arises about the potential of extrapolating short-term observations to the timescales over which glacial landscape with typical U-shaped cross-sectional valleys and stepped longitudinal profiles form, which typically develop over multiple glacial cycles (i.e. tens to hundreds of thousand years; Valla et al., 2011; Pederson and Egholm, 2013). Although various numerical models with a particular focus on subglacial erosion have been performed to reproduce glacial landscapes (Herman et al., 2011, 2018; Pederson and Egholm, 2013), these rely strongly both on our knowledge of the ice rheology and the ice-flow mechanisms, as well as on observational data of the glacial bedrock morphology. This potential lack of knowledge on the details of the erosional mechanisms and the underlying physical controls also concerns the questions of how glacial cirques are formed, and how subglacial processes actively sculpt the underlying bedrock (Hooke, 1991; MacGregor et al., 2009; Sanders et al., 2010, 2012) in these high-elevation regions.

A key information for improving our understanding of the landscape response to glacial erosion is offered by the bedrock topography from past-glaciated areas and beneath present-day active glaciers, mainly because the bedrock topography directly reflects the erosional patterns and mechanisms at work underneath a glacier (Brocklehurst and Whipple, 2002, 2004; Herman et al., 2011). This has been the major motivation for (1) exploring the bedrock topography using drilling information to map the landscape response to past glaciations (Dürst Stucki and Schlunegger, 2013); and (2) employing several geophysical techniques including seismic surveys and gravity measurements, ground penetrating radar surveys, and topographic modelling to reconstruct the bedrock topography of formerly glaciated areas or underneath active glaciers (Fisher, 1989; Adams and Hinze, 1990; Sharp, 1993; Annecchione et al., 2001; Studinger et al., 2004; Barnaba et al., 2010; Huss and Farinotti, 2012; Mey et al., 2016). Despite the progress of such technologies, the bedrock morphology along the sides of a glacier, particularly in remote high-elevation alpine areas, has been hardly constrained, because these methods are mainly performed from above the glaciers' surfaces. In addition, most of the alpine cirques are hardly accessible particularly in their accumulation areas where they originate. Where surveys were possible, the resolution of the data decreases rapidly towards the glaciers' bases and lateral sides. This is related to (1) the presence of non-consolidated sediment deposits on the glacier margin and (2) the steep dip of the bedrock surface underlying most of the surveyed glaciers. In addition, in the case of temperate glaciers, high fluid pressure ratios lower the resolution of seismic and radar surveys (Murray et al., 2007; Schrott

and Sass, 2008), thereby thwarting a high-resolution reconstruction of the bedrock shape underneath modern glaciers.

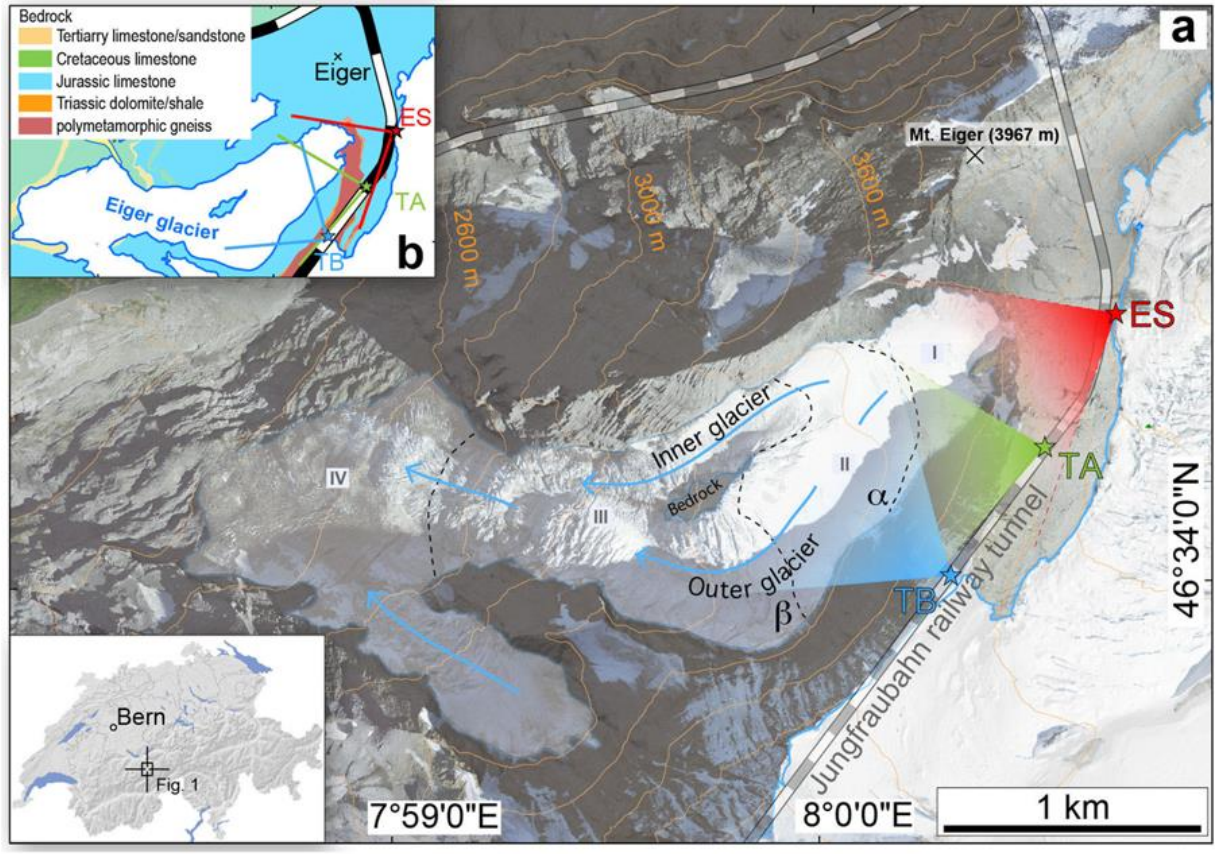

Figure II.1. Overview of the study site in the Central Swiss Alps. (a) Eiger glacier with distinct morphological domains (I to IV; see main text for discussion) and railway tunnel. Subsurface detector sites (ES: Eismeer station, TA: tunnel site A, TB: tunnel site B) are given with the corresponding view field. (b) Simplified geological map (Mair et al., 2018) illustrating the main rock types of the study area. The topographic data of both figures has been reproduced with permission by swisstopo (BA18111).

In the present work we apply the cosmic-ray muon radiography technology to map the lateral margin of the Eiger glacier (Fig. II.1) situated in Switzerland (Central European Alps at 46°34′05″N latitude and 7°59′56″E longitude). This method is based on the high penetration power of cosmic-ray muons that hit the Earth's surface continuously (Patrignani et al., 2016), where the attenuation rate of the muon flux mainly depends on the density of the traversed material (Nishiyama et al., 2017). The idea dates back to 1955 with the measurements of the thickness of rock above an underground tunnel (George, 1955), followed by the pyramid's inspection by L. Alvarez in 1970's (Alvarez et al., 1970), and it has spread to multiple fields such as volcanology (Tanaka et al., 2007; Carbone et al., 2014), geology (Guardincerri et al., 2017), and the non-destructive inspection of reactors (Fujii et al., 2013) in the past decade. In 2015, Nishiyama et al. (2015) launched a pilot survey for the application of such a technology in an Alpine environment using emulsion films as muon detectors. These authors successfully mapped a small portion of the bedrock underneath the uppermost part of the Aletsch glacier (Central European Alps) over an area of c. 50 × 100 m2. Based on the success of this pilot work, the present study aims at imaging

of a much larger region where a glacier originates and where active erosion and bedrock sculpting are likely to occur.

Muon radiography requires muon detectors to be placed at an elevation lower than the surveyed target because of the downward going path of cosmic rays. We benefited from the railway tunnel of the Jungfraubahn, which runs through the bedrock surrounding and beneath the headwall reaches of the Eiger glacier (Fig. II.1). In 2017, we installed muon detectors made of emulsion films at three sites along this tunnel (sites ES, TA and TB, Fig. II.1). Emulsion films, which have been applied in various experiments on fundamental physics (Ereditato, 2013; Ariga et al., 2018), record the trajectories of incoming muon particles, which can be observed with optical microscopes as sequences of tiny silver grains after chemical development (Ariga et al., 2018). The microscopic analysis of the films allowed the attenuation pattern of muon intensity to be measured (Ariga et al., 2018), which in turn gives the information on the density of overburden material (Nishiyama et al., 2017). The observed density information is then quantitatively converted to the location of the boundary separating the low-density ice from the high-density bedrock (Nishiyama et al., 2017), providing a unique and high-resolution reconstruction of the bedrock topography at the bottom and lateral margins of the Eiger glacier.

II.3 Results

II.3.1 Morphology of the Eiger glacier

We explored the morphology of the Eiger glacier, which is the target of our survey (Fig. II.1). The nearly 2.1 km^2 large glacier originates on the western flank of Mt. Eiger at approximately 3600 m a.s.l., from where it flows and terminates at an elevation of approximately 2400 m a.s.l. over a length of c. 2 km (Fig. II.1). The bedrock geology of the study area comprises a suite of NW-dipping recrystallized micritic limestones that display a penetrative horizontal foliation and that overly polymetamorphic gneisses (inset Fig. II.1b; Mair et al., 2018). The bedrock has thus a constant fabric and comprises the same lithology within the entire glacial catchment (Mair et al., 2018). The mean value of the bulk density of the bedrock in this region is 2.68 g cm^{-3}, determined from 16 bedrock samples (Nishiyama et al., 2017), and its standard deviation is 0.02 g cm^{-3}. The Eiger glacier consists of four morphologic domains I-IV (Fig. II.1): (I) a headwall reach forming a concave amphitheatre-shaped cirque with c. 50° steep flanks (including the headwalls), (II) a relatively flat domain, and (III) a middle segment where a prominent bedrock ridge forces the ice flow to diverge over c. 250 m distance before converging again farther downslope. There, the bedrock ridge, which most likely corresponds to a “roche moutonée” (i.e. a distinctive bump of 10–100-m scale typical of glacially-scoured landscapes with smooth abraded slopes facing upglacier, and abrupt slopes on its downglacier face), is exposed in the middle of the glacier, and the ice surface in segment (iii) is rugged and dissected by several transverse crevasses. Segment (III) also evidences a drastic change in ice-flow direction from South-West to West. The exposed bedrock ridge separates the Eiger glacier in two parts: a slip-off, steep margin situated on the inner northern-side of the glacier (referred hereafter to the “inner glacier”; Fig. II.1), and a cut-bank,

flatter glacier part on its southern outer margin (referred hereafter to the "outer glacier"; Fig. II.1). The down-slope end of segment III also lies within the altitudinal range of the modern ELA, which is situated at c. 3000 m a.s.l. (Huss and Fisher, 2016). Finally, segment IV is characterized by a terminal lobe with longitudinal crevasses and a till.

A closer inspection of the glacier morphology discloses further details, particularly along segment II where the Eiger glacier starts to separate into two branches. Downslope of segment II where the ice-flow bifurcation begins, the ice-surface strongly differs between the inner and outer glaciers. The inner glacier has a straight ice flow, with a relatively small ice surface, and the surface elevation rapidly drops from 3400 to 3100 m a.s.l. over a short distance of c. 650 m, yielding in an average surface slope of c. 25°. Contrariwise, the outer glacier follows a large bend where the ice-flow orientation changes by 90° within a few hundred meters. Along this bend, the ice-surface elevation drops of about 300 m over a distance c. 1000 m. Interestingly, this glacier segment is also the location where cuts into its bedrock wall are visible, forming two secondary concave niches α and β with a shape that is similar to an incipient cirque (Fig. II.1). While the upper niche α is situated slightly upstream the bend and only weakly developed, the lower niche β is located within the bend and characterized by a distinct concavity. The ice surface maintains a constant dip of c. 10° above the 90°-direction bend, and then steepens to c. 22° farther downslope after the flow direction has changed to the West. At this point, transverse crevasses suggest that the ice is under extension, while the absence of any crevasses along the flatter segments implies that the glacier is under compression. Visual inspection shows that the outer glacier has a surface area of c. 300,000 m^2 and is thus > 200 % larger than the inner glacier (Fig. II.1).

II.3.2 Muon attenuation pattern

Figure II.2 shows the direction of arriving muons at the three detector sites (ES = Eismeer Station, TA = Tunnel site A and TB = Tunnel site B; Fig. II.1). In these diagrams, the direction is represented as azimuth and elevation angles (θ_x, θ_y). The number of observed muons are 2.3, 5.3 and 7.9×10^3 for ES (exposure time: 106.8 days, effective area: 1512 cm^2), TA (164.9 days, 1296 cm^2) and TB (106.8 days, 1080 cm^2) sites, respectively. The population of the recorded muons is clearly anti-correlated with the thickness of the bedrock and the ice along the straight muon trajectories (Fig. II.2). Specifically, the shadows on each plot where the data density is low (sparsely distributed data points) coincide with the regions where the obstacle thickness is greater than 1 km. This indicates that most of the muons from these directions were absorbed in the thick mountain edifice. We binned these registered muons in a rectangular histogram ($\tan_{\theta x}$, $\tan_{\theta y}$) and converted the data into a normalized flux ($cm^{-2}\,sr^{-1}\,sec^{-1}$).

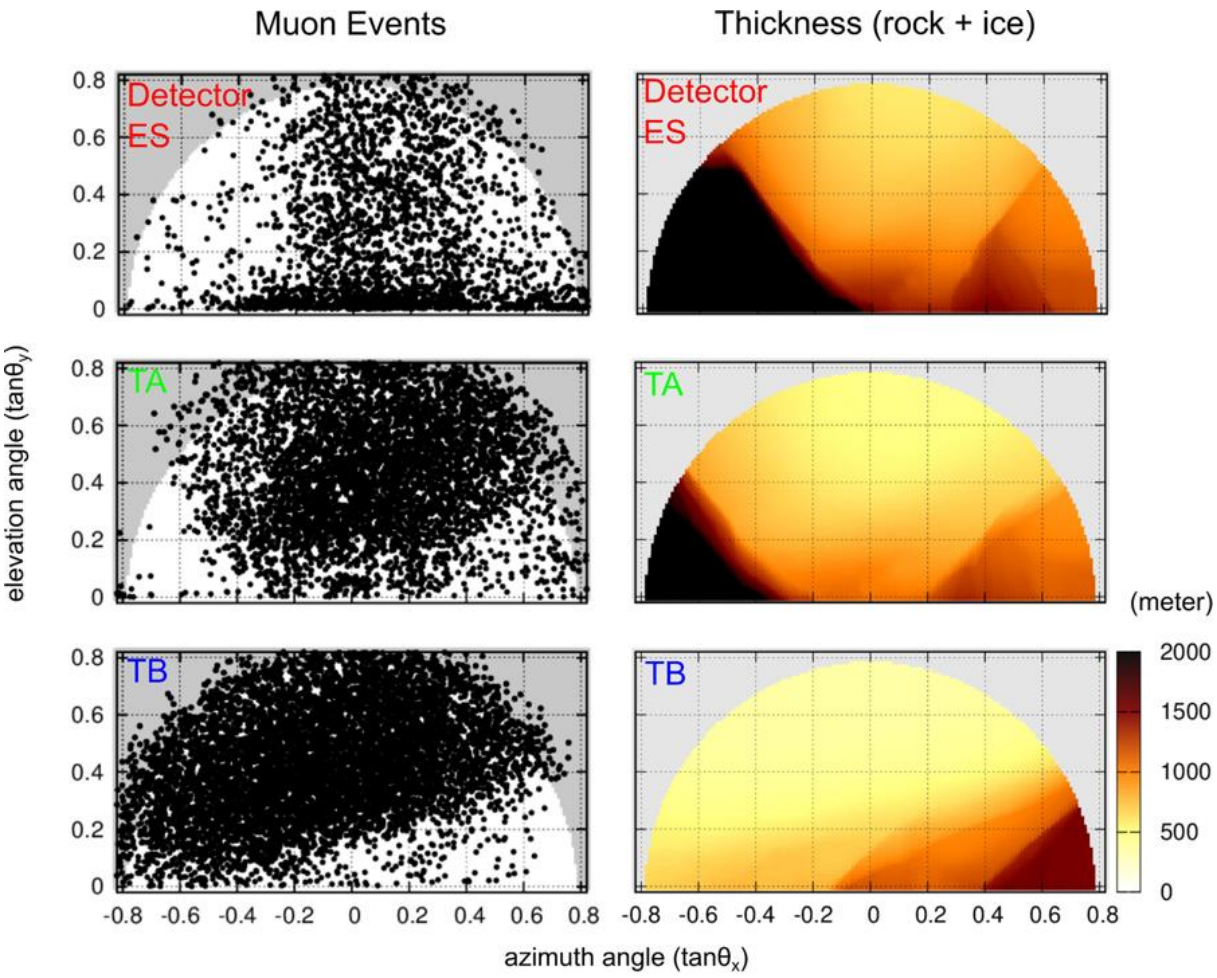

Figure II.2. Distribution of recorded muons. Angular distribution of observed tracks at site ES (top), TA (middle) and TB (bottom) with muon trajectories displayed on the left and edifice thickness (ice and/or bedrock) corresponding to muon trajectories displayed on the right. The grey region (left panels) indicates the limit of the effective angular space of the microscope. The muon events in these regions are thus not used for the attenuation quantification.

Figure II.3 illustrates how the muon flux data is used to infer the density of the traversed material. First, we focus on the flux data of muons, which passed purely inside the bedrock without crossing the glacier. Such data are available from the TA detector (Fig. II.3: open circles, and Fig. II.1 for location of detector). As seen in Fig. II.3, the flux decreases nearly exponentially with the increase of the bedrock thickness, and its attenuation depends also on the zenith angle of the muons (represented by the colours of the data points). These features of the muon flux attenuation in the bedrock are well reproduced by the simulation for different zenith angles (45°, 60° and 75°) under the assumption of a uniform bulk rock density of 2.68 g cm^{-3} (Fig. II.3: solid curves; Nishiyama et al., 2017). This agreement assures that the variety of the bulk density inside the bedrock is small, as is observed with the standard deviation of the density sampling (0.02 g cm^{-3}). On the other hand, trajectories where muons cross partially the glacial ice before arriving at the detectors yield flux values that are by a factor of up to 2 higher than these theoretical calculations (Fig. II.3: solid circles). This excess of the muon flux is due to the lower bulk density of ice compared to that of bedrock, thus allowing a higher muon transmission. We benefitted from these differences in muon attenuation between ice and rock: the magnitude of the muon flux attenuation

recorded at the different tunnel sites can be quantitatively interpreted in terms of the ice-bedrock proportion along the muons' trajectories (Nishiyama et al., 2017), which is then converted into the position of the boundary between the basal ice and its underlying bedrock. The three detectors surrounding the glacier provided information about the bedrock shape from different perspectives. The bedrock positions were first estimated for individual detectors, and the results are combined and re-sampled into a three-dimensional representation of the interface geometry (see Method section).

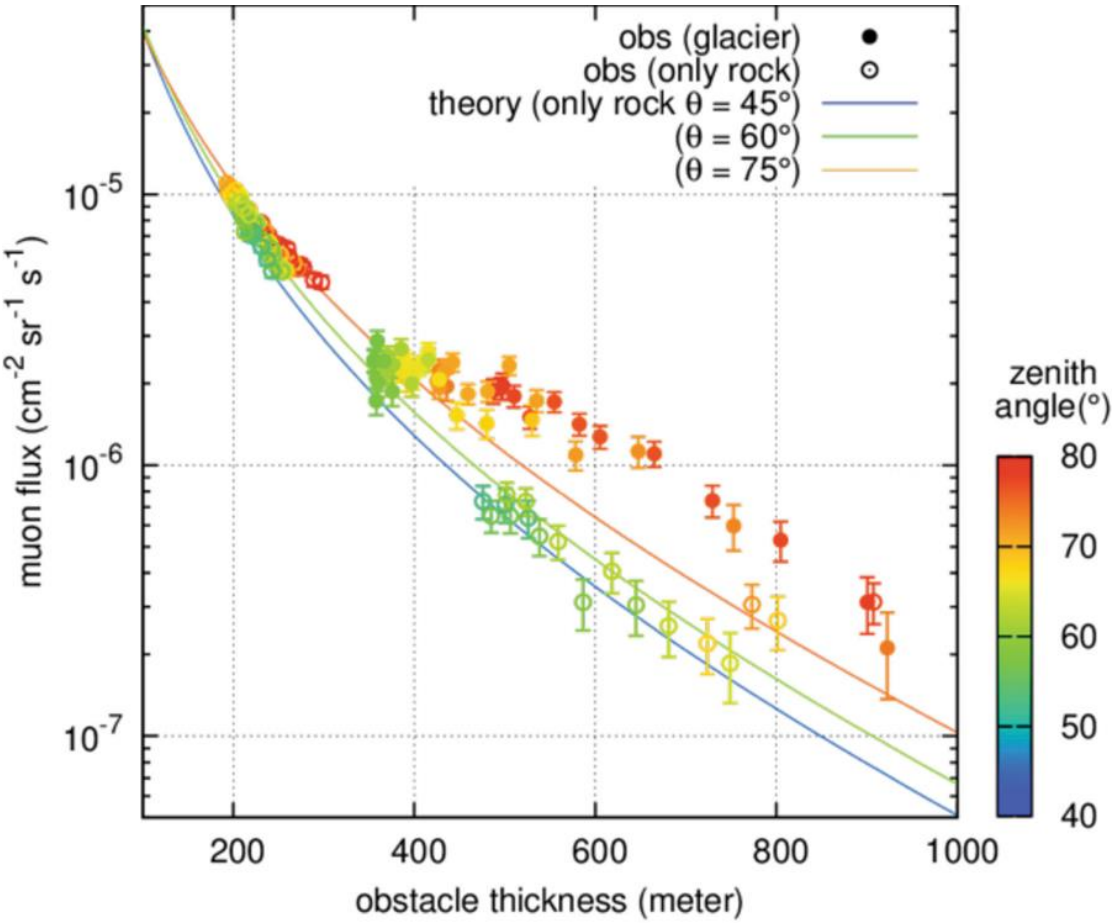

Figure II.3. Muon fluxes. Attenuation of muon flux (vertical axis) as a function of the obstacle thickness (horizontal axis). The colours of the data point represent the zenith angle of muons arriving at the detector. The open circles denote muons, which passed only through the bedrock and were observed at the TA site detector. These data are used for calibration purposes (see Method section) by comparing them with the theoretical predictions of the flux attenuation in pure rock (density 2.68 g cm^{-3}) reported as solid lines for different zenith angles (45°, 60° and 75°). The solid circles denote muons, which crossed both the ice and the underlying bedrock (displayed data are the ones from the TB site detector).

II.3.3 Reconstruction of the bedrock shape

We determined the bedrock shape underneath the Eiger glacier over a 600 m-long (NE-SW) and 300 m-wide reach (NW-SE) (Fig. II.4). This corresponds to the segment where the glacier surface is relatively flat and where it dips at c. 10° (segment II on Fig. II.1) just below the >30°–50° steep headward reach (segment I on Fig. II.1). The elevation resolution of the inferred bedrock surface ranges from 10 m (1σ) in vertical dimension along the relatively flat segment (which is very close to the TB detector), to about

30 m (1σ) in the headward reach where statistics are deteriorated due to the thick mountain edifices. The inferred glacier thickness is typically around 50 m (down-slope segment II on Fig. II.1) to 100 m (up-slope segment I on Fig. II.1). Along the thalweg axis, the bedrock surface continuously dips in the downslope direction, and neither an overdeepening nor transverse bedrock knobs could be observed (Figs 4 and 5).

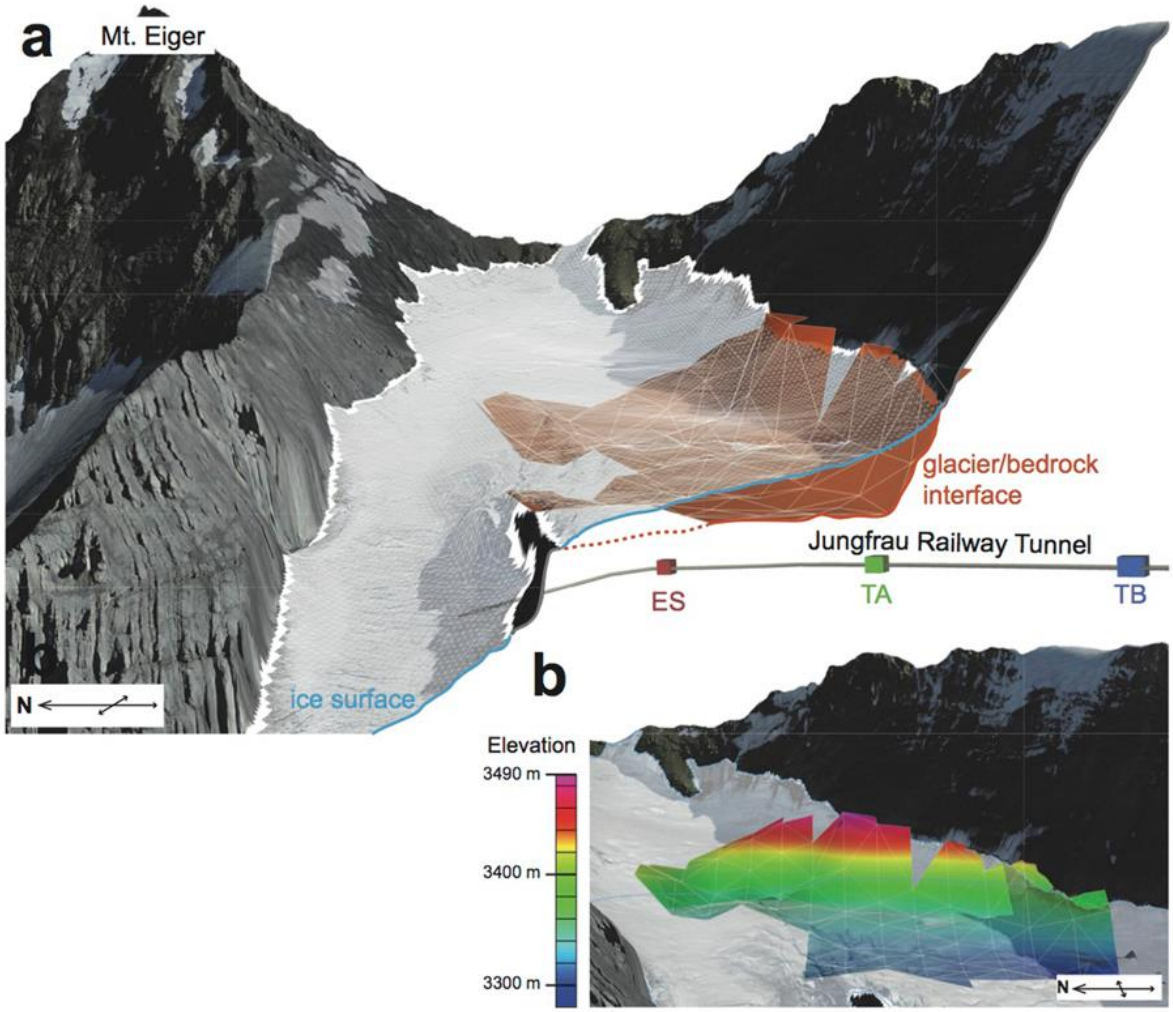

Figure II.4. Bedrock topography underneath the Eiger glacier. (a) Grid segments that were imaged by the muons at the three detector sites. (b) 3D representation of the reconstructed bedrock underneath the Eiger glacier, in which the colours indicate the altitude of the boundary between the glacial ice and the underlying bedrock. The topographic data has been reproduced with permission by swisstopo (BA18111) with a different view.

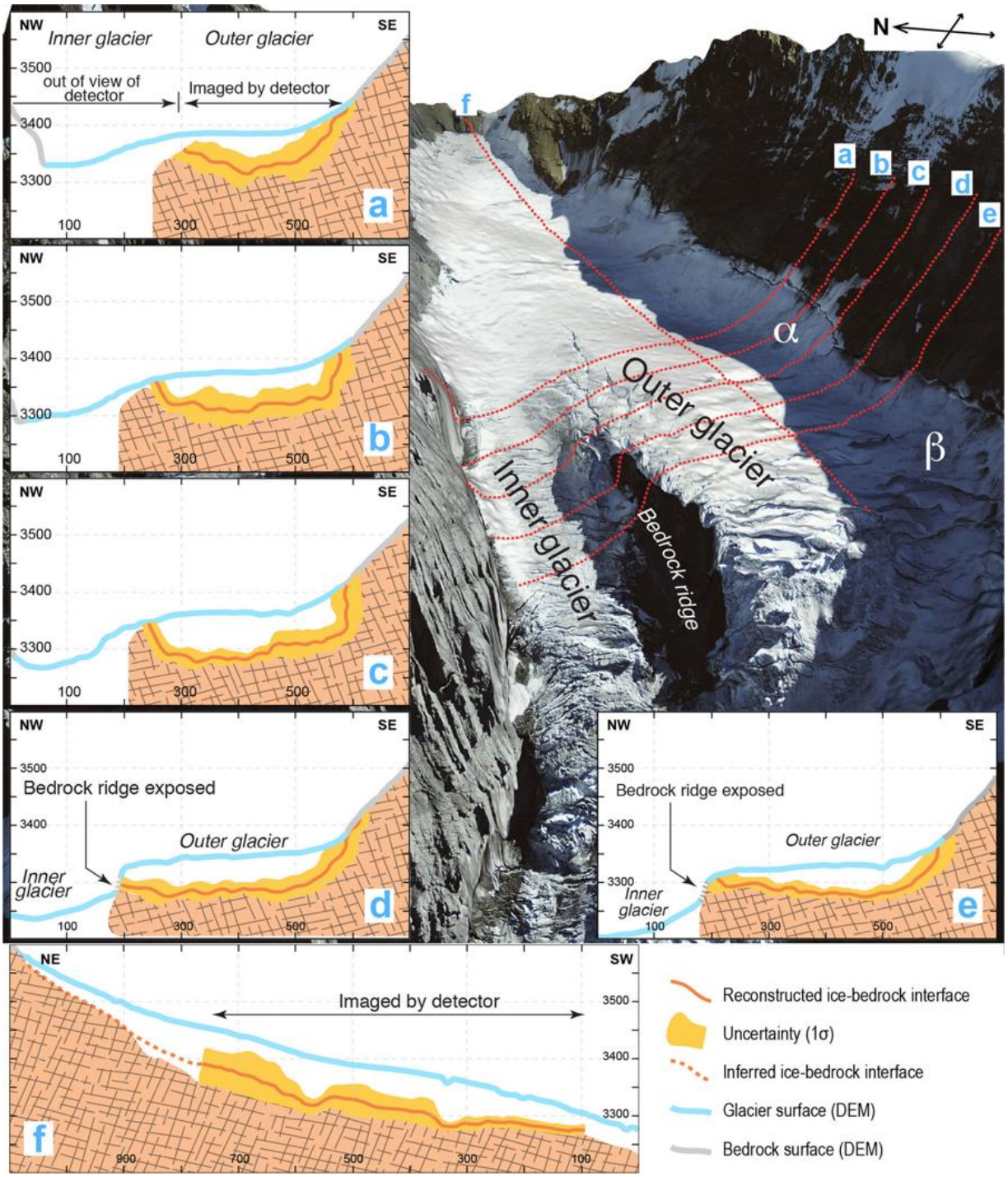

Figure II.5. Cross-sections illustrating the bedrock geometry underneath the Eiger glacier. Cross-sectional views of the reconstructed bedrock under the Eiger glacier, along five parallel locations (a) to (e) perpendicular to the flow direction, and one (f) parallel to the flow direction. Orange curves show the best-fitted bedrock positions and yellow bands show associated uncertainties (1σ) due to the statistical fluctuations of muon events. Grey and blue curves represent the hillslope topography and the ice surface. See general view (right) for location of cross- sections. The topographic data has been reproduced with permission by swisstopo (BA18111).

The cross-sectional views (Fig. II.5) present quantitative information on the bedrock shape beneath the Eiger glacier, particularly on the southern outer side of the bedrock ridge. In the up-slope reach (segment II), represented by cross-section (a) on Fig. II.5, the bedrock steeply dips at a constant angle >50° from the lateral valley wall above the glacier down to 50 m beneath the ice surface. There, the transition to the flat glacier base is gradual without any distinct break-in-slope. The situation markedly changes

farther down-slope where the boundary between the aerial and subglacial lateral margin is characterized by a sharp break-in-slope (sections (b) and (c) on Fig. II.5). There, the dip angle of the bedrock surface changes from c. 50° above the glacier to sub-vertical at the ice contact. In addition, cross-section (c) suggests that some undercutting may occur along this segment (Fig. II.5c). At c. 50–60 m depth, the cross-sectional base of the subglacial bedrock is flat and nearly horizontal, resulting in a L-shaped cross-sectional geometry of the bedrock surface underneath the ice. This is also the area where the ice surface starts to bend from a South-West to a West-oriented flow direction together with the development of a niche (α) similar to an incipient cirque (Figs 1 and 5). Farther downslope of cross-section (c), the cross-sectional geometry changes again. Above the glacier, the bedrock surface dips at 40°−50° and steepens by a few degrees at the ice surface, thus forming a break-in-slope where the bedrock plunges beneath the glacier (sections (d) and (e) on Fig. II.5). Along these sections, the base of the glacier is flat to slightly tilted towards the glacier's outer side, and the transition to the lateral margin is much more gradual than for the upslope reaches (sections (b) and (c) on Fig. II.5).

While the outer glacier is covered by many muon trajectories (Figs 1 and 5), the inner glacier on the northern side of the bedrock ridge is out of the field views of the detectors. Therefore, the elevation of the bedrock underneath the inner glacier has to be constrained through indirect evidence. Here, we use information from the elevation of the bedrock ridge itself (Fig. II.5) to infer the elevation of the bedrock underneath the inner glacier. In particular, the bedrock depth along the outer glacier is situated at the same elevation, or even higher, than the ice surface of the straight inner glacier at least along cross-sections 'd' and 'e' in Fig. II.5. This suggests that the underlying bedrock underneath the steep and straight inner glacier is likely to be at a lower elevation than the reconstructed bedrock below the outer glacier, at least along a section perpendicular to the ice flow.

II.4 Discussion

We verify our subglacial bedrock reconstruction within the Eiger headward region (segments I and II) following two pieces of evidence. First, the reconstructed bedrock positions agree with the mapped hillslope walls above the lateral glacier margin (Fig. II.5). Second, the reconstructed bedrock positions also match with the domain where the bedrock is partially exposed. This is mainly the case for the bedrock ridge that separates the inner from the outer glacier (cross-sections in Fig. II.5). These observations are supporting evidence for a reliable performance of the muon-flux attenuation analysis and the related calibration for our study site (see Methods). The muon radiography method thus yields quantitative information on the ice thicknesses (c. 10–30 m precision) of remote Alpine glaciers, if suitable detector sites such as natural bedrock galleries or tunnels are available underneath the target glacier. We thus propose that the technology of cosmic-ray muon radiography with emulsion detectors offers a quantitative tool that complements established geophysical methods (Horberg and Anderson, 1956). In the case of the Eiger glacier, the steep bedrock slopes below the glacier even sharpen the density contrasts in the retrieved muon-derived images, while other methods (such as seismic or radio-

echo soundings) often fail to yield information with acceptable resolution for similar bedrock geometries. Moreover, our present survey suggests that this novel technology works well in remote and harsh environments with the advantage of the emulsion films as muon detectors. The emulsion films showed an excellent performance in the remote and cold environment during the entire measurement period (spanning several months) without electricity or regular maintenance. This passive and robust feature of the measurement device cannot be attained by electronic detectors such as digital detectors including plastic scintillation and gaseous detectors, which have so far been applied to muon radiography in many prior works (Ambrosino et al., 2015; Jourde et al., 2016; Asorey et al., 2017; Saracino et al., 2017; Oláh et al., 2018).

With respect to the Eiger glacier and its erosional mechanisms, the most prominent result of our work is the reconstructed shape of the lateral margin along the outer glacier. In the upper reach of our surveyed area (section (a) on Fig. II.5), the shape of the bedrock-ice interface is characterized by a generally smooth transition from the lateral margin to the base of the glacier. In the reach where the glacier begins to curve and where a bedrock niche points to the occurrence and possibly ongoing development of an incipient cirque, the bedrock underneath the lateral glacier margin appears much steeper than the exposed hillslope (sections (d) and (e) on Fig. II.5) and almost vertical-to-overhanging in some reaches (sections (b) and (c) in Fig. II.5). Such bedrock-slope variations over short distances (few tens to hundred meters) require a strong lateral and headward erosional component to shape the nearly vertically-oriented margin of the subglacial bedrock. Interestingly, this is also the glacier segment where no crevasses are observed on the ice surface. This implies that the glacier is likely under compression along this reach, which provides a precondition for erosion on the lateral margin of a glacier to occur. Along the inner glacier reach, vertical glacial carving has been more efficient than along the outer curved glacier. We based this inference on the observation that the subglacial bedrock under the inner glacier is situated at lower elevations than along the outer curved reach.

The erosional mechanisms of an alpine glacier, related efficiencies and controls thereof have been explored through both empirical observations and numerical investigations over the past decades. This resulted in the overall notion that the local erosional capacity of an Alpine glacier depends on its flow velocity raised to some power, modulated by different controlling factors such as subglacial hydrology, fracture spacing of the underlying bedrock and debris concentration in the basal ice (Braun et al., 1999; Egholm et al., 2009; Herman et al., 2011; Sternai et al., 2013; Herman, 2015; Ugelvig et al., 2016). It has also been proposed that the ice-flow velocity and the basal shear stresses are closely related, where shear increases with flow velocity raised to some power (Herman, 2015). This likewise suggests that subglacial erosion and thus the glacial impact on mountainous landscapes exponentially increase with the basal shear stress at the ice-bedrock interface. Under warm-based glaciers, shear stresses and erosion rates can also be modulated by the subglacial hydrology (Herman et al., 2011). In the case of the Eiger glacier, the curved geometry of the glacier reaches along the outer part of segments II and III may additionally result in a highly asymmetric pattern of shear stresses and flow velocities due to the

curvature. This is explained by the contrasts in the slopes between the inward and outward segments of a curved glacier. As a consequence, the flow velocity and stress centre line, commonly situated in the middle of a straight glacier, may be shifted toward the inner side of a bend, where the amount of this shift increases with the curvature of the ice flow[51]. We use these mechanisms to explain the lower depth at which the bedrock has been carved along the straight and steep inner reach of the Eiger glacier (Fig. II.5).

While the larger bottom shear stresses along the straight inner glacier could be invoked to interpret the lower elevations of the bedrock topography (see cross-sections of Fig. II.5), these mechanisms alone are not capable of explaining the nearly vertical lateral dip of the ice-bedrock interface along the southern margin of the outer glacier. Such an erosional component, operating on the side of a glacier, requires substantial shear stresses on the lateral ice margin. This suggests that glacial erosion depends not only on the ice thickness and the slope, but also on the momentum of the flowing ice particularly where glaciers appear under compression (segment II, Fig. II.1). Ice flow thus shows similarities with a fluid when considering the erosional mechanisms: both apparently have a vertical and a lateral component where concave banks can experience stronger erosion. This L-shape sculpting acts to widen the glacial thalweg in the lateral direction with a strong over-steepening of the lateral margin. After the glacier retreats, such oversteepened cliffs would be exposed above the glacier and collapse due to the loss of mechanical support or activated hillslope/fluvial processes[52]. This could be a reason why we do not observe this morphology in deglaciated areas. Alternatively, the oversteepened bedrock could represent the headwall of an incipient cirque, which additionally feeds, or starts to feed, the Eiger glacier from the southwest. We base this inference on the plan-view shape of the ice margin, which is nearly straight along segment I (Fig. II.1) and then curves towards the headwall in the middle of segment II. Accordingly, the vertical to nearly over steepened glacier margin, which was imaged through the cosmic-ray muon radiography (sections (b) and (c) of Fig. II.5) better reflects the erosional work along the cirque headwall through backward erosion.

The search for the controls on cirque wall retreat has received much attention in the past years (MacGregor et al., 2009; Sanders et al., 2010; Herman et al., 2018), yet with diverging conclusions, which range from bedrock shattering through freeze-thaw cycles (Scherler, 2014), to bedrock carving in response to rotational flow of ice, and to quarrying (MacGregor et al., 2009). In addition, using numerical simulations where glacial erosion has been treated as a function of basal sliding, McGregor et al. (2009) proposed that cirques are preferentially formed hundreds of meters below the ELA, and several studies suggested that the position of the cirque floor may reflect the averaged ELA position over multiple glacial-interglacial cycles (MacGregor et al., 2009; Anders et al., 2010; Mitchell and Humphries, 2014). Because our results highlight the occurrence of erosional carving at the inferred incipient cirque, and since the modern ELA (and thus also the long-term averaged ELA) is lower than the elevation of this incipient cirque, we suggest that glaciers are also capable of efficient headwall scouring above the ELA. In addition, the bedrock geometry underneath the cirque does correspond to

the shape that is expected if a rotational flow, paired with shear along the lateral margin, is responsible for the occurrence of cirque wall retreat, supporting current views on the erosional mechanisms of glaciers and cirque evolution.

As a summary, we have illustrated a successful application of the cosmic-ray muon radiography, where we reconstructed the bedrock topography under an active glacier over an area of several hundreds of meters. Our results suggest that this technology is capable for mapping the interface between ice and bedrock at a resolution of 10–30 m, suitable for this study. It also allows the imaging of steep and nearly overhanging boundaries between ice and bedrock, which would not be depicted with other geophysical methodologies. From a geomorphological perspective, the results of our survey imply that active glacial backward erosion does occur in the accumulation area above the modern ELA (situated at c. 3000 m a.s.l., Huss and Fisher, 2016) and that this mechanism can be invoked to explain the formation and the long-term evolution of glacial cirques. Further high-resolution constrains on the bedrock topography for high-elevation glaciers will allow us to improve our understanding on the erosional mechanisms at work in cirque environments where glaciers originate.

II.5 Methods

II.5.1 Emulsion detectors and analysis

Double-side coated emulsion films were used as muon detectors (Ariga et al., 2018). The thicknesses of the plastic base and emulsion layers were 180 μm and 60 μm, respectively. The emulsion gels, which were produced by the Nagoya University (Nishio et al., 2015), were poured onto the plastic base at the underground facility at the University of Bern. The produced films were transported to the experiment sites and installed in the detector frames mounted onto the wall of the railway tunnel. In the detector frames, five or six films were layered, and 2-mm-thick stainless steel plates were inserted between each adjacent film (Nishiyama et al., 2016). The location and size of the detectors, as well as the exposure time are reported in Table II.1.

The films were chemically developed after extraction and scanned with the automated readout microscopes at the Laboratory for High Energy Physics, at the University of Bern. The microscope consists of a CMOS camera, a motorized microscope stage and illumination (Ariga et al., 2018). This allows to take tomographic profiles of silver grains in the emulsion layers and to measure the position and direction of incident charged particles (Ariga et al., 2018). The procedure is as follows: (i) a sequence of silver grains in each emulsion layer is selected as muon track candidates (micro-tracks); (ii) micro-tracks from two layers of a film, which penetrate the plastic base in a straight way, are selected (base-tracks); (iii) base-tracks aligned in consecutive films are identified as muon trajectories, here defined by at least three base-tracks out of the total of five (TB) or six films (ES and TA). The processes (i) and (ii) were performed by means of an in-house developed software (Ariga et al., 2014), while (iii) was performed with the FEDRA software (Tioukov et al., 2006). Figure II.2 shows the incident angle distribution for the reconstructed tracks, where the angular resolution of the tracks is 3–10 milliradian.

The number of detected muons was then determined in rectangular bins and converted into a muon flux (cm^{-2} s^{-1} sr^{-1}) by normalizing with respect to the scanned area, the exposure time and the solid angle. The inefficiency of the films was estimated to ~10% at base-track level, which leads to the muon detection efficiency of 95–99%. We performed a correction of the measurement results taking the detection efficiency into consideration.

Table II.1: Description of detector site.

	Position (Lng/Lat/Alt)	Facing (azimuth)	Effective area (cm^2)	Exposure time
ES (Eismeer Station)	8°0′37.72″E	239.1°N	1512	9.227×10^6 sec (15
	46°34′21.40″N 3159.9 m			Mar – 30 Jun, 2017)
TA (Tunnel Site A)	8°0′28.37″E	260.5°N	1296	1.4245×10^7 sec (30
	46°34′8.44″N 3186.4 m			Jun – 12 Dec, 2017)
TB (Tunnel Site B)	8°0′14.99″E	305.1°N	1080	9.229×10^6 sec (15
	46°33′56.07″N 3215.8 m			Mar – 30 Jun, 2017)

II.5.2 Flux simulation and calibration

Before reconstructing the bedrock shape, a calibration of the flux attenuation analysis was performed by comparing the observed flux of muons through pure rock with the corresponding simulated flux. TA site provides such data (18 bins from forward direction and 60 bins from backward). The simulation is performed assuming a rock density ρ_rock of 2.68 g cm^{-3}, which is the average bulk density of the local limestone, determined from 16 samples (2.68 ± 0.02 g cm^{-3}) collected inside the railway tunnel and at the surface (Nishiyama et al., 2017)[1]. The calculation of the muon flux is based on the energy spectrum model of cosmic-ray muons and the interaction of muons with matter. We employed the spectrum model proposed by Tang et al. (2006) and the muon range for standard rock tabulated by Groom et al. (2001). The topography of the mountain and the glacier surface is taken from a 2 m mesh digital elevation model (Swisstopo© with elevation uncertainty of < 3 m) to derive the length of the muon trajectories from the topographic surface to the tunnel sites (L). Since this obstacle length varies within the bin due to the steep topography of the mountain, the bin is further divided into small hundred bins so that the roughness within the subdivided bin can be negligible. For each subdivided bin, the density-length traversed by muons is calculated by multiplying the rock density (ρ_{rock}) and the length of the muon trajectory (L). The minimum energy of muons (E_{min}) needed to penetrate this density-length can be looked up from the range table (Groom et al., 2001). The muon flux is obtained by integrating the energy spectrum from E_{min} to infinity. The muon flux values calculated for hundred subdivided bins are then averaged out and set to the representative value of the original rectangular bin.

Figure II.3 shows the observed flux as a function of rock thickness and zenith angle. The observed data at the TA site generally agrees with the theoretical curves. The ratio between the observed and simulated flux is found to be 0.94 ± 0.04 (stat), independent of the zenith angle and the rock thickness. A small deviation of this ratio (0.94) from one can be regarded as a bias of this observation due to the systematic uncertainties in the detector efficiency and the muon energy spectrum model. The statistical fluctuation (4%) is comparable to the effect of the intrinsic variability of the bedrock density (1% from rock sample measurements) on the resultant muon flux (3%). In a further analysis, therefore, this difference is calibrated when comparing the observed and simulated flux by multiplying the simulated flux by this factor (0.94).

II.5.3 Bedrock shape reconstruction

We followed the approach by Nishiyama et al. (2017) upon reconstructing the shape of the bedrock underneath the Eiger glacier. The observed muon flux for each bin yields the average bulk density $< \rho >$ of the material confined in the viewing range of the bin. Since the confined region is a mixture of bedrock and ice, the fraction of the bedrock (x) is related to the bulk density of a bedrock (ρ_{rock}) and that of an ice component ρ_{ice} = 0.85 g.cm^{-3} by Huss (2013) through the relationship:

$$< \rho > = \rho_{rock} \cdot x + \rho_{ice} \cdot (1 - x)$$

Once x is obtained for each bin, the boundary position can be plotted at a distance Lx from the detector position. Here, a constant density is inferred for the ice because snow and firn exhibit a lower density in only the uppermost 10 m of the glacier (Huss, 2013), with significant density changes only occurring in the varying snow cover layer or in the presence of crevasses (Fischer, 2011), which are almost absent along the reconstructed glacier reach (Fig. II.1). The resulting uncertainty is in the order of the DEM error (Fischer, 2011) and thus negligible compared to the scale of our observation. The three-dimensional representation and error estimation are performed as follows. First, the observed muon flux dataset is multiplied to hundred synthetic datasets by adding a statistical fluctuation for each bin. Specifically, a random variable following a Gaussian distribution with a standard deviation of N is added when the number of muons in the bin is N. Subsequently, the ice-rock boundary position is calculated for each flux data in every synthetic dataset and plotted in a 3D space. In the end the plotted point clouds are re-sampled in a cylindrical coordinate system with the axis parallel to the glacial flow direction (south-west) with a division of Δz = 40 m along the axis and $\Delta\varphi$ = 12° in azimuth. For each divided cylindrical bin (z, φ), the best position of the ice-bedrock boundary is given by taking the average of the radial coordinates of the points. The error of the boundary position is given by their standard deviation (yellow bands in Fig. II.5). A synthetic data reproduction was introduced so that the magnitude of the statistical fluctuations is properly taken into account after re-sampling. Cylindrical bins, which contain less than 10 points, were neglected as lack of statistics and resolving power.

II.6 Acknowledgements

This research is supported by Swiss National Science Foundation as an interdisciplinary research project (159299). We warmly acknowledge M. Nakamura and his colleagues from F-lab, Nagoya University. We would like to express our gratitude to the Jungfraubahnen for the enormous help with the detector installation, especially S. Michel. The digital elevation model and high-resolution orthophoto of the Jungfrau region were provided by the Federal office of topography, Swisstopo. We would like to acknowledge the precious contributions of the technical staff from the LHEP and the Institute for Geological Sciences of the University of Bern. P.G.V. acknowledges support from SNFS Grant PP00P2_170559.

II.7 Author contributions

R.N. performed the data analysis. R.N. and D.M. produced the figures. R.N. and F.S. wrote the text, with contributions by P.G.V., T.A. was responsible for the film production and related technical developments. M.V. and A.A. developed and maintained the automatic readout microscope for emulsion films. D.M. and A.L. performed the geologic surveys at the Jungfrau region. C.P. was responsible for the film scanning. P.S., A.E. and F.S. designed the research together with R.N. and coordinated the collaboration.

II.8 References

Adams, J. M. and Hinze, W. J.: *The gravity-geologic technique of mapping varied bedrock topography*. In: Geotechnical and environmental geophysics, Vol. 3, ed. Ward, S. H., 99–106, Soc. Explor. Geophys. 1990.

Alvarez et al.: *Search for Hidden Chambers in the Pyramids*, Science, 167, 832-839, https://doi.org/10.1126/science.167.3919.832, 1970.

Ambrosino, F. et al.: *Joint measurement of the atmospheric muon flux through the Puy de Dôme volcano with plastic scintillators and Resistive Plate Chambers detectors*, J. Geophys. Res. Solid Earth, 120, 7290-7307, https://doi.org/10.1002/2015JB011969, 2015.

Anders, A. M., Mitchell, S. G., and Tomkin, J. H.: *Cirques, peaks, and precipitation patterns in the Swiss Alps: Connections among climate, glacial erosion and topography*, Geology, 38, 239-242, https://doi.org/10.1130/G30691.1, 2010.

Annecchione, M. A., Chouteau, M., and Keating, P.: *Gravity interpretation of bedrock topography: the case of the Oak Ridges Moraine, southern Ontario, Canada*, J. Appl. Geophys., 47, 63-81, https://doi.org/10.1016/S0926-9851(01)00047-7, 2001.

Ariga, A. and Ariga, T.: *Fast 4π track reconstruction in nuclear emulsion detectors based on GPU technology*, J. Instrum., 9, P04002, https://doi.org/10.1088/1748-0221/9/04/P04002, 2014.

Ariga, A.: *A nuclear emulsion detector for the muon radiography of a glacier structure*, Instruments, 2, 7, https://doi.org/10.3390/instruments2020007, 2018.

Asorey, H. et al.: *Muon Tomography sites for Colombia volcanoes*. arXiv:1705.09884, 2017.

Barnaba, C., et al.: *The buried shape of an alpine valley from gravity surveys, seismic and ambient noise analysis*, Geophys. J. Int., 180, 715-733, https://doi.org/10.1111/j.1365-246X.2009.04428.x, 2010.

Bindschadler, R.: *The importance of pressurized subglacial water in separation and sliding at the glacier bed*, J. Glaciol., 29, 3-19, https://doi.org/10.1017/S0022143000005104, 1983.

Braun, J., Zwartz, D., and Tomkin, J. H.: *A new surface process model combining glacial and fluvial erosion*, Ann. Glaciology, 28, 282-290, https://doi.org/10.3189/172756499781821797, 1999.

Brocklehurst, S. H. and Whipple, K. X.: *Glacial erosion and relief production in the eastern Sierra Nevada, California*, Geomorphology, 42, 1-24, https://doi.org/10.1016/S0169-555X(01)00069-1, 2002.

Brocklehurst, S. H. and Whipple, K. X.: *Hypsometry of glaciated landscapes*, Earth Surf. Process. Landf., 29, 907-926, https://doi.org/10.1002/esp.1083, 2004.

Carbone, D., et al.: *An experiment of muon radiography at Mt Etna (Italy)*, Geophys. J. Int., 196, 633-643, https://doi.org/10.1093/gji/ggt403, 2014.

Cossart, E., Braucher, R., Fort, M., Bourlès, D. L., and Carcaillet, J.: *Slope instability in relation to glacial debuttressing in alpine areas (Upper Durance catchment, southeastern France): Evidence from field data and 10Be cosmogenic ray exposure ages*, Geomorphology, 95, 3-6, https://doi.org/10.1016/j.geomorph.2006.12.022, 2008.

Dürst Stucki, M. and Schlunegger, F.: *Identification of erosional mechanisms during past glaciations based on a bedrock surface model of the Central European Alps*, Earth Planet. Sci. Lett., 384, 57-70, https://doi.org/10.1016/j.epsl.2013.10.009, 2013.

Echelmayer, K. and Kamb, B.: *Glacier flow in a curving channel*, J. Glaciology, 33, 281-292, https://doi.org/10.1017/S0022143000008856, 1987.

Egholm, D. L., Nielsen, S. B., Pedersen, V. K., and Lesemann, J. E.: *Glacial effects limiting mountain height*, Nature, 460, 884-887, https://doi.org/10.1038/nature08263, 2009.

Ereditato, A.: *The study of neutrino oscillations with emulsion detectors*, Adv, High Energy Phys., 2013, 382172, 2013.

Fischer, A.: *Comparison of direct and geodetic mass balances on a multi-annual time scale*, Cryosph., 5, 107-124, https://doi.org/10.5194/tc-5-107-2011, 2011.

Fisher, E., et al.: *Determination of bedrock topography beneath the Greenland ice sheet by three-dimensional imaging radar sounding data*, J. Geophys. Res., 94, 2874-2882, https://doi.org/10.1029/JB094iB03p02874, 1989.

Fujii, H., et al.: *Performance of a remotely located muon radiography system to identify the inner structure of a nuclear plant*, Prog. Theor. Exp. Phys., 2013, 073C01, https://doi.org/10.1093/ptep/ptt046, 2013.

George, E. P.: *Cosmic rays measure overburden of tunnel*, Commonwealth Engineer, 455, 1955.

Godon, C., Mugnier, J. L., Fallourd, R., Paquette, J. L., and Pohl, A., and Buoncristani: *The Bossons glacier protects Europe's summit from erosion*, Earth Planet. Sci. Lett., 375, 135-147, https://doi.org/10.1016/j.epsl.2013.05.018, 2013.

Groom, D. E., Mokhov, N. V., and Striganov, S. I.: *Muon stopping power and range tables 10 MeV-100 TeV*, At. Data Nucl. Data Tables, 78, 183-356, https://doi.org/10.1006/adnd.2001.0861, 2001.

Guardincerri, E., et al.: *3D cosmic ray muon tomography from an underground tunnel*, Pure Appl. Geophys., 174, 2133-2141, https://doi.org/10.1007/s00024-017-1526-x, 2017.

Hallet, B.: *A theoretical model of glacial abrasion*, J. Glaciol., 17, 209-222, https://doi.org/10.1017/S0022143000013551, 1979.

Hallet, B.: *Glacial quarrying: a simple theoretical model*, Ann. Glaciol., 22, 1-8, https://doi.org/10.1017/S0260305500015147, 1996.

Hallet, B., Hunter, L., and Bogen, J.: *Rates of erosion and sediment evacuation by glaciers: A review of field data and their implications*, Glob. Planet. Change, 12, 213-235, https://doi.org/10.1016/0921-8181(95)00021-6, 1996.

Herman, F., Beaud, F., Champagnac, J.-. D., Lemieux, J.-. M., and Sternai, P.: *Glacial hydrology and erosion patterns: A mechanism for carving glacial valleys*, Earth Planet. Sci. Lett., 310, 498-508, https://doi.org/10.1016/j.epsl.2011.08.022, 2011.

Herman, F., et al.: *Erosion by an Alpine glacier*, Science, 350, 193-195, https://doi.org/10.1126/science.aab2386, 2015.

Herman, F., Braun, J., Deal, E., and Prasicek, G.: *The response time of glacial erosion*. J. Geophys. Res. – Earth Surface, 123, 801–817, 2018.

Hooke, R. L. B.: *Positive feedbacks associated with erosion of glacial cirques and overdeepenings*, Geol. Soc. Amer. Bull., 103, 1104-1108, 1991.

Horberg, L. and Anderson, R. C.: *Bedrock topography and Pleistocene glacial lobes in central United States*, J. Geology, 64, 101-116, https://doi.org/10.1086/626328, 1956.

Huss, M.: *Density assumptions for converting geodetic glacier volume change to mass change*, Cryosphere, 7, 877-887, https://doi.org/10.5194/tc-7-877-2013, 2013.

Huss, M. and Farinotti, D.: *Distributed ice thickness and volume of all glaciers around the globe*, J. Geophys. Res., 117, F04010, https://doi.org/10.1029/2012JF002523, 2012.

Huss, M. and Fischer, M.: *Sensitivity of very small glaciers in the Swiss Alps to future climate change*, Frontiers in Earth Science, 4, 34, https://doi.org/10.3389/feart.2016.00034, 2016.

Jourde, K., Gibert, D., Marteau, J., Bremond dArs, J., and Komorowski, J. C.: *Muon dynamic radiography of density changes induced by hydrothermal activity at the La Soufrière of Guadeloupe volcano*, Scientific Reports, 6, 33406, https://doi.org/10.1038/srep33406, 2016.

MacGregor, K. R., Anderson, R. S., and Waddington, E. D.: *Numerical modeling of glacial erosion and headwall processes in alpine valleys*, Geomorphology, 103, 189-204, https://doi.org/10.1016/j.geomorph.2008.04.022, 2009.

Mair, D., Lechmann, A., Herwegh, M., Nibourel, L., and Schlunegger, F.: *Linking Alpine deformation in the Aar Massif basement and its cover units – the case of the Jungfrau-Eiger mountains (Central Alps, Switzerland)*, Solid Earth, 9, 1099-1122, https://doi.org/10.5194/se-9-1099-2018, 2018.

Mey, J., et al.: *Glacial isostatic uplift of the European Alps*, Nat. Comm., 7, 13382, https://doi.org/10.1038/ncomms13382, 2016.

Mitchell, S. G. and Humphries, E. E.: *Glacial cirques and the relationship between equilibrium line altitudes and mountain range height*, Geology, 43, 35-38, https://doi.org/10.1130/G36180.1, 2014.

Murray, T., Booth, A., and Rippin, D. M.: *Water-content of glacier-ice: Limitations on estimates from velocity analysis of surface ground-penetrating radar surveys*, J. Environ. Eng. Geophys., 12, 87-99, https://doi.org/10.2113/JEEG12.1.87, 2007.

Nishio, A., et al.: *Development of nuclear emulsion detector for muon radiography*, Phys. Procedia, 80, 74-77, https://doi.org/10.1016/j.phpro.2015.11.084, 2015.

Nishiyama, R., et al.: *Monte Carlo simulation for background study of geophysical inspection with cosmic-ray muons*, Geophys. J. Int., 206, 1039-1050, https://doi.org/10.1093/gji/ggw191, 2016.

Nishiyama, R., et al.: *First measurement of ice-bedrock interface of alpine glaciers by cosmic muon radiography*, Geophys. Res. Lett., 44, 6244-6251, https://doi.org/10.1002/2017GL073599, 2017.

Oláh, L., Tanaka, H. K. M., Ohminato, T., and Varga, D.: *High-definition and low-noise muography of the Sakurajima volcano with gaseous tracking detectors*, Sci. Rep., 8, 3207, https://doi.org/10.1038/s41598-018-21423-9, 2018.

Patrignani, C., et al.: *The review of particle physics*, Chin. Phys. C 40, 100001, https://doi.org/10.1088/1674-1137/40/10/100001, 2016.

Pederson, V. K. and Egholm, D. L.: *Glaciations in response to climate variations preconditioned by evolving topography*, Nature, 493, 206-210, https://doi.org/10.1038/nature11786, 2013.

Sanders, J. W., Cuffey, K. M., MacGregor, K. R., Kavanaugh, J. L., and Dow, C. F.: *Dynamics of an alpine cirque glacier*, Am. J. Sci., 310, 753-773, https://doi.org/10.2475/08.2010.03, 2010.

Sanders, J. W., Cuffey, K. M., Moore, J. R., MacGregor, K. R., and Kavanaugh, J. L.: *Periglacial weathering and headwall erosion in cirque glacier bergschrunds*, Geology, 40, 779-782, https://doi.org/10.1130/G33330.1, 2012.

Saracino, G., et al.: *The MURAVES muon telescope: technology and expected performances*, Ann. Geophys., 60, S0103, https://doi.org/10.4401/ag-7378, 2017.

Scherler, D.: *Climatic limits to headwall retreat in the Khumbu Himalaya*, eastern Nepal, Geology, 42, 1019-1022, https://doi.org/10.1130/G35975.1, 2014.

Schrott, L. and Sass, O.: *Application of field geophysics in geomorphology: advances and limitations exemplified by case studies*, Geomorphology, 93, 55-73, https://doi.org/10.1016/j.geomorph.2006.12.024, 2008.

Sharp, M., et al.: *Geometry, bed topography and drainage system structure of the Haut Glacier d'Arolla, Switzerland*. Earth Surf. Proc. Landf., 18, 557-571, https://doi.org/10.1002/esp.3290180608, 1993.

Sternai, P., Herman, F., Valla, P. G., and Champagnac, J.-. D.: *Spatial and temporal variations of glacial erosion in the Rhône valley (Swiss Alps): Insights from numerical modeling*, Earth Planet Sci. Lett., 368, 119-131, https://doi.org/10.1016/j.epsl.2013.02.039, 2013.

Studinger, M., Bell, R. E., and Tikku, A. A.: *Estimating the depth and shape of subglacial Lake Vostok's water cavity from aerogravity data*, Geophys. Res. Lett., 31, L12401, https://doi.org/10.1029/2004GL019801, 2004.

Tanaka, H. K. M., et al.: *High resolution imaging in the inhomogeneous crust with cosmic-ray muon radiography: The density structure below the volcanic crater floor of Mt. Asama, Japan*, Earth Planet. Sci. Lett., 263, 104-113, https://doi.org/10.1016/j.epsl.2007.09.001, 2007.

Tang, A., Horton-Smith, G., Kudryavtsev, V. A., and Tonazzo, A.: *Muon Simulations for Super-Kamiokande, KamLAND and CHOOZ*, arXiv:hep-ph/0604078, 2006.

Tioukov, V., et al.: *The FEDRA—Framework for emulsion data reconstruction and analysis in the OPERA experiment*, Nucl. Instrum. Meth. A, 559, 103-105, https://doi.org/10.1016/j.nima.2005.11.214, 2006.

Ugelvig, S. V., Egholm, D. L., and Iverson, N. R.: *Glacial landscape evolution by subglacial quarrying: A multiscale computational approach*, J. Geophys. Res. Earth Surf., 121, 2042-2068, https://doi.org/10.1002/2016JF003960, 2016.

Valla, P. G., Shuster, D. L., and Beek, P.: *Significant increase in relief of the European Alps during mid-Pleistocene glaciations*, Nat. Geosci., 4, 688-692, https://doi.org/10.1038/ngeo1242, 2011.

Declaration of Consent

on the basis of Article 30 of the RSL Phil.-nat. 18

Name/First Name:	Lechmann Alessandro Diego
Matriculation Number:	08-911-810
Study program:	Earth Sciences Bachelor ☐ Master ☐ Dissertation ☐
Title of the thesis:	An integrated geological-geophysical approach to subsurface interface reconstruction of muon tomography measurements in high alpine regions
Supervisors:	Prof. Dr. Fritz Schlunegger & Prof. Dr. Paola Scampoli

I declare herewith that this thesis is my own work and that I have not used any sources other than those stated. I have indicated the adoption of quotations as well as thoughts taken from other authors as such in the thesis. I am aware that the Senate pursuant to Article 28. RSL Phil.-nat. 05 is authorised to revoke the title awarded on the basis of this thesis.
For the purposes of evaluation and verification of compliance with the declaration of originality and regulations governing plagiarism, I hereby grant the University of Bern the right to process my personal data and to perform the acts of use this requires, in particular, to reproduce the written thesis and to store it permanently in a database, and to use said database, or to make said database available, to enable comparison with future theses submitted by others.

Place/Date

Signature